UNIVERSITY OF
LIVERPOOL
Department of Chemistry

Intracellular delivery and fate of peptide-capped gold nanoparticles

Thesis submitted in accordance with the requirements of the University of Liverpool for the degree of Doctor in Philosophy

by

Yann Sébastien Romain Cesbron

OCTOBER 2010

To Martyna and Zoé

This work is supported by the Engineering and Physical Sciences Research Council and the Biotechnology and Biological Sciences Research Council

Intracellular delivery and fate of peptide-capped gold nanoparticles

Yann Cesbron

Abstract

Gold nanoparticles have unique properties that make them very attractive molecular imaging probes. The thiol chemistry provides an easy and direct functionalisation route and their strong absorption cross-section allow their imaging down to diameters of 1.4 nm by the absorption-based photothermal microscopy. The development of the new Liverpool photothermal microscope presented here opens new avenues in molecular imaging as the necessary extensive study of peptide-capped nanoparticles internalisation and intracellular fate could then be probed.

The non-specific endosomal mediated uptake of gold nanoparticles in mammalian cells was shown to increase over time (plateau after 2.5–3h) and also linearly with the nanoparticle concentration, and induced a proteolytic degradation of the monolayer by cathepsin L. Protease cathepsin L was demonstrated to have a broad cleavage potential and would therefore be detrimental to nanoparticle functionalisation strategies without careful planning. A combined protease inhibition and chloroquine endosomal disruption reduced the degradation significantly, but the interaction of the nanoparticles with the endosomal membrane debris prevented a cytosolic dispersion. Likewise, CPP Tat and HA2 fusion peptides functionalised nanoparticles were also used in a endosome disruption strategy. An increase of uptake was observed with Tat and HA2, but no additive effect was observed and no cytosolic localisation was detected.

A streptolysin O pore forming mediated entry was then examined in combination with a variation of the monolayer non-specific properties regulated by the introduction of a proportion of poly(ethylene glycol) in the monolayer. In absence of toxin, PEG was shown to reduce the nanoparticle internalisation, when an increased uptake of the PEG terminated nanoparticles was observed otherwise. However, in both cases no cytosolic nanoparticles could be observed. Interestingly, the effect was more important when the non-specific interactions were only partially reduced, with a proportion of 10 % of PEG terminated ligands in the monolayer, suggesting that an interaction with the cell membrane was necessary to promote the internalisation.

A series of over ten articles on "stripy nanoparticles" and their supposed extraordinary properties was critically reviewed and revisited. FFT analysis of the published STM images revealed the artefact origin of the stripes observed on alkane thiol functionalised gold nanoparticles. The interaction of mixed MUS/OT functionalised gold nanoparticles with cells was further shown to display a clear endocytosis mediated internalisation and broke down the claim of cytosolic delivery without membrane disruption.

Finally, with a view of using them as delivery agents, the damage of the wall of nanoparticles filled hollow polymer microcapsules was achieved upon laser illumination. Photothermal images of a capsule revealed a map of the nanoparticle density within the inside of the cavity and subsequent targeting of high nanoparticle density in the vicinity of the wall did not result in successful shell damage, when the illumination at a less dense point exhibited a disruption of the capsule.

Acknowledgments

The author is really grateful to Dr. Raphaël Lévy and would like to thank him for his help throughout his research and for his supervision, and for the many profitable scientific and more general discussions. Pr. Mathias Brust is also thanked for supervising this project, together with EPSRC for funding it.

The research presented in this manuscript is the result of collaborations with multiple people from the School of Biological Sciences and the Chemistry Department at the University of Liverpool, but also from Université Bordeaux I in France and from the Philipps Universität Marburg in Germany.

Therefore Pr. Brahim Lounis is thanked for hosting the author in his Nanophotonics group for a few days to get a first experience with their optical set up and Dr. David Lasne for his help with the optical part of the set up and showing the whereabouts of their photothermal microscope.

The authors also express gratitude to Dr. Violaine Sée for the fluorescence confocal microscopy imaging and its subsequent analysis in chapter 3, Sect. 3.1 and Sect. 3.2 and in chapter 4, Sect. 4.1.1 and more generally for her central role in the planning of the experiments conducted in these sections.

Credits must also be given to Dr. Paula Nativo for the TEM images in chapter 3, Sect. 3.1 and in chapter 4, Sect. 4.1, to Pr. Mathias Brust for discussions and experiments planning related to daunorubicin-functionalised nanoparticles, to Samia Saleemi for daunorubicin-functionalised nanoparticles preparation and cell the related work in Sect. 3.3.1, to Dr. Daniel J Rigden for the Bioinformatics cleavage prediction of cathepsin L, to Dr. Loretta del Mercato who produced the microcapsules that were used in chapter 6 and Dr. Pilar Rivera Gil and Pr. Wolfgang Parak have participated in conversations related to the microcapsule, to Dr. Spiller for some useful advices on optics and microscopy related issues, but also on cell imaging and his help in the laser exposition test of the micro-capsules with different laser sources, and to Pr. Fernig for many instructive informal scientific (*et al.*) discussions and their incidental interesting suggestions.

Dr. Paul Free had a central role and did the gold nanoparticles preparation,

cell culture and nanoparticles incubation in chapter 3, Sect. 3.1 and Sect. 3.2, in chapter 4, Sect. 4.1 and in chapter 5, Sect. 5.2.2; the *in vitro* unquenching of nanoparticles and protease induced monolayer degradation experiments in chapter 3.

Likewise, Umbreen Shaheen did a lot of work and carried on the nanoparticles preparation, cell culture, nanoparticles incubation and streptolysin O concentration optimisation in chapter 3 Sect. 3.3.2 and chapter 4 Sect. 4.2 and the TEM imaging in the later section.

Chris P Shaw did also bring his skills in nanoparticles synthesis in chapter 3 Sect. 3.3.2, chapter 4 Sect. 4.2 and performed the synthesis, TEM imaging, colloidal stability and solubility assays of "stripy" nanoparticles in chapter 5, Sect. 5.2.2.

In conclusion the author would also like to thank the numerous persons, coming from all around the world, who were involved in building a great working, friendly and multi-cultural atmosphere in his former office and laboratory, and last but not least, a special *dziękuję* is sent to Martyna for her support during the writing of this manuscript.

Table of Contents

List of Figures

List of Tables

List of Abbreviations

ACS	Absorption correlation spectroscopy
AMPA	2-amino-3-(5-methyl-3-oxo-1,2- oxazol-4-yl)propanoic acid
AOM	Acousto-optic modulator
BSA	Bovine serum albumin
CCD	Charge-coupled device
CFP	Cyan fluorescent protein
CPP	Cell penetrating peptide
CW	Continuous wave
DNA	Desoxyribonucleic acid
DTT	Dithiothretiol
EBFP	Enhanced blue fluorescent protein
ECFP	Enhanced cyan fluorescent protein
ECM	Extracellular matrix
EGFP	Enhanced green fluorescent protein
EMCCD	Electron-multiplying charge-coupled device
EYFP	Enhanced yellow fluorescent protein
FCS	Fluorescence correlation spectroscopy
FDA	Fluorescein diacetate
FFT	Fast Fourier transform
FITC	Fluorescein isothiocyanate
FP	Fluorescent protein
FRAP	Fluorescence recovery after photobleaching
FRET	Förster resonance energy transfer
FWHM	Full width at half maximum
GFP	Green fluorescent protein
GSD	Ground state depletion
HR-TEM	High resolution transmission electron microscopy
ICP-AES	Inductively coupled plasma atomic emission spectroscopy
IR	Infrared
LbL	Layer-by-layer
LISNA	Laser induced scattering around a nano-absorber
MPA	Mercaptopropionic acid
mRFP	Monomeric red fluorescent protein
MUS	Sodium 11-mercapto-1-undecanesulphonate
Nd:YLF	Neodymium-doped yttrium lithium fluoride
NIR	Near infrared

NLS	Nuclear localisation signal
nM	Nano molar
NP	Nanoparticle
OT	1-octanethiol
PA-GFP	Photoactivable green fluorescent protein
PAH	poly(allylamine hydrochloride)
PALM	Photoactivable localisation microscopy
PDADMAC	poly(diallyl dimethyl ammonium chloride)
PEG	Poly(ethylene glycol)
PHI	Photothermal heterodyne imaging
PI	Propidium iodide
PSS	poly(styrene sulfonate)
QD	Quantum dot
ROI	Region of interest
SAM	Self-assembled monolayer
SD	Standard deviation
SE	Standard error of the mean
SERS	Surface enhanced raman spectroscopy
SLO	Streptolysin O
SNaPT	Single nanoparticles photothermal tracking
SPR	Surface plasmon resonance
SSIM	Saturated structured illumination microscopy
STED	Stimulated emission-depletion
STM	Scanning tunnelling microscopy
STORM	Stochastic optical reconstruction microscopy
TEM	Transmission electron microscopy
THF	Tetrahydrofuran
TIFF	Tagged image file format
UV	Ultraviolet
YFP	Yellow fluorescent protein

Chapter 1

Introduction

Biomolecular imaging is at a crossroad between three of the major historical scientific fields of biology, chemistry and physics and benefits from advances in those three fields. Its growing influential input in cell biology since the second half of the twentieth century has essentially been driven by advances in imaging techniques, probes development and technological progress.

Köhler bright field illumination, Zernike's discovery of phase contrast[1] — celebrated with a Nobel Prize in physics in 1953 — and the differential interference contrast developed by Nomarski pioneered light microscopy and set the bases of modern optical microscopy. It provided the necessary tools to access the subcellular level on live cells, as shown by the first observations of the birefringence of the mitotic spindle in sea urchins by Schmidt[2,3] in 1937 or years later (1953) of their detailed structure[4] by Inoué.

Alongside optical microscopy, Ruska made the transmission electron microscope come into light in 1931. After surpassing the resolution of optical microscope (1933) it became increasingly important by obtaining growlingly detailed view at the cellular and subcellular level,[5,6] from the first electron micrograph of an intact whole fibroblast cell made by Porter *et al.*[7] in 1945 to the 3D structure of a membrane channel at the end of the twentieth century.[8]

The principles of confocal laser scanning microscopy were introduced in 1957 by Minsky, but only started to fulfill their potential during the 1980's and 1990's with the improvement of laser technology and detection capabilities. The development of synthetic organic dyes, fluorescent protein or quantum dots could be fully exploited by laser scanning confocal fluorescence microscopy in the last twenty years to label and follow intracellular components and their interactions. The latest challenge of a molecular resolution has just started to be tackled in the recent years with the development of the new super resolution techniques such as the stimulated emission-depletion (STED) microscope or the photoactivable localisation microscopy

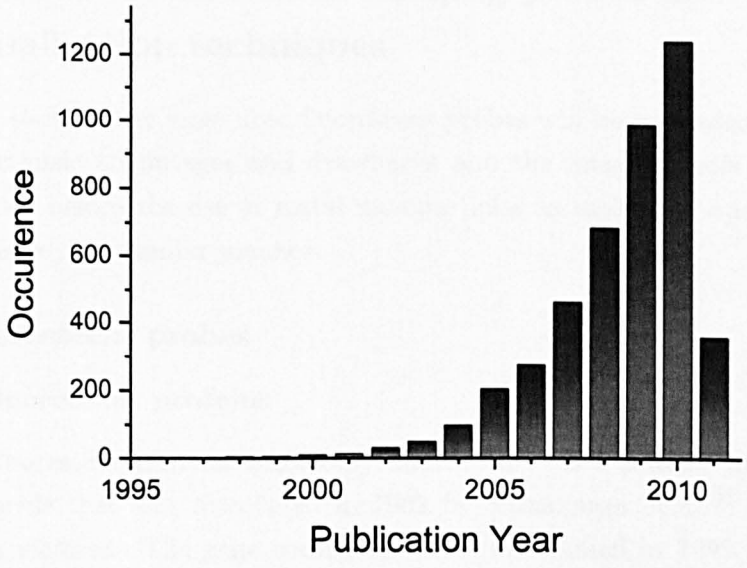

Fig. 1.1 – Uprising interest at the interface between nanoparticles and biology. A search on the database publication of ISI Web of Knowledge (26 April 2011) with the fields "gold nanoparticle∗" and "cell∗" (chosen as topics) has returned a number of 4447 papers.

(PALM), and the concomitant development of photoactivable or photoswitchable fluorescent proteins or dyes.

Although these super resolution techniques enhance the possibilities of molecular imaging by increasing dramatically the resolution, the time resolution or the long term imaging are still issues that remains to be tackled.

Therefore complementary techniques and probes able to bring other information are needed. Photothermal microscopy[9,10] and metal nanoparticles probes[11,12] are one candidate. Indeed, the absorption-based technique photothermal microscopy was shown to allow imaging of metal nanoparticles,[13] quantum dots[14] and carbon nanotubes.[15] Diffusion properties of gold nanoparticles are also accessible with tracking[16] and absorption correlation spectroscopy.[17] Among those nanomaterials, stable and water-soluble gold nanoparticles[11,12] can be functionalised to various specific targets[12] in a controlled manner.[18,19]

Since the breakthrough in the synthesis of gold nanoparticles by the Brust-Schiffrin method[20] in 1994, their internalisation in cells has attracted a rising interest in the scientific community and is now growing exponentially (Fig. 1.1). However, strategies for a controlled internalisation of gold bioconjugates are still to be developed, and a meticulous assessment of the integrity of their function inside cells will also need to be demonstrated before their intracellular conjugation with molecular imaging targets can be trustfully assayed.

1.1 Current biomolecular imaging probes and visualisation techniques

Examples of some of the most used fluorescent probes will be presented here alongside their intrinsic advantages and drawbacks and the imaging tools available to visualise them, before the use of metal nanoparticles as molecular imaging probes will be discussed in a similar manner.

1.1.1 Fluorescent probes

1.1.1.1 Fluorescent proteins

The green fluorescent protein, commonly named GFP, is a protein constituted of 238 amino acids that was discovered in 1962 by Shimomura *et al.*[21] in the jellyfish *Aequora victoria.* The gene coding for GFP was cloned in 1992.[22] It is only two years later that GFP was first demonstrated to monitor gene expression and protein localisation in the bacteria *Escherichia coli* and the nematode *Caenorhabditis elegans* by Chalfie *et al.*[23] The wild type GFP possesses two excitation peaks at 395–397 nm and 470–475 nm (variation depending on the conditions)[24] and one emission peak at 504 nm. The enhanced green fluorescent protein (eGFP) was created by modifying the sequence of the wild type GFP to improve its brightness and photostability in cells and allow for the common 488 nm argon laser line to be used for its excitation (λ_{exc} = 488 nm, λ_{em} = 509 nm). Tsien *et al.* did other sequence alterations, which provided three additional colours[24,25] with blue (eBFP: λ_{exc} = 380 nm, λ_{em} = 440 nm), cyan (eCFP: λ_{em_1} = 434 nm, λ_{em_1} = 476 nm; λ_{em_2} = 452 nm, λ_{em_2} = 505 nm) and yellow (eYFP: λ_{exc} = 514 nm, λ_{em} = 527 nm). In 1999, Matz *et al.*[26] added red to the set of available colours, when they identified and cloned the fluorescent protein DsRed (λ_{exc} = 558 nm, λ_{em} = 583 nm) coming from the reef coral *Anthozoa* species *Discosoma striata* "red". In the last ten years a series of further advances in fluorescent proteins were reported starting in 2002 with the monomeric DsRed[27] (mRFP1; λ_{exc} = 584 nm, λ_{em} = 607 nm), the first photoconvertible Kaede[28] and the first photoactivable fluorescent proteins[29] (PA-GFP), continuing in 2004 with the new monomeric fruit FPs[30] derived from the mRFP1 (mHoneydew, mBanana, mOrange, tdTomato, mTangerine, mStrawberry, and mCherry). A modest sample of the colours available is presented in Fig. 1.2.

1.1.1.2 Organic fluorescent dyes

In 1942, Coons *et al.* did the first observation of pneumococcal antigen by immunofluorescence conjugating for the first time the antibody to fluorescein-isocyanate.[31] In the end of the sixties and seventies appeared two of the blue stains that are still

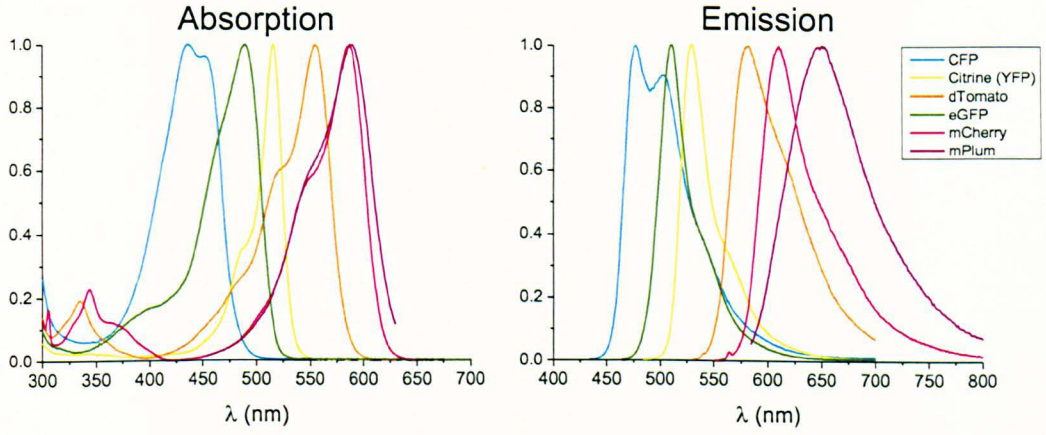

Fig. 1.2 – Absorption and emission spectra of some fluorescent proteins. Example of historical and recent engineered fluorescent proteins with emission spread along the visible spectrum: CFP, YFP, dTomato, eGFP, mCherry and mPlum. Left: plot of the absorption spectra of the fluorescent proteins. Right: plot of the emission spectra of the fluorescent proteins. The data was downloaded from the Tsien Laboratory website: http://tsienlab.ucsd.edu.

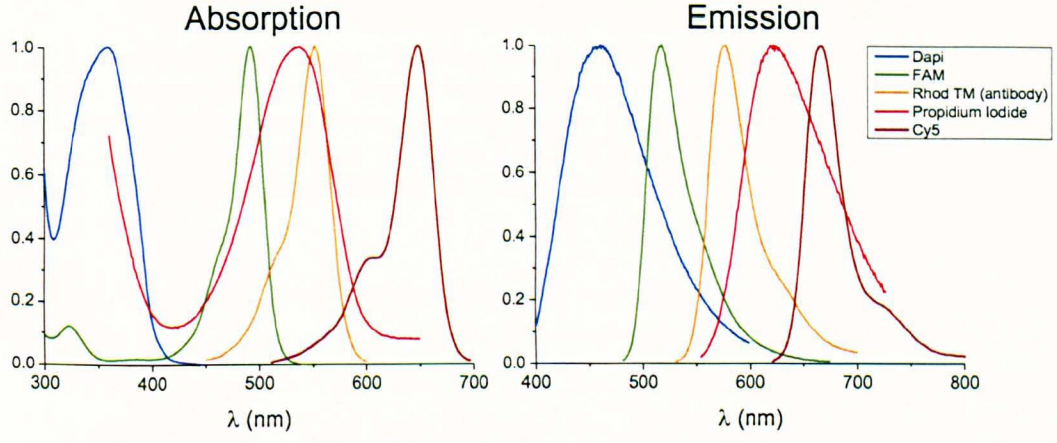

Fig. 1.3 – Absorption and emission spectra of some fluorescent dyes. Example of historical and recent engineered fluorescent proteins with emission spread along the visible spectrum: DAPI, FAM, Rhod TM (antibody), propidium iodide and Cy5. Left: plot of the absorption spectra of the fluorescent dyes. Right: plot of the emission spectra of the fluorescent dyes. The data was downloaded from the Tsien Laboratory website: http://tsienlab.ucsd.edu.

the main used ones to mark cell nuclei, Hoechst[32] ($\lambda_{exc} = 345\,\text{nm}$, $\lambda_{em} = 480\,\text{nm}$) and DAPI[33] ($\lambda_{exc} = 345\,\text{nm}$, $\lambda_{em} = 455\,\text{nm}$; see Fig. 1.3), which bind to DNA, but also a red dye, propidium iodide[34] ($\lambda_{exc} = 538\,\text{nm}$, $\lambda_{em} = 617\,\text{nm}$), which is commonly used to label cells to assess DNA content (binds to it) and their viability (cell impermeable). They can be both used on live and fixed cells, although Hoechst is more efficient in crossing the plasma membrane than DAPI and is therefore often preferred for live cells. Still in the end of the seventies, Wulf *et al.*[35] demonstrated

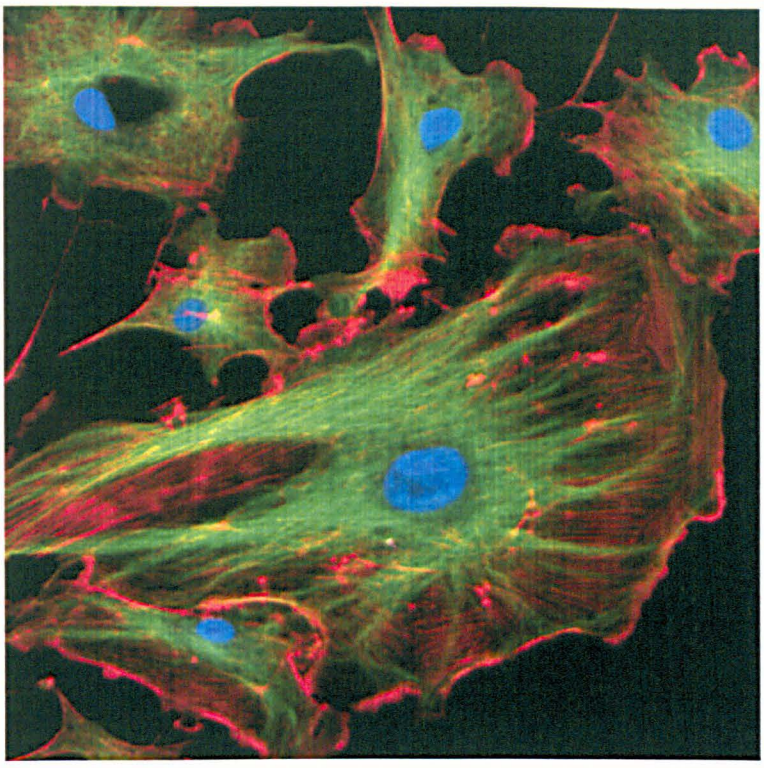

Fig. 1.4 – Bovine pulmonary arthery endothelial cells stained by a combination of three fluorescent dyes. Merged image of the three fluorescence channels (blue, green, red). DAPI (blue) stains the nuclei, while Bodipy FL goat anti-mouse IgG (green) stains tubulin and F-actin is stained by Texas Red X-Phalloidin. This image is in the public domain and was downloaded from the following source: http://rsb.info.nih.gov/ij/images.

the first labelling of a cell component, actin microfilaments (Fig. 1.4), with a synthetic dye (FITC conjugated to phalloidin) that was not an antibody.

In 1980, Tsien *et al.*[36] reported the first fluorescent probes (BAPTA and Quin2) of intracellular Ca^{2+}. They later improved the ion selectivity and fluorescence intensity of the dyes,[37] before an other major advancement with the visible wavelength excitable dyes Rhod-2, Fluo-2 and Fluo-3.[38] Other broadly used synthetic organic dyes include cyanines dyes with Cy3 in the yellow ($\lambda_{exc} = 550\,\text{nm}$, $\lambda_{em} = 570\,\text{nm}$) and Cy5 in the red ($\lambda_{exc} = 650\,\text{nm}$, $\lambda_{em} = 670\,\text{nm}$), and one of the brightest family, the Alexa dyes,[39] with wavelengths matching the most used dyes and laser lines within the spectra with excitations such as 343 nm, 401 nm, 517 nm, 530 nm, 579 nm or 632 nm.

1.1.1.3 Quantum dots

The synthesis of quantum dots was first reported in 1981 by Ekimov[40] and in 1982 by Efros.[41] Quantum dots (QDs) are nanocrystals made of two types of semiconductor arranged in a core/shell manner. Their small sizes, which range in the order of 2-10 nm,[42,43] grant them special electronic properties, which are the consequence of

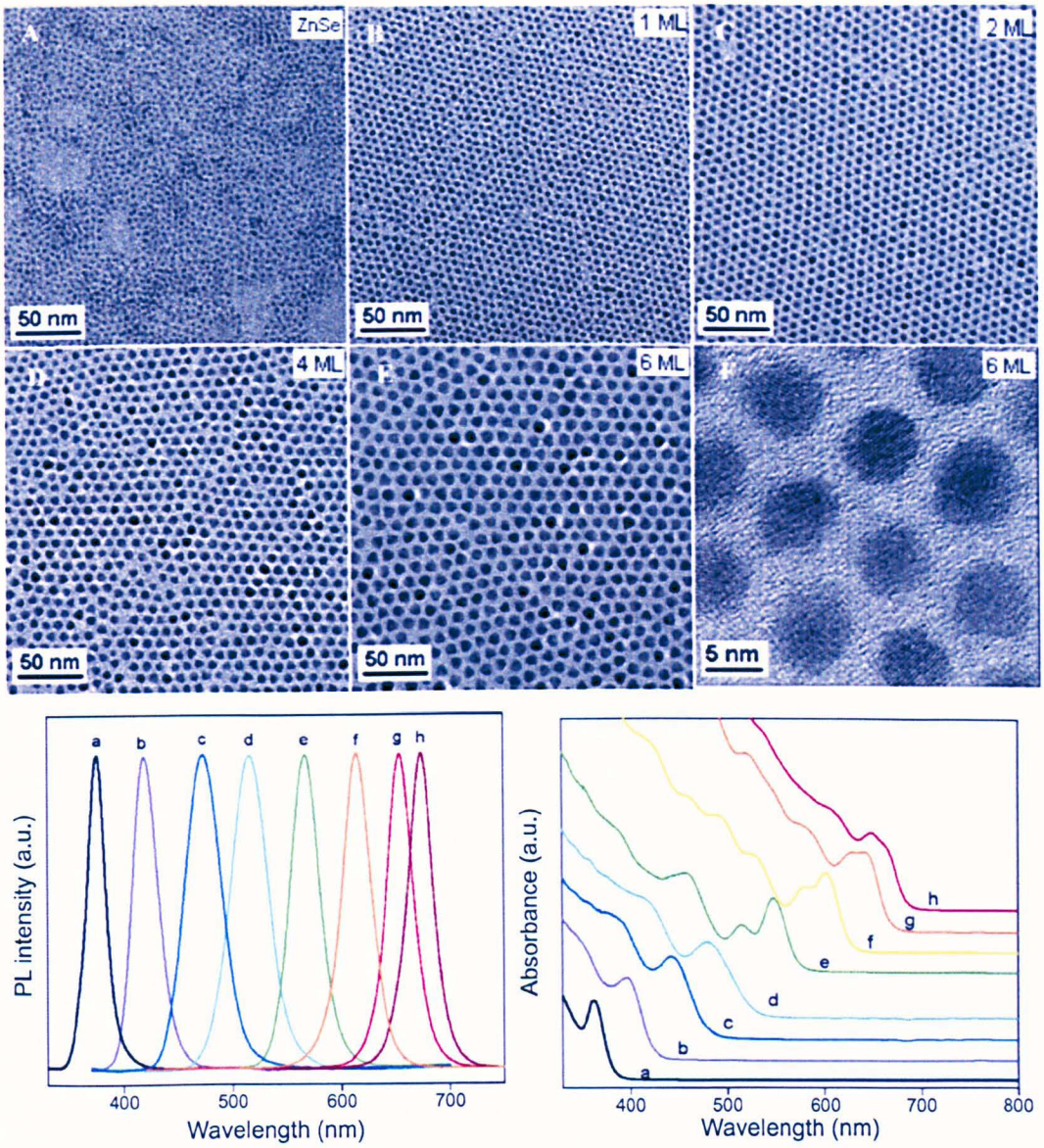

Fig. 1.5 – Dependence of the absorption/emission spectra on the QDs shell size. Top: TEM images of ZnSe/CdSe core/shell nanocrystals with 0, 1, 2, 4 and 6 CdSe monolayers. Bottom: normalised luminescence (left) and absorption (right) spectra of ZnSe/CdSe nanocrystals, with the CdSe monolayer number: a, 0; b, 0.1; c, 0.2; d, 0.5; e, 1; f, 2; g, 4; h, 6. Adapted with permission from Zhong *et al.*[47] Copyright 2005, American Chemical Society.

the electron confinement in the three dimensions, leading to quantised energy levels directly related to the nanocrystal size.[42,44]

They have a broad absorption from the UV, through the visible and to the near infrared spectra and narrow symmetrically peaked fluorescence emission spectra that vary from the visible to the near infrared[42,45,46] (Fig. 1.5). For a given material, the fluorescence emission peak wavelength can be finely tuned by varying the size of the nanocrystal, and depends on the core semiconductors composition.[42,45,46] Thus,

a CdSe core would be used for an emission in the 450–650 nm range, while the 500–750 nm range would be better covered by CdTe.[43]

Their photophysical characteristics have proven to display intensity fluctuations, known as the QDs blinking, when the photoluminescence is alternating between on or off states. The off period was proposed to correspond to an ionised state of the nanocrystals.[48] However, recent reports have shown that the blinking could be significantly reduced with a thick crystalline shell,[49,50] and even almost fully suppressed by using a gradient of composition of the ternary core of the core/shell CdZnSe/ZnSe nanocrystals.[51]

In order to maintain their colloidal stability, to obtain the necessary water solubility and to bypass the nanotoxicity, quantum dots need a protective self-assembled monolayer to be implemented at their surface. As their synthesis is mainly completed in organic solvents, they need to be transferred in water and their hydrophobic ligands should be replaced by hydrophilic ones. This can be achieved with various molecules and either by ligand exchange, encapsulation in a layer or by addition of multiple layers of different materials.[42] Yet the hydrodynamic size of the quantum dots after functionalisation can be important. Another problem lies in the internalisation of the bioconjugates, for which specific targeted labelling after non-specific uptake still has to be found. Courty *et al.* bypassed this internalisation route by loading the cells by osmotic lysis of pinocytic vesicles. They observed and tracked the motion of individual kinesin motors tagged with QDs and could infer the velocity of the molecular motors.[52]

1.1.2 Imaging fluorescent probes

The different types of fluorescent probes (dyes, FPs, QDs) available to target intracellular molecules have intrinsic advantages and inconvenients (Tab. 1.1), but the diversity of their possibilities can be used to get the most appropriate labelling in every experimental condition, especially when multiple targeting is sought.

A huge number of organic dyes are available with various wavelengths,[54] which allows to follow several objects concomitantly, but small organic dyes lack protein specificity and are therefore predominantly used in immunofluorescence, with fixed or permeabilised cells.[53]

The fluorescent proteins (FPs) can be introduced in cells by transfection and live cell imaging is then routinely possible. Modern FPs are available in a broad range of colours.[55] They are therefore appropriate for labelling of multiple targets or observing their interaction (e.g. FRET). They are also bright and their photostability allows imaging by conventional techniques such as laser confocal scanning microscopy.[55]

Quantum dots are more photostable, but the hydrodynamic sizes of the currently available QDs after coating can be important (10–30 nm). Their broad absorption

Fluorophores for examination of	Small organic dyes (antibody-targeted)	Quantum dots (antibody-targeted)	Fluorescent proteins	Genetic tags with small dyes
Endogenous proteins	++	+	−	−
Clinical specimens	++	+	−	−
Animals	*Ex vivo*	*Ex vivo*	Transgene live	Transgene *ex vivo*
Primary tissues	++	+	Transgene/virus	Transgene/virus
Live cells in culture	Surface	Surface	++	+
Multiple proteins at once	++	++	++	−
Dynamic interactions	+/−	+/−	++	Combination with FP
Turnover/synthesis	−	−	+	+
Activation state	Phospho-specific	Phospho-specific	FRET sensors	Combination with FP
CALI	+	−	+	++
EM	+/−	++	+/−	+
Protein microarrays	++	+	−	−
In-gel fluorescence	−	−	+	+
Western blot	−	+	−	−
Major advantages	Diversity of properties	Bright and photostable	Live cells and specificity	Live cells and small size
Major limitations	Targeting in live cells	Targeting and penetration	Ectopic expression	Ectopic expression, background staining
Improvements expected	Generic conjugated primary antibodies.	Smaller, diversity of properties	Better properties, generic sensors	New applications

Tab. 1.1 – Application of fluorophores in protein detection. Applicability ranges from most optimal (++) to generally not applicable (−), and (+/−) indicates applicable in some cases. From Giepmans *et al.* [53] Reprinted with permission from AAAS.

spectra allow to excite several QDs colours with the same wavelength. They complement organic dyes and fluorescent proteins, especially in single molecule experiments on long time scale, where their photostability is a precious advantage. Single-particle tracking of fluorescent entities is best done by QDs, due to their brightness and the absence of photobleaching. However, this is mainly limited to observation on the outside membrane of the cell owing to the difficulty of a controlled internalisation, and the blinking (commercial QDs) requires some additional work in the trajectory analysis.

Other dynamical information, such as protein diffusion constants, can be inferred from the movement of fluorescently tagged proteins in and out of an immobile focal volume by fluorescence correlation spectroscopy,[56] or alternatively, by the recovery of the fluorescence of FPs after their intended photobleaching (FRAP).[57] Photoconversion of FPs can target specific cell compartments and allows to follow proteins or organelles linked to the photoactived FPs. The newly developed photoconvertible, irreversible and especially reversible photoactivable fluorescent proteins[58,59] have also opened new possibilities in super resolution imaging.

From the development of the 4-Pi and then the two-photon 4-Pi microscope[60] by Hell, which improved the axial resolution (~100 nm) by a factor of two over confocal fluorescence microscopy, a range of new far field optical microscopy techniques have emerged. These techniques include the ground state depletion (GSD),[61] the saturated structured illumination microscopy (SSIM)[62,63] and the stimulated emission-depletion microscopy (STED),[64] which are based on the saturation property of the dark and bright states of the fluorophores, but also the photoactivated localisation microscopy (PALM)[65] or the stochastic optical reconstruction microscopy (STORM),[66] which are able to detect single fluorophores.[67] Those techniques are sometimes referred to as nanoscopy techniques and not microscopy, as their resolution is below the diffraction limit of half the wavelength of light formulated by Abbe in 1873.

The imaging of *E. coli* membrane and the vacuolar membrane of yeast cells with a resolution of ~100 nm in the radial directions[68] in 2000 was the first demonstration of the possibilities of STED. Recently a ~20 nm resolution was demonstrated by three different groups. Rust *et al.*[66] imaged DNA-protein complexes *in vivo* (PALM), while Betzig *et al.*[69] have observed mitochondria substructures and focal adhesion regions in COS-7 cells (STED) and Donner *et al.*[70] resolved the nanostructure of speckles of SC35 proteins in the nuclei of HeLa cells (STED).

1.1.3 Imaging of gold nanoparticles

In order to use nanoparticles as molecular imaging probes to follow intracellular processes, the first essential step is to find a controlled way of internalising them inside cell. Then a careful assessment of the integrity of their capping layer would

need to be demonstrated, in order to prove that the functions born by the metal core are intact and ready to interact with their target. Photothermal microscopy (see Sect. 2.1 for details on photothermal microscopy) as an imaging technique has the potential to bring meaningful information about the interaction of intracellular entities. Indeed, this technique is able to image gold nanoparticles down to a diameter of 1.4 nm in a non scattering environment.[10]

Like quantum dots, the use of this technique in intracellular imaging is currently hampered by the difficulties in controlling the localisation of the probes after their internalisation (endosomal localisation). However, it has been successfully used to track the lateral diffusion of individual transmembrane glutamate AMPA receptors (AMPAR) conjugated to single 5 nm gold nanoparticles on the plasma membrane of live neurons for several minutes,[16] owing to the stability of the signal which does not change over hours of measurements. Absorption correlation spectroscopy (ACS) is an absorption-based equivalent to fluorescence correlation spectroscopy. Like its fluorescence equivalent it consists in acquiring a signal coming from molecules going through the detection volume of an immobile laser beam and analysing it to derive diffusion constants of gold nanoparticles that would have diffused.[17] Nevertheless it has a great advantage over its fluorescence counterpart as photobleaching does not occur. Information about nanoparticles diffusion constants can therefore be acquired over long period of time, without decrease of the signal to noise ratio. Photothermal microscopy has also been used in combination with fluorescence microscopy to image the intracellular fate of gold peptide monolayer in cells.[71] Transmission electron microscopy was also used to assess the intracellular localisation of the nanoparticles, which was possible as gold nanoparticles are electron dense objects.

A few other techniques, such as dark field microscopy or surface raman resonance scattering (SERS) are available to detect nanoparticles in cells (see review by Lévy *et al.*[12] for more examples). For example dark field microscopy can image nanoparticles in cells,[72] but the detection is limited to nanoparticle sizes above 40 nm for single particle imaging, due to the scattering environment inside the cells. Similarly, SERS can be used to detect nanoparticles in cells, but also for sensing inside intracellular compartments such endosomes.[73]

1.2 Nanoparticle surface functionalisation

The functionalisation of metal nanoparticles with bioconjugates can be achieved at the same time as the synthesis of the metal core or post synthesis, by adding the functional groups to the stabilising molecules or by replacing them by ligand exchange.[74,75] The post synthesis approach can be perform by various ways,[76] such as electrostatic adsorption of oppositely charged nanoparticles and ligands *e.g.* antibody,[77] binding of the terminal carbon of an alkyne terminated ligand,[78]

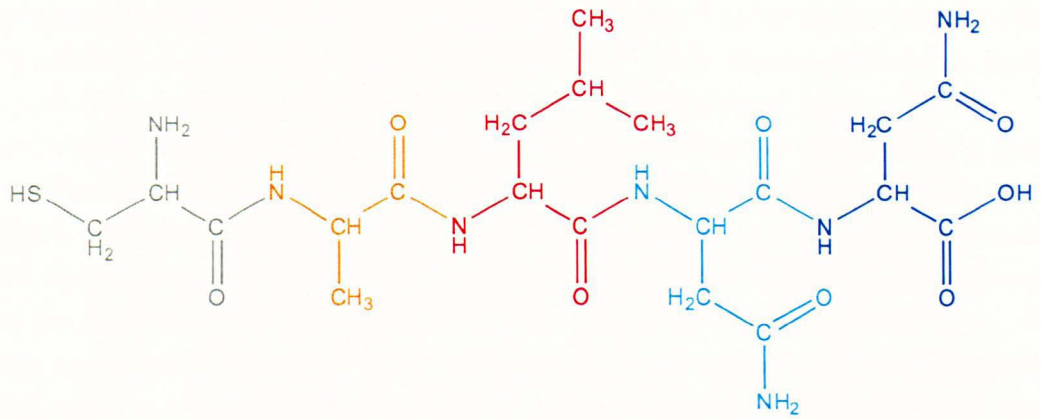

Fig. 1.6 – Structure of the matrix peptide CALNN.

amide bonds between amine groups at the nanoparticle surface and NHS-terminated bioconjugates like biotin.[79] However, thiolated molecules are the main functionalisation platform due to the strong bond formed between the sulfur of the thiol group of the bioconjugate and a gold atom from the nanoparticle surface. Functions can be further added as necessary by ligand exchange with the stabilising molecule at the surface of the core. Numerous functionalisation have been reported in the literature, such as single cysteine amino acid,[80] thiol-modified oligonucleotides,[81–83] PEG-terminated ligands,[19,84–86] mercapodextrans,[87] BSA[88] or tiopronin.[89]

Among the various stabilisation and functionalisation strategies, the use of peptides as capping agent is particularly attractive. In order to obtain stable, water-soluble and easy to functionalise particles from citrate stabilised ones, Lévy *et al.* have employed a combinatorial approach to test the design of a pentapeptide for self-assembled monolayer protection of gold nanoparticles. The five amino acid peptide CALNN was engineered with a cysteine to anchor the peptide to the gold core by covalently binding its thiol group to it. Then two amino acids with hydrophobic side chains (alanine and leucine) are present to promote a good packing of the self-assembled monolayer. Finally, two hydrophilic asparagine amino acids provide water solubility (Fig. 1.6). The carboxylic group at the C-terminal end is also bringing a net negative charge to the surface of the self-assembled monolayer, providing the necessary colloidal stability through repulsive interactions.

The peptide-capped nanoparticles are fully compatible with standard biological methods for protein handling. Indeed, they can be freeze-dried, redissolved and filtrated and can therefore undergo size-exclusion chromatography, ion-exchange chromatography, electrophoresis and centrifugation. Additionally, the authors reported that including a small proportion of a longer peptide in the self-assembled monolayer does not destabilise the monolayer, opening a route to adding functional end groups on the monolayer surface.

Functionalisation was demonstrated with peptides starting with CALNN and

terminated with biotin,[11] DNA,[90] biotinylated His-tag,[18] nickel nitrilo-triacetic acid (Ni-NTA),[19] poly(ethylene glycol),[91] fluorescein,[91] while their stoichiometry could be precisely controlled to yield for example to single functional groups.[18,19]

In 2004 Jackson *et al.*[92] reported the functionalisation of the surface of gold nanoparticles with a mixture of two types — hydrophilic and hydrophobic — of alkane thiolated ligands. From the observation of the surface of these nanoparticles by scanning tunnelling microscopy they concluded that the ligands self-organise at the surface of the nanoparticles to form ripples of alternate ligand type. In this paper and in a series of follow up ones they attributed a number of attractive properties to the postulated structure of those nanoparticles. They claimed that the ligand organisation at the surface of the nanoparticles helps them to avoid non-specific absorption of proteins,[92] but most prominently, that it confers them the ability to penetrate the plasma membrane of cells without bilayer disruption.[93] Such property would be very useful for nanoparticle internalisation in the cell cytosol, but the evidences presented by the authors are subject to controversy.[94] This will be developed further in chapter 5.

1.3 Nanoparticles journey to the cell

1.3.1 Extracellular environment and plasma membrane

The outside surface of mammalian cells is covered by the extracellular matrix (ECM), which is a mesh of carbohydrates "filling" the space between cells. Those carbohydrates are proteoglycans and are continuously delivered by the cells via exocytosis. The extracellular matrix is involved in cell adhesion and motility through its binding to membrane receptors, some of which in turn bind to the cytoskeleton, and back and forth communication between the ECM and the cytoskeleton is observed. The extracellular matrix is also participating in the regulation of signalling with e.g. growth factors, of which a large number are bound to the ECM, although they are not considered as ECM entities. Glycoproteins are also taking part in cell-cell interactions and cell differentiation.[95,96]

The extracellular environment is also constituted of a liquid part, the medium, where a large number of protein (fetal calf serum) are present. Nanomaterials can therefore easily capture some serum proteins on their surface. The influence of this protein corona was investigated by Chen *et al.*[97] on iron oxide nanoparticles. The nanoparticles were prepared with different surface charges by functionalisation with silanes terminated by either amino groups, PEGs or carboxylic groups and were further incubated with cells in medium containing or not serum. The internalisation in absence of proteins was shown to depend on the surface charge, charged particles being more internalised[a] than neutral ones. However, the introduction of serum

[a] negatively and positively charged particles had the same degree of internalisation

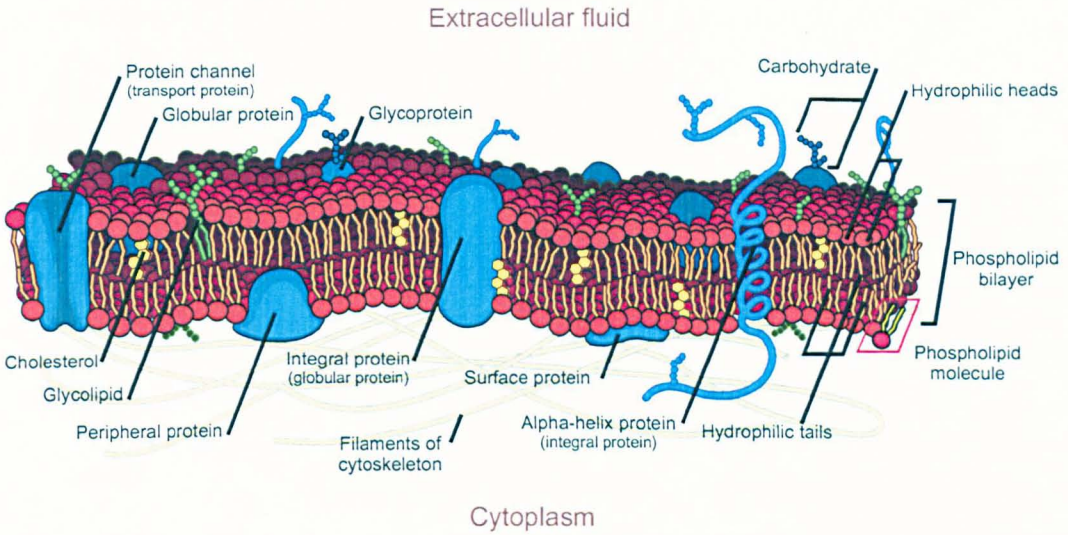

Fig. 1.7 – Cell plasma membrane. The membrane is essentially composed of a lipid bilayer and various proteins. This image is in the public domain and was adapted from the file available at the address: http://en.wikipedia.org/wiki/File:Cell_membrane_detailed_diagram_en.svg.

proteins cancelled out the influence of the charge, as all three types of nanoparticles had the same degree of internalisation.[97] Nevertheless, the degree of nanoparticle internalisation had increased in presence of the serum proteins, suggesting that the interaction of the serum proteins with the cell membrane was the essential driving mechanism, at least in this particular case.

The plasma membrane of the cell is the barrier that defines topologically the limit of the cell, separating the extracellular medium from the intracellular components in the cytoplasm. Its main components are phospholipids and membrane proteins.

The lipids are organised to form a bilayer, where the hydrophobic tails point inwards and the hydrophilic heads point either towards the extracellular fluid or the cytoplasm. They are self-organised in fluid phase at a physiological temperature, which allows the rapid diffusion of lipid domains and of membrane proteins. A broad variety of protein is inserted in the lipids, which can be isolated in integral membrane proteins and peripheral membrane proteins. Within the former category can be distinguished anchored membrane proteins, which are inserted in the lipid bilayer and have a hydrophilic end in contact with either the cytosol or the extracellular medium, and the transmembrane proteins. The peripheral membrane proteins are bound either to phospholipids or to integral membrane proteins, and can also bind to the cytoskeleton filaments inside the cell.[96] The membrane is thus asymmetrical, with some proteins directed exclusively towards the extracellular matrix and others towards the cytoplasm. Transmembrane pumps and channels are regulating the transmembrane potential (negatively charged inside) via the diffusion of ions (Na^+,

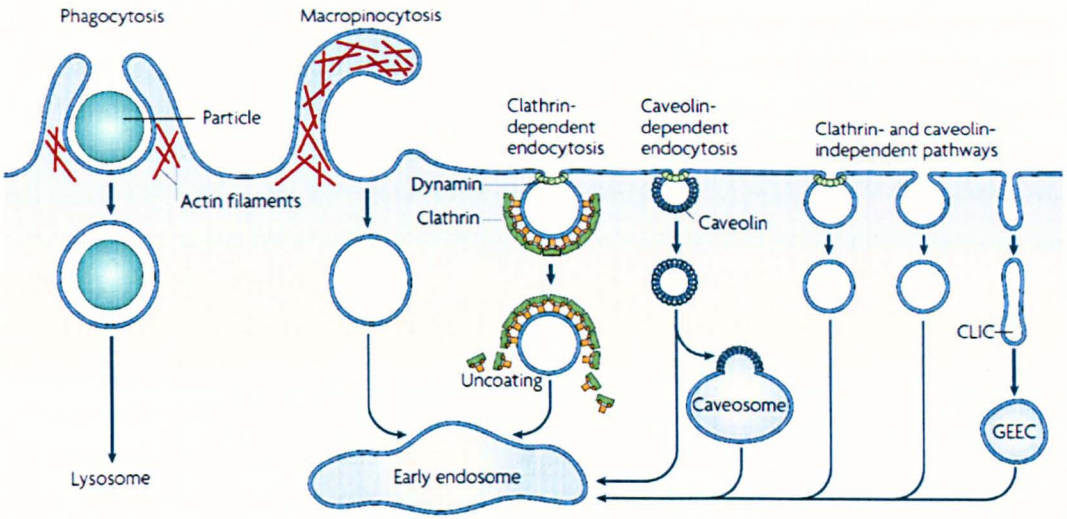

Fig. 1.8 – Different mechanisms of endocytosis into mammalian cells. Multiple pathways are possible for the entry of particles and solutes. The internalisation involves engulfment of the cargo from the plasma membrane leading to intracellular vesicles. Large vesicles are formed by phagocytosis and micropinocytosis, which are dependent on actin-mediated remodelling of the membrane. Most cargoes are delivered to early endosomes through vesicles (clathrin- or caveolin-coated) or tubular (CLIC) intermediates and may reside first in intermediate compartments (caveosomes, GEECs). Abbreviations: CLIC: clathrin- and dynamin-independent carrier; GEEC: glycosyl phosphatidylinositol-anchored protein enriched early endosomal compartment. Reprinted by permission from Macmillan Publishers Ltd: Nature[101], copyright (2007)

K^+, Cl^-, Ca^{2+}) and help keeping the membrane polarised by adjusting the ions concentrations on both sides.[96,98,99]

The plasma membrane is semi-permeable to small non-polar molecules, but bigger object such as nanomaterials require an other uptake mechanism, namely endocytosis.

1.3.2 Intracellular entry of molecules: endocytosis

Endocytosis is an internalisation mechanism by which cells exert their control over the membrane composition (essentially lipids and proteins) and by that regulate the interactions with their environment, e.g. nutrient uptake, cell signaling, cell shape change.[100]

The two main categories of endocytosis in mammalian cells are the phagocytosis and the pinocytosis. The word phagocytosis is coming from the Greek $\varphi\alpha\gamma\epsilon\iota\nu$ (eat) and $\kappa\upsilon\tau\sigma\varsigma$ (cell), and correspond to the process of cell eating, while the pinocytosis, coming from the $\pi\iota\nu\epsilon\iota\nu$ (drink) and $\kappa\upsilon\tau\sigma\varsigma$ (cell), constitutes the process of cell drinking. Phagocytosis is mainly dealing with large particles (micron-sized), while pinocytosis is handling fluids, solutes and small objects such as nanomaterials (Fig. 1.8). Pinocytosis is itself divided in clathrin-dependent and clathrin-independent endocytosis, and the later divides in micropinocytosis, caveolae-mediated, and caveolae-

and clathrin-independent pathways. Finally, the caveolae- and clathrin-independent pathway is separated into the four classes of Arf6-dependent, Cdc42–dependent, flotillin-dependent and RhoA-dependent.[100,102] The difference between pathways lies essentially in the lipids and protein involved, the later including clathrin, caveolin, flotillin1, GRAF1, kinases, small G proteins, actin and dynamin.[100] Cargo internalisation can occur by a single pathway, but their entry can be achieved by various pathways.[100,102]

Nanomaterials internalisation can be specific or non-specific. In the context of nanoparticles, targeted specific entry has been shown via the functionalisation of their surface with specific targeting ligands. Transferrin, a marker of clathrin-mediated endocytosis,[102] was for example functionalised to gold nanoparticles that were further engulfed by cell after binding to the transferrin receptor on the cell membrane.[103] Similarly, nanoparticles coated with an antibody to aminopeptidase P, an enzyme abundant in caveolae, were shown to be localised in caveolae.[104]

However, the further trafficking pathway of nanomaterials internalised by a specific endocytotic pathway may not follow the same route as the free ligands. Transferrin functionalised quantum dots, for example, were directed to the perinuclear region through endosomes,[105] while free transferrin is normally going to lysosomes and back to the cell membrane.

The non-specific interaction may also play a role in nanoparticles internalisation. Quantum dots functionalised with different surface charges, PEG-, PEG-amine- or carboxylic acid-coated, have been shown to have different quantity of uptake in HEK cells, suggesting that charge may play a role in the internalisation. The QDs were shown to follow a clathrin-independent endocytotic pathway, and negatively charged QDs were specifically entering cells via a caveolae-mediated endocytosis, unlike neutral and positive ones.[106] However, the effect of the medium proteins in changing the effective nanoparticles surface[97] and therefore potentially changing the surface charge has to be taken into consideration while evaluating of the influence of the charge.

Other surface modifications have been applied to promote the internalisation of nanoparticles, like the use of the cell penetrating peptide Tat,[85,107] or to target specific cell compartments, like with the fusion peptide HA2, to escape the endosomal entrapment[72] (see Lévy *et al.*[12] for a review).

1.3.3 Intracellular environment

If one admits that nanomaterials can be efficiently delivered to the cell cytosol, before gold nanoparticles can be readily used as molecular imaging agents, an assessment of the fate of their protecting self-assembled monolayer must be proceeded to. Indeed, two mechanism are likely to happen within the cytosol. First, considering the intracellular concentration of glutathione (2 μM) there is a high probability that a

free thiol would replaced ligands on the nanoparticles surface, either by ligand exchange or disulphide exchange.[108] Then proteolysis can also happen inside cells and potentially cleave surface molecules on the nanoparticles, removing the necessary function. Sée *et al.* have observed that the protecting peptide self-assembled monolayer of gold nanoparticles was degraded inside the endosomal compartments after internalisation in mammalian cells. They found that the fairly ubiquitous endosomal protease cathepsin L was responsible for this behaviour.

It is therefore patent that observing the fate of the internalised nanomaterials is particularly crucial in the development of molecular imaging probes, sensors or drug delivery cargoes, and should be kept under carefully scrutiny.

1.4 Thesis outline

This manuscript will describe the internalisation of gold nanoparticles in mammalian cells. After introducing the photothermal microscopy technique in chapter 2, where the set up built by the author in the Liverpool Centre for Cell Imaging will be presented, different strategies of nanoparticle internalisation will be examined. First, the non-specific endocytosis mediated uptake of peptide-capped gold nanoparticles will be scrutinised in chapter 3, in order to characterise the gold nanoparticles internalisation in mammalian cells. Then, the investigations will concentrate on avoiding the endosomal entrapment in chapter 4 to facilitate their cytosolic delivery. The endosome disruption using either a facilitated endosomal escape of the nanoparticles with the endosome disrupting drug chloroquine or by functionalising the monolayer with a combination of cell-penetrating peptides and membrane fusion peptides will be examined first. A second strategy will then involve looking at a membrane pore formation mediated entry of the nanoparticles. After that, chapter 5 will revisit the evidences published in a series of over ten articles on the existence and the properties of alkane thiol functionalised gold nanoparticles, namely "stripy" nanoparticles. Finally, with the aim of using polyelectrolyte microcapsules as delivery agents of nano-objects to the cell cytosol, the photophysically induced capsule damages will be examined by laser illumination of the capsules wall.

1.5 Bibliography

1. F. Zernike. Phase contrast, a new method for the microsopic observation of transparent objects. *Physica*, 9, 686–698, 1942.

2. W. J. Schmidt. Zur doppelbrechung der chromosomen in den speicheldrüsenkernen der chironomuslarven. *Naturwissenschaften*, 25(31), 506–507, 1937.

3. W. J. Schmidt. Doppelbrechung der kernspindel und zugfasertheorie der chromosomenbewegung. *Chromosoma*, 1(1), 253–264, 1939.

4. S. Inoue. Polarization optical studies of the mitotic spindle 1. The demonstration of spindle fibers in living cells. *Chromosoma*, 5(5), 487–500, 1953.

5. B. R. Masters. History of the electron microscope in cell biology. In *eLS*. John Wiley & Sons, Ltd, Chichester, 2001.

6. F. Haguenau, P. W. Hawkes, J. L. Hutchison, B. Satiat-Jeunemaitre, G. T. Simon and D. B. Williams. Key events in the history of electron microscopy. *Microscopy and Microanalysis*, 9(2), 96–138, 2003.

7. K. R. Porter, A. Claude and E. F. Fullam. A study of tissue culture cells by electron microscopy - Methods and preliminary observations. *Journal of Experimental Medicine*, 81(3), 233–246, 1945.

8. V. M. Unger, N. M. Kumar, N. B. Gilula and M. Yeager. Three-dimensional structure of a recombinant gap junction membrane channel. *Science*, 283(5405), 1176–1180, 1999.

9. D. Boyer, P. Tamarat, A. Maali, B. Lounis and M. Orrit. Photothermal imaging of nanometer-sized metal particles among scatterers. *Science*, 297(5584), 1160–1163, 2002.

10. S. Berciaud, L. Cognet, G. A. Blab and B. Lounis. Photothermal heterodyne imaging of individual nonfluorescent nanoclusters and nanocrystals. *Physical Review Letters*, 93(25), 257402, 2004.

11. R. Levy, N. T. K. Thanh, R. C. Doty, I. Hussain, R. J. Nichols, D. J. Schiffrin, M. Brust and D. G. Fernig. Rational and combinatorial design of peptide capping Ligands for gold nanoparticles. *Journal of the American Chemical Society*, 126(32), 10076–10084, 2004.

12. R. Lévy, U. Shaheen, Y. Cesbron and V. Sée. Gold nanoparticles delivery in mammalian live cells: a critical review. *Nano Reviews*, 1, 4889, 2010. DOI: 10.3402/nano.v1i0.4889.

13. S. Berciaud, D. Lasne, G. A. Blab, L. Cognet and B. Lounis. Photothermal heterodyne imaging of individual metallic nanoparticles: Theory versus experiment. *Physical Review B*, 73(4), 045424, 2006.

14. S. Berciaud, L. Cognet and B. Lounis. Photothermal absorption spectroscopy of individual semiconductor nanocrystals. *Nano Letters*, 5(11), 2160–2163, 2005.

15. S. Berciaud, L. Cognet, P. Poulin, R. B. Weisman and B. Lounis. Absorption spectroscopy of individual single-walled carbon nanotubes. *Nano Letters*, 7(5), 1203–1207, 2007.

16. D. Lasne, G. A. Blab, S. Berciaud, M. Heine, L. Groc, D. Choquet, L. Cognet and B. Lounis. Single nanoparticle photothermal tracking (SNaPT) of 5-nm gold beads in live cells. *Biophysical Journal*, 91(12), 4598–4604, 2006.

17. V. Octeau, L. Cognet, L. Duchesne, D. Lasne, N. Schaeffer, D. G. Fernig and B. Lounis. Photothermal Absorption Correlation Spectroscopy. *ACS Nano*, 3(2), 345–350, 2009.

18. R. Levy, Z. X. Wang, L. Duchesne, R. C. Doty, A. I. Cooper, M. Brust and D. G. Fernig. A generic approach to monofunctionalized protein-like gold nanoparticles based on immobilized metal ion affinity chromatography. *Chembiochem*, 7(4), 592–594, 2006.

19. L. Duchesne, D. Gentili, M. Comes-Franchini and D. G. Fernig. Robust ligand shells for biological applications of gold nanoparticles. *Langmuir*, 24(23), 13572–13580, 2008.

20. M. Brust, M. Walker, D. Bethell, D. J. Schiffrin and R. Whyman. Synthesis of thiol-derivatized gold nanoparticles in a 2-phase liquid-liquid system. *Chemical Communications*, (7), 801–802, 1994.

21. O. Shimomura, F. H. Johnson and Y. Saiga. Extraction, purification and properties of aequorin, a bioluminescent protein from luminous hydromedusan, aequorea. *Journal of Cellular and Comparative Physiology*, 59(3), 223–239, 1962.

22. D. C. Prasher, V. K. Eckenrode, W. W. Ward, F. G. Prendergast and M. J. Cormier. Primary structure of the aequorea-victoria green-fluorescent protein. *Gene*, 111(2), 229–233, 1992.

23. M. Chalfie, Y. Tu, G. Euskirchen, W. W. Ward and D. C. Prasher. Green fluorescent protein as a marker for gene expression. *Science*, 263(5148), 802–805, 1994.

24. R. Y. Tsien. The green fluorescent protein. *Annual Review of Biochemistry*, 67, 509–544, 1998.

25. L. D. Hebshi, B. M. Angres, X. L. Li and S. R. Kain. Green fluorescent protein. In *eLS*. John Wiley & Sons, Ltd, Chichester, 2001.

26. M. V. Matz, A. F. Fradkov, Y. A. Labas, A. P. Savitsky, A. G. Zaraisky, M. L. Markelov and S. A. Lukyanov. Fluorescent proteins from nonbioluminescent Anthozoa species. *Nature Biotechnology*, 17(10), 969–973, 1999.

27. R. E. Campbell, O. Tour, A. E. Palmer, P. A. Steinbach, G. S. Baird, D. A. Zacharias and R. Y. Tsien. A monomeric red fluorescent protein. *Proceedings of the National Academy of Sciences of the United States of America*, 99(12), 7877–7882, 2002.

28. H. Mizuno, T. K. Mal, K. I. Tong, R. Ando, T. Furuta, M. Ikura and A. Miyawakil. Photo-induced peptide cleavage in the green-to-red conversion of a fluorescent protein. *Molecular Cell*, 12(4), 1051–1058, 2003.

29. G. H. Patterson and J. Lippincott-Schwartz. A photoactivatable GFP for selective photolabeling of proteins and cells. *Science*, 297(5588), 1873–1877, 2002.

30. N. C. Shaner, R. E. Campbell, P. A. Steinbach, B. N. G. Giepmans, A. E. Palmer and R. Y. Tsien. Improved monomeric red, orange and yellow fluorescent proteins derived from Discosoma sp red fluorescent protein. *Nature Biotechnology*, 22(12), 1567–1572, 2004.

31. A. H. Coons, H. J. Creech, R. N. Jones and E. Berliner. The demonstration of pneumococcal antigen in tissues by the use of fluorescent antibody. *Journal of Immunology*, 45(3), 159–170, 1942.

32. A. Herzog and H. R. Schutze. Fluorochromierung von Saugetierchromosomen mit einem basisch substituierte Bis-Benzimidazol-Derivat (Praparat 33258 "Hoechst"). *Deutsche Tieraerztliche Wochenschrift*, 75(19), 476–479, 1968.

33. D. Schweizer. Reverse fluorescent chromosome-banding with chromomycin and DAPI. *Chromosoma*, 58(4), 307–324, 1976.

34. A. Krishan. Rapid flow cytofluorometric analysis of mammalian-cell cycle by propidium iodide staining. *Journal of Cell Biology*, 66(1), 188–193, 1975.

35. E. Wulf, A. Deboben, F. A. Bautz, H. Faulstich and T. Wieland. Fluorescent phallotoxin, a tool for the visualization of cellular actin. *Proceedings of the National Academy of Sciences of the United States of America*, 76(9), 4498–4502, 1979.

36. R. Y. Tsien. New calcium indicators and buffers with high selectivity against magnesium and protons: design, synthesis, and properties of prototype structures. *Biochemistry*, 19(11), 2396–2404, 1980.

37. G. Grynkiewicz, M. Poenie and R. Y. Tsien. A new generation of Ca2+ indicators with greatly improved fluorescence properties. *Journal of Biological Chemistry*, 260(6), 3440–3450, 1985.

38. A. Minta, J. P. Y. Kao and R. Y. Tsien. Fluorescent indicators for cytosolic calcium based on rhodamine and fluorescein chromophores. *Journal of Biological Chemistry*, 264(14), 8171–8178, 1989.

39. N. Panchuk-Voloshina, R. P. Haugland, J. Bishop-Stewart, M. K. Bhalgat, P. J. Millard, F. Mao, W. Y. Leung and R. P. Haugland. Alexa dyes, a series of new fluorescent dyes that yield exceptionally bright, photostable conjugates. *Journal of Histochemistry & Cytochemistry*, 47(9), 1179–1188, 1999.

40. A. I. Ekimov and A. A. Onushchenko. Quantum size effect in 3-dimensional microscopic semiconductor crystals. *JETP Letters*, 34(6), 345–349, 1981.

41. A. L. Efros and A. L. Efros. Interband absorption of light in a semiconductor sphere. *Soviet Physics Semiconductors-Ussr*, 16(7), 772–775, 1982.

42. X. Michalet, F. F. Pinaud, L. A. Bentolila, J. M. Tsay, S. Doose, J. J. Li, G. Sundaresan, A. M. Wu, S. S. Gambhir and S. Weiss. Quantum dots for live cells, in vivo imaging, and diagnostics. *Science*, 307(5709), 538–544, 2005.

43. A. M. Smith, H. W. Duan, A. M. Mohs and S. M. Nie. Bioconjugated quantum dots for in vivo molecular and cellular imaging. *Advanced Drug Delivery Reviews*, 60(11), 1226–1240, 2008.

44. A. P. Alivisatos. Semiconductor clusters, nanocrystals, and quantum dots. *Science*, 271(5251), 933–937, 1996.

45. M. Bruchez, M. Moronne, P. Gin, S. Weiss and A. P. Alivisatos. Semiconductor nanocrystals as fluorescent biological labels. *Science*, 281(5385), 2013–2016, 1998.

46. P. Reiss, M. Protiere and L. Li. Core/shell semiconductor nanocrystals. *Small*, 5(2), 154–168, 2009.

47. X. H. Zhong, R. G. Xie, Y. Zhang, T. Basche and W. Knoll. High-quality violet- to red-emitting ZnSe/CdSe core/shell nanocrystals. *Chemistry of Materials*, 17(16), 4038–4042, 2005.

48. A. L. Efros and M. Rosen. Random telegraph signal in the photoluminescence intensity of a single quantum dot. *Physical Review Letters*, 78(6), 1110–1113, 1997.

49. B. Mahler, P. Spinicelli, S. Buil, X. Quelin, J. P. Hermier and B. Dubertret. Towards non-blinking colloidal quantum dots. *Nature Materials*, 7(8), 659–664, 2008.

50. Y. Chen, J. Vela, H. Htoon, J. L. Casson, D. J. Werder, D. A. Bussian, V. I. Klimov and J. A. Hollingsworth. "Giant" multishell CdSe nanocrystal quantum dots with suppressed blinking. *Journal of the American Chemical Society*, 130(15), 5026–5027, 2008.

51. X. Y. Wang, X. F. Ren, K. Kahen, M. A. Hahn, M. Rajeswaran, S. Maccagnano-Zacher, J. Silcox, G. E. Cragg, A. L. Efros and T. D. Krauss. Non-blinking semiconductor nanocrystals. *Nature*, 459(7247), 686–689, 2009.

52. S. Courty, C. Luccardini, Y. Bellaiche, G. Cappello and M. Dahan. Tracking individual kinesin motors in living cells using single quantum-dot imaging. *Nano Letters*, 6(7), 1491–1495, 2006.

53. B. N. G. Giepmans, S. R. Adams, M. H. Ellisman and R. Y. Tsien. The fluorescent toolbox for assessing protein location and function. *Science*, 312(5771), 217–224, 2006.

54. U. Resch-Genger, M. Grabolle, S. Cavaliere-Jaricot, R. Nitschke and T. Nann. Quantum dots versus organic dyes as fluorescent labels. *Nature Methods*, 5(9), 763–775, 2008.

55. N. C. Shaner, P. A. Steinbach and R. Y. Tsien. A guide to choosing fluorescent proteins. *Nature Methods*, 2(12), 905–909, 2005.

56. E. Haustein and P. Schwille. Single-molecule spectroscopic methods. *Current Opinion in Structural Biology*, 14(5), 531–540, 2004.

57. D. S. Lidke, K. A. Lidke, B. Rieger, T. M. Jovin and D. J. Arndt-Jovin. Reaching out for signals: filopodia sense EGF and respond by directed retrograde transport of activated receptors. *Journal of Cell Biology*, 170(4), 619–626, 2005.

58. K. A. Lukyanov, D. M. Chudakov, S. Lukyanov and V. V. Verkhusha. Photoactivatable fluorescent proteins. *Nature Reviews Molecular Cell Biology*, 6(11), 885–891, 2005.

59. J. Lippincott-Schwartz and G. H. Patterson. Photoactivatable fluorescent proteins for diffraction-limited and super-resolution imaging. *Trends in Cell Biology*, 19(11), 555–565, 2009.

60. S. Hell and E. H. K. Stelzer. Fundamental improvement of resolution with a 4Pi-confocal fluorescence microscope using 2-photon excitation. *Optics Communications*, 93(5-6), 277–282, 1992.

61. S. W. Hell and M. Kroug. Ground-state-depletion fluorescence microscopy: a concept for breaking the diffraction resolution limit. *Applied Physics B-Lasers and Optics*, 60(5), 495–497, 1995.

62. M. G. L. Gustafsson. Surpassing the lateral resolution limit by a factor of two using structured illumination microscopy. *Journal of Microscopy-Oxford*, 198, 82–87, 2000.

63. R. Heintzmann, T. M. Jovin and C. Cremer. Saturated patterned excitation microscopy - a concept for optical resolution improvement. *Journal of the Optical Society of America a-Optics Image Science and Vision*, 19(8), 1599–1609, 2002.

64. S. W. Hell and J. Wichmann. Breaking the diffraction resolution limit by stimulated-emission: stimulated-emission-depletion fluorescence microscopy. *Optics Letters*, 19(11), 780–782, 1994.

65. S. T. Hess, T. P. K. Girirajan and M. D. Mason. Ultra-high resolution imaging by fluorescence photoactivation localization microscopy. *Biophysical Journal*, 91(11), 4258–4272, 2006.

66. M. J. Rust, M. Bates and X. W. Zhuang. Sub-diffraction limit imaging by stochastic optical reconstruction microscopy (STORM). *Nature Methods*, 3(10), 793–795, 2006.

67. M. Fernandez-Suarez and A. Y. Ting. Fluorescent probes for super-resolution imaging in living cells. *Nature Reviews Molecular Cell Biology*, 9(12), 929–943, 2008.

68. T. A. Klar, S. Jakobs, M. Dyba, A. Egner and S. W. Hell. Fluorescence microscopy with diffraction resolution barrier broken by stimulated emission. *Proceedings of the National Academy of Sciences of the United States of America*, 97(15), 8206–8210, 2000.

69. E. Betzig, G. H. Patterson, R. Sougrat, O. W. Lindwasser, S. Olenych, J. S. Bonifacino, M. W. Davidson, J. Lippincott-Schwartz and H. F. Hess. Imaging intracellular fluorescent proteins at nanometer resolution. *Science*, 313(5793), 1642–1645, 2006.

70. G. Donnert, J. Keller, R. Medda, M. A. Andrei, S. O. Rizzoli, R. Lurmann, R. Jahn, C. Eggeling and S. W. Hell. Macromolecular-scale resolution in biological fluorescence microscopy. *Proceedings of the National Academy of Sciences of the United States of America*, 103(31), 11440–11445, 2006.

71. V. Sée, P. Free, Y. Cesbron, P. Nativo, U. Shaheen, D. J. Rigden, D. G. Spiller, D. G. Fernig, M. R. H. White, I. A. Prior, M. Brust, B. Lounis and R. Lévy. Cathepsin L Digestion of Nanobioconjugates upon Endocytosis. *ACS Nano*, 3(9), 2461–2468, 2009.

72. S. Kumar, N. Harrison, R. Richards-Kortum and K. Sokolov. Plasmonic nanosensors for imaging intracellular biomarkers in live cells. *Nano Letters*, 7(5), 1338–1343, 2007.

73. J. Kneipp, H. Kneipp, B. Wittig and K. Kneipp. Novel optical nanosensors for probing and imaging live cells. *Nanomedicine-Nanotechnology Biology and Medicine*, 6(2), 214–226, 2010.

74. M. J. Hostetler, A. C. Templeton and R. W. Murray. Dynamics of place-exchange reactions on monolayer-protected gold cluster molecules. *Langmuir*, 15(11), 3782–3789, 1999.

75. H. D. Hill and C. A. Mirkin. The bio-barcode assay for the detection of protein and nucleic acid targets using DTT-induced ligand exchange. *Nature Protocols*, 1(1), 324–336, 2006.

76. E. Katz and I. Willner. Integrated nanoparticle-biomolecule hybrid systems: synthesis, properties, and applications. *Angewandte Chemie-International Edition*, 43(45), 6042–6108, 2004.

77. W. Shenton, S. A. Davis and S. Mann. Directed self-assembly of nanoparticles into macroscopic materials using antibody-antigen recognition. *Advanced Materials*, 11(6), 449–452, 1999.

78. S. Zhang, K. L. Chandra and C. B. Gorman. Self-assembled monolayers of terminal alkynes on gold. *Journal of the American Chemical Society*, 129(16), 4876–4877, 2007.

79. R. A. Sperling, T. Pellegrino, J. K. Li, W. H. Chang and W. J. Parak. Electrophoretic separation of nanoparticles with a discrete number of functional groups. *Advanced Functional Materials*, 16(7), 943–948, 2006.

80. K. Naka, H. Itoh, Y. Tampo and Y. Chujo. Effect of gold nanoparticles as a support for the oligomerization of L-cysteine in an aqueous solution. *Langmuir*, 19(13), 5546–5549, 2003.

81. T. A. Taton, C. A. Mirkin and R. L. Letsinger. Scanometric DNA array detection with nanoparticle probes. *Science*, 289(5485), 1757–1760, 2000.

82. A. G. Kanaras, Z. X. Wang, A. D. Bates, R. Cosstick and M. Brust. Towards multistep nanostructure synthesis: Programmed enzymatic self-assembly of DNA/gold systems. *Angewandte Chemie-International Edition*, 42(2), 191–194, 2003.

83. N. L. Rosi, D. A. Giljohann, C. S. Thaxton, A. K. R. Lytton-Jean, M. S. Han and C. A. Mirkin. Oligonucleotide-modified gold nanoparticles for intracellular gene regulation. *Science*, 312, 1027–1030, 2006.

84. A. G. Kanaras, F. S. Kamounah, K. Schaumburg, C. J. Kiely and M. Brust. Thioalkylated tetraethylene glycol: a new ligand for water soluble monolayer protected gold clusters. *Chemical Communications*, (20), 2294–2295, 2002.

85. P. Nativo, I. A. Prior and M. Brust. Uptake and intracellular fate of surface-modified gold nanoparticles. *ACS Nano*, 2(8), 1639–1644, 2008.

86. Y. L. Liu, M. K. Shipton, J. Ryan, E. D. Kaufman, S. Franzen and D. L. Feldheim. Synthesis, stability, and cellular internalization of gold nanoparticles containing mixed peptide-poly(ethylene glycol) monolayers. *Analytical Chemistry*, 79(6), 2221–2229, 2007.

87. R. Wilson. Haptenylated mercaptodextran-coated gold nanoparticles for biomolecular assays. *Chemical Communications*, (1), 108–109, 2003.

88. A. G. Tkachenko, H. Xie, D. Coleman, W. Glomm, J. Ryan, M. F. Anderson, S. Franzen and D. L. Feldheim. Multifunctional gold nanoparticle-peptide complexes for nuclear targeting. *Journal of the American Chemical Society*, 125(16), 4700–4701, 2003.

89. A. C. Templeton, S. W. Chen, S. M. Gross and R. W. Murray. Water-soluble, isolable gold clusters protected by tiopronin and coenzyme A monolayers. *Langmuir*, 15(1), 66–76, 1999.

90. Z. Wang, R. Levy, D. G. Fernig and M. Brust. The peptide route to multifunctional gold nanoparticles. *Bioconjugate Chemistry*, 16(3), 497–500, 2005.

91. P. Free, C. P. Shaw and R. Levy. PEGylation modulates the interfacial kinetics of proteases on peptide-capped gold nanoparticles. *Chemical Communications*, (33), 5009–5011, 2009.

92. A. M. Jackson, J. W. Myerson and F. Stellacci. Spontaneous assembly of subnanometre-ordered domains in the ligand shell of monolayer-protected nanoparticles. *Nature Materials*, 3(5), 330–336, 2004.

93. A. Verma, O. Uzun, Y. H. Hu, Y. Hu, H. S. Han, N. Watson, S. L. Chen, D. J. Irvine and F. Stellacci. Surface-structure-regulated cell-membrane penetration by monolayer-protected nanoparticles. *Nature Materials*, 7(7), 588–595, 2008.

94. Y. Cesbron, C. P. Shaw, J. P. Birchall, P. Free and R. Lévy. Stripy nanoparticles revisited. *Submitted*, 2011.

95. J. A. Davies. Extracellular matrix. In *eLS*. John Wiley & Sons, Ltd, Chichester, 2001.

96. P. L. Yeagle. Cell membrane features. In *eLS*. John Wiley & Sons, Ltd, Chichester, 2009.

97. Z. P. Chen, R. Z. Xu, Y. Zhang and N. Gu. Effects of proteins from culture medium on surface property of silanes-functionalized magnetic nanoparticles. *Nanoscale Research Letters*, 4(3), 204–209, 2009.

98. W. R. Glomm. Functionalized gold nanoparticles for applications in bionanotechnology. *Journal of Dispersion Science and Technology*, 26(3), 389–414, 2005.

99. N. J. Lane. Cell structure. In *eLS*. John Wiley & Sons, Ltd, Chichester, 2001.

100. G. J. Doherty and H. T. McMahon. Mechanisms of Endocytosis. *Annual Review of Biochemistry*, 78, 857–902, 2009.

101. S. Mayor and R. E. Pagano. Pathways of clathrin-independent endocytosis. *Nature Reviews Molecular Cell Biology*, 8(8), 603–612, 2007.

102. G. Sahay, D. Y. Alakhova and A. V. Kabanov. Endocytosis of nanomedicines. *Journal of Controlled Release*, 145(3), 182–195, 2010.

103. P. H. Yang, X. S. Sun, J. F. Chiu, H. Z. Sun and Q. Y. He. Transferrin-mediated gold nanoparticle cellular uptake. *Bioconjugate Chemistry*, 16(3), 494–496, 2005.

104. P. Oh, P. Borgstrom, H. Witkiewicz, Y. Li, B. J. Borgstrom, A. Chrastina, K. Iwata, K. R. Zinn, R. Baldwin, J. E. Testa and J. E. Schnitzer. Live dynamic imaging of caveolae pumping targeted antibody rapidly and specifically across endothelium in the lung. *Nature Biotechnology*, 25(3), 327–337, 2007.

105. C. Tekle, B. van Deurs, K. Sandvig and T. G. Iversen. Cellular trafficking of quantum dot-ligand bioconjugates and their induction of changes in normal routing of unconjugated ligands. *Nano Letters*, 8(7), 1858–1865, 2008.

106. L. W. Zhang and N. A. Monteiro-Riviere. Mechanisms of quantum dot nanoparticle cellular uptake. *Toxicological Sciences*, 110(1), 138–155, 2009.

107. G. Ruan, A. Agrawal, A. I. Marcus and S. Nie. Imaging and tracking of Tat peptide-conjugated quantum dots in living cells: new insights into nanoparticle uptake, intracellular transport, and vesicle shedding. *Journal of the American Chemical Society*, 129, 14759–14766, 2007.

108. C. K. Kim, P. Ghosh and V. M. Rotello. Multimodal drug delivery using gold nanoparticles. *Nanoscale*, 1(1), 61–67, 2009.

Chapter 2

Photothermal heterodyne microscopy

Imaging of individual gold clusters as small as 2.5 nm in size was first demonstrated by a far-field optical method in 2002, when Boyer *et al.*[1] introduced the photothermal interference contrast. The technique was later improved[2,3] and designated as photothermal heterodyne microscopy (PHI) by the same group in Bordeaux (France), and allowed them the unprecedented detection of gold nanoparticles down to 1.4 nm, with a signal to noise ratio over ten. As photothermal imaging is based on the absorption of the nano-objects, metal nanoparticles such as gold or silver nanoparticles[3] can be detected, but also semiconductor nanocrystals[2] or single-walled carbon nanotubes,[4,5] and very recently, Gaiduk *et al.* also demonstrated the detection of individual chromophore-DNA complexes in favourable conditions.[6]

In biological applications the technique was labelled as laser-induced scattering around a nanoabsorber (LISNA) by the Bordeaux group. Blab *et al.* have taken advantage of the sensitivity of this imaging technique to demonstrate its potential in the biotechnology domain by establishing a precise quantification of 20 nm gold nanoparticles bound oligonucleotides in DNA microarrays[7] over an extended range of concentration. They adapted LISNA in a dynamical version, designated as single nanoparticles photothermal tracking (SNaPT), and revealed the lateral diffusion of the transmembrane glutamate AMPA receptor (AMPAR) by tracking individual 5 nm gold nanoparticles conjugated AMPAR in the plasma membrane of live rat hippocampal neurons.[8] In parallel to these single molecule studies, photothermal microscopy was also used in combination with TEM and confocal fluorescence microscopy to study the intracellular fate of peptide-capped gold nanoparticles in mammalian cells[9] or to demonstrate that supposedly "stripy" nanoparticles have an endocytosis-like internalisation pattern[10], which will be presented later in this manuscript.

This chapter will first introduce the different characteristics of the photothermal microscopy technique as they were demonstrated in the literature in the last eight years before presenting the set up that was built in the Centre for Cell Imaging in Liverpool by the author, together with the software that was developed to control it. It will finish by presenting some of the imaging parameters used throughout this manuscript and details about image analysis.

2.1 Principles of the photothermal microscope

Photothermal microscopy is an absorbtion based technique which allows the imaging of various nano-objects. To introduce its principles, the example of metal nanoparticles as imaging targets will be used in this section and often particularly gold nanoparticles. Some of the properties of the technique presented below will be illustrated by figures (Fig. 2.1 and 2.2) reprinted — with permission from the author — from the work of Stéphane Berciaud who developed the technique in Bordeaux (France) during the course of his PhD and published, as first or co-author, most of the theory and experimental single molecule evidences that will be presented here.

2.1.1 Photothermal detection

Standard far field optical detection of metal nanoparticles,[11] as dark field microscopy[12] or total internal reflection microscopy[13] relies on the scattering cross-section of the nanoparticles, which decreases rapidly as d^6 with the diameter d of the particle,[14] for particles sizes significantly smaller than the wavelength of light λ ($\pi d \ll \lambda$). It therefore limits the possibilities of these now classical types of detection to "large" nanoparticles with sizes above 20 nm and larger when observed in scattering environments such as the intracellular medium.[15,16] Conversely, photothermal microscopy relies on the absorption cross-section of the nanoparticles, which varies in a slower manner, as d^3, with the diameter of the absorbing nano-object. For gold nanoparticles excited with a wavelength of 532 nm in water, the absorption is thus typically dominating over the scattering for diameters below 100 nm.[14]

The photothermal method uses two laser beams, a probe beam and a heating beam, overlapped and focused by means of a high numerical aperture objective on the sample containing the nanoparticles. A time-modulated laser beam at a wavelength close to the peak of the surface plasmon resonance band of the nanoparticles ($\lambda_{max} \simeq 520$ nm for 10 nm diameter nanoparticles) is used to induce a local temperature increase around the nanoparticles. Indeed, metal nanoparticles exhibit a large absorbtion cross-section when excited at a wavelength near their surface plasmon resonance (SPR). Additionally, as they possess a fast electron-phonon relaxation time of a few picoseconds[17] (1-4 ps) and exhibit a very weak photoluminescence (especially above 5 nm),[18] the absorbed energy is then efficiently released as

heat to the surrounding medium. A nanoparticle in the focus of the time-modulated (frequency Ω) heating beam is therefore acting as a heat point source dissipating the energy and induces a local spatially-modulated refractive index profile around itself at a given time point. The non-resonant probe beam[a] is scattered by the refractive index profile, producing a frequency shifted scattered field. The beams are further collected, by the same objective for reflection or by an other objective for transmission, and the heating beam is filtered. The interaction between the scattered field and the reference field, either transmitted or reflected, is detected by a fast photodiode. A lock-in amplifier is then used to extract the beat note at the modulation frequency Ω to yield a photothermal signal whose voltage can in turn be recorded by an acquisition card linked to a computer.

A complete demonstration of the calculus of the photothermal signal was given by Berciaud *et al.*[3] This signal is proportional to the beatnote power $P_{B/F}$ that is detected on the photodiode in the backward/forward configuration and writes:

$$P_{B/F}(\Omega) = \eta_{B/F}\sqrt{\alpha_{B/F}}\,P_{probe}\left[2^{\frac{3}{2}}\pi n\frac{\partial n}{\partial T}\frac{P_{heating}}{C_p\lambda^2 w}\right]\sqrt{F_{B/F}(\Omega)^2+G_{B/F}(\Omega)^2} \quad (2.1)$$

where $\eta_{B/F}$ is the transmission factor in the backward or forward configuration, $\alpha_{B/F}$ the intensity reflection/transmission coefficient, n the refractive index of the surrounding medium, C_p the medium heat capacity per unit volume, λ the wavelength of the probe beam, w the probe beam waist in the sample plane, $F_{B/F}$ and $G_{B/F}$ respectively in phase and in quadrature with the modulation frequency components of the signal[b], P_{probe} the power of the probe beam and $P_{heating}$ the power of the heating beam.

The images are acquired by moving the sample over the fixed heating beam by means of a piezoelectric device, each of the collected pixel being acquired with an integration time in the millisecond range (typically 10 ms).

The theoretical dependence of the signal on the nanoparticle cross-section was verified experimentally with gold nanoparticles of different diameters ranging from 1.4 nm to 75 nm (Fig. 2.1A) by Berciaud *et al.*[2] and showed, as expected from the Mie theory, that the signal is proportional to the nanoparticle volume. The linear dependence of the photothermal signal with the heating beam intensity (Fig. 2.1B) was also demonstrated using 10 nm gold nanoparticles. The dependence of the photothermal signal on frequency is hidden in the theoretical expression Eq. 2.1 within the functions $F(\Omega)$ (in phase) and $G(\Omega)$ (in quadrature). Figure 2.1C–D display the intensity of the photothermal signal measured from an individual 10 nm gold nanoparticle in the forward and backward configuration at several frequency of the heating beam, together with the in phase and out of phase theoretical components of the signal. Markedly, the forward configuration shows a significantly better signal from frequencies below $\sim$5MHz.

[a] the probe beam wavelength is typically above the SPR as the absorption is lower

[b] see Berciaud *et al.* for a complete description of the functions $F(\Omega)$ and $G(\Omega)$

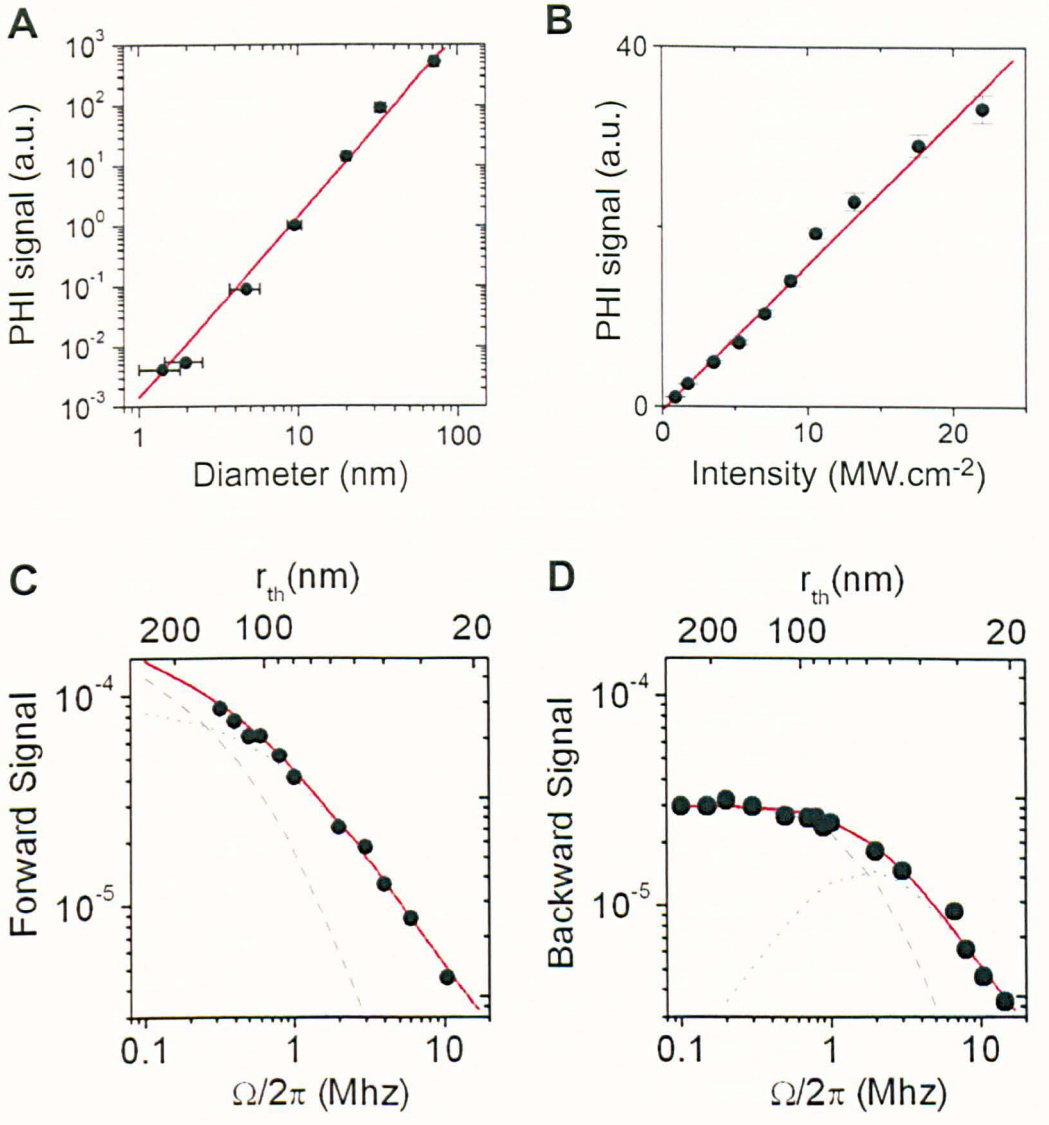

Fig. 2.1 – Photothermal intensity dependence on nanoparticle size, heating beam intensity and modulation frequency. (**A**) Mean photothermal intensity as a function of the gold nanoparticle diameter (black dots) and comparison with the third-order law of the absorbtion cross-section from the Mie theory[19] (red line). (**B–D**) Photothermal intensity measured on individual 10 nm nanoparticles with a heating beam with a wavelength λ=532 nm. (**B**) Photothermal signal as a function of the heating intensity (black dots) and linear fit (red line). (**C–D**) Theoretical (red line) and experimental (black dots) dependence of the forward (C) and backward (D) photothermal signal on the modulation frequency Ω. The in phase (dashed line) and in quadrature (dotted line) — with respect to the modulation — parts of the signal are indicated. (A) is reproduced with permission from Berciaud *et al.*[2] Copyright (2004) by The American Physical Society. (B–D) are reproduced with permission from Berciaud *et al.*[3] Copyright (2006) by The American Physical Society.

2.1.2 Photothermal lateral resolution

As most optical techniques, to the exception of some emerging techniques such as STED and PALM,[20] photothermal microscopy is a diffraction limited technique and should therefore have a resolution of about half the wavelength of light in the direction perpendicular to the beams. Berciaud *et al.* have measured the beam profiles of their 532 nm wavelength heating beam and 633 nm wavelength probe beam and extracted the corresponding full width at half maximum $FWHM_h$ and $FWHM_p$. They conjointly imaged by photothermal microscopy a gold nanoparticle with a high spatial resolution and compared its profile with the product of the heating and probe beams profiles (Fig. 2.2). In conditions where the beams presented a gaussian profile, away from an optimised resolution, they found that the lateral photothermal image profile was similar to that of the product of the two beams profiles (Fig. 2.2A) and had a full width at half maximum ($FWHM_{PHI}$) of 365 nm, which was smaller than that of the two beams ($FWHM_h$=495 nm, $FWHM_p$=520 nm, $FWHM_{p\times h}$=360 nm). When the beams were well filling the objective back focal plane, which corresponds to conditions where diffraction rings of the Airy pattern are observed, they found a $FWHM_{PHI}$ value of 235 nm, which corresponded to the one of the heating beam ($FWHM_h$=235 nm, $FWHM_p$=400 nm, $FWHM_{p\times h}$=213 nm).

Gaiduk *et al.* have used the same method to measure the resolution of their instrument in the three directions. They found values that are close to the ones of Berciaud in the X-Y plane perpendicular to the beam path axis, with $FWHM_{PHI}$ values of 220 and 250 respectively along the x-axis and y-axis.[21] Interestingly, they used a scan in the X-Z plane parallel to the beam axis to find a $FWHM_{PHI}$ of 730 nm.

2.1.3 Application to biological systems

In order to improve the detection performances in photothermal microscopy, one approach is to increase the heating beam intensity. However, when used in live cells, the temperature generated in and around the nanoparticles upon excitation need to be compatible and the heating beam therefore needs to be kept at a reasonable intensity. For example, for 5 nm nanoparticles in water and excited with a heating beam of 500 $kW.cm^{-2}$, the temperature increases of $\sim$1.5 K.[3] This is only at the surface of the nanoparticle and as the temperature is decreasing rapidly away from the nanoparticle as the inverse of the distance the whole cell is not perturbed by the local temperature change.

In cell biology, photothermal microscopy was used in combination with confocal fluorescence microscopy to study the internalisation of peptide-capped gold nanoparticles in mammalian cells and infer the fate of their capping layer inside cells.[9] This will be discussed in the next chapter.

Lasne *et al.* have discovered that cells display an intrinsic photothermal signal coming from the mitochondria.[22] Although they managed to eliminate the previously

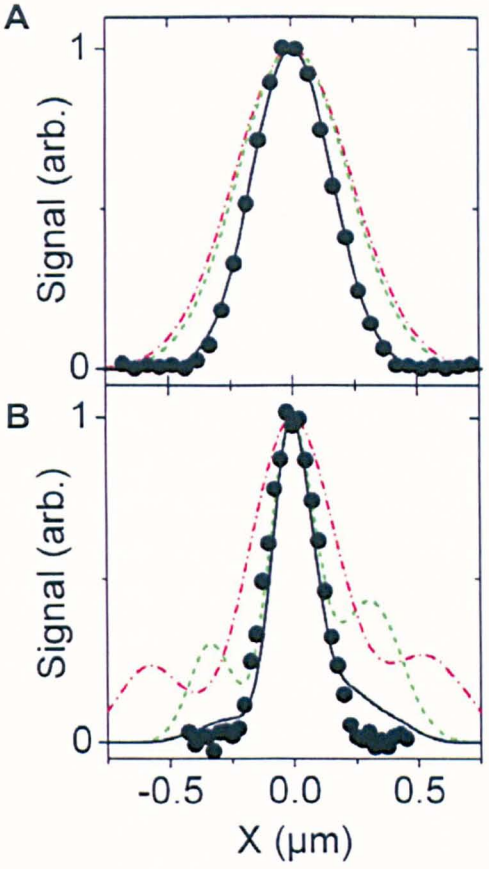

Fig. 2.2 – Experimentally measured resolution of a photothermal microscope. The lateral resolution of the photothermal technique was measured by Berciaud *et al.*[3] for low and high numerical apertures of the beam. Dashed green and red lines correspond respectively to the profile of the heating and probe beams in the focal plane. The solid black line corresponds to the product of the two beams profiles, when the black dots represent the experimentally acquired measures. (**A**) Low aperture gaussian beams; FWHM $= 365 \pm 5$ nm. (**B**) High aperture beams presenting diffraction rings, testimonial of close to diffraction limited spot; FWHM $= 235 \pm 5$ nm. Reproduced with permission from Berciaud *et al.*[3] Copyright (2006) by The American Physical Society.

proposed candidate cytochrome c as potential cause, they could not find the precise origin of the signal. This property of the cells could advantageously be used for label-free mitochondria imaging, but need to be looked after when imaging targets such as nanoparticles are the purpose.

As well as imaging gold nanoparticles in a static way, through individual images, photothermal microscopy also allows the tracking of individual nanoparticles. Indeed, by using a triangulation method the single particle tracking of 5 nm diameter gold nanoparticles linked by antibodies to a glutamate AMPA receptor has been demonstrated by Lasne *et al.*[8] at the surface of the plasma membrane of live rat hippocampal neurons.[8] The nanoparticle tracking made it possible to characterise the lateral diffusion of the receptor and trajectories of several minutes were recorded

at video rates, owing to the stability over time of the photothermal signal. However, the tracking rate of this technique was limited to ~ 30 Hz in 2D, due to the necessity of signal integration time (5 ms) and mechanical stability induced waiting times between movements of the piezo-scanner. Furthermore, the authors state that using a triangulation diameter of 360 nm ($\sim 1.5 \times \mathrm{FWHM_{PHI}}$), the method only allows the following of targets that possess diffusion constants not higher than $0.2\,\mu\mathrm{m.s^{-1}}$. The 2D photothermal tracking method determines the position of a nanoparticle in a plane perpendicular to the laser beams based on the hypothesis that the photothermal signal can be represented by a 2D gaussian distribution. The nanoparticle position at a time t is estimated on a 2D plane from three photothermal signal measurements acquired around the nanoparticle previous position (t-1) — nanoparticle at the geometric centre of an equilateral triangle. The new position is then set to be at the maximum of the inferred 2D Gaussian distribution. This method could therefore be adapted to 3D tracking, but it would necessitate a fourth point (out of plane coordinate) to be acquired during the tracking process to upgrade from 2D to 3D detection, and would further slow down the possibilities.

To access smaller time scale diffusion, the absorption-based version of fluorescence correlation spectroscopy (FCS), namely absorbtion correlation spectroscopy (ACS), would provide the time resolution needed. This technique consists in acquiring the photothermal signal at high sampling rates, with both heating and probe beams and sample being immobile. The signal arises when at least one nanoparticle enters the focal volume and using the autocorrelation function on the recorded signal allows one to derive a characteristic diffusion time of nanoparticles of a known size. As for the tracking of nanoparticles, this technique take advantage of the stability of the photothermal signal over long periods of time, which is a limiting factor in its fluorescence counterpart FCS due to the photobleaching of the dyes. Alternatively, ACS can be used to determine the hydrodynamic diameter of objects of unknown sizes after diffusion time calibration with different nanoparticles of known sizes. Octeau *et al.* demonstrated these possibilities and showed for example that bare gold nanoparticles of ~ 7.4 nm diameter exhibited an increase of 1.2 nm in diameter of when coated with a self-assembled monolayer composed of CALNN peptides.[23]

2.2 Liverpool photothermal microscope set up

In this section, the photothermal microscope built by the author in the Centre for Cell Imaging at the University of Liverpool will be presented. This instrument was assembled by joining optical and electronic hardware to a software that was built for the purpose and that controls the acquisition and links the electronic hardware parts together. First, the set up will be introduced and then a brief overview of the software controlling the acquisition and image building will be given.

2.2.1 Set up overview

The set up built in Liverpool is presented in a schematic view in Fig. 2.3. The probe beam is provided by a HeNe laser (λ=632.8 nm) with a maximum power at the window output of 20 mW. In order to image gold nanoparticles with the highest efficiency, the heating beam is provided by a frequency doubled Nd:YLF laser with a wavelength at 523 nm, which is closer to the plasmon band peak wavelength[c] than more common 532 nm or 514 nm green laser lines. The laser is modulated by an acousto-optic modulator at the reference frequency $\Omega/2\pi$ of 692.5kHz provided by a function generator. The two lasers are overlapped by means of a cold mirror and focused on the sample via a 50×/0.9 NA oil objective. The sample is deposited on the glass coverslip of an Iwaki dish, filled with medium, water or a phosphate buffer saline solution. The dish is attached by the mean of a home built adaptor in the middle of a 3D piezoelectric scanner that possess a 300 μm travel distance in the three directions and that is controlled by a home-built LabVIEW software. The microscope is used in a forward configuration to allow the imaging of nanoparticles that are not in the close vicinity of the glass surface. Additionally, this configuration provide the flexibility of adding solutions to the medium during the imaging, owing to the fact that the sample is not enclosed. Therefore a long working distance water objective (40×/0.8 NA) is dipping in the medium to collect the forward scattered field, which is then going through a redpass filter to discard the heating beam and sent to a fast photodiode. The signal is sent to a lock-in amplifier which extracts the beat note at the modulation frequency. The signal is acquired by an acquisition card, which is attached to a computer.

To acquire a photothermal image, the operator is first moving the microscope motorised stage to the area of interest. Then, an image is built by scanning this area of the sample with the piezoscanner and treating the acquired data to form an image (see next section for details). This is done by a home built software that was created with the LabVIEW graphical programming software and will be described in Sect. 2.2.2.

Additionally to the photothermal microscopy, bright field and wide field fluorescence images can be acquired. The light necessary for these applications is provided by a home built system, which illuminate the sample through the top objective. The light is collected by the second objective and sent to an ultra sensitive EMCCD camera, located at the bottom port of the microscope. For fluorescence imaging excitation and emission filters are added before and after the sample.

A second CCD camera displaying the light reflected from the sample is also available and is essentially used for laser alignment purposes in photothermal microscopy, to ensure that the two beams are focused in the same plane and at the same point.

[c] $\lambda_{max} \sim 520$ nm for 10 nm gold nanoparticles

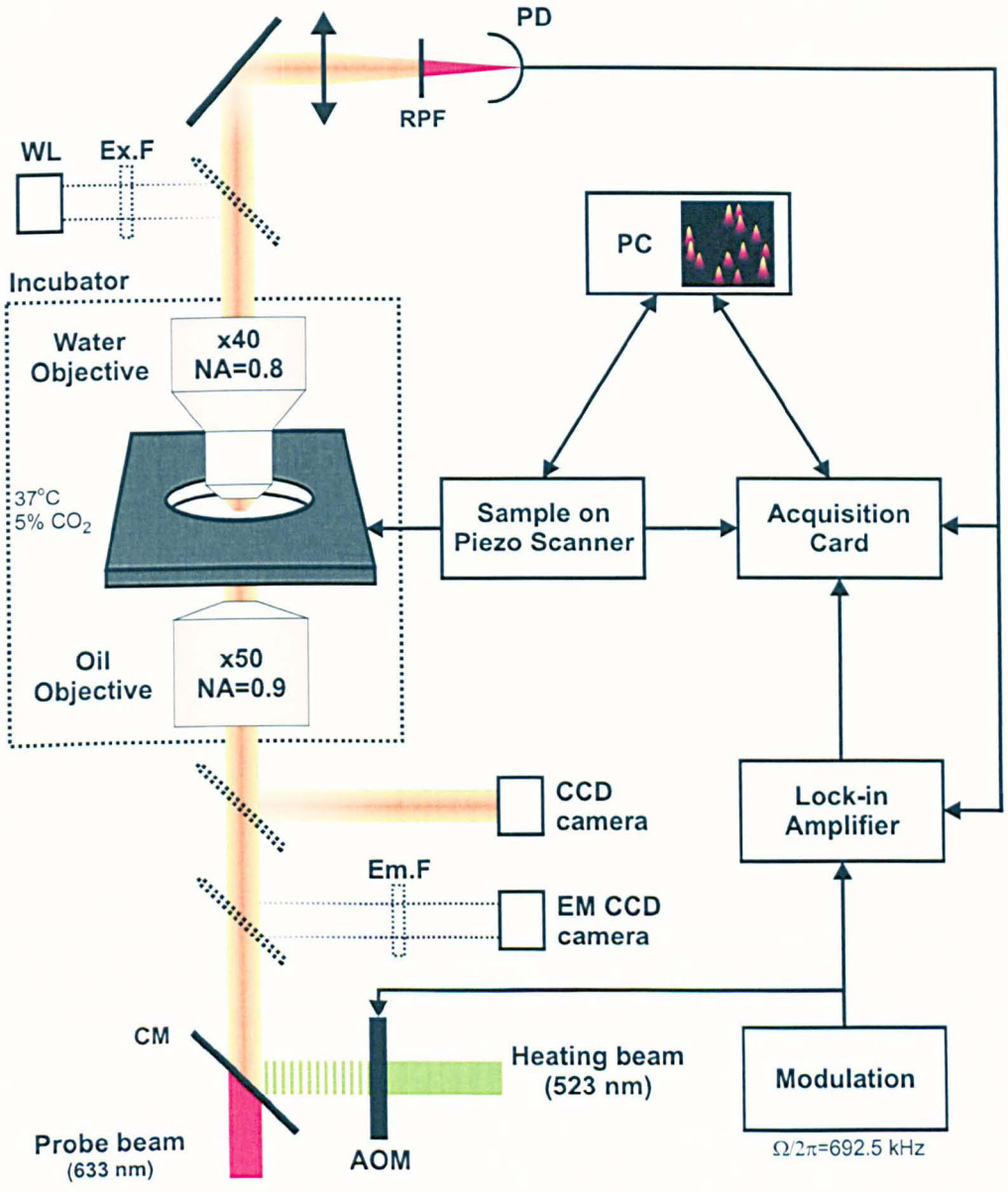

Fig. 2.3 – Liverpool photothermal microscope set up scheme.
Scheme of the experimental set up, with photothermal, bright field and wide field fluorescence microscopy joined on a single instrument. The dashed line outlined box represents the incubator which encloses the microscope stage and the objectives to regulate the temperature to 37 °C and the CO_2 to a 5 % concentration. WL: white light, Ex.F: excitation filter (fluorescence), Em.F: emission filter (fluorescence), AOM: acousto-optic modulator, CM: cold mirror, PD: photodiode, RPF: redpass filter.

The microscope is enclosed in an incubator system that allows to regulate the temperature and the CO_2 percentage to provide the conditions necessary for live cell imaging.

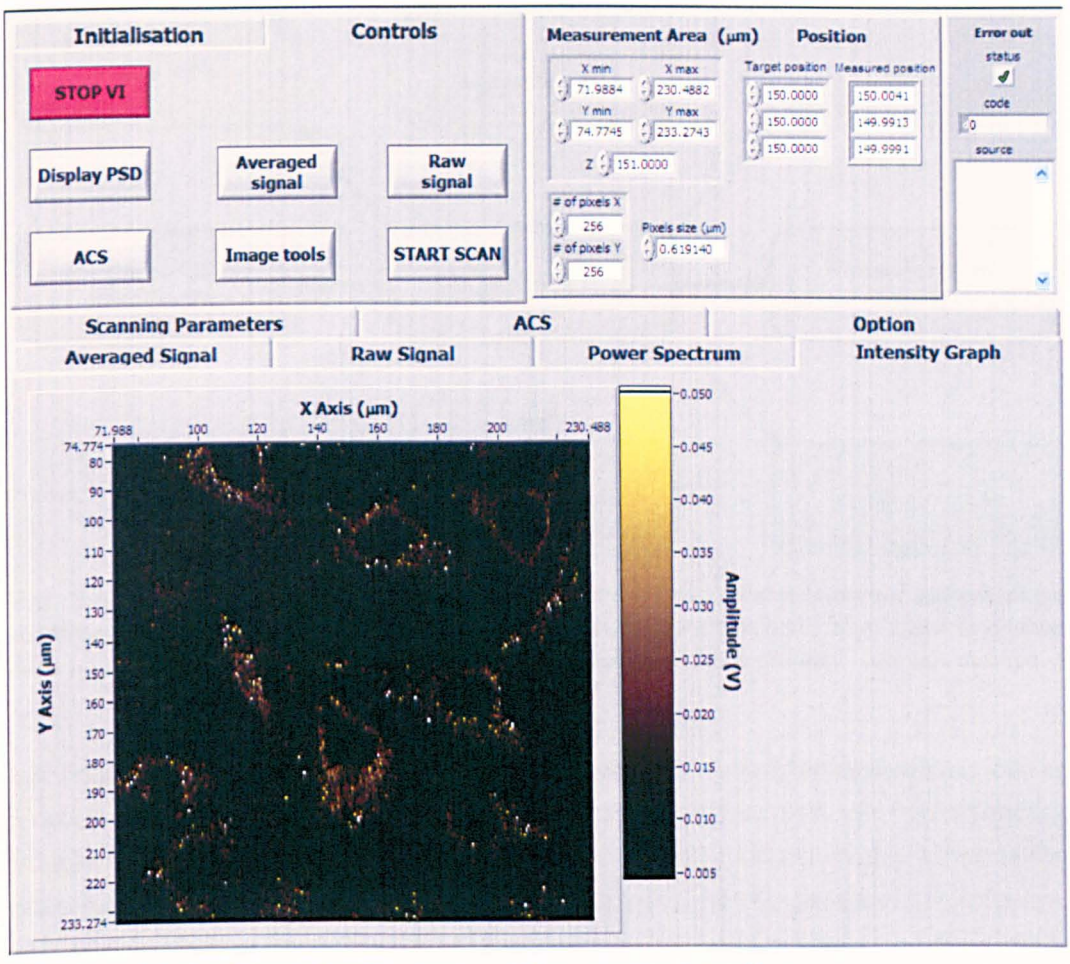

Fig. 2.4 – Photothermal microscope software user interface
The front panel of the software controlling the photothermal microscope was developed with the programming language LabVIEW by the author.

2.2.2 Software development

2.2.2.1 Program kernel

The control of the photothermal microscope is provided by a program written in graphical programming language LabVIEW (program front panel presented in Fig. 2.4). The necessity of building this software arose from the very different elements that need to be connected together to form the scanning and acquisition chain of events. The acquisition card and the piezoelectric controller are connected to the computer respectively by a PCIe and a PCIe-GPIB card. This allows to move the sample and acquire a photothermal signal at the same time. The core of the software is composed of five functions and two additional optional ones were included without any function for future development (Fig. 2.5). Four functions are dedicated to signal acquisition and measure the following: the instantaneous signal from the photodiode, the signal extracted from the lock-in amplifier at the modulation frequency (photothermal signal), the signal power spectrum, the photothermal sig-

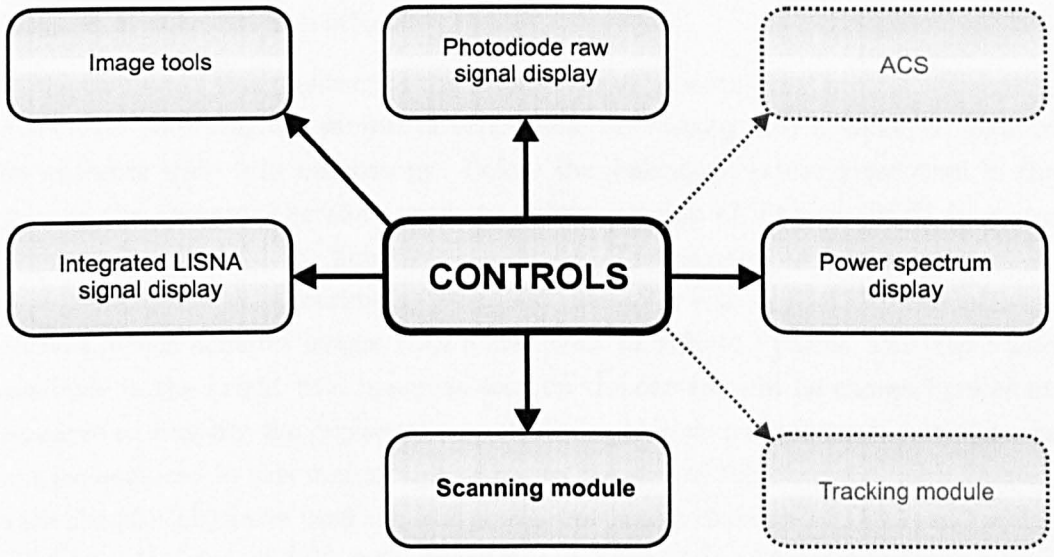

Fig. 2.5 – Schematic of the different functions of the photothermal microscope software. The functions implemented in the software are presented. The boxes in dashed lines represent the future modules for which the development is planned, but not started.

nal acquired over a chosen area (scanning module). Operator movements of the piezoelectric device are possible in the first three functions and the corresponding sample coordinate are measured permanently. The scanning module, which is the main module developed and the one that motivated the development of the software, will be described in Sect. 2.2.2.2. A fifth function is dedicated to image treatments and allows in particular to save the data acquired during an image scan in a TIFF image file format.

2.2.2.2 Scanning module and image building

The creation of a photothermal image is a two step process. First, an area chosen by the operator is scanned while the photothermal signal is simultaneously acquired, and then the data is transformed in a TIFF image file format.

The piezo-electric device is scanning the area chosen line by line by moving at a constant speed in a back and forth manner. As the beginning and the end of each line require the movement to be respectively accelerated and decelerated the area scanned is longer than the one chosen for the image along the fast scanning axis. To provide the time integration of choice[d] 100 photothermal signal measures are acquired within the width of each pixel and an averaging is done post imaging after a synchronisation to retrieve the values of the pixels. The scanning speed is set to correspond to the desired integration time, which is chosen before the start of the scan. A detailled view of the process is presented stepwise in Fig. 2.6 and will be explained in the following paragraphs.

[d] 10 ms were used throughout this manuscript

Region of interest selection

In the context of this manuscript the acquisition of photothermal images was mostly done after observing the sample in bright field microscopy and in some occasion in fluorescence wide field microscopy. Before the scanning module is involved in the process the operator therefore needs to define a region of interest (ROI) to image from the bright field (or fluorescence) image. The camera used to acquire those type of images in the experiments described thereafter was an EMCCD Hamamatsu camera, which acquires images with a maximum of 512×512 pixels. The whole field available in the bright field image as seen on the camera will be chosen here as an example to simplify the explanation, but also as this choice was made in numerous images acquired in this manuscript owing to the size of the observed field. Indeed, with the 50× objective used the 512 pixels represent a distance of 158.5 μm,[e] which allows the imaging of 7–20 cells, depending on their sizes and densities.

Images parameters definition

Once the ROI is chosen, then the operator press the *Start Scan* button and the software is guiding the operator. Several variables need an input from the operator, although default values are present at the first start of the module. The values used for the last scan are remembered when the module was already used (after the first scan), allowing repeated scans of the same area with a minimum of operations.

The operator then enters the following parameters: the laser beams position as seen on the camera (centre of the spot), the number of pixels of the ROI in the X and Y directions in the bright field image (here 512 and 512), the X and Y origin of the ROI (here 0 and 0), the size of a pixel on the camera (objective dependent) and a scaling factor (here 2).

The scaling factor is used to define the photothermal pixel width as a function of the camera pixel size and therefore also defines the number of pixels of the photothermal image. To allow an easy overlay of the bright field and photothermal images, which can be needed to ascertain the nanoparticles localisation to precise cell areas, the number of pixels of the photothermal images (in the X and Y directions) was often chosen by dividing the number of pixels of the camera ROI by a power of two, depending on the resolution desired. As in most cases the bright field images were 512×512 pixels images, the photothermal images acquired were mostly 256×256 pixels images (scaling factor=2).

Scan initialisation

The rest of the process is fully automated and do not require user input. The software then translate the camera frame of reference into the one of the piezoelectric device.

[e] this distance was measured using bright field visualisation and the piezoelectric device

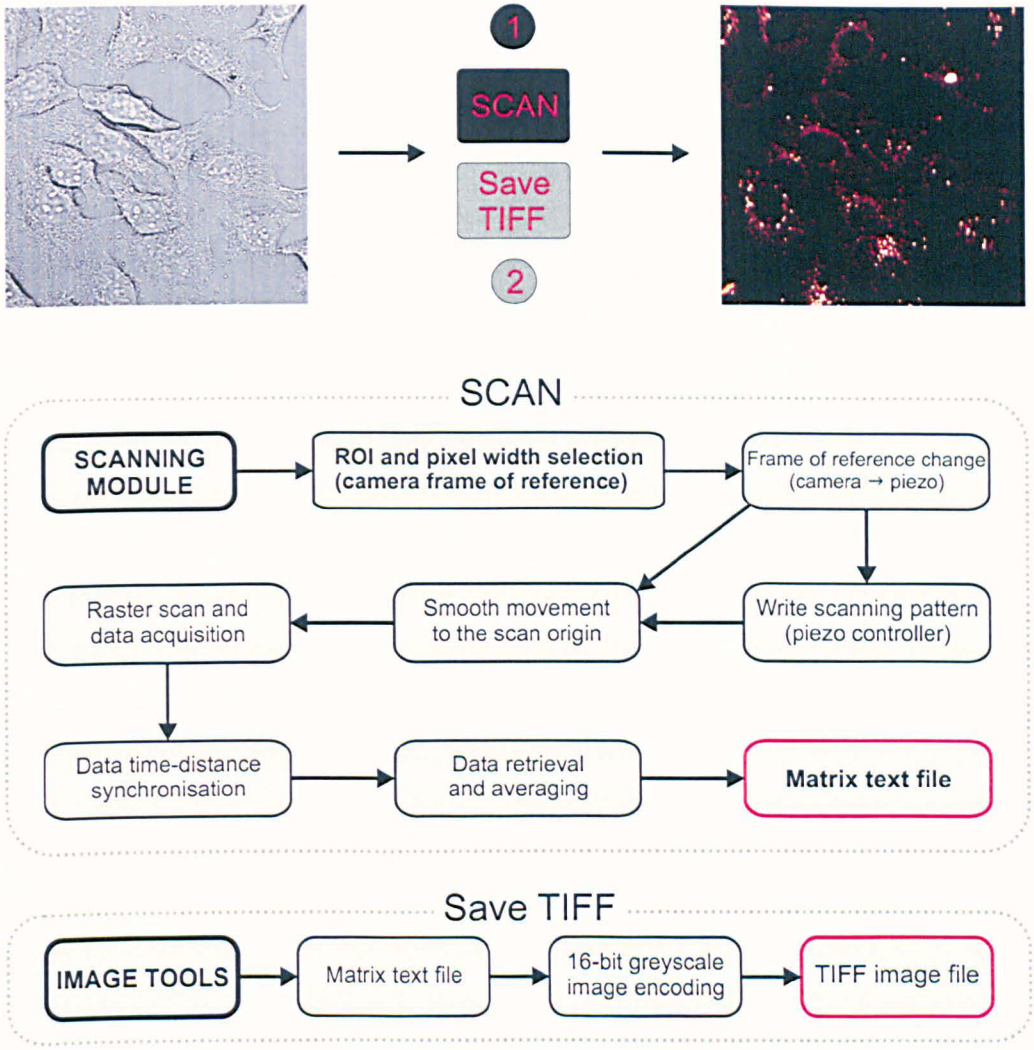

Fig. 2.6 – Schematic of the photothermal image acquisition process. To obtain a photothermal image two steps are required: a scan of the area of choice by the piezo-electric device and the transformation of the acquired data into a TIFF image file format.

Then a waveform is written in the piezo-electric device controller. This sets the trajectory that the piezo-electric device will scan during the acquisition and the scanning speed. This step can be quite time inefficient as it takes about 18 minutes to complete for images of 256×256 pixels, but it only needs to be performed once if all the images acquired on the same experiment are of the same size (pixels width and number of pixels). This waveform can be preloaded before the experiment in order to save this time and this step will be skipped if the scan parameters do not change between scans. After that the piezo-electric device moves towards the scan origin and the acquisition is software initiated.

Scan

The scan is started by sending a command to the piezo-electric device, which will then not need any more input from the controller during the whole scan. Time references are sent from the piezo-electric device to its controller during the scan at regular intervals. The first of them is acquired by the acquisition card and is used as a trigger to fire the beginning of the acquisition. Additionally, the controller stores the position of the piezo-electric device in the fast scanning direction at those time points during the course of the scan.

Synchronisation, data averaging and image storage

The positions stored in the controller are read and used to find the time points at which each line of the image should start and finish. Then the synchronisation is done using those references and the averaging are processed to produce the values of individual pixels. Those values are further stored in a text file as a matrix, each of the value corresponding to the average voltage measured by the photodiode for these pixels. The software then display the scanned image with a representation of the matrix and returns to an idle state.

TIFF file format

To transform the text file saved during the scan the operator needs to use the *Image tools* control button to open a new programm in a new window. Among other functionalities there is a *Save image as TIFF* control button, which allows to save the image in a TIFF image file format. This format was chosen because it allows encoding the images in 16-bit, which corresponds to 65536 shades of grey, and is widely used and supported by numerous softwares. This format also allows to change the image contrast in a non-destructive manner, as it can always be adjusted to the full scale no matter how many time it was adjusted and saved. Additionally, the TIFF image file format can be used as a container to combine different images, such as bright field and photothermal images, in a single image with different image planes corresponding to the original images.

2.2.3 Imaging parameters

The images that were acquired and that will be displayed in this manuscript have a full range of parameters in common. The material that compose the Liverpool photothermal microscope is described in detail in Appendix A and the parameters used for imaging will be described here.

Lasers and modulation

To quantify the power used in the experiments in this manuscript, a transmission coefficient between the entry of the microscope and the output of the objective (without oil) was evaluated. The transmission was 44% for the 523 nm laser and 57% for the HeNe (633 nm) laser. Based on that the power used for photothermal imaging throughout was 0.44 mW for the heating beam, as it was always set at a 1.00 mW value at the entry of the microscope. The probe beam intensity varied and powers between 10.03 mW and 10.65 mW were used, although the most commonly used power was often around 10.4 mW. The modulation frequency provided to the acousto-optic device was 692.5 kHz.

Objectives

As stated earlier the pair of objectives used was composed of a 50×/0.9 NA oil focusing objective and a 40×/0.8 NA water dipping long focal distance collecting objective.

Photodiode and lock-in amplifier

The photodiode (New Focus, USA) was set with a 10^2 gain and frequency filters were set at 100 kHz for the lower frequency and 5 MHz for the higher one. The lock-in amplifier (Signal Recovery, USA) was used in normal mode with a 0 dB AC gain, a sensitivity of 20 mV and a time constant of 5 ms.

Image acquisition

The image acquisition was provided by the combination of the acquisition card, the piezo-electric device and the home built software, as described in Sect. 2.2.2.2. The integration time supplied by the software averaging of 100 measures of the photothermal signal was not varied and was kept at a value of 10 ms.

Imaging altitude

Finally the altitude at which the images were acquired was set by first focusing the beams on the glass coverslip where the sample was situated, to define the origin z=0 μm of the altitude. This was done, when possible, in an area of the dish where only glass could be seen in bright field microscopy. The altitude of imaging was then set to 1 μm[f] in the user interface of the software controlling the photothermal microscope. This altitude was chosen after observing the dependence of the photothermal intensity of a single cell with the altitude to maximise the number of gold nanoparticles probed within cells. HeLa cells were incubated with 10 nm diameter

[f] this was used throughout the manuscript unless otherwise stated in the text or the figure legends

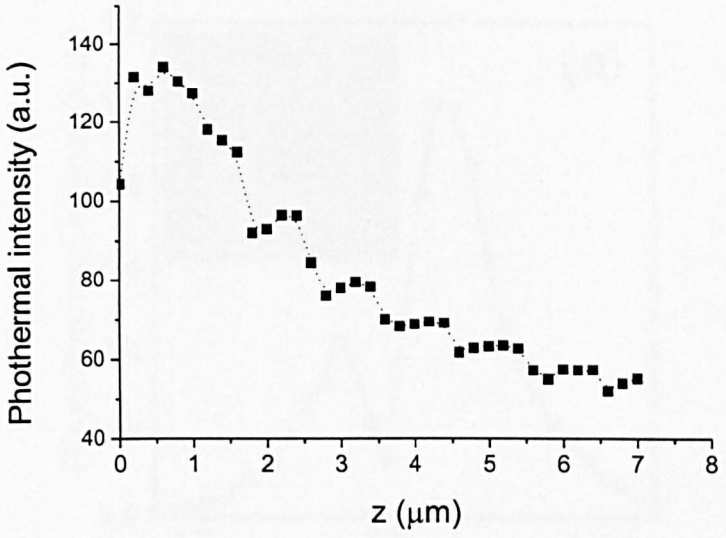

Fig. 2.7 – Dependence of the photothermal intensity on the imaging altitude of one cell. HeLa cells were incubated with CALNN peptides coated 10 nm diameter gold nanoparticles (6 nM final concentration) for three hours before fixation. Photothermal images were then acquired at different altitudes from the origin (glass coverslip) to 7 μm with 0.2 μm steps. The photothermal intensity of the images, which contained only one cell, was averaged for each altitude and is plot as a function of the imaging altitude z.

gold nanoparticles (6 nM final concentration) coated with a self-assembled monolayer exclusively composed of densely packed CALNN peptides for three hours at 37 °C (5 % CO_2) before their fixation[g]. Photothermal images[h] were then acquired at different altitudes from the origin (glass coverslip) to 7 μm with 0.2 μm steps. The photothermal intensity of the images, which contained only one cell, was averaged for each altitude to yield a mean photothermal intensity value of the cell at a given altitude and is plot as a function of the imaging altitude z in Fig. 2.7. The plot shows a maximum of the photothermal signal located at an altitude between 0.5 and 1 μm, before the intensity is decreasing gradually to reach a value that is probably close to that of the background.

This singularity could be explained in the case of a cell by the spreading of its shape in the z-axis. Indeed, a cell attached to a glass dish is rather flat, and beside around the nucleus, is not extended in the z-axis. It is therefore reasonable to hypothesise that most of the internalised nanoparticles are within 1–2 μm from the glass coverslip where the cells are attached. However, this should be linked to the dependence of the photothermal signal of single nanoparticles as a function of the altitude. Giblin *et al.* have imaged a single 40 nm gold nanoparticle on a glass coverslip and have found that the maximum of photothermal signal along the z-axis is surprisingly not located at the origin (Fig. 2.8). Instead, the signal is increasing

[g]nanoparticle and cell work: P. Free
[h]image size: 62 × 62 μm, pixel width: 0.62 μm

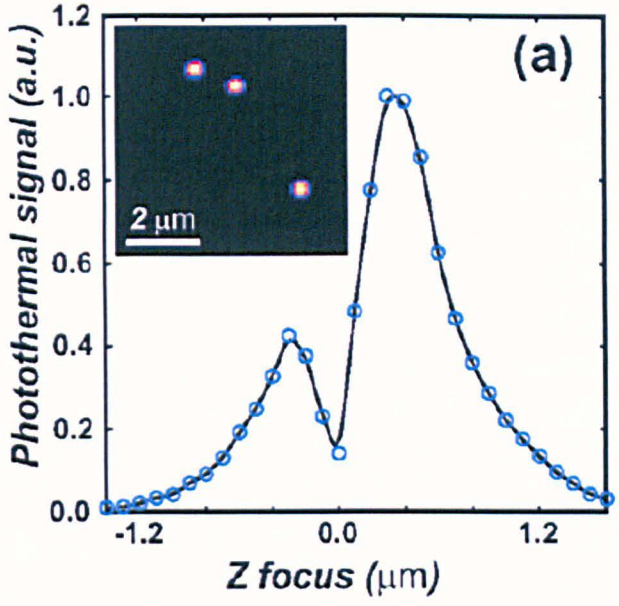

Fig. 2.8 – Dependence of the photothermal signal on the altitude for a single nanoparticle. An individual 40 nm gold nanoparticle was imaged by photothermal microscopy by Giblin *et al.*[24] The plot shows the dependence of the photothermal signal on the altitude of the focused beams. Adapted with permission from Fig.4 in Giblin *et al.*[24] Copyright 2010 American Chemical Society.

from 0 μm to reach a maximum around 0.35 μm to then decrease rapidly.

2.3 Image analysis

Two methods were used in this manuscript to analyse the photothermal images. The goal was to find a measure of the cells gold nanoparticle content to assess the amount of nanoparticles internalised by cells, and especially to allow a comparison between different conditions, such as different self-assembled monolayer coating subsequently assessing the influence of the surface chemistry on the nanoparticle uptake.

Whole field method

The method consists in drawing a region of interest (ROI) around the cells in a photothermal image and measuring the photothermal intensity of that region above a threshold. The analysis was processed using the software AQM Advance 6.0.2.23 (Kinetic Imaging Ltd, UK). The bright field and photothermal images, both encoded in a 16-bit TIFF file format, were joined in a TIFF image file container composed of two image planes (bright field, photothermal). A single region of interest (ROI) was drawn on the bright field image around all the cells that were appearing as whole in that field of view using the free hand polygon image tool of the AQM Advance software, leaving the areas which did not include cells outside of it as much

as possible. A few regions were drawn on the image using the ellipse tool of AQM Advance in areas where no cells were present and the mean photothermal intensity of these regions was used to produce a mean photothermal background intensity. The mean photothermal intensity of the ROI including all the whole cells was measured by setting up a threshold corresponding to 1.5 times the mean background photothermal intensity of the field of view, to yield a mean photothermal intensity of the ROI. This procedure was repeated for each of the images acquired for a given condition and for each condition. For each condition, the mean photothermal intensities of the fields were averaged to produce a mean photothermal intensity and a standard error, representing respectively a measure of the mean nanoparticle uptake per cell for the given condition and its accuracy.

Single cell method

The method consists in drawing a region of interest (ROI) around each of the cells present in an image and measuring the photothermal intensity of these regions once a mean background value is subtracted. The analysis was processed using the software AQM Advance 6.0.2.23 (Kinetic Imaging Ltd, UK). The bright field and photothermal images, both encoded in a 16-bit TIFF file format, were joined in a TIFF image file container composed of two image planes (bright field, photothermal). A region of interest was drawn around each of the cells that were appearing as whole in that field of view using the bright field image and the free hand polygon image tool of the AQM Advance software. A few regions were drawn on the image using the ellipse tool of AQM Advance in areas where no cells were present and the mean photothermal intensity of these regions was used to produce a mean photothermal background intensity. The mean photothermal intensity of each of the ROIs including the cells was measured after subtraction of the average photothermal background intensity of the field of view, to yield a mean photothermal intensity for each whole cell. This procedure was repeated for each of the images acquired for a given condition and for each condition. For each condition, the mean single cell photothermal intensities were then averaged to produce a mean photothermal intensity and a standard error, representing respectively a measure of the mean nanoparticle uptake per cell for the given condition and its accuracy.

2.4 Bibliography

1. D. Boyer, P. Tamarat, A. Maali, B. Lounis and M. Orrit. Photothermal imaging of nanometer-sized metal particles among scatterers. *Science*, 297(5584), 1160–1163, 2002.

2. S. Berciaud, L. Cognet, G. A. Blab and B. Lounis. Photothermal heterodyne imaging of individual nonfluorescent nanoclusters and nanocrystals. *Physical Review Letters*, 93(25), 257402, 2004.

3. S. Berciaud, D. Lasne, G. A. Blab, L. Cognet and B. Lounis. Photothermal heterodyne imaging of individual metallic nanoparticles: Theory versus experiment. *Physical Review B*, 73(4), 045424, 2006.

4. S. Berciaud, L. Cognet, P. Poulin, R. B. Weisman and B. Lounis. Absorption spectroscopy of individual single-walled carbon nanotubes. *Nano Letters*, 7(5), 1203–1207, 2007.

5. S. Berciaud, L. Cognet and B. Lounis. Luminescence decay and the absorption cross section of individual single-walled carbon nanotubes. *Physical Review Letters*, 101(7), 077402, 2008.

6. A. Gaiduk, M. Yorulmaz, P. V. Ruijgrok and M. Orrit. Room-Temperature Detection of a Single Molecule's Absorption by Photothermal Contrast. *Science*, 330(6002), 353–356, 2010.

7. G. A. Blab, L. Cognet, S. Berciaud, I. Alexandre, D. Husar, J. Remacle and B. Lounis. Optical readout of gold nanoparticle-based DNA microarrays without silver enhancement. *Biophysical Journal*, 90(1), L13–L15, 2006.

8. D. Lasne, G. A. Blab, S. Berciaud, M. Heine, L. Groc, D. Choquet, L. Cognet and B. Lounis. Single nanoparticle photothermal tracking (SNaPT) of 5-nm gold beads in live cells. *Biophysical Journal*, 91(12), 4598–4604, 2006.

9. V. Sée, P. Free, Y. Cesbron, P. Nativo, U. Shaheen, D. J. Rigden, D. G. Spiller, D. G. Fernig, M. R. H. White, I. A. Prior, M. Brust, B. Lounis and R. Lévy. Cathepsin L Digestion of Nanobioconjugates upon Endocytosis. *ACS Nano*, 3(9), 2461–2468, 2009.

10. Y. Cesbron, C. P. Shaw, J. P. Birchall, P. Free and R. Lévy. Stripy nanoparticles revisited. *Submitted*, 2011.

11. M. A. van Dijk, M. Lippitz and M. Orrit. Far-field optical microscopy of single metal manoparticies. *Accounts of Chemical Research*, 38(7), 594–601, 2005.

12. S. Schultz, D. R. Smith, J. J. Mock and D. A. Schultz. Single-target molecule detection with nonbleaching multicolor optical immunolabels. *Proceedings of the National Academy of Sciences of the United States of America*, 97(3), 996–1001, 2000.

13. C. Sonnichsen, S. Geier, N. E. Hecker, G. von Plessen, J. Feldmann, H. Ditlbacher, B. Lamprecht, J. R. Krenn, F. R. Aussenegg, V. Z. H. Chan, J. P. Spatz and M. Moller. Spectroscopy of single metallic nanoparticles using total internal reflection microscopy. *Applied Physics Letters*, 77(19), 2949–2951, 2000.

14. M. A. van Dijk, A. L. Tchebotareva, M. Orrit, M. Lippitz, S. Berciaud, D. Lasne, L. Cognet and B. Lounis. Absorption and scattering microscopy of single metal nanoparticles. *Physical Chemistry Chemical Physics*, 8(30), 3486–3495, 2006.

15. J. Aaron, E. de la Rosa, K. Travis, N. Harrison, J. Burt, M. Jose-Yacaman and K. Sokolov. Polarization microscopy with stellated gold nanoparticles for robust, in-situ monitoring of biomolecules. *Optics Express*, 16(3), 2153–2167, 2008.

16. L. H. Xiao, L. Wei, Y. He and E. S. Yeung. Single Molecule Biosensing Using Color Coded Plasmon Resonant Metal Nanoparticles. *Analytical Chemistry*, 82(14), 6308–6314, 2010.

17. S. Link and M. A. Ei-Sayed. Optical properties and ultrafast dynamics of metallic nanocrystals. *Annual Review of Physical Chemistry*, 54, 331–366, 2003.

18. J. P. Wilcoxon, J. E. Martin, F. Parsapour, B. Wiedenman and D. F. Kelley. Photoluminescence from nanosize gold clusters. *Journal of Chemical Physics*, 108(21), 9137–9143, 1998.

19. G. Mie. Beiträge zur optik trüber medien, speziell kolloidaler metallösungen. *Annalen Der Physik*, 25(3), 377–445, 1908.

20. S. W. Hell. Far-field optical nanoscopy. *Science*, 316(5828), 1153–1158, 2007.

21. A. Gaiduk, P. V. Ruijgrok, M. Yorulmaz and M. Orrit. Detection limits in photothermal microscopy. *Chemical Science*, 1(3), 343–350, 2010.

22. D. Lasne, G. A. Blab, F. De Giorgi, F. Ichas, B. Lounis and L. Cognet. Label-free optical imaging of mitochondria in live cells. *Optics Express*, 15, 14184–14193, 2007.

23. V. Octeau, L. Cognet, L. Duchesne, D. Lasne, N. Schaeffer, D. G. Fernig and B. Lounis. Photothermal Absorption Correlation Spectroscopy. *ACS Nano*, 3(2), 345–350, 2009.

24. J. Giblin, M. Syed, M. T. Banning, M. Kuno and G. Hartland. Experimental Determination of Single CdSe Nanowire Absorption Cross Sections through Photothermal Imaging. *ACS Nano*, 4(1), 358–364, 2010.

Chapter 3

Non-specific delivery of gold nanoparticles

Gold nanoparticles have unique absorption properties that make them attractive probes for molecular imaging.[1–6] There are though many steps to climb up before they can be used as such. First, a protective monolayer should be implemented at their surface, in order to prevent them from aggregating, and then potentially desired functions are to be added. To enable high resolution real time imaging of intracellular processes, it is critical to understand and control the process of nanoparticle internalisation. Such an understanding is also important for applications of nanomaterials in medicine. There is therefore a need to understand how nanoparticles can be internalised inside cells in a controlled manner. Different strategies can be applied for this internalisation. One of the most commonly used path for nanomaterial cell delivery is through endocytosis,[7,8] which is a mechanism by which molecules that are not membrane-permeable are delivered to the cell interior through vesicles formed at the surface of the cell membrane. An other important question is the evolution of the chemical and physical properties of the nanoparticles after entry, in particular, the biochemical integrity of the capping layer.

In order to comply with the long term goal of using them as molecular imaging labels, the nanoparticles used to study their internalisation ought to be not too small, to allow for their detection inside the cells, but also small enough not to interfere with the cells mechanisms and to be mobile enough within the cells. The size range of 5–10 nm was thus chosen for the nanoparticles used throughout these studies, as they are not too small to be observed by both transmission electron microscopy and photothermal microscopy within cells.

Short peptide sequences were chosen to form the protective monolayer as they were previously shown to provide good solubility and stability in physiological condition, limit the non-specific interactions and also to bring an easy functionalisation

route.[9–12] More precisely, the peptide CALNN was used as a matrix to implement a densely packed monolayer on the gold nanoparticles, while other peptides bearing groups of interest were added to the content of the monolayer during its self-assembled formation when a precise function was needed.

Finally, HeLa cells were predominantly used throughout this study of the uptake of gold nanoparticles in mammalian cells, as they are a widely available and well characterised cell line, with no peculiar transport or signalling behaviour, and are therefore a good mammalian cell model.

This chapter first describes some characteristics of the intracellular internalisation of peptide-capped gold nanoparticles by endocytosis, before taking a closer look at the fate of the self-assembled monolayer after the uptake of the nanoparticles, and finishing by presenting how the tuning of the monolayer is changing the way the nanoparticles are internalised.

3.1 Nanoparticles internalisation: endosomal pathway

3.1.1 Intracellular nanoparticle localisation

In order to observe nanoparticles localisation inside cells, transmission electron microscopy (TEM) is a logical technique to use. Classical TEM — as opposed to High Resolution TEM (HR-TEM) — possesses a resolution that allows imaging of individual peptide-capped gold nanoparticles of 5 or 10 nm diameter in cells. This is possible because of the good contrast provided by the electron dense gold core. However, cell compartments and organelles have contrasts that can make it difficult for nanoparticles below 5 nm to be assigned as such or even really unmanageable to distinguish them from the cell background.

Other drawbacks in the use of TEM in cell imaging, and in the study of the uptake of nanoparticles in cells in particular, range from the necessity of cells fixation or sectioning to the important number of images required to build a representative picture of a phenomenon through quantification.

Nevertheless, TEM provides a level of detail on the localisation of nanoparticles within cells that is difficult to compete with. Figure 3.1 shows an example of the typical nanoparticle endocytotic uptake pathway, where the nanoparticles have been engulfed by cells in endosomal vesicles[a]. The black arrow points towards an endosome filled with several peptide-capped 10 nm diameter nanoparticles, located near the cell membrane. The light grey area at the bottom right corner of the image corresponds to the outer side of the cell, suggesting that the endosome is seen shortly after its formation.

Although TEM is helpful in looking at details at the subcellular level, it is not the most appropriate technique to look at the level of a whole cell. To achieve that,

[a] nanoparticle and cells preparation, TEM imaging: P. Nativo

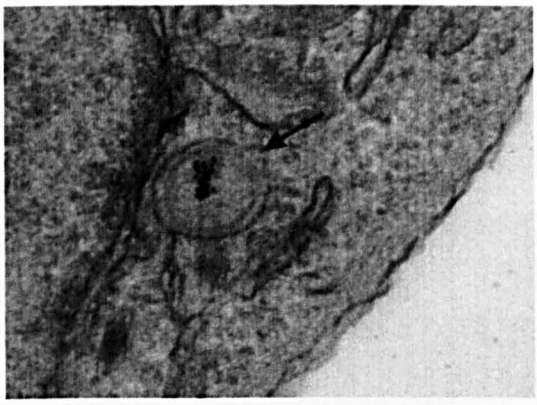

Fig. 3.1 – Endosomal localisation of peptide-capped gold nanoparticles in HeLa cells. 10 nm gold nanoparticles were incubated at a final concentration of 6 nM for 3 h in serum-containing medium with HeLa cells. The cells were further fixed, prepared for and imaged by TEM (P. Nativo). The arrow points towards an endosome containing several particles, characteristic of the uptake of CALNN-capped gold nanoparticles.

photothermal microscopy and confocal fluorescence microscopy were used. Photothermal microscopy is able to image directly individual gold nanoparticles as small as 1.4 nm in ideal conditions[2] and to track 5 nm gold nanoparticles in live cells[5] through their strong absorption cross-section. It will therefore be used to assess unambiguously the amount of nanoparticles taken up by the cells. Confocal fluorescence microscopy is a powerful tool as it allows a routinely fast and precise imaging of fluorescent molecules in living cells. However, the gold nanoparticles that were used here (5–10 nm) are not intrinsically fluorescent as smaller nanoparticles can be.[13] Additionally the use of fluorescent molecules functionalised on the gold core does not allow to follow the nanoparticles as the fluorescence would be quenched due to non-radiative energy transfer to the gold core (Fig. 3.2A, left). It is thus not possible to use fluorescence directly to image the internalisation of the gold nanoparticles themselves.

Yet the quenching property provides an alternate way of following the entry of fluorescently labelled nanoparticles in cells, through the release or the degradation of ligands holding the fluorescent label from the nanoparticle monolayer (Fig. 3.2A, right). A mixed peptide monolayer composed predominantly of the matrix peptide CALNN (95 %) and a small proportion (5 %) of fluorescently tagged peptides CALNN-th-fam (Fig. 3.2B) was therefore used to assess the intracellular fate of the monolayer following the gold nanoparticles entry. The fluorescently labelled CALNN-th-fam peptide, starting with the same amino acid sequence as the matrix peptide (CALNN), is extended by a thrombin cleavage sequence and terminated by a fluorescent dye, fluorescein, in the fam group. The thrombin cleavage sequence (LVPRGS) can be cleaved by the protease thrombin and was added in the design to allow *in vitro* experiments. Although the presence of the cleavage sequence could be seen as being a potential problem in assessing the nanoparticles monolayer de-

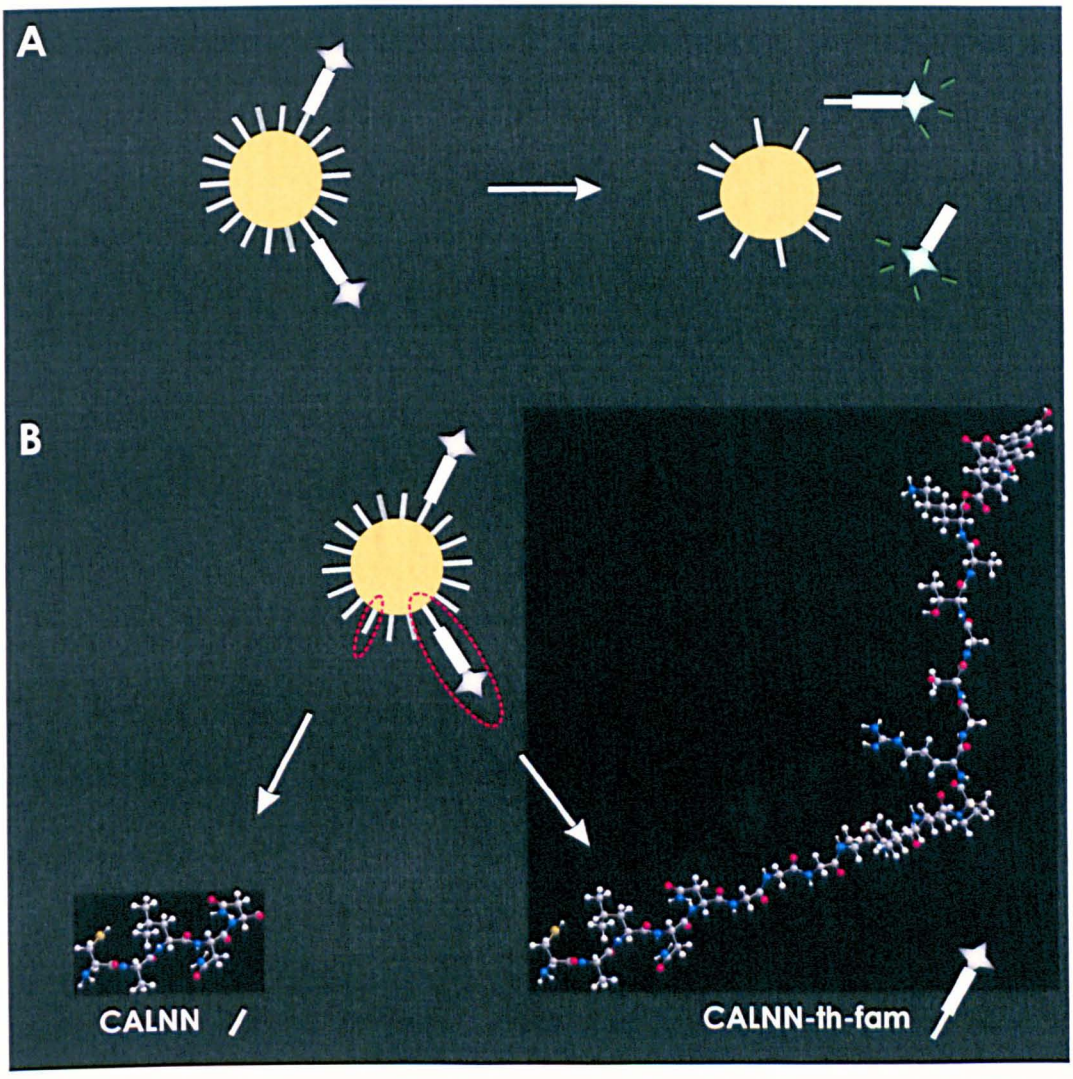

Fig. 3.2 – Quenched/unquenched fluorescently labelled peptide-capped gold nanoparticles. (**A**) The nanoparticles are capped by peptides of which a few are terminated by a fluorescent dye (fam). Left: upon excitation the fluorescence is quenched by the gold core. Right: the dyes are further away from the gold core after release or degradation of the peptide monolayer and fluorescence is emitted upon excitation. (**B**) Nanoparticles are coated with two types of ligands, the matrix peptides CALNN and a few fam dye terminated CALNN-th-fam (th: GGGALVPRGSGTAK) peptides, to form a densely packed protective self-assembled monolayer.

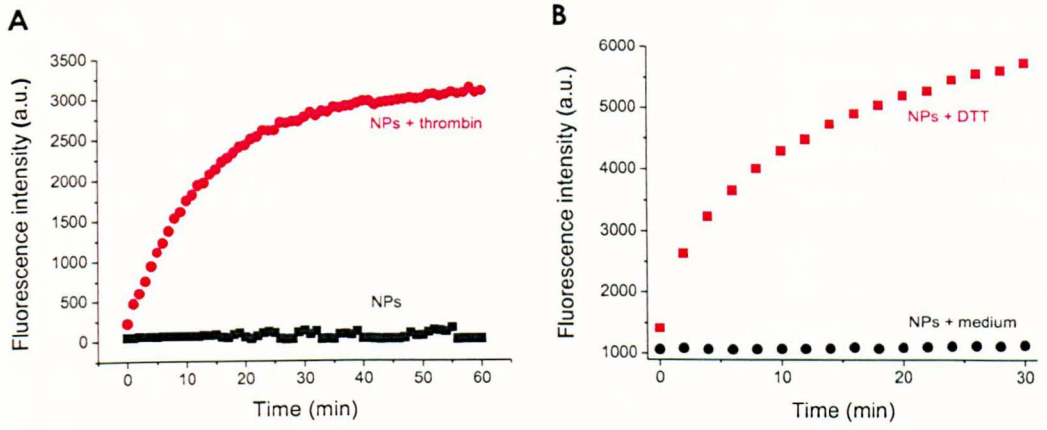

Fig. 3.3 – *In vitro* induced unquenching of a fluorescent dye at the surface of a nanoparticle by proteolysis and ligand exchange. Quenched fluorescently labelled gold nanoparticles were coated with a peptide self-assembled monolayer composed of 5 % CALNN-th-fam (fam dye terminated) and 95 % CALNN. (**A**) *In vitro* assay (P. Free) shows fluorescence release (red dots) after the enzyme thrombin cleaved the peptides bearing fam groups compared to control conditions without thrombin (black squares) and no fluorescence release. (**B**) *In vitro* assay (P. Free) using nanoparticles incubated with DTT shows fluorescence release due to ligand exchange (red squares). No fluorescence release can be observed from nanoparticles incubated with serum-containing medium (black dots), showing that serum does not induce ligand exchange on the peptide-capped nanoparticles.

gradation, thrombin is an extracellular enzyme, and is not present in its active form inside cells. There is therefore no risk that the thrombin cleavage sequence would promote the degradation of the self-assembled monolayer and provoke a release of fluorescence during the internalisation of the nanoparticles in cells. The major part of the nanoparticles is covered by CALNN peptides, which end with a polar uncharged side chain of the asparagine providing the necessary hydrophilicity. The part of CALNN-th-fam exposed to the solution (GGGALVPRGSGTAK-fam) possesses two amino acids (lysine and arginine) with positively charged side chains, but overall the terminal carboxylic groups of the asparagine amino acid on the CALNN peptides, in a large excess (19:1) with respect to CALNN-th-fam, leaves the surface of the nanoparticles with a negative net charge at basic, neutral and slightly acidic pH (terminal carboxylic group pK_a=4[9]).

Figure 3.3A presents an *in vitro* assay[b] where quenched fluorescently labelled nanoparticles (5 % CALNN-th-fam — 95 % CALNN) were incubated with (red dots) or without thrombin (black squares). This gives a proof of principle that the nanoparticle constructs can be used to monitor the degradation of the self-assembled monolayer during the entry of those nanoparticles in cells, should any release or degradation of some of the peptides in the monolayer occur during this process.

To use fluorescence as a proxy to assess the integrity of the monolayer after internalisation of the nanoparticles, it is also important to verify that thiolated

[b]nanoparticle preparation and fluorescence assay: P. Free

ligands in the medium do not exchange with the peptide ligands of the self-assembled monolayer. Ligand exchange with the peptides bearing the fluorescent dye during incubation would lead to a loss of fluorescent markers and make it impossible to use fluorescence to study the degradation of the monolayer inside the cells. Similarly, if a functional peptide was included in the monolayer — a cell penetrating peptide for example — ligand exchange could impair partially or totally the cell entry strategy due to a loss of functionality. Figure 3.3B displays an *in vitro* assay[c] showing that no fluorescence release can be observed for nanoparticles incubated with serum-containing medium (black dots), as opposed to DTT — known to promote ligand exchange[14] — provoking the release of the dyes. This leads to the conclusion that serum-containing medium does not induce ligand exchange at the surface of the monolayer during the nanoparticles incubation.

To follow the internalisation of peptide-capped gold nanoparticles, and their subsequent monolayer degradation, HeLa cells were incubated with the same 10 nm gold nanoparticles coated with a mixed peptide (5 % CALNN-th-fam — 95 % CALNN) self-assembled monolayer (6 nM final concentration) for three hours[d]. They were subsequently imaged by confocal fluorescence microscopy[e] (live cells) and photothermal microscopy (fixed cells). Photothermal microscopy images clearly show an endosomal distribution of the uptaken nanoparticles (Fig. 3.4A), which was already observed by TEM in the same conditions (Fig. 3.1), when confocal fluorescence microscopy images point towards the same pattern of internalisation, through the vesicularly shaped fluorescence release (Fig. 3.4C) due to the peptide monolayer degradation of those nanoparticles. It indicates that the release of fluorescence, owing to the degradation of the peptide self-assembled monolayer coating the nanoparticles, could be used as a tool to study the internalisation of the nanoparticles.

3.1.2 Nanoparticle uptake dynamics

Although many groups have studied the entry of various nano-objects in cells, very little is usually reported about the dynamics of entry. In order to gain insights into the gold nanoparticle uptake kinetics, the unquenching property of the fluorescently labelled nanoparticles constructs was used, aiming to follow the internalisation of the nanoparticles through the monolayer degradation consecutive to the nanoparticles endocytosis.

For that, 10 nm gold nanoparticles coated with a mixed peptide (5 % CALNN-th-fam — 95 % CALNN) self-assembled monolayer, as used previously, were incubated with HeLa cells in a microscope incubator over more than ten hours.[f] The fluorescence release was monitored by time-lapse imaging on a fluorescence confocal micro-

[c] nanoparticle preparation and fluorescence assay: P. Free
[d] nanoparticle preparation: P. Free
[e] cell work and fluorescence imaging: V. Sée
[f] nanoparticle preparation: P. Free; cell work, fluorescence imaging and image analysis: V. Sée

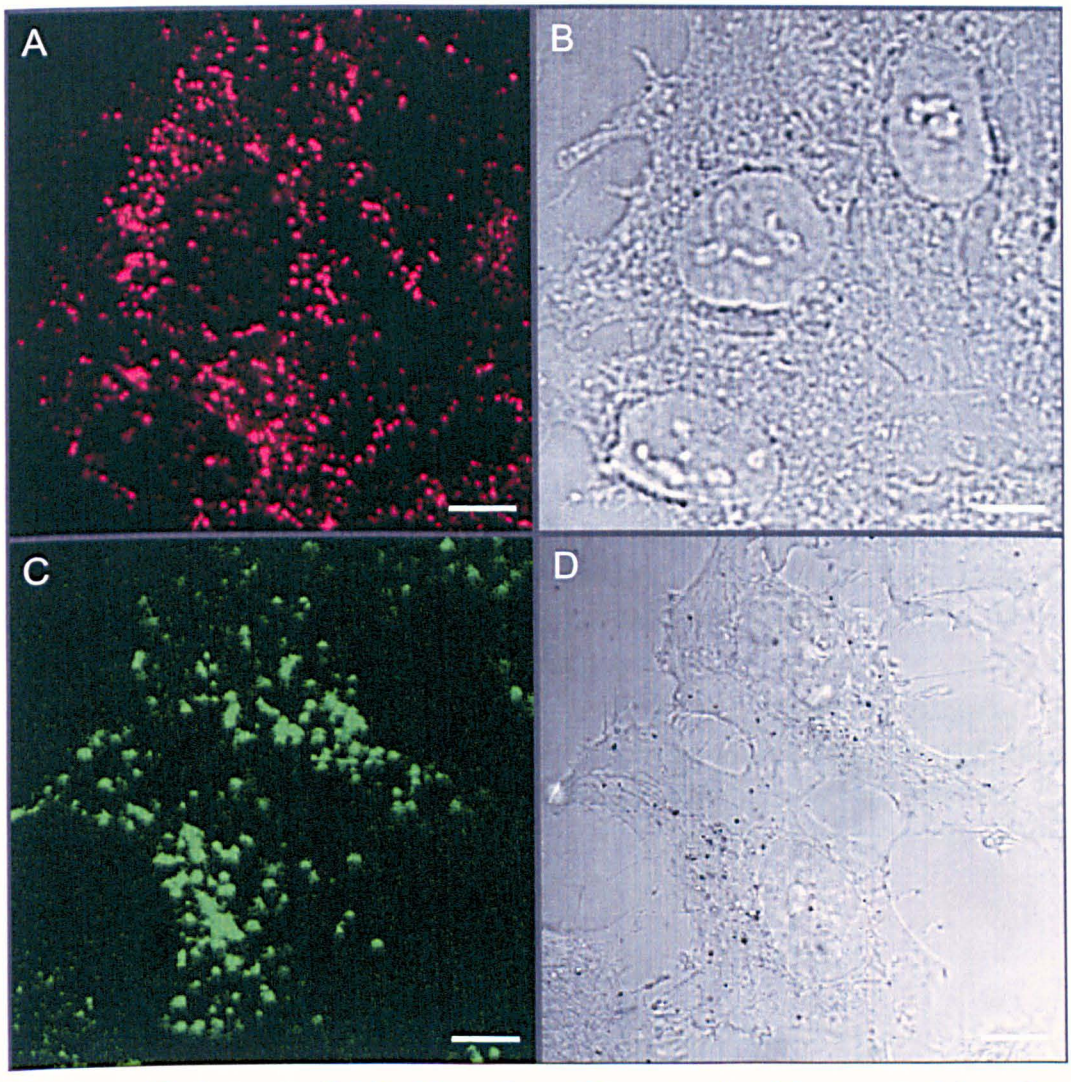

Fig. 3.4 – Endosomal distribution of peptide-capped gold nanoparticles after uptake in HeLa cells. HeLa cells were incubated for 3 h with 10 nm gold nanoparticles coated with a mixed peptide (5 % CALNN-th-fam — 95 % CALNN) self-assembled monolayer (6 nM final concentration), imaged by confocal fluorescence microscopy (V. Sée), fixed and later imaged by photothermal microscopy. (**A**) Photothermal microscope image. (**B**) Bright field image corresponding to (A). (**C**) Confocal fluorescence microscope image. (**D**) Bright field image corresponding to (C). Scale bars represent 10 μm.

scope, to allow a timed quantification of the self-assembled monolayer degradation from several fields of view.

The images show an increase of the fluorescence release over time (Fig. 3.5A). Just after the beginning of the incubation with the nanoparticles almost no fluorescence can be detected. One hour after, the fluorescence release is then visible and its level increases over time, allowing a real-time visualisation of the entry and degradation of the peptide monolayer through the unquenching of the fluorescein molecules.

An analysis of the intensity of fluorescence over time was done on a single cell basis. The different cells analysed present a variation of their fluorescence intensities for given time points, but a similar trend can be observed. Individual cells display monotonously increasing intensities from the beginning of the incubation to later stabilise and remain at a constant level (Fig. 3.5B).

The analysis of the fluorescence intensities of ~ 200 single cells over time uncovers that trend (Fig. 3.5C), showing that the average behaviour is well represented by a linearly increasing fluorescence release followed by a plateau value appearing around 2.5–3 hours. To explain that plateau, two hypotheses are proposed. Either most of the fam fluorescent groups have been taken away from the nanoparticles monolayers (on average), which is then probably considerably degraded, resulting in this constant level of fluorescence inside the cells, or a slower degradation of the monolayer — possibly due to few fam groups still on the monolayer — balanced with a photobleaching and/or some exocytosis of the dyes leaves the fluorescence at a constant level. Looking at the level of the background over time with both fluorescence and photothermal microscopy could provide some information related to the exocytosis of the nanoparticles/dyes, but this would require some new measurements and analysis in a significant quantitative study.

3.1.3 Nanoparticle uptake quantification

A systematic quantitative study of uptake was undertaken with the objective of learning more on the processes of internalisation of the nanoparticle as a function of the quantity of nanoparticle incubated with the cells. Investigating the response of cells to different nanoparticle incubation concentrations allows to identify the concentration range that provides good images (good contrasts) with both confocal fluorescence and photothermal microscopy. It consequently brings ease in image analysis, good statistics, and the possibility to draw comparisons/conclusions between images resulting from the two techniques.

HeLa cells were incubated for four hours with different concentrations (0, 0.07, 0.2, 0.6, 2, 6 nM) of 10 nm diameter gold nanoparticles coated with a 5 % CALNN-th-fam — 95 % CALNN monolayer, and then imaged by both photothermal and

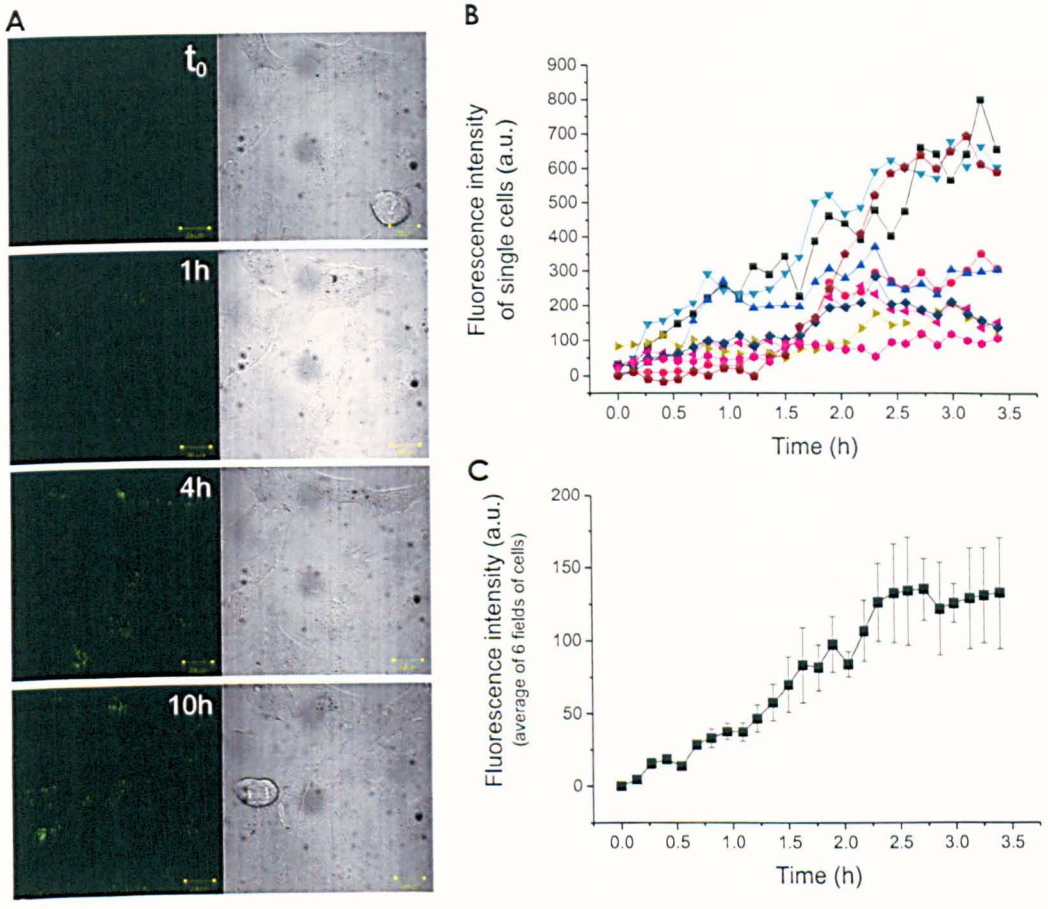

Fig. 3.5 – Intracellular fluorescence release reveals the SAM degradation dynamics. (**A**) HeLa cells were incubated with 10 nm gold nanoparticles coated with a mixed peptide (5 % CALNN-th-fam — 95 % CALNN) self-assembled monolayer (6 nM final concentration) in a microscope incubator (37 °C, 5 % CO_2). Time-lapse images of 10 different fields were taken every 5 min by laser scanning confocal microscopy (V. Sée). The left panels show the fluorescence images and the right panels show brightfield images at indicated times. (**B**) Fluorescence intensity of nine single cells over 3.5 h incubation. (**C**) Average of the mean fluorescence intensities of 200 single cells as a function of nanoparticle incubation time. A characteristic plateau appears at 2.5–3h. Error bars represent the SE. Scale bars represent 20 μm.

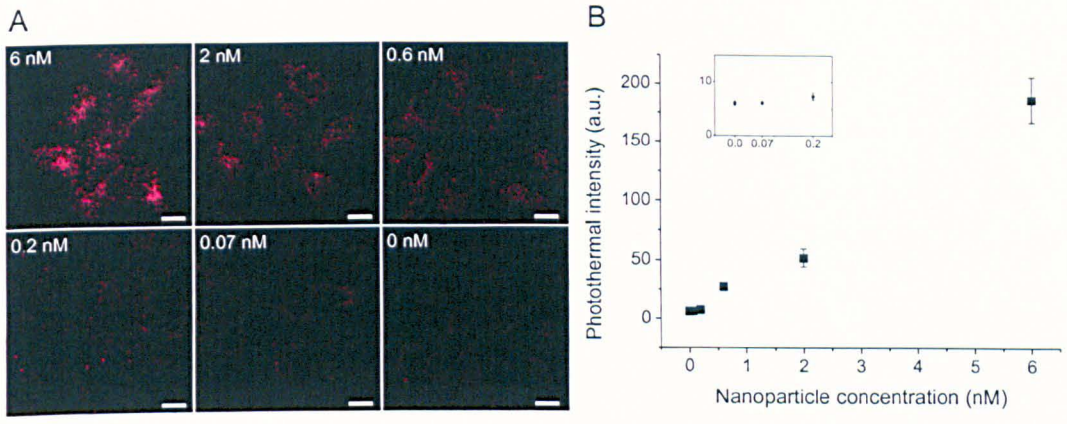

Fig. 3.6 – The number of nanoparticles taken up increases linearly with the nanoparticle incubation concentration. (**A**) HeLa cells incubated for 4h with gold nanoparticles coated with 5 % CALNN-th-fam — 95 % CALNN were imaged by photothermal microscopy under increasing concentrations of nanoparticles (0, 0.07, 0.2, 0.6, 2, 6 nM). (**B**) Plot of the mean photothermal intensity for the six nanoparticle incubation concentrations shown in (A). Single cells mean photothermal intensities were evaluated for ~35 cells for each nanoparticle concentration. Insert: mean photothermal intensity values at low concentrations (0, 0.07, 0.2 nM). Error bars represent the SE (B). Scale bars represent 20 μm (A).

laser scanning confocal fluorescence microscopy (Figs. 3.6A and 3.7A).[g]

The photothermal images hints that the nanoparticles uptake is in proportion with the incubation concentration, although no more precise relation could be drawn from a simple visual assessment. A single cell analysis of three to four fields of view, representing ~42 cells (mean value) for each incubation concentration, show more clearly that the cell mean photothermal intensity, hence the mean amount of internalised nanoparticles per cell, is proportional to the nanoparticle incubation concentration (Fig. 3.6B).

The confocal fluorescence images also suggest that the fluorescence release is evolving proportionally to the incubation concentration. A single cell analysis of the fluorescence intensity of ~50 cells for each nanoparticle incubation concentration shows a linear relation between the mean fluorescence intensity of single cells and the nanoparticle incubation concentration.

To summarise, linear correlations between the quantity of nanoparticles present during the incubation and both the quantity of nanoparticles that have been internalised (photothermal microscopy) and the amount of fluorescence release (fluorescence microscopy) were established. Ultimately, knowing the two aforementioned relationships provides a correlation between the internalisation of the nanoparticles and their monolayer degradation, allowing to unveil a direct link between the quantity of fluorescence release observed and the quantity of nanoparticles that have been taken up inside the cells.

[g] nanoparticle preparation: P. Free; cell work, fluorescence imaging and image analysis: V. Sée

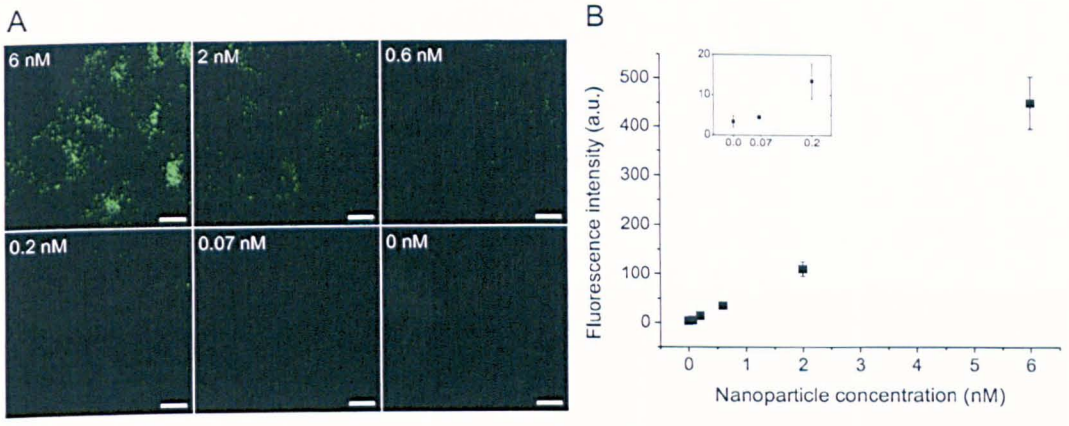

Fig. 3.7 – Fluorescence release increases linearly with the nanoparticle incubation concentration. (**A**) HeLa cells incubated for 4h with gold nanoparticles coated with 5 % CALNN-th-fam — 95 % CALNN were imaged by confocal fluorescence microscopy (V. Sée) under increasing concentrations of nanoparticles (0, 0.07, 0.2, 0.6, 2, 6 nM). (**B**) Plot of the mean fluorescence intensity for the six nanoparticle incubation concentrations shown in (A). Single cells mean fluorescence intensities were evaluated for ~50 cells for each nanoparticle concentration. Insert: mean fluorescence intensity values at low concentrations (0, 0.07, 0.2 nM). Error bars represent the SE (B). Scale bars represent 20 μm (A).

A comparison of the entry of the same fluorescently labelled gold nanoparticles (10 nm diameter, 6 nM final concentration, 5 % CCALNN-th-fam — 95 % CALNN peptide monolayer) was made between various cell lines.[h] Markedly, the DAOY cell line monolayer degradation was found to be more important than that of other cell lines (Fig. 3.8A). TEM images confirmed that there were more nanoparticles in the endosomes after uptake in DAOY cells (Fig. 3.8B) than had been observed previously in HeLa cells (see Fig. 3.1 for a comparison) with the same nanoparticle incubation concentration, size and monolayer composition. Nevertheless human adherent (HeLa, SK-N-AS, DAOY), non-adherent (D-283 Med) and mouse (MEF) cells lines did all display a degradation of the self-assembled monolayer through fluorescence release (Fig. 3.8A).

Together with the direct correlation between the fluorescence release observed and the amount of nanoparticles taken up by the cells provided by the nanoparticle concentration titration analysis, it confirms that the monolayer degradation upon internalisation of the nanoparticles is a general process in mammalian cells taking place in the endosomes. The cause of the monolayer degradation upon internalisation of the quenched fluorescently labelled nanoparticles constructs is examined in the next section.

[h] nanoparticle preparation: P. Free; cell work, fluorescence imaging: V. Sée; TEM imaging: P. Nativo

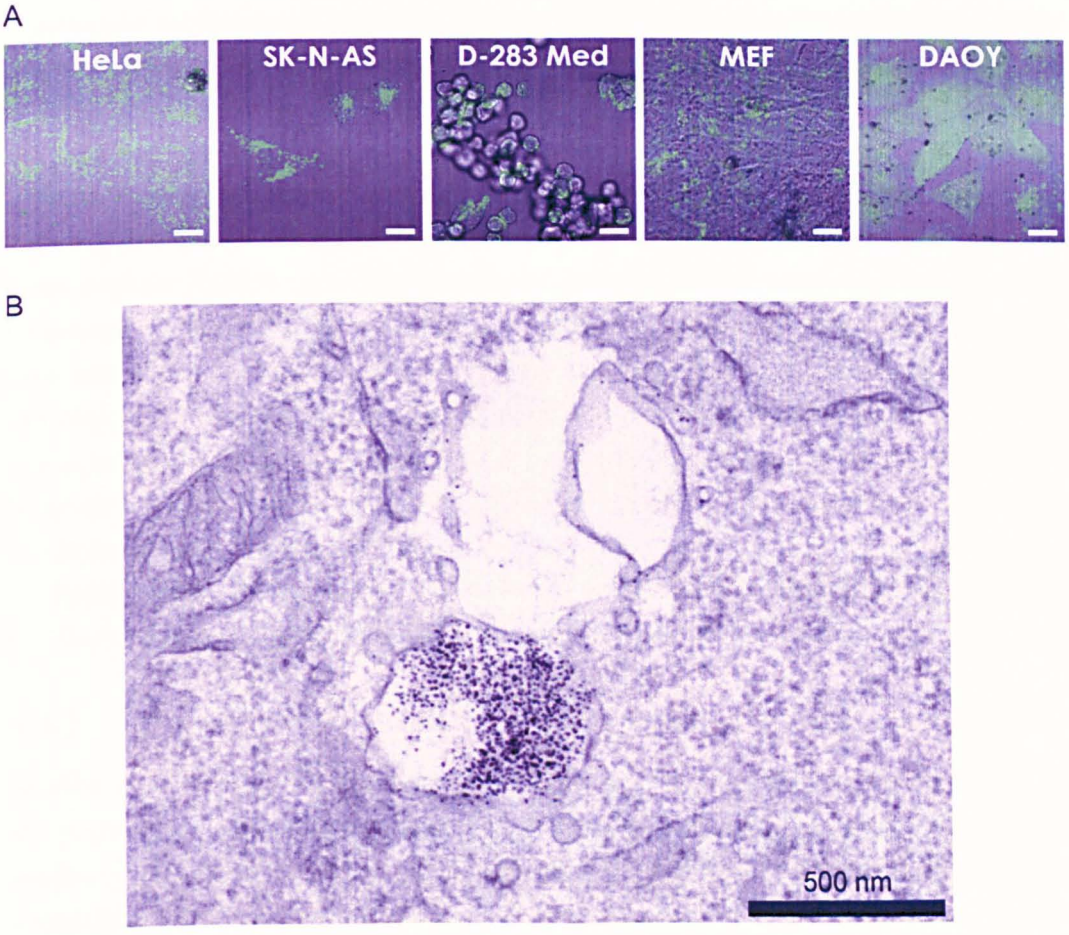

Fig. 3.8 – Uptake of 5 % CCALNN-th-fam — 95 % CALNN coated gold nanoparticles in five different cell lines. (**A**) Different cell lines were incubated for 3 h with 10 nm gold nanoparticles (6 nM final concentration) coated with a 5 % CCALNN-th-fam — 95 % CALNN monolayer. The nanoparticles endocytosis and the degradation of their monolayer can be observed by confocal fluorescence microscopy (V. Sée) as previously described for HeLa cells. From left to right: HeLa cells (human cervical cancer), SK-N-AS (human neuroblastoma), D-283 Med (human medulloblastoma), MEF (mouse embryonic fibroblasts), and DAOY (human medulloblastoma). (**B**) TEM image (P. Nativo) of 6 nM CALNN-capped gold nanoparticles incubated for 3 h in DAOY cells. The endosomes include a very large number of nanoparticles. Scale bars represent 20 μm (A).

3.2 Self-assembled monolayer degradation

The degradation of the gold nanoparticles peptide monolayer has been observed during their internalisation in mammalian cells. Although this property can be very useful in monitoring the entry of gold nanoparticles in cells, the reason for this degradation needs to be understood, should the degradation require to be prevented. This would be the case if the self-assembled monolayer was tailored with particular functional peptides, for example either in a nanoparticle internalisation strategy or in order to follow some molecules of interest after their intracellular conjugation to the gold nanoparticles.

The peptide monolayer degradation could be resulting from ligand exchange. This hypothesis would feature free intracellular thiol-containing ligands replacing some peptide ligands from the monolayer, amongst which some of the fluorescein terminated peptide (CALNN-th-fam), which would see them released from the gold core and allow the fluorescence to be emitted from the fam groups. Conversely, the degradation could also be due to a protease, whose activity would cleave the sequence of the CALNN-th-fam peptide at some place between where the thiol is bond to the gold core (cysteine) and the fam group bearing the fluorescein, firing the unquenching of the fluorescein.

Both hypotheses would result in a release of fluorescence inside the cells, explaining the monolayer degradation, and will therefore be tested thereupon.

3.2.1 Influence of the monolayer composition on ligand exchange

With a view to better understand what promotes or prevents ligand exchange at the surface of a self-assembled monolayer of peptide-capped gold nanoparticles, the tendency to ligand exchange of different mixed-peptide monolayer coatings were investigated *in vitro*. The mixed-peptide monolayer composed of the matrix peptide CALNN and the peptide CCALNN, bearing an additional cysteine towards its N-terminus as compared to CALNN, presented an interesting relation between the monolayer composition and its propensity to ligand exchange.

Nanoparticles capped with five different mixed-peptide monolayers and two homogenous monolayers of CALNN/CCALNN were prepared (see Tab. 3.1 for the compositions). The different nanoparticle solutions were then incubated separately with four different concentrations (0, 1.2, 2.4, 3.6 μM) of free CALNN-Histag peptides to initiate potential ligand exchange reactions and later eluted by centrifugation through a Ni-NTA beads-based gel to exclude the nanoparticles that had undergone ligand exchange with CALNN-Histag peptides for one or more of their ligands. The absorbance at 522 nm of the eluted solutions was measured. The measurement gave four values corresponding to the Histag incubation concentration of 0, 1.2, 2.4 and 3.6 μM for each nanoparticle monolayer type (Tab. 3.1). These values were normal-

Type of monolayer	Composition/Ratio
Homogenous	CALNN
	CCALNN
	CALNN : CCALNN
Mixed-peptide	1 : 5
	1 : 2
	1 : 1
	2 : 1
	5 : 1

Tab. 3.1 – Composition of the gold nanoparticle monolayers assessed for their propensity to ligand exchange with CALNN-Histag peptides.

ised to 1 for the concentration at 0 μM (no induced ligand exchange) and a linear fit of the four values was done (intercept fixed to 1). The modulus of the slope and its standard error were taken from these fits to produce a measure of the degree of ligand exchange that underwent in the different monolayers.

The results show that the more CCALNN peptide there is in a mixed-peptide monolayer, the less sensitive to ligand exchange the nanoparticles are. Regarding the homogeneous monolayer coated nanoparticles, CCALNN appears less prone to ligand exchange than CALNN (red squares, Fig. 3.9). This is unsurprising as the release of CCALNN requires the concomitant exchange of the two thiol bonds.

3.2.2 Effect of ligand exchange on the monolayer degradation

It was shown in the previous section that a self-assembled monolayer composed of CCALNN peptides, with two cysteine amino acids at their N-terminus ends rather than one is less prone to ligand exchange than a monolayer built with the peptide CALNN. With this in mind the impact of ligand exchange on the intracellular monolayer degradation will be assessed.

The aim is to compare the resistance of two differently anchored fluorescent peptides to ligand exchange, with one or two thiol bond anchoring the fluorescent peptide to the gold core. If ligand exchange is significant inside the cells and therefore induces the release of fluorescence observed during the nanoparticles internalisation, then increasing the fluorescent peptide binding strength to the gold core should decrease the intracellular release of fluorescence. Similarly if ligand exchange does not play an important role in the process, then the difference should be insignificant.

For this assessment, the comparison was made between the same fluorescently labelled peptide (CALNN-th-fam) as used previously to study the nanoparticles internalisation (Sect. 3.1) and a second one for which a cysteine was added at the N-terminus end (CCALNN-th-fam). Nanoparticles (10 nm diameter) coated with either

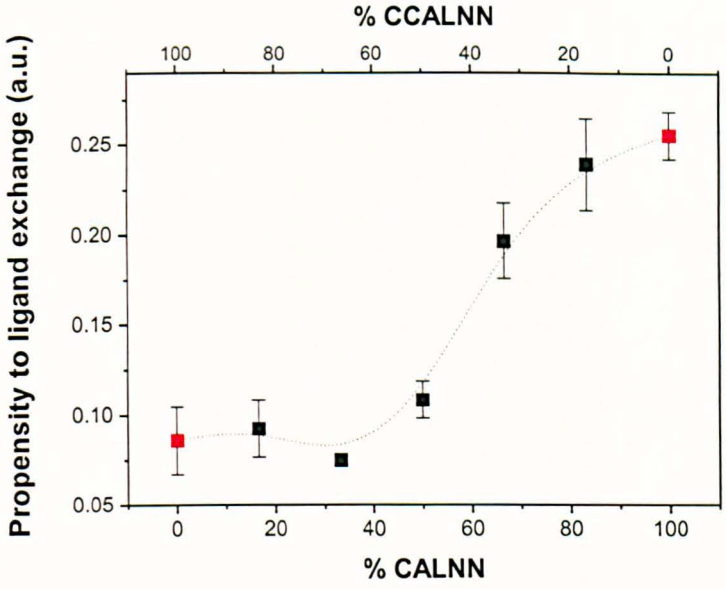

Fig. 3.9 – Propensity of gold nanoparticles to ligand exchange as a function of the monolayer composition. Nanoparticles were coated by CALNN and CCALNN peptides as components of their capping monolayer. Composition ratio 1:5, 1:2, 1:1, 2:1 and 5:1 and homogenous monolayers of CALNN and CCALNN were incubated with CALNN-Histag to assess their propensity to ligand exchange. Ni-NTA beads based gel filtration was used to trap nanoparticles presenting ligand exchange of one or more of the ligands, and then compare the eluted ones with nanoparticles that were not incubated with CALNN-Histag. The results show that CCALNN is more prone to ligand exchange than CALNN. Error bars represent the SE.

a 5 % CALNN-th-fam — 95 % CALNN or a 5 % CCALNN-th-fam — 95 % CCALNN monolayer were incubated separately for four hours with HeLa cells and imaged by confocal fluorescence microscopy.[i] The images were further analysed and a mean fluorescence intensity value was produced from the number of fluorescent vesicles per cell in ~ 200 cells for each condition (Fig. 3.10). The mean fluorescence intensities did not show any significant difference between the two samples.

This proves that ligand exchange is not responsible for the nanoparticle monolayer degradation during their internalisation. As a consequence, the release of fluorescence observed when the nanoparticles enter the cells must come from the cleavage of the CALNN-th-fam peptide holding the fluorescein by an intracellular enzyme.

3.2.3 Cathepsin L proteolytic activity

As the nanoparticles enter cells by endocytosis and are observed to be confined to endosomal vesicles, it is logical to consider that the monolayer proteolytic degradation should take place in these endosomes. The main proteases present in endosomes

[i] nanoparticle preparation: P. Free; cell work, fluorescence imaging and image analysis: V. Sée

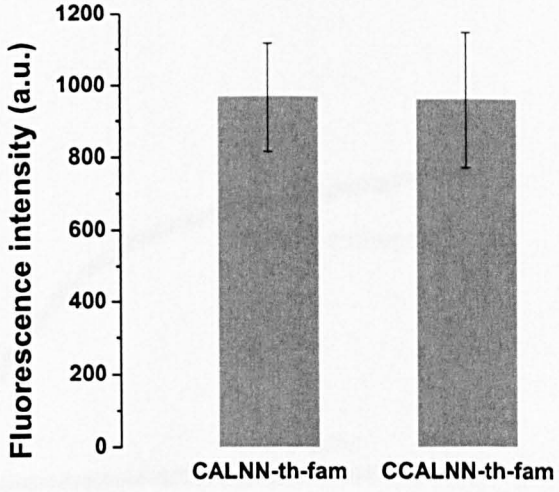

Fig. 3.10 – Ligand exchange is not responsible for the monolayer degradation. HeLa cells were incubated for 4 h with 10 nm gold nanoparticles (6 nM final concentration) coated with either a 5 % CALNN-th-fam — 95 % CALNN or a 5 % CCALNN-th-fam — 95 % CCALNN monolayer and imaged by confocal microscopy (V. Sée). The average number of fluorescent vesicles in ~200 cells was plotted for both condition. No statistical difference was found between the two samples (ANOVA test). Error bars represent the SE.

are cathepsins, a family of peptidase with a broad specificity, and whose members in endosomes and lysosomes are cathepsin B and L.

The cleavage potential of cathepsin L was estimated in an *in vitro* assay,[j] where fluorescent tag bearing 10 nm diameter nanoparticles (98 % CALNN — 2 % CALNN-th-fam monolayer composition) at a final concentration of 6 nM were incubated with or without cathepsin L. The fluorescence intensity (Fig. 3.11) displays an increase over time for the nanoparticles incubated with cathepsin L (red dots) and no change for those incubated without cathepsin L (black squares). This shows that the protease cathepsin L is able to cleave efficiently the CALNN-th-fam peptide bearing the fluorescein from the surface of gold nanoparticles in solution.

In order to verify if the protease cathepsin L activity in the endosomal vesicles was responsible for the monolayer degradation after the nanoparticles internalisation and in the view of blocking it, a comparison of this degradation after nanoparticle incubation in the presence and absence of a cathepsin inhibitor was carried out. Benzyloxycarbonyl-Phe-Phe fluoromethyl ketone (Z-FF-fmk, Fig. 3.12) is an irreversible inhibitor of cathepsins B and L, covalently binding its fmk group to the thiol of a cysteine residue of the protease to induce an irreversible inhibition.

HeLa cells were incubated with 10 nm gold nanoparticles (6 nM concentration) bearing the previously used mixed-peptide (5 % CALNN-th-fam — 95 % CALNN) self-assembled monolayer for four hours in the presence or in the absence of Z-FF-fmk (irreversible cathepsin B and L inhibitor). The cells incubated without or with

[j] nanoparticle preparation and fluorescence assay: P. Free

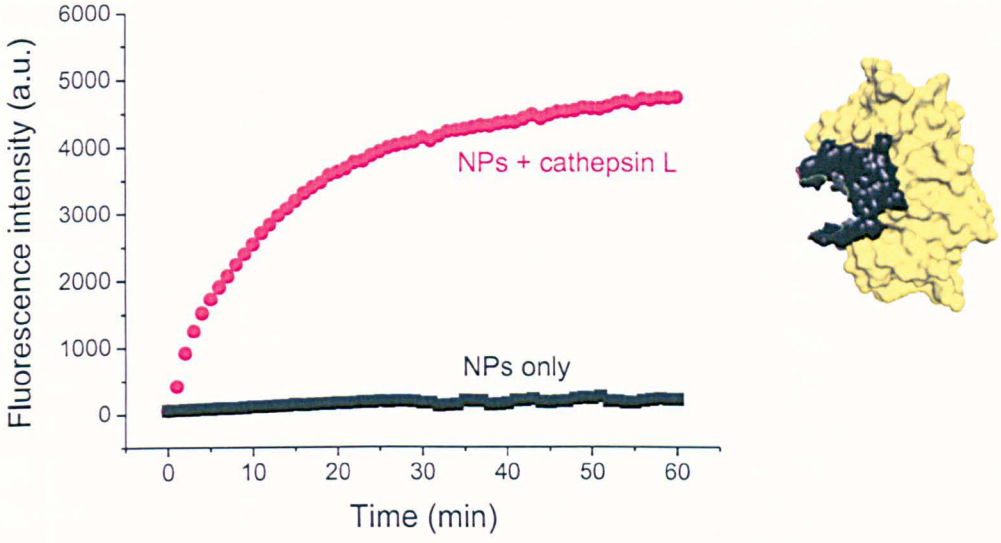

Fig. 3.11 – *In vitro* cathepsin L induced proteolysis of CALNN-th-fam capped gold nanoparticles. 10 nm diameter gold nanoparticles coated with a 98 % CALNN — 2 % CALNN-th-fam monolayer at a final concentration of 6 nM were incubated with 1 mU of purified cathepsin L in a 0.1 M sodium-acetate buffer (pH 5.6) in Corning black NBS plates. The fluorescence was measured (P. Free) with a BMG labtech POLARstar fluorimeter. Left: plot of the fluorescence intensity over time from nanoparticles incubated with (red dots) and without cathepsin L (black squares). The release of fluorescence in presence of cathepsin L show the cleavage potential of the protease towards the CALNN-th-fam peptide present in the nanoparticle monolayer. Right: protease cathepsin L with its active site highlighted in black.

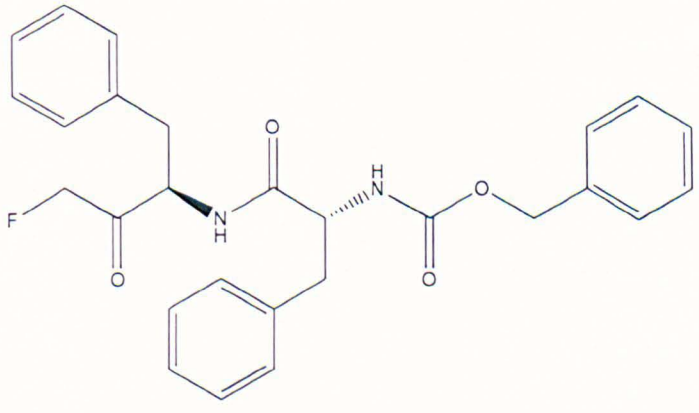

Fig. 3.12 – Structure of the cathepsin L inhibitor benzyloxycarbonyl-Phe-Phe fluoromethyl ketone (Z-FF-fmk).

Z-FF-fmk were then imaged by confocal fluorescence microscopy to detect the quantity of fluorescence released (Fig. 3.13A and B, respectively), and further fixed and imaged by photothermal microscopy to detect the quantity of internalised nanoparticles (Fig. 3.13D and E, respectively). The fluorescence and photothermal images were subsequently analysed at a single cell level to determine mean fluorescence and mean photothermal intensity values for both conditions.[k]

As can be seen on the images (Fig. 3.13A–B), the fluorescence release was significantly reduced by adding the cathepsin L inhibitor. The quantification specify that a six fold reduction was achieved in the presence of cathepsin inhibitor (Fig. 3.13C). At the same time, the quantification of the amount of internalised nanoparticles provided by photothermal microscopy (Fig. 3.13F) does not show a statistically significant difference between the two samples. The fall in the fluorescence release intensity is therefore not due to a decline in the number of internalised nanoparticles, which could have been hypothesised as arising from the use of Z-FF-fmk, but to a reduced monolayer degradation.

Altogether this means that cathepsin L plays an important role in the degradation of the nanoparticle peptide self-assembled monolayer and that this degradation can be seriously impaired by cathepsin inhibition. Despite this solution not been perfect, it protects markedly the nanoparticle monolayer from being degraded in the endosomal vesicles. A more active and better protection of the monolayer based on a combined cathepsin inhibition and endosomal disruption will be presented later (Chapter 4, Sect. 4.1.1).

The degradation observed in this particular situation has general implications, as internalisation strategies or intracellular conjugation often require a specific peptide sequence to be implemented on the surface of the nanomaterial cargo (nanoparticle, nanotube, ...). With this in mind the cleavage potential of cathepsin L on human proteins was investigated.[l] After a cleavage site pattern[m] had been established with the help of the literature,[15–17] a Uniprot database search revealed that 37 % of the human proteome could be cleaved at least in one place by cathepsin L (Fig. 3.14). Consequently, while functionalising a nanoparticle with a specific peptide sequence, bearing a function that needs to be preserved intracellularly, the potential degradation resulting from the cathepsin L protease activity should be appraised.

3.3 Effect of the monolayer composition on the uptake

Before showing how introducing poly-ethylene glycol in the monolayer of the gold nanoparticles is affecting the uptake of the nanoparticles in the cells, a short example

[k] nanoparticle preparation: P. Free; cell work, fluorescence imaging and analysis: V. Sée

[l] Bioinformatics prediction: D. J. Rigden

[m] [WYFLASKH]-[AIKRH]-[FYVLI]-[KRH]-[VGNQSRHAFL]-[AVIGPNQSRHWYFLK]-[WYFLASNKHPD]

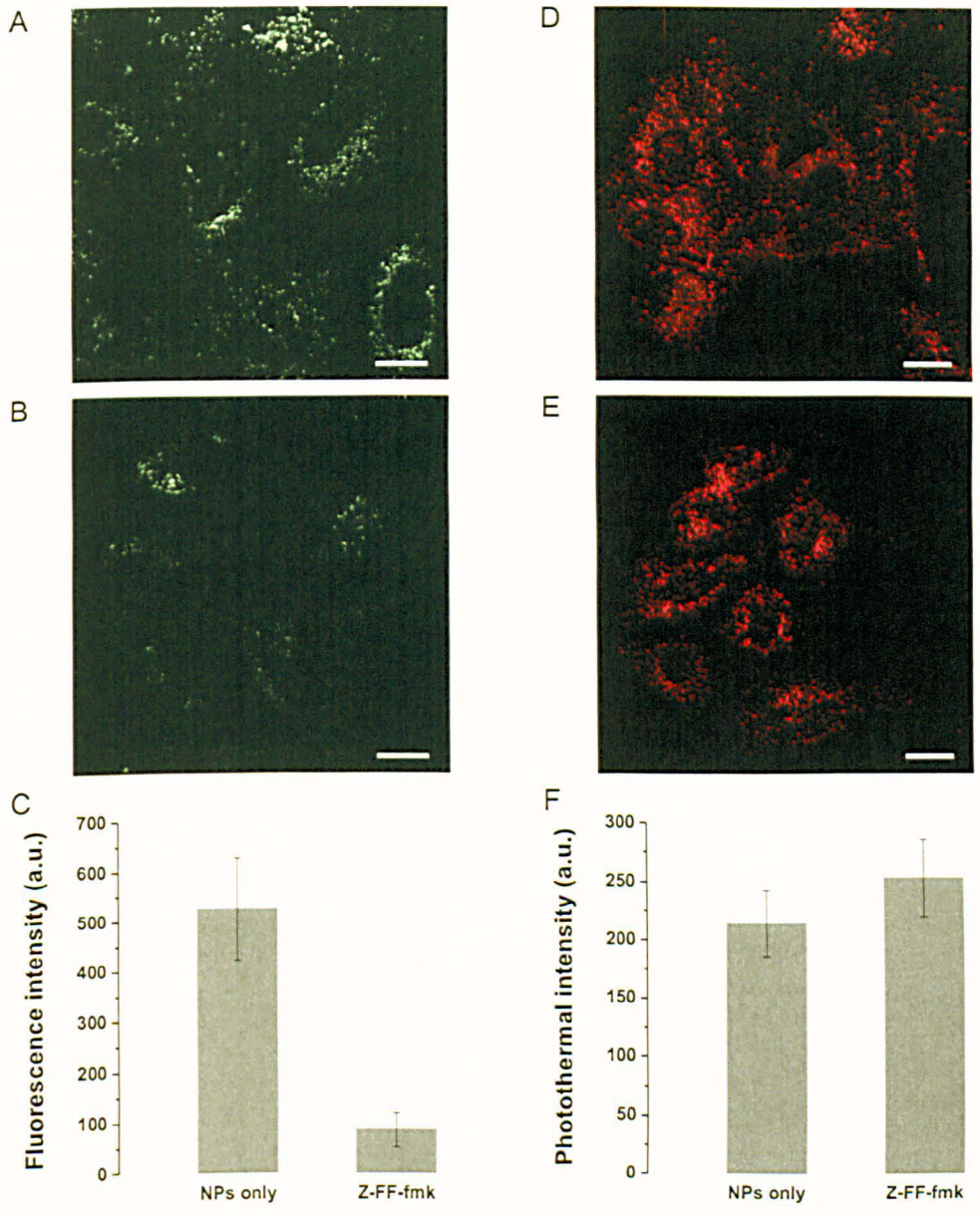

Fig. 3.13 – Protease cathepsin L inhibition by Z-FF-fmk limit significantly the nanoparticle monolayer degradation. HeLa cells were incubated for 4 h with 10 nm gold nanoparticles coated with a mixed-peptide (5 % CALNN-th-fam — 95 % CALNN) self-assembled monolayer (6 nM final concentration). (**A–B**) Confocal microscopy images of the fluorescence release in the cells (V. Sée). (**A**) Gold nanoparticles only, (**B**) gold nanoparticles with 20 μM of the irreversible cathepsin L inhibitor Z-FF-fmk. (**C**) Quantification of five different fields for the conditions shown in (A) and (B). (**D–E**) Photothermal microscopy images of the gold nanoparticles uptake. (**D**) Gold nanoparticles only, (**E**) gold nanoparticles with 20 μM of Z-FF-fmk. (**F**) Quantification for the conditions shown in (D) and (E), with at least 40 cells analysed per condition. The means differences between the samples were found to be statistically significant for the fluorescence intensities and not significant for the photothermal intensities with one-way ANOVA tests. Error bars represent the SD. Scale bars represent 20 μm.

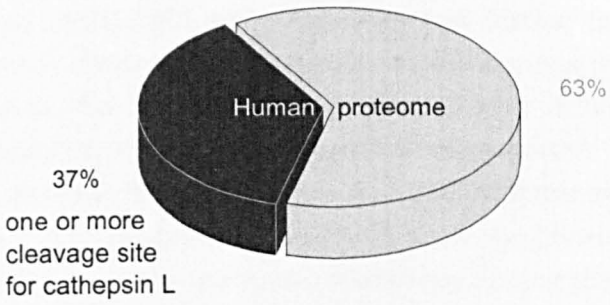

Fig. 3.14 – Cathepsin L predicted cleavage potential on human proteome.
A pattern defining the cathepsin L cleavage site was formulated, [WYFLASKH]-[AIKRH]-[FYVLI]-[KRH]-[VGNQSRHAFL]-[AVIGPNQSRHWYFLK]-[WYFLASNKHPD], by allowing at each substrate position any residue which gave a specificity constant (kcat/Km) of at least 10 % of that of the most favoured residue at that position (D. J. Rigden). In a non-redundant set of 18593 predicted human proteins (taken from Uniprot), around one third (6875) were predicted to be cut at least once.

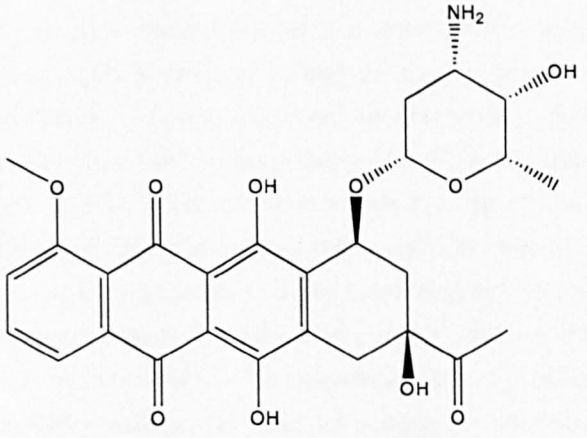

Fig. 3.15 – Structure of daunorubicin.

of the importance of a good assessment of the chemical stability of the monolayer will be presented.

3.3.1 Nanoparticle delivery to the nucleus?

Daunorubicin (Fig. 3.15) is a cell permeable chemotherapeutic drug of the anthracycline family used in some leukemia treatments. It is fluorescent with a broad absorption band with a maximum around 470–500 nm[18,19] and a broad emission in the red,[20,21] with a maximum around 600 nm. Its activity inside cells was attributed to the intercalation of the drug between DNA base pairs, inhibiting the replication.[22] The full signalling pathway is complex and not yet totally understood,[23] but a known effect of daunorubicin is to induce the cell apoptosis.[23–25]

Daunorubicin functionalised nanoparticles were prepared with the aim to improve the efficacy and delivery of the drug. The nanoparticles were coated with

poly-ethylene glycol (PEG-NHS-ester) molecules and further functionalisation of the amine-terminated daunorubicin molecules to the nanoparticles was achieved through amide bonds. SK-N-AS cells were incubated with 10 nm diameter daunorubicin-functionalised nanoparticles (nanoparticle concentration 6 nM) for 40 min, fixed and imaged by wide field fluorescence and photothermal microscopy (on the same microscope).[n] The images (Fig. 3.16A–C) show the presence of fluorescence and photothermal signals in the cell nuclei, where they appear to be disseminated in a well dispersed manner. In addition to the diffuse signal observed in the nuclei, a few areas of stronger vesicularly shaped signal are also observed, but only in the photothermal images. A comparison with cells incubated without nanoparticles shows that almost no photothermal signal could be seen within the cells (Fig. 3.16D–E), acknowledging the fact that the cells do not have a strong intrinsic photothermal signal.

The fluorescence channel presented in this figure shows the signal coming from the excitation of the daunorubicin molecules in green, when in reality those images should be represented with a reddish colour as the emission wavelength of daunorubicin is around 600 nm (images acquired in grayscale). Green was chosen for two reasons. First, the "red hot" lookup table (LUT) was chosen to represent the photothermal images in Fig. 3.16, because a fine tuning of the contrast allows to display both the regions of dispersed signal (red) and the ones with higher intensities (colour gradient from orange to white) where some aggregation is observed, but also for consistency throughout this chapter where either red or "red hot" LUTs were used to represent the variation of the intensities on the photothermal images. Then the choice of green was made to be able to produce a meaningful overlay of the fluorescence and photothermal images. This is indeed the case with green, as a region of co-localised fluorescence and photothermal signal produces a yellow/orange colour in the overlay.

A co-localisation of the fluorescence and photothermal signals is observed in the nuclei (orange colour in Fig. 3.16A–C, right), but is only partial in some cells. This discrepancy could be explained by the fact that the fluorescence and photothermal images were not taken at the same altitude. Indeed, if the glass slide onto which the cells are bound is considered as the altitude origin, the fluorescence images were taken at z=3.5 μm, when the photothermal images were taken at z=1 μm. Yet another reason could be necessary to explain the partial absence of nuclei co-localisation, as the axial resolution of the photothermal microscope is probably in the order of 2.5 μm,[6] but this would need more investigation on the system used.

These images are difficult to interpret as they are, as a nuclear localisation of gold nanoparticle would be a surprising result. Instead of trying to interpret at that level, an other control needs to be presented. Daunorubicin coated nanoparticles

[n] nanoparticle preparation and cell work: S. Saleemi

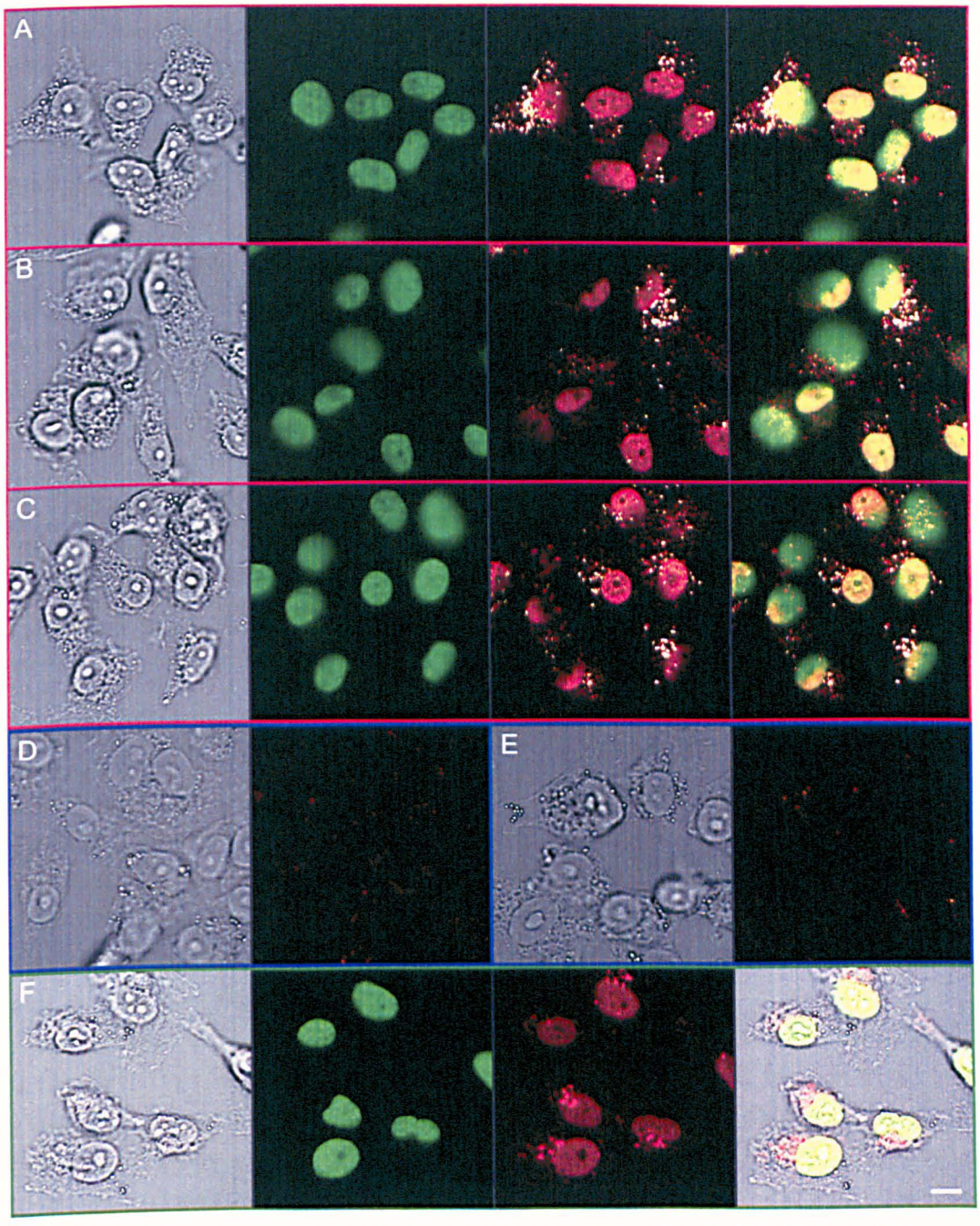

Fig. 3.16 – Uptake of daunorubicin coated nanoparticles in SK-N-AS cells.
(**A–C**) SK-N-AS cells incubated with nanoparticles loaded with ~800 daunorubicin molecules for 40 min, fixed and imaged. From left to right for each series: Bright field image, fluorescence image, photothermal image, overlay of fluorescence and photothermal images. (**D–E**) Bright field and photothermal images of cells incubated without nanoparticles. (**F**) Daunorubicin coated nanoparticles were incubated overnight in medium (10 % FCS), then centrifuged. The nanoparticles were discarded and SK-N-AS cells were incubated with the resulting supernatant for 40 min, fixed and imaged. Images from left to right: bright field, fluorescence channel, photothermal channel, overlay of the three previous images. Scale bar represents 10 μm.

were incubated overnight with serum-containing medium, centrifuged to discard the nanoparticles and the supernatant was incubated with SK-N-AS cells for 40 min. The cells were fixed and further imaged by wide field fluorescence and photothermal microscopy. Figure 3.16F shows fluorescence and photothermal signals in the nuclei and, as previously, some photothermal signal outside of the nuclei, but with a weaker level than observed before (all photothermal images have the same contrast). The photothermal signal is in this case surprising, as no nanoparticles were incubated with the cells, and should therefore be associated with the daunorubicin itself. The drug has probably gone off the nanoparticles during the incubation with the medium, resulting in free daunorubicin molecules in the medium. The photothermal signal observed in the nuclei and in some vesicles, would then be easily explained, as daunorubicin in known to go in the nuclei. Daunorubicin was for example observed to be localised essentially in nuclei and lysosomes in rat embryo fibroblasts.[26]

Although no further investigation was made to understand the photothermal signal coming from the daunorubicin molecules inside cells, the binding of the daunorubicin with an intracellular compound with good absorption properties could be hypothesised. Metal ions, for instance were shown to bind daunorubicin,[27] but more work would though be needed to only start answering this question.

3.3.2 Influence of polyethylene glycol in the monolayer

The internalisation of CALNN capped gold nanoparticles has been studied in the previous sections (Sect. 3.1 and 3.2) and presented an endosomal uptake of the gold nanoparticles in cells. The peptide CALNN was used to form a self-assembled protective monolayer at the surface of the nanoparticles, as it has been shown to provide a densely packed monolayer and ease in functionalisation,[9–11] allowing an overall good colloidal stability.

Although a self-assembled monolayer formed with CALNN limits the non-specific interactions at the surface of the nanoparticles, it may not be enough to protect them against aggregation during and after internalisation, as could be seen by TEM (Fig. 3.1) or photothermal microscopy (Fig. 3.13D), even when protecting the monolayer against proteolysis deterioration (Fig. 3.13E). Changing the surface chemistry of the nanoparticles could thus both provide a stronger resistance against intracellular aggregation and change the nanoparticle entry mechanism.

In order to try and change the intracellular dispersion of the nanoparticles and reduce the endocytosis, CCALNN-PEG peptides were chosen to be added in the composition of the capping monolayer (Fig. 3.17). Polyethylene glycol (PEG) is known to reduce the non-specific interaction of gold nanoparticles with serum proteins[28] and to limit interactions of nanomaterials with cells, to a degree where it would prevent their internalisation when functionalised with a high content of PEG molecules in the monolayer.[29]

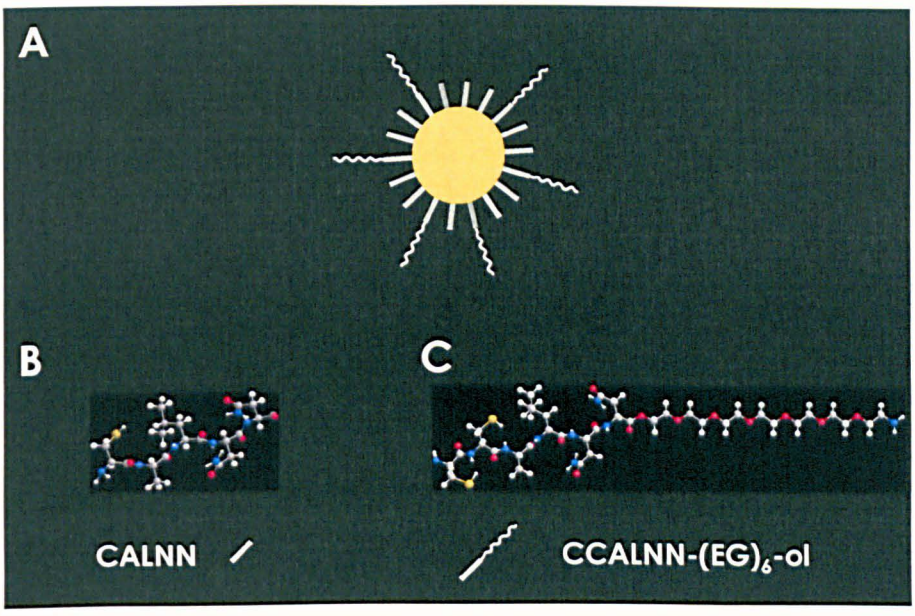

Fig. 3.17 – Introducing PEG in the SAM of gold nanoparticles to modulate the influence of non-specific interactions. (**A**) Gold nanoparticles are coated with a mixed-peptide self-assembled monolayer composed of the matrix peptide CALNN and the PEG terminated CCALNN-PEG (CCALNN–$(EG)_6$–ol). (**B**) Scheme of the structure of CALNN. (**C**) Scheme of the structure of CCALNN-PEG.

Monolayer composition	
CALNN	CCALNN–PEG
100 %	0 %
90 %	10 %
80 %	20 %
70 %	30 %

Tab. 3.2 – Self-assembled monolayer compositions used to assess the influence of PEG monolayer content on cellular uptake.

Since the proportion of CCALNN–PEG necessary to modify the internalisation process was unknown in this system, four monolayer compositions with increasing proportion of CCALNN–PEG were tested (Tab. 3.2).

HeLa cells were incubated separately in suspension with 5 nm gold nanoparticles (final concentration 100 nM) coated with the four different CALNN / CCALNN-PEG mixed-peptide monolayer compositions (Tab. 3.2) for 10 min in serum-free medium and a further 40 min in complete medium (10 % FCS). Nanoparticles/medium were then discarded by centrifugation of the cells, which were then transferred to a dish and left to attach to the dish for 4 h in complete medium in order to allow their fixation. They were subsequently fixed and later imaged by photothermal micro-

scopy.° The incubation procedure was chosen in order to comply with the one used in Sect. 4.2, where a comparison between toxin assisted delivery and endocytosis mediated internalisation of gold nanoparticles will be made.

The photothermal images show that the quantity of nanoparticles in the cells diminishes when the proportion of CCALNN–PEG in the monolayer of the nanoparticles increases (Fig. 3.18A–D), with a very low internalisation yield for the 20 % and 30 % proportions of CCALNN–PEG in the monolayer, where almost no nanoparticle uptake can be seen on the images (Fig. 3.18C–D).

An analysis of the images acquired by photothermal microscopy was performed on individual cells (~ 50 cells per condition) to evaluate single cells mean photothermal intensities, which would provide a measure of the quantity of the nanoparticles taken up by the cells. Figure 3.18E shows the quantification of cell mean photothermal intensity ($\pm$ SE) for the four monolayer compositions, acknowledging the decrease of cellular uptake with the increase of the proportion of CCALNN–PEG in the monolayer that was visible on the images.

A one-way ANOVA test followed by a Holm-Bonferroni test showed that two statistical groups of CCALNN–PEG monolayer proportions appear to be discernible for their influence on cells uptake: [0 %, 10 %] and [20 %, 30 %] (displayed respectively in dark and light gray in Fig. 3.18E). When comparing nanoparticle uptake of pairs of samples incubated with nanoparticles bearing different monolayers, a pair belonging to the same group (intra-group), like 0 % and 10 % or 20 % and 30 %, does not show a statistically significant difference between its members' means, when a significant difference ($p < 0.01$) is observed for members of inter-group pairs.

Although the quantity of nanoparticles taken up by the cells can be reduced by tuning the self-assembled monolayer, the distribution of the internalised nanoparticles stays still. Indeed, if one compares the uptake of cells after incubation with gold nanoparticles without addition of PEG in the monolayer (100 % CALNN, Fig. 3.19A) to the uptake of some that are functionalised with 20 % of CCALNN–PEG within the content of their capping ligands (Fig. 3.19B), the distribution of the nanoparticles inside the cells shows a substantial endocytosis in both cases, with numerous regions within the cells that have vesicularly shaped objects showing a high content of nanoparticles (endosomes).

Even if the amount of internalised nanoparticles is lower for the PEG containing monolayer, despite a six fold more important incubation concentration as compared to the 100 % CALNN coated nanoparticles, the nanoparticles are nonetheless concentrated in endosomes. No significant non-endosomal localisation of nanoparticles could be found with the different monolayers tested (Tab. 3.2).

Although some cells are showing what is looking like a fainted dispersed localisation with 20 % CCALNN–PEG in the photothermal image shown in Fig. 3.19B,

°nanoparticle preparation and cell work: U. Shaheen

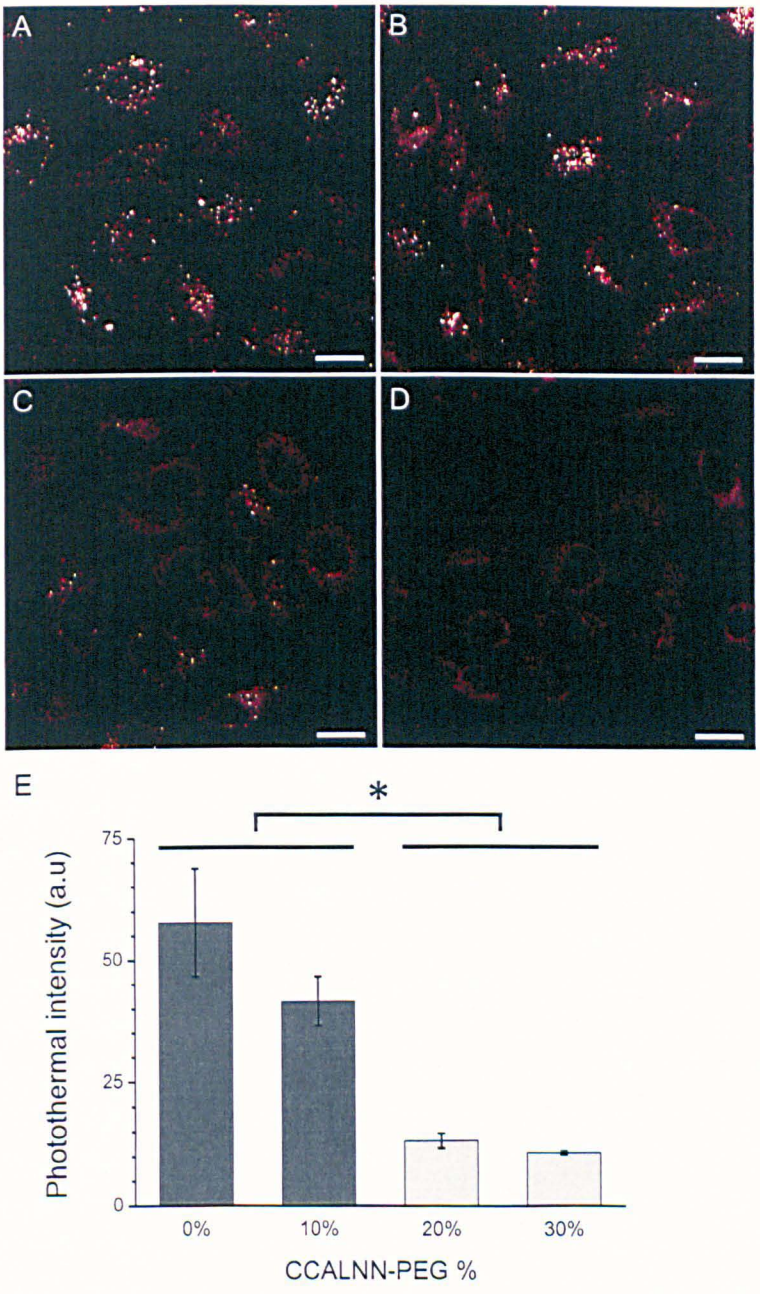

Fig. 3.18 – CCALNN-PEG monolayer proportion influence on gold nanoparticles uptake. HeLa cells were incubated in suspension with 5 nm gold nanoparticles coated with four different CALNN — CCALNN-PEG mixed-peptide monolayer compositions (final concentration 100 nM) for 10 min in serum-free medium and further 30 min in complete medium (10 % FCS). Nanoparticles/medium were then discarded, cells transferred to a dish and left to attach for 4 h in complete medium, fixed and later imaged by photothermal microscopy. (**A-D**) Photothermal microscopy images of the internalised nanoparticles. (**A**) 100 % CALNN — 0 % CCALNN-PEG. (**B**) 90 % CALNN — 10 % CCALNN-PEG. (**C**) 80 % CALNN — 20 % CCALNN-PEG. (**D**) 70 % CALNN — 30 % CCALNN-PEG. (**E**) Quantification of single cells mean photothermal intensities ($\sim$ 50 cells per condition) for the four monolayer compositions shown in A-D. $*$ show a statistical difference between pairs of conditions with non-matching bar colours ($p < 0.01$), no significant difference between the other pairs of conditions. Error bars represent the SE. Scale bars represent 20 μm.

it should be pointed out that it is unlikely to be of any significance. Firstly, the contrast range chosen in the photothermal images in Fig. 3.19A–B is only showing part of the images. This is due to the difficulty to estimate the information contained in the full contrast range of a photothermal image with a single image, even when a lookup table (LUT) is used to provide a colour coding, such as the "red hot" LUT used in Fig. 3.19, helping in the visualisation. In these images, the contrast range is displayed between a minimum which corresponds to the mean photothermal intensity of the background of the individual images and a maximum of 600 for both images, allowing a visualisation of the less intense areas of the cells in terms of photothermal intensity (nanoparticles content) together with the more intense, which are therefore saturated. Changes of the contrast range deliver different information with respect to the cell uptake. For example, in Fig. 3.20A and Fig. 3.20B, which display the same images as in Fig. 3.19A and Fig. 3.19B (respectively), the upper contrast limit was increased to 2000, and fewer and smaller endosomes are visible. Fewer are present because the lower intensities became either less visible or not visible at all and they are smaller, for some of them, because the endosomes showing bigger aggregates have lower intensities on their outer part, which in turn fades or disappears. If now the images are displayed with the full range of values present in the respective images, $[0, 15525]$ for 100 % CALNN and $[0, 53844]$ for 80 % CALNN — 20 % CCALNN-PEG, very few areas containing nanoparticles are still visible, showing the need for a contrast adjustment. Secondly, the potential fainted diffuse localisation referred to earlier could also be provoked by many very small endosomes containing very few nanoparticles that would all be in a close proximity to one another or could simply be coming from the cell intrinsic background.[30] Only TEM could provide a clearer answer on that subject, should this be possible. Overall it is unlikely to be representing non-endosomal nanoparticles and more investigation would be needed to produce a statement on that matter in any case.

To summarise, introducing PEG in gold nanoparticles self-assembled monolayer helps to minimise the endocytosis. Poly-(ethylene glycol) helps to minimise the non-specific interactions of the serum proteins with the surface of the nanoparticles, leading to a weakened interaction of their surface with the cell membrane, in turn resulting in a reduced internalisation through endocytosis.

3.4 Conclusion

The non-specific internalisation of peptide-capped gold nanoparticles in mammalian cells was studied and resulted in an endosomal localisation. The uptake was illustrated by fluorescence confocal microscopy through the nanoparticle monolayer degradation, with fluorescence arising as the fluorescent peptides included in the monolayer were released and increasing over time until $\sim$ 2.5–3 h where a plateau

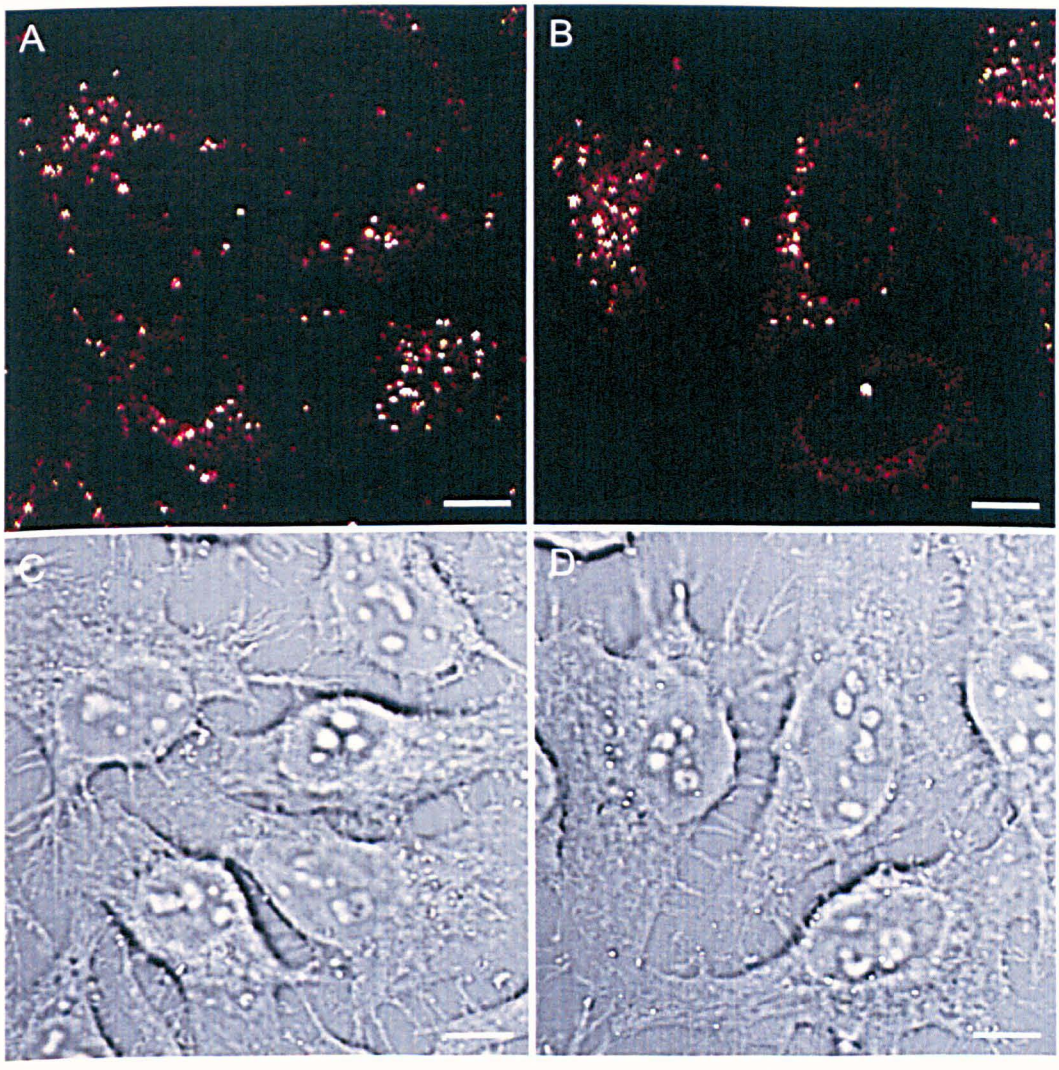

Fig. 3.19 – Localisation of 100 % CALNN and 80 % CALNN — 20 % CCALNN-PEG coated gold nanoparticles in HeLa cells. HeLa cells were incubated in suspension with 5 nm gold nanoparticles coated with either a 100 % CALNN peptide monolayer (nanoparticle concentration 100 nM) or a 80 % CALNN — 20 % CCALNN-PEG mixed-peptide monolayer (nanoparticle concentration 600 nM) for 10 min in serum-free medium and a further 30 min in complete medium (10 % FCS). Nanoparticles/medium were then discarded, cells transferred to a dish and left to attach for 4 h in complete medium, fixed and later imaged by photothermal microscopy. (**A**) Photothermal microscopy image of the uptake of 100 % CALNN coated nanoparticles (100 nM). (**B**) Photothermal microscopy image of the uptake of 80 % CALNN — 20 % CCALNN-PEG coated nanoparticles (600 nM). (**C**) Bright field image corresponding to (A). (**D**) Bright field image corresponding to (B). Scale bars represent 10 μm.

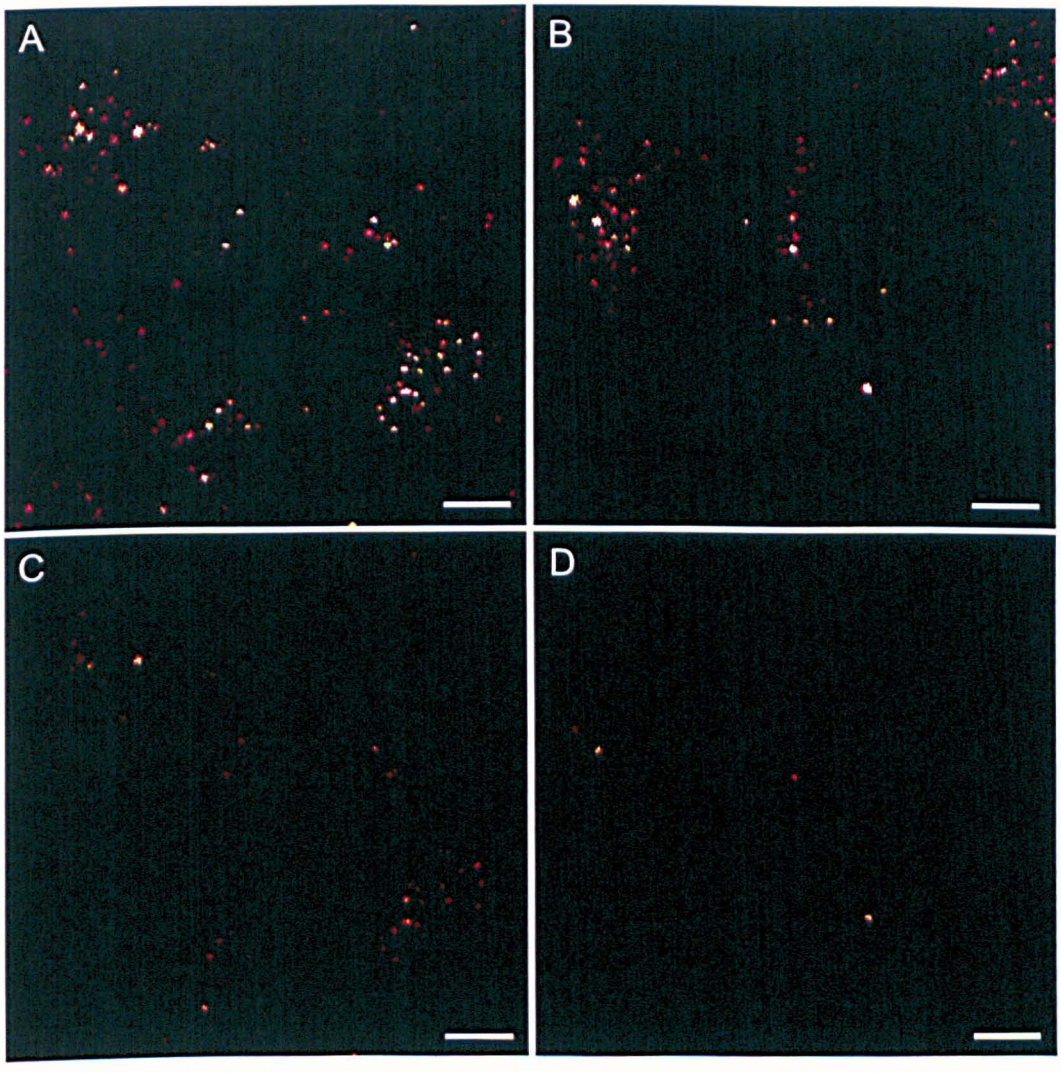

Fig. 3.20 – Importance of the contrast in images interpretation.
The images displayed here are the same as in Fig. 3.19, but with different contrast ranges. Previously, the contrast was adjusted individually between the background mean intensity (areas without cells) and a value of 600, when here the maximum value was changed to higher values of 2000 for A–B and the images maximum for C–D. (**A**) Photothermal image shown in Fig. 3.19A (100 % CALNN) with a contrast range of $[58, 2000]$. (**B**) Photothermal image shown in Fig. 3.19B (80 % CALNN — 20 % CCALNN-PEG) with a contrast range of $[67, 2000]$. (**C**) Same image as in (A), contrast range $[0, 15525]$. (**D**) Same image as in (B), contrast range $[0, 53488]$. Scale bars represent 10 μm.

appeared. Fluorescence and photothermal microscopy showed an internalisation which was correlated to the nanoparticle incubation concentration. The monolayer degradation was observed to happen upon internalisation of peptide-capped gold nanoparticles in various mammalian cells lines, attesting that the degradation is a general process. The monolayer degradation was shown not to be resulting from intracellular ligand exchange. It was further ascribed to the activity of the endosomal protease cathepsin L, which was cleaving part of the CALNN-th-fam peptide sequence releasing the fam group and allowing the fluorescein not to be quenched any more and therefore to fluoresce. An inhibition of cathepsin L was subsequently undergone upon internalisation of nanoparticles and showed that the monolayer degradation could be significantly prevented and the fluorescence release reduced to a low level. Cathepsin L has a broad cleavage potential, as it was also shown to be able to cleave more than a third of the human proteins, unveiling the need for carefully designed functional ligand included at the surface of nanomaterials, especially if their function is to be crucial inside the cells, such as when probing intracellular interactions. Finally an investigation of the influence of polyethylene glycol end groups in the peptide monolayer composition on the uptake of gold nanoparticles was performed and showed that the more polyethylene glycol in the monolayer the less internalised nanoparticles there are.

Materials and methods available in Appendix B.1

3.5 Bibliography

1. L. Cognet, C. Tardin, D. Boyer, D. Choquet, P. Tamarat and B. Lounis. Single metallic nanoparticle imaging for protein detection in cells. *Proceedings of the National Academy of Sciences of the United States of America*, 100(20), 11350–11355, 2003.

2. S. Berciaud, L. Cognet, G. A. Blab and B. Lounis. Photothermal heterodyne imaging of individual nonfluorescent nanoclusters and nanocrystals. *Physical Review Letters*, 93(25), 257402, 2004.

3. S. Berciaud, L. Cognet, P. Tamarat and B. Lounis. Observation of intrinsic size effects in the optical response of individual gold nanoparticles. *Nano Letters*, 5(3), 515–518, 2005.

4. S. Berciaud, D. Lasne, G. A. Blab, L. Cognet and B. Lounis. Photothermal heterodyne imaging of individual metallic nanoparticles: Theory versus experiment. *Physical Review B*, 73(4), 045424, 2006.

5. D. Lasne, G. A. Blab, S. Berciaud, M. Heine, L. Groc, D. Choquet, L. Cognet and B. Lounis. Single nanoparticle photothermal tracking (SNaPT) of 5-nm gold beads in live cells. *Biophysical Journal*, 91(12), 4598–4604, 2006.

6. V. Octeau, L. Cognet, L. Duchesne, D. Lasne, N. Schaeffer, D. G. Fernig and B. Lounis. Photothermal Absorption Correlation Spectroscopy. *ACS Nano*, 3(2), 345–350, 2009.

7. S. D. Conner and S. L. Schmid. Regulated portals of entry into the cell. *Nature*, 422(6927), 37–44, 2003.

8. G. J. Doherty and H. T. McMahon. Mechanisms of Endocytosis. *Annual Review of Biochemistry*, 78, 857–902, 2009.

9. R. Levy, N. T. K. Thanh, R. C. Doty, I. Hussain, R. J. Nichols, D. J. Schiffrin, M. Brust and D. G. Fernig. Rational and combinatorial design of peptide capping Ligands for gold nanoparticles. *Journal of the American Chemical Society*, 126(32), 10076–10084, 2004.

10. Z. Wang, R. Levy, D. G. Fernig and M. Brust. The peptide route to multifunctional gold nanoparticles. *Bioconjugate Chemistry*, 16(3), 497–500, 2005.

11. R. Levy. Peptide-capped gold nanoparticles: Towards artificial proteins. *Chembiochem*, 7(8), 1141–1145, 2006.

12. R. Levy, Z. X. Wang, L. Duchesne, R. C. Doty, A. I. Cooper, M. Brust and D. G. Fernig. A generic approach to monofunctionalized protein-like gold nanoparticles based on immobilized metal ion affinity chromatography. *Chembiochem*, 7(4), 592–594, 2006.

13. N. Schaeffer, B. Tan, C. Dickinson, M. J. Rosseinsky, A. Laromaine, D. W. McComb, M. M. Stevens, Y. Q. Wang, L. Petit, C. Barentin, D. G. Spiller, A. I. Cooper and R. Levy. Fluorescent or not? Size-dependent fluorescence switching for polymer-stabilized gold clusters in the 1.1-1.7 nm size range. *Chemical Communications*, (34), 3986–3988, 2008.

14. H. D. Hill and C. A. Mirkin. The bio-barcode assay for the detection of protein and nucleic acid targets using DTT-induced ligand exchange. *Nature Protocols*, 1(1), 324–336, 2006.

15. R. Menard, E. Carmona, C. Plouffe, D. Bromme, Y. Konishi, J. Lefebvre and A. C. Storer. The specificity of the S(1)' subsite of cysteine proteases. *Febs Letters*, 328(1-2), 107–110, 1993.

16. F. C. V. Portaro, A. B. F. Santos, M. H. S. Cezari, M. A. Juliano, L. Juliano and E. Carmona. Probing the specificity of cysteine proteinases at subsites remote from the active site: analysis of P-4, P-3, P-2 ' and P-3 ' variations in extended substrates. *Biochemical Journal*, 347, 123–129, 2000.

17. L. Puzer, S. S. Cotrin, M. F. M. Alves, T. Egborge, M. S. Araujo, M. A. Juliano, L. Juliano, D. Bromme and A. K. Carmona. Comparative substrate specificity analysis of recombinant human cathepsin V and cathepsin L. *Archives of Biochemistry and Biophysics*, 430(2), 274–283, 2004.

18. P. Agrawal, S. K. Barthwal and R. Barthwal. Studies on self-aggregation of anthracycline drugs by restrained molecular dynamics approach using nuclear magnetic resonance spectroscopy supported by absorption, fluorescence, diffusion ordered spectroscopy and mass spectrometry. *European Journal of Medicinal Chemistry*, 44(4), 1437–1451, 2009.

19. A. Dicko, S. Kwak, A. A. Frazier, L. D. Mayer and B. D. Liboiron. Biophysical characterization of a liposomal formulation of cytarabine and daunorubicin. *International Journal of Pharmaceutics*, 391(1-2), 248–259, 2010.

20. S. W. Sherwood, Y. G. Assaraf, A. Molina and R. T. Schimke. Flow Cytometric Characterization of Antifolate Resistance in Cultured Mammalian Cells Using Fluoresceinated Methotrexate and Daunorubicin. *Cancer Research*, 50(16), 4946–4950, 1990.

21. T. Perez-Ruiz, C. Martinez-Lozano, A. Sanz and E. Bravo. Simultaneous determination of doxorubicin, daunorubicin, and idarubicin by capillary electrophoresis with laser-induced fluorescence detection. *Electrophoresis*, 22(1), 134–138, 2001.

22. G. Aubel-Sadron and D. Londos-Gagliardi. Daunorubicin and doxorubicin, anthracycline antibiotics, a physicochemical and biological review. *Biochimie*, 66(5), 333–352, 1984.

23. G. Laurent and J. P. Jaffrezou. Signaling pathways activated by daunorubicin. *Blood*, 98(4), 913–924, 2001.

24. V. Mansat-De Mas, C. Bezombes, A. Quillet-Mary, A. Bettaib, A. D. D'Orgeix, G. Laurent and J. P. Jaffrezou. Implication of radical oxygen species in ceramide generation, c-Jun N-terminal kinase activation and apoptosis induced by daunorubicin. *Molecular Pharmacology*, 56(5), 867–874, 1999.

25. D. B. Sawyer, R. Fukazawa, M. A. Arstall and R. A. Kelly. Daunorubicin-induced apoptosis in rat cardiac myocytes is inhibited by dexrazoxane. *Circulation Research*, 84(3), 257–265, 1999.

26. G. Noel, C. Peterson, A. Trouet and P. Tulkens. Uptake and subcellular-localization of daunorubicin and adriamycin in cultured fibroblasts. *European Journal of Cancer*, 14(4), 363–368, 1978.

27. R. Kiraly and R. B. Martin. Metal ion binding to daunorubicin and quinizarin. *Inorganica Chimica Acta-Bioinorganic Chemistry*, 67(1), 13–18, 1982.

28. P. Free, C. P. Shaw and R. Levy. PEGylation modulates the interfacial kinetics of proteases on peptide-capped gold nanoparticles. *Chemical Communications*, (33), 5009–5011, 2009.

29. Y. L. Liu, M. K. Shipton, J. Ryan, E. D. Kaufman, S. Franzen and D. L. Feldheim. Synthesis, stability, and cellular internalization of gold nanoparticles containing mixed peptide-poly(ethylene glycol) monolayers. *Analytical Chemistry*, 79(6), 2221–2229, 2007.

30. D. Lasne, G. A. Blab, F. De Giorgi, F. Ichas, B. Lounis and L. Cognet. Label-free optical imaging of mitochondria in live cells. *Optics Express*, 15, 14184–14193, 2007.

Chapter 4

Facilitated delivery of gold nanoparticles

Endocytosis was shown in the previous chapter to allow the internalisation of nanoparticles in cells and the subsequent entrapment in endosomal acidic vesicles. However, during their stay in the endosomes they are susceptible to the protease activity, which are degrading their protective monolayer, and are unavailable to interact with the population of proteins present in the cytosol. Therefore other entry mechanisms or an adapted strategy need to be employed for intracellular nanoparticles delivery, especially if a cytosolic delivery is to be fulfilled.

The facilitated delivery of nanoparticles with the aspiration of a cytosolic localisation will therefore be investigated here. Three strategies for a cytosolic delivery of the nanoparticles will be examined in this chapter. First, endosomal escape will be scrutinised using either the endosomal disrupting drug chloroquine or membrane destabilising peptides functionalised on the gold nanoparticles. In a second part, the entry of gold nanoparticles through a cell membrane pore formation will be assessed with the help of the pore-forming bacterial toxin streptolysin O.

4.1 Assisted endosomal escape

4.1.1 Endosome disruption

Peptide-capped gold nanoparticles have been shown previously to experience a degradation of their monolayer upon internalisation in mammalian cells (Chapter 3, Sect. 3.1). Indeed, nanoparticles coated with CALNN peptides and additional fluorescent peptides CALNN-th-fam, were exhibiting a release of fluorescence after the protease cathepsin L was cleaving the peptide sequence of CALNN-th-fam. However this could be limited by inhibiting the activity of cathepsin L using the irreversible

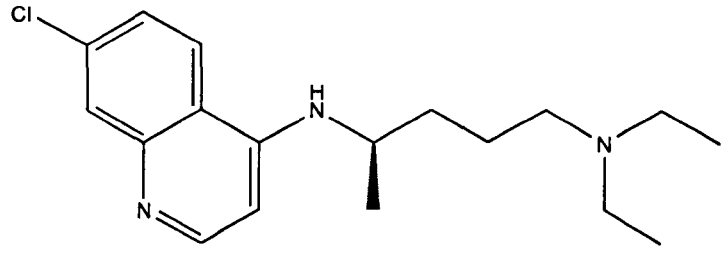

Fig. 4.1 – Structure of chloroquine.

cathepsin L inhibitor Z-FF-fmk. Yet, the monolayer degradation was not totally unimpaired, as the largely reduced fluorescence release could though still be observed.

In order to try and protect further the nanoparticle monolayer and deliver the nanoparticles to the cytosol a different strategy of endosome disruption will be examined thereafter using the lysosomotropic agent chloroquine.

Chloroquine is a cell-permeable weak base (Fig. 4.1) which once internalised increases the pH in the endosomes and lysosomes[1] and induces their disruption, although this later process is not fully understood. It has been successfully used to enhance DNA transfection and further gene expression[2] or the nuclear delivery of Tat-fusion proteins[3] internalised by endocytosis in fibroblast cells. An increase of the splicing efficiency of peptide nucleic acids coupled to CPPs was also observed in HeLa cells[4,5] by chloroquine induced endosomal disruption, again after an endocytosis mediated internalisation. In the context of non-viral gene delivery, it was suggested that chloroquine plays a role at different levels in the enhancement of gene expression, where it is not only involved in neutralising the acidity of the endosomes, but also in conformational changes of internalised exogenous DNA through binding and electrostatic interactions,[6] and protecting DNA from degradation in the endosomal compartments.[7] Sandhu *et al.* used chloroquine in serum containing medium to improve the transfection efficiency of DNA/gold nanoparticles complexes,[8] but did not specify a mode of action of chloroquine in the improvement of the transfection.

4.1.1.1 Enhanced monolayer protection

To assess the effect of endosome disruption by chloroquine and to compare it with the protease cathepsin L inhibition, HeLa cells were incubated for 4 h with 10 nm gold nanoparticles coated with a mixed-peptide (5 % CALNN-th-fam — 95 % CALNN) self-assembled monolayer (6 nM final concentration), solely or in presence of a combination of the cathepsin L inhibitor Z-FF-fmk and/or the endosome disrupting drug chloroquine, and imaged by confocal fluorescence microscopy.[a]

[a]nanoparticle preparation: P. Free; cell work, fluorescence imaging and analysis: V. Sée

The images depict a decrease in fluorescence release of the cells that were incubated with nanoparticles in conjunction with chloroquine (Fig. 4.2B) as compared those which were incubated in the absence of drug (Fig. 4.2A). The decrease was more important with the use of the cathepsin L inhibitor Z-FF-fmk during the incubation of the nanoparticles with the cells (Fig. 4.2C), as it was already examined previously (Sect. 3.2.3). Remarkably the combination of chloroquine and Z-FF-fmk displayed an almost undiscernible level of fluorescence release on the images (Fig. 4.2D). This was further confirmed by the quantification of the mean single cell fluorescence for the different conditions, which showed a 93 % reduction of the fluorescence released in the cells incubated with the addition of both Z-FF-fmk and chloroquine, as compared to 84 % for Z-FF-fmk alone.

Following the confocal fluorescence imaging, the cells where fixed and later imaged by photothermal microscopy. A representative sample of the images is shown for each condition in Fig. 4.3A–D. The images do not disclose a singular difference between the cells incubated only with nanoparticles and the other cells incubated with added chloroquine or/and Z-FF-fmk or even between the cells incubated with one or two of the drugs. A quantification of the nanoparticles uptake by the cells in the different conditions was proceeded using the whole field method. The mean photothermal intensities in the different conditions, which attest of the amount of nanoparticle in the cells for these conditions, did not show a markedly different cellular uptake between the different conditions with or without the addition of chloroquine and Z-FF-fmk (Fig. 4.3E).

A one-way ANOVA test showed that the fluorescence intensity means of the four conditions are significantly different. A follow up Holm-Bonferroni multiple comparison test established that the means differences between pairs of conditions are significant at the 0.01 level for all the pairs to the exception of the comparison of Z-FF-fmk and Z-FF-fmk plus chloroquine. Nevertheless, the same tests performed exclusively on the two aforementioned conditions did show a difference between their means that was found to be significant, which is more in line with the difference that can be seen on the images (Fig. 4.2C–D). At the same time, the same ANOVA and Holm-Bonferroni tests performed on the photothermal intensities did not point any significant difference between the population means.

Taken together these results imply that the uptake of the nanoparticles is not altered by the use of either chloroquine or Z-FF-fmk and that the combination of endosome disruption by chloroquine and cathepsin L inhibition by Z-FF-fmk allows an improved protection of the nanoparticles from the degradation of their monolayer.

4.1.1.2 Nanoparticles intracellular localisation: cytosolic delivery?

In order to verify the effect of chloroquine on the endosomes and eventually on the nanoparticles delivery, a direct imaging of the endosomes is necessary to appraise the

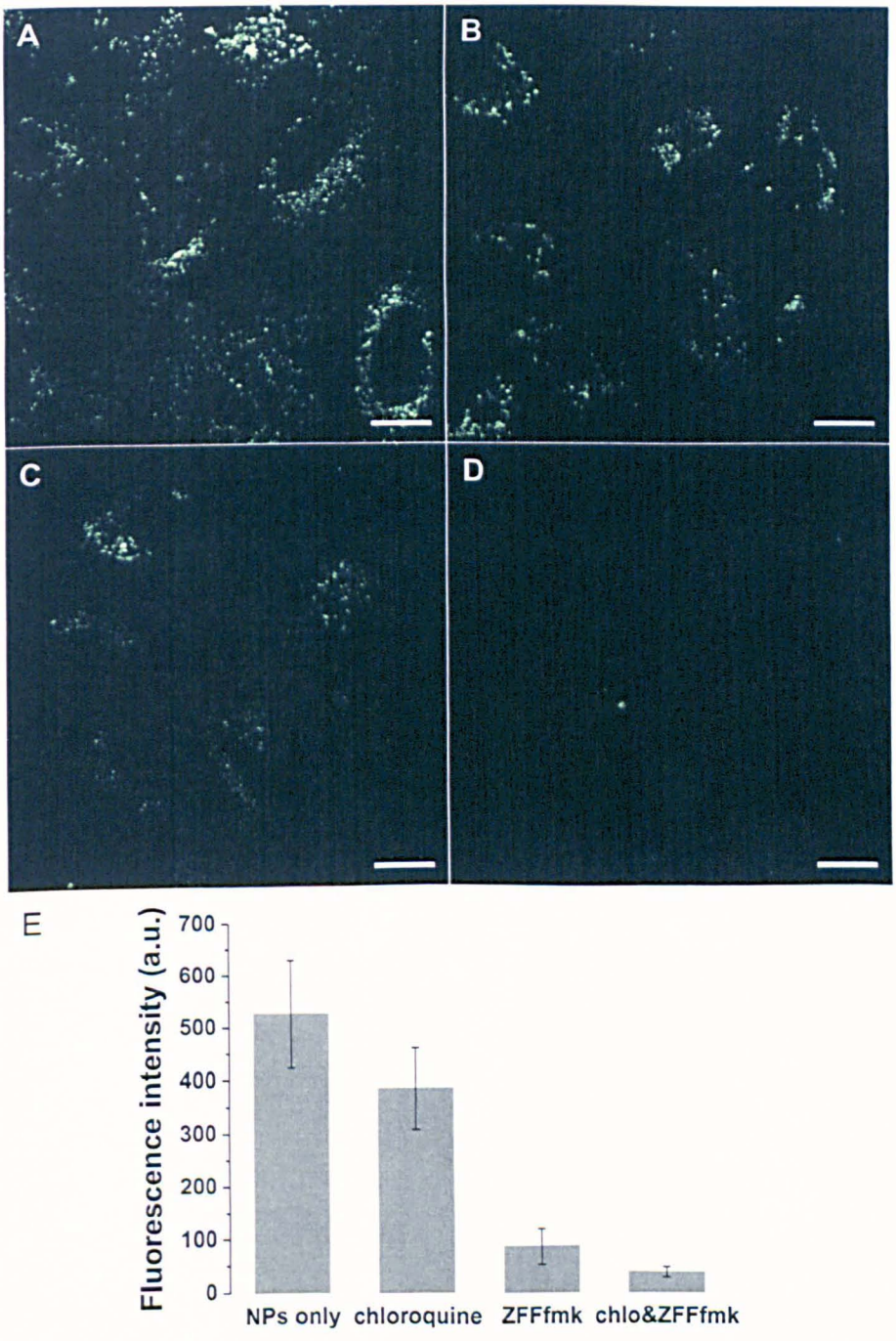

Fig. 4.2 – Combined protease cathepsin L inhibition and endosome disruption block the nanoparticle monolayer degradation. HeLa cells were incubated for 4 h with 10 nm gold nanoparticles coated with a mixed-peptide (5 % CALNN-th-fam — 95 % CALNN) self-assembled monolayer (6 nM final concentration) solely or in presence of a combination of the cathepsin L inhibitor Z-FF-fmk and/or the endosome disrupting drug chloroquine, and imaged by confocal fluorescence microscopy. (**A–D**) Confocal microscopy images of the fluorescence release in live cells (V. Sée). (**A**) Gold nanoparticles only; (**B**) gold nanoparticles with 100 μM of chloroquine; (**C**) gold nanoparticles with 20 μM of the irreversible cathepsin L inhibitor Z-FF-fmk; (**D**) gold nanoparticles with both 100 μM of chloroquine and 20 μM of Z-FF-fmk. (**E**) Quantification of five different fields for the conditions shown in (A–D). The means differences between the samples were found to be statistically significant with a one-way ANOVA test. Error bars represent the SD. Scale bars represent 20 μm.

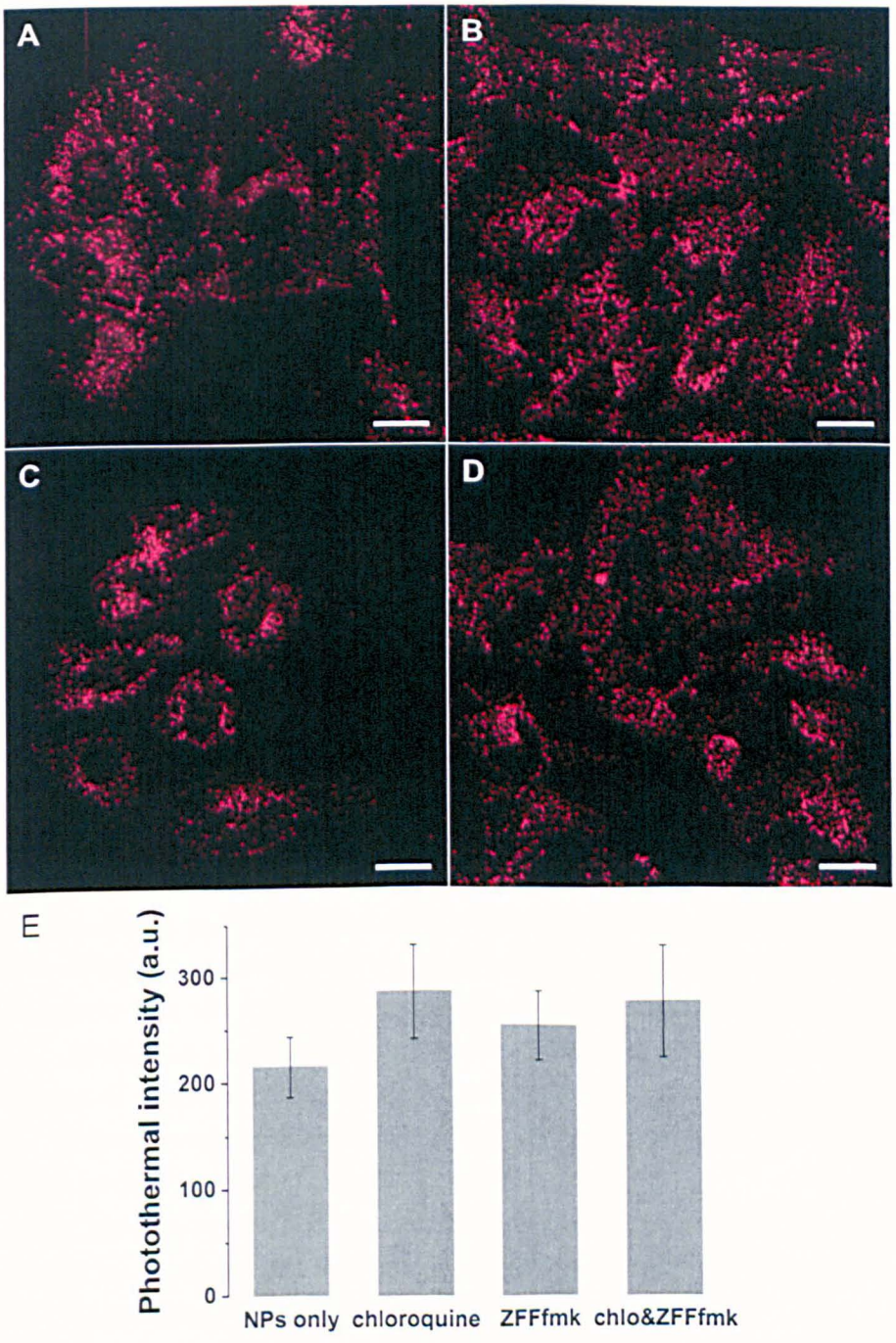

Fig. 4.3 – Combined protease cathepsin L inhibition and endosome disruption does not impede nanoparticle uptake. HeLa cells were incubated for 4 h with 10 nm gold nanoparticles coated with a mixed-peptide (5 % CALNN-th-fam — 95 % CALNN) self-assembled monolayer (6 nM final concentration) solely or in presence of a combination of the cathepsin L inhibitor Z-FF-fmk and/or the endosome disrupting drug chloroquine. They were further imaged by confocal fluorescence microscopy, fixed and imaged by photothermal microscopy. (**A**–**D**) Photothermal microscopy images of the gold nanoparticles uptake. (**A**) Gold nanoparticles only; (**B**) gold nanoparticles with 100 μM of chloroquine; (**C**) gold nanoparticles with 20 μM of the irreversible cathepsin L inhibitor Z-FF-fmk; (**D**) gold nanoparticles with both 100 μM of chloroquine and 20 μM of Z-FF-fmk. (**E**) Quantification for the conditions shown in (A–D), with at least 40 cells analysed per condition. The means differences between the samples were found to be statistically not significant with a one-way ANOVA test. Error bars represent the SD. Scale bars represent 20 μm.

change in the membrane structuring together with the possibility of nanoparticles visualisation. Transmission electron microscopy was chosen to assess the effect of chloroquine, since it can bring both the structural membrane information and the nanoparticle localisation in a direct manner.

For this purpose, HeLa cells were incubated for 3 h with gold nanoparticles coated with the matrix peptide CALNN (without CALNN-th-fam), prepared and imaged by transmission electron microscopy.[b] The images confirm the disruption of the endosomes by chloroquine and exhibit nanoparticles present in the cytosol (Fig. 4.4).

In spite of a cytosolic localisation, it is noticeable that the nanoparticles appear to stay in the vicinity of the disrupted endosomes. Some nanoparticles are seemingly still interacting with some membranes debris and although a few individual nanoparticles are scattered aside of the others, quite a substantial part of them are aggregated. This is also apparent on the photothermal image in Fig. 4.3B where, for the same nanoparticle size and concentration and chloroquine concentration (with additional CALNN-th-fam peptides in the nanoparticles monolayer), vesicularly shaped distributions of nanoparticles are omnipresent in the cells. In fact, neither chloroquine (Fig. 4.3B) nor Z-FF-fmk (Fig. 4.3C), nor the combination of both (Fig. 4.3D) did disclose a different distribution of the nanoparticles than in the absence of drugs (Fig. 4.3A), as observed by photothermal microscopy. The photothermal microscope in the conditions used for the experiment most probably did not have the ability to distinguish individual nanoparticles in the cell background.[9] Furthermore the presence of those cytosolic solitary nanoparticles could have been partially masked on the images by the accumulation of nanoparticle dense areas in the cells, disallowing their discrimination from the aggregates. However, if a significant part of them was freely moving inside the cells, not interacting with each others or with endosome/lysosome debris, the photothermal images would show well distributed intensities located evenly the cytosol.

None of the treatments did change the way the distribution of the nanoparticles appears by photothermal microscopy, which in all cases showed an endosomal pattern, whether drugs were present or not.

The number of endosomes that are exposed by photothermal microscopy in presence of chloroquine does not seem diminished either as compared to the absence of the drug, but at the same time a decrease in the release of fluorescence is observed.

Therefore it could be hypothesised that the presence of chloroquine in intact endosomes could play a second role in the monolayer protection aside of its endosomal disrupting action. Indeed, the reduced fluorescence release could be either due to the increase in pH provoked by chloroquine inside the endosomes, inducing conformational changes in cathepsin L and decreasing its activity[10,11] or resulting from a

[b] nanoparticle preparation, cell work, TEM imaging: P. Nativo

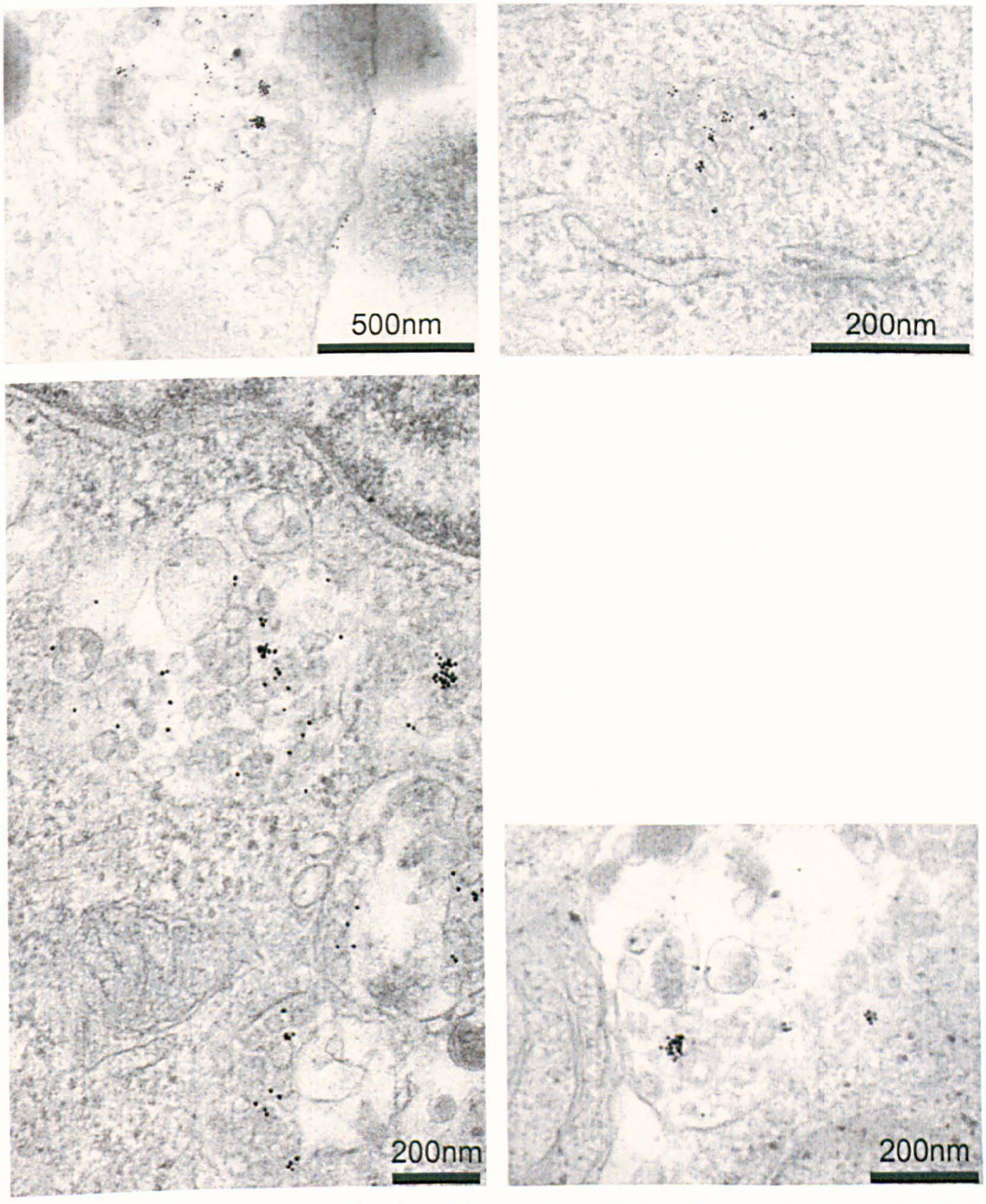

Fig. 4.4 – Endosome disruption by chloroquine. HeLa cells were incubated for 3 h in complete medium with 10 nm diameter gold nanoparticles (6 nM final concentration) coated with a self-assembled monolayer composed of the matrix peptide CALNN in presence of 100 μM chloroquine, prepared for and imaged by TEM (P. Nativo). The TEM images of the cells show disrupted endosomes and many particles not enclosed in membrane compartments, although most particles are still located close to the disrupted endosome.

hinderance in accessing the cleavage sequence by the protease following interactions between chloroquine and the nanoparticles. An answer to these questions cannot be given by the current data though and more in depth experiments would be needed for it.

4.1.1.3 Nanoparticles and degraded monolayer: co-localisation?

In order to appraise the degree of co-localisation between the fluorescent fam dyes, released from the nanoparticles functionalised with fluorescent peptides (CALNN-th-fam) after monolayer degradation, and the nanoparticles themselves inside cells, the nanoparticle internalisation needs to be observed on the same microscope for both fluorescence and photothermal imaging.

For this purpose, HeLa cells were therefore incubated with 5 nm gold nanoparticles (100 nM concentration) coated with a mixed-peptide (5 % CALNN-th-fam/ 95 % CALNN) self-assembled monolayer, solely or in presence of a combination of the cathepsin L inhibitor Z-FF-fmk and/or the endosome disrupting drug chloroquine for 3 h, before the medium was changed to remove the excess nanoparticles.[c] Live cells were then imaged successively by wide field fluorescence and photothermal microscopy on the same microscope (t = 4.5 h), to allow a visualisation of the nanoparticle/degraded monolayer co-localisation.

As seen previously, the combination of chloroquine and Z-FF-fmk does favour a good protection of the monolayer from cathepsin L proteolysis and the fluorescence observed in this case is almost not visible (Fig. 4.5E), with a level comparable to the one shown by cells incubated without nanoparticles (Fig. 4.5A). There is consequently no possible co-localisation to observe in this situation.

The cells incubated with only nanoparticles and the ones incubated with nanoparticles and 20 μM of Z-FF-fmk show a partial co-localisation, with a few areas in the cells where both fluorescence and photothermal signals can be observed at the same place.

Surprisingly the co-localisation is only partial. This could be explained by the mobility of either the nanoparticles or more probably the dyes or could also be associated with the way the images were acquired. Indeed in all conditions, the wide field fluorescence image is taken first, at 3 μm above the glass slide with an integration time of 0.62 s, and then the photothermal image is acquired at 1 μm above the glass slide, line by line in a back and forth movement with a 10 ms integration time per pixels, to finally perform the total image acquisition in $\sim$ 13.5 min for a 256×256 pixels image, as it was for these images. The altitude at which the fluorescence images were acquired was chosen in order to obtain images that had the best focus for all fields of view on average, after observation of various areas where cells were showing fluorescence release. The altitude chosen for the photo-

[c] nanoparticle preparation and cell work: P. Free

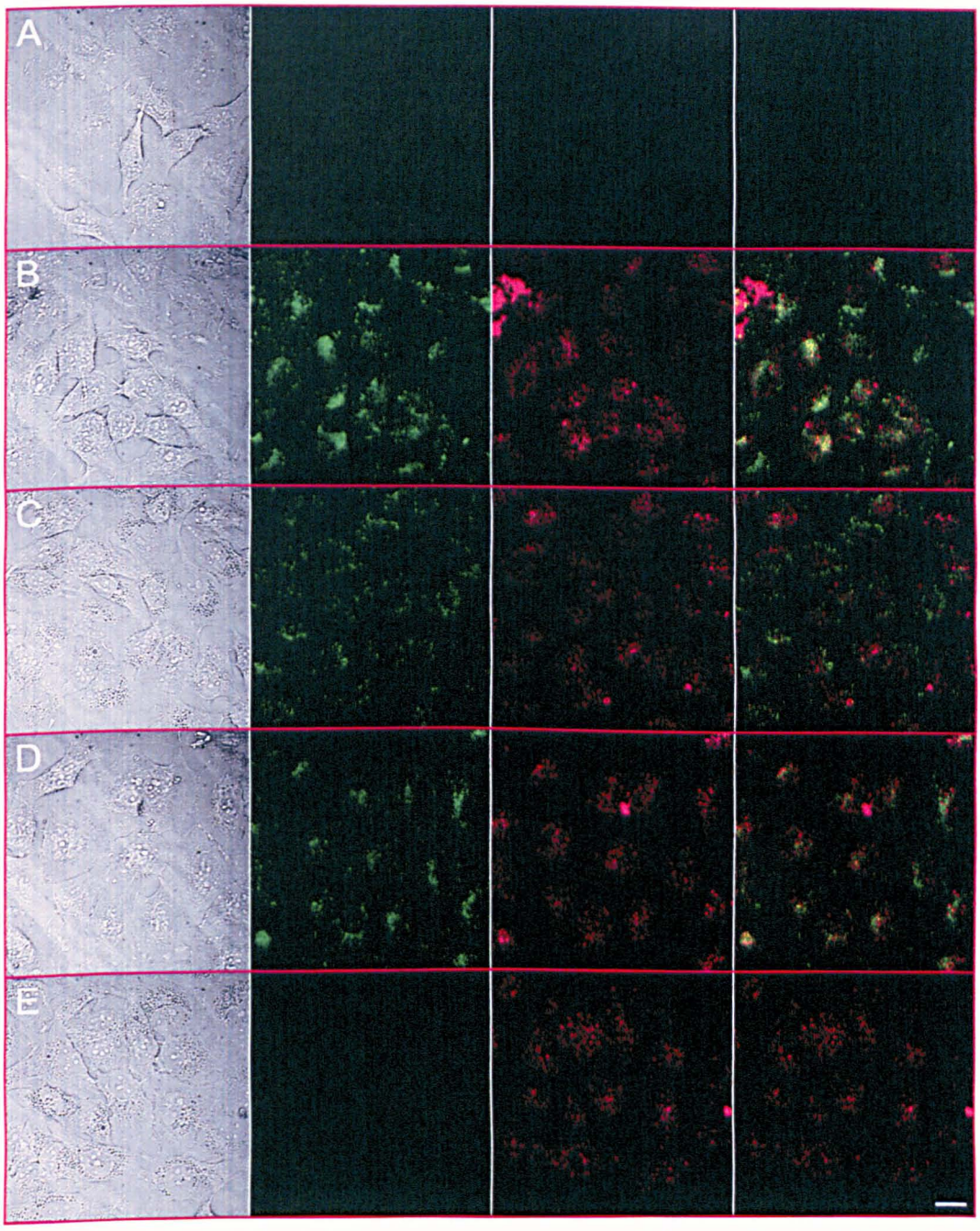

Fig. 4.5 – Co-localisation of nanoparticles and degraded monolayer with/without endosome disrupting drug chloroquine and/protease inhibitor Z-FF-fmk.
HeLa cells were incubated with 5 nm gold nanoparticles (100 nM concentration) coated with a mixed-peptide (5 % CALNN-th-fam/ 95 % CALNN) self-assembled monolayer, solely or in presence of a combination of the cathepsin L inhibitor Z-FF-fmk and/or the endosome disrupting drug chloroquine for 3 h, before the medium was changed to remove the excess nanoparticles. Live cells were imaged successively by wide field fluorescence and photothermal microscopy on the same microscope (t = 4.5 h), to allow a visualisation of the nanoparticle/ degraded monolayer co-localisation. (**A**–**E**) From left to right: bright field image, fluorescence image, photothermal image and overlay of fluorescence and photothermal images. (**A**) Cells without nanoparticles; (**B**) cells with gold nanoparticles only; (**C**) cells with gold nanoparticles and 100 μM of chloroquine; (**D**) cells with gold nanoparticles and 20 μM of the irreversible cathepsin L inhibitor Z-FF-fmk; (**E**) cells with gold nanoparticles and both 100 μM of chloroquine and 20 μM of Z-FF-fmk. Scale bar represents 20 μm.

thermal images was coming from previous observation of the dependance of the intensity on the altitude observed in one cell incubated with nanoparticles showing a maximum around 1 μm and other tests showing that the signal is decreasing above $\sim 1\,\mu$m while increasing the altitude. Although this does not represent a statistically representative sample, it was considered as a reasonable assumption that the signal will be around its maximum at this 1 μm altitude. Furthermore, although the photothermal intensity of nanoparticles located at the same altitude as the fluorescent dyes (3 μm) is likely to be lower when detected at 2 μm below it (detection focus), a strong signal would probably still be detected.

Altogether and for the aforementioned reasons, an observed co-localisation is likely to represent a significant presence of both nanoparticles and fluorescent dyes resulting from the monolayer degradation.

The areas where co-localisation was observed in the cells incubated with nanoparticles, with or without the addition of Z-FF-fmk, should therefore represent a significant amount of nanoparticles and dyes in a relative close proximity.

To estimate better the extend of the co-localisation, Fig. 4.6 shows the images of cells incubated with only nanoparticles represented earlier in Fig. 4.5B with two different contrasts. In both series of images (A and B) the contrasts minima were chosen to minimise the background in both fluorescence and photothermal images in the areas where no cells were present, minimising the presence of pixels due to the noise visible on the images. The maxima of the contrast in both fluorescence and photothermal images in Fig. 4.6A were chosen to show better the low intensities in both fluorescence and photothermal images (saturating the higher ones), in order to better display the extend of the co-localisation. The contrasts maxima in Fig. 4.6B where chosen higher to display the strength/weakness of the respective signals where co-localisation can be observed.

Singularly, enhancing the contrast in Fig. 4.6A did not unveil extensive areas of co-localisation in the cells incubated without drugs.

The same way of choosing the contrast was also applied in Fig. 4.7, which display the co-localisation of cells incubated with nanoparticles in the presence of chloroquine (same image as in Fig. 4.5C). In this case hardly any area of the cells were exhibiting the joint presence of nanoparticles and fluorescent dyes coming from the monolayer degradation. This is consistent with the effect of disrupting the endosomes that chloroquine was shown to have. However, in line with the observation of relatively low co-localisation observed in absence of chloroquine (Fig. 4.6), it cannot be excluded that part of co-localisation could not be observed due to the experimental conditions.

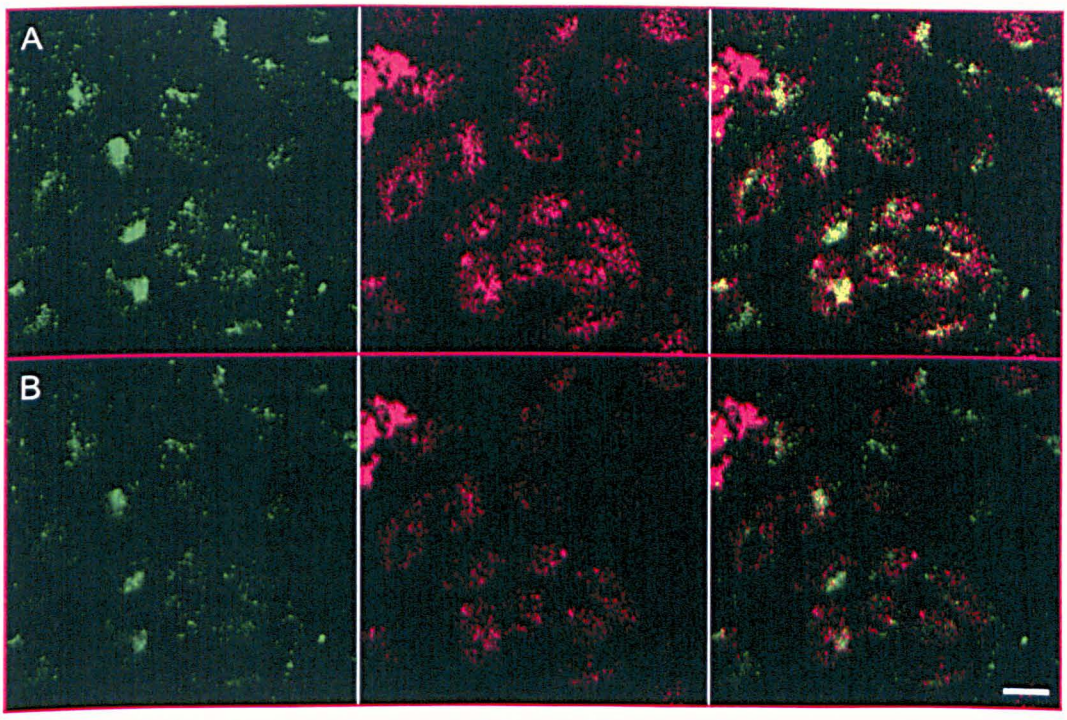

Fig. 4.6 – Co-localisation of nanoparticles and degraded monolayer with no added drugs. HeLa cells were incubated for 3 h with 5 nm gold nanoparticles (100 nM final concentration) coated with a mixed-peptide (5 % CALNN-th-fam — 95 % CALNN) self-assembled monolayer for 3 h, before the medium was changed to remove the excess nanoparticles. Live cells were imaged successively by wide field fluorescence and photothermal microscopy on the same microscope (t = 4.5 h), to allow a visualisation of the nanoparticle/degraded monolayer co-localisation. (**A**–**B**) The same field of view is shown with two different contrasts to allow an estimation of the importance of the co-localisation. From left to right: fluorescence image, photothermal image and overlay of fluorescence and photothermal images. (**A**) Small contrast range (fluorescence: [10900,11900]; photothermal: [100,200]) displaying the maximum area of co-localisation. (**B**) Larger contrast range (fluorescence: [10900,11900]; photothermal: [90,1000]) displaying the degree of co-localisation. Scale bar represents 20 μm.

4.1.2 Nanoparticle mediated endosome membrane destabilisation

In this section the fusion sequence of the peptide HA2, which causes the rupture of endosomes after its uptake and the subsequent acidification of the endosomes, was used in conjunction to the cell penetrating peptide Tat to functionalise nanoparticles in a strategy aiming to increase their uptake and at the same time deliver them in the cytosol.

The Tat protein is a transcription activation factor of the human immunodeficiency virus. Its peptide transduction sequence YGRKKRRQRRR[d] is known as a cell penetrating peptide,[12] which designates short cationic peptides that have the ability to translocate across the cell membrane without disrupting it. The name of CPP was given as it was believed originally that the peptides were not internalised by endocytosis but were going directly to the cytosplasm. Frankel *et al.*

[d]Tat minimal transduction domain is residues 49–57: RKKRRQRRR

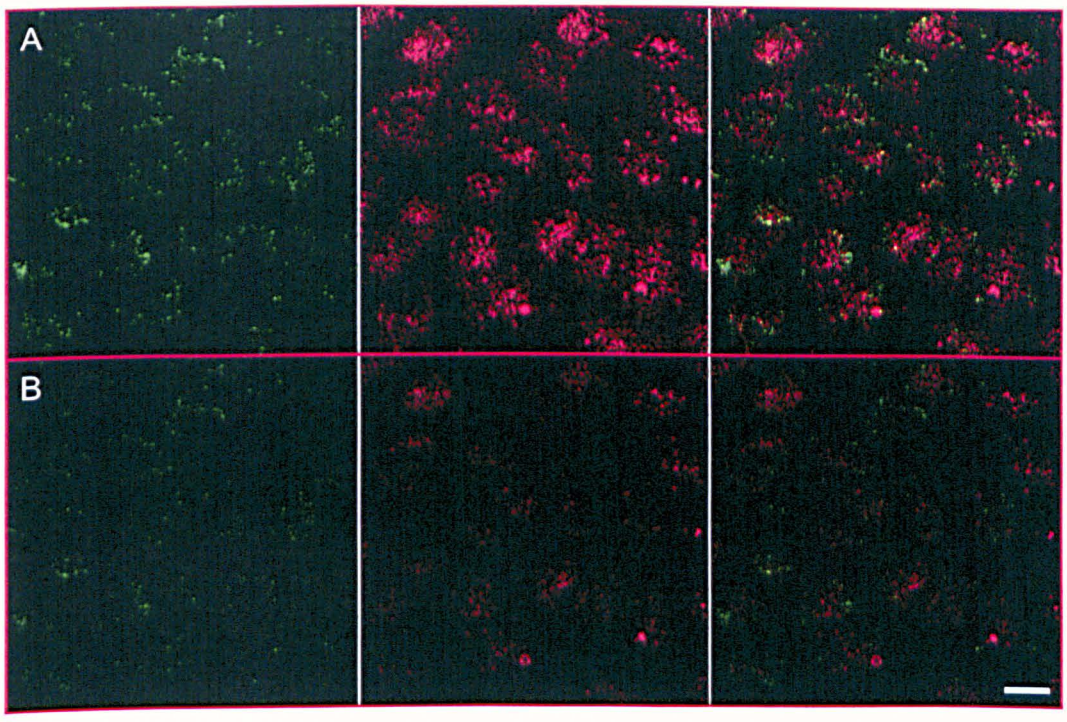

Fig. 4.7 – Co-localisation of nanoparticles and degraded monolayer in presence of endosome disrupting drug chloroquine. HeLa cells were incubated for 3 h with 5 nm gold nanoparticles (100 nM final concentration) coated with a mixed-peptide (5 % CALNN-th-fam — 95 % CALNN) self-assembled monolayer with 100 μM of chloroquine for 3 h, before the medium was changed to remove the excess nanoparticles. Live cells were imaged successively by wide field fluorescence and photothermal microscopy on the same microscope (t = 4.5 h), to allow a visualisation of the nanoparticle/degraded monolayer co-localisation. (**A**–**B**) The same field of view is shown with two different contrasts to allow an estimation of the importance of the co-localisation. From left to right: fluorescence image, photothermal image and overlay of fluorescence and photothermal images. (**A**) Small contrast range (fluorescence: [10374,11374]; photothermal: [100,200]) displaying the maximum area of co-localisation. (**B**) Larger contrast range (fluorescence: [10374,14374]; photothermal: [90,1000]) displaying the degree of co-localisation. Scale bar represents 20 μm.

demonstrated in 1988 that the Tat protein is taken up in HL3T1 cells and further observed their nuclear localisation[13] which was dramatically increased after using chloroquine to deliver them in the cytosol. Later the Tat protein transduction domain was shown to interact with lipid rafts in the cell membrane before entering cell by micropinocytosis.[14]

De la Fuente *et al.*[15] have reported the nuclear localisation of small ($\sim$2.8 nm) gold nanoparticles functionalised with Tat by EDC coupling to a tiopronin monolayer coating at a concentration of $\sim$1 μM after incubation with cells hTERT-BJ1 human fibroblast cells. The nanoparticles were demonstrated to go in the nuclei by TEM, but unfortunately only one single image was shown as evidence of the nuclear delivery. This group did a follow up study in which they were comparing the uptake of 5 nm gold functionalised with tiopronin to others with tiopronin terminated with either Tat or PEG or Tat terminated PEG. They studied by immunofluorescence

the quantity and distribution of antibody conjugated clathrin and dynamin, which are proteins both involved in endocytosis processes, the cell surfaces by SEM and the nuclear localisation by TEM. They concluded that the non-Tat-containing nanoparticles were internalised by clathrin-mediated endocytosis and the Tat terminated ones were not.[16] The Tat nanoparticles were again observed in the nucleus — although they chose the same image as in their previous paper[15] — unlike the other nanoparticle types. However, the statistics presented (clathrin and dynamin fluorescence) lacks significance (10 cells means) and presents only very indirect evidence to back up the claim of clathrin-mediated endocytosis, and the TEM images were highlighted as needing caution in their interpretation as they further mentioned that the fixation was having a potential in bringing the 5 nm nanoparticles in the nuclei through the nuclear pore. Ruan *et al.* have demonstrated that Tat functionalised quantum dots are internalised by endocytosis in HeLa cells and established that they stayed in the endosomes that were further transported near the nucleus to the microtubule organising centre.[17]

HA2 is a subunit of the influenza A virus hemagglutinin glycoprotein HA and contains a fusion peptide sequence that allows membrane destabilisation at low pH (see Cross *et al.*[18] for a recent review on structure-function of HA fusion peptide).

Wadia *et al.* conjugated the fusion peptide HA2 to the CPP Tat to achieve a destabilisation of micropinocytosome internalised HA2-Tat peptides and deliver the peptides to the cytosol, to allow them to interact with DNA and subsequently induce the expression of EGFP.[14] Kumar *et al.* have used 20 nm gold nanoparticle multifunctionalised with anti-actin antibody to target actin filaments and antibody bond Tat-HA2 peptides for a targeted cytosplamic delivery in 3T3 mouse fibroblast cells.[19] They used a combination of TEM and darkfield reflectance microscopy to show that nanoparticles lacking the HA2 sequence were delivered but stayed in endosomes and that the fully functional (HA2 containing) nanoparticles seemed to have escaped the endosomes as they were shown to label efficiently actin filaments.

4.1.2.1 HA2 membrane destabilisation process

HA0 is a precursor polypeptide chain of 550 amino acids that constitutes a non-covalently linked trimer that dissociates after proteolysis into two subunits HA1 and HA2 linked by a disulfide bond to form HA.[20,21] The proteolytic cleavage transforms the precursor HA0 polypeptide into the pH-sensitive HA, which allows conformational changes upon acidification[20,22–24] in endosomes and which leads to the virus linked to HA to fuse its membrane[25,26] with the endosomal membrane and be released in the cytosol of the targeted cell. To achieve that the fusion peptide located on the N-terminal of the HA2 subunit is inserted in the endosome membrane and destabilises it. The exact process by which irreversible conformational changes leads to membrane fusion is not fully understood. This is partly because the fusion pep-

tides and the ten residues that link them to the part of the HA2 structure that has been resolved are very hydrophobic (not possible to crystallise) and their structure is therefore still unknown at acidic pH.

4.1.2.2 HA2/Tat peptides improve the nanoparticle uptake

With the view of improving the nanoparticles uptake and promoting their cytosolic delivery upon internalisation, Tat and HA2 peptides will be added to the nanoparticle monolayer (Fig. 4.8A).

As seen previously, at basic to slightly acidic pH (typically above 4) the nanoparticle surface has a negative net charge coming from the terminal carboxylic group of the asparagine exposed to the solution. In presence of CALNN-PEG, this situation does not change. The addition in the self-assembled monolayer of the CALNN-HA2 peptide (CALNNGDIMGEWGNEIFGAIAGFLG-amide), which possesses three negatively charged residues (1 Asp, 2 Glu), does therefore not change the net charge of the nanoparticles at any pH above a slightly acidic value (CALNN-HA2 isoelectric point: 3.57). The addition of the peptide CALNN-Tat (CALNNAGRKKRRQRRR, pI=12.3) in the monolayer brings hydrophilic residues to the nanoparticles surface, together with a total of eight positively charged residues (6 Arg, 2 Lys). CALNN-Tat does not change the net surface charge of the nanoparticles when present in the monolayer with the CALNN and CALNN-PEG matrix peptides due to the huge excess of those later ones. However, it provides a few local patches of positive charges on the nanoparticles, which are difficult to quantify, since the peptides self-assembly process may favour some peptides with respect to others and the derived exact monolayer content is therefore unknown.

Gold nanoparticles (5 nm diameter) solutions were prepared with self-assembled monolayers composed of the matrix peptides CALNN and CALNN-PEG (4:1 ratio) with (and without) the addition of the functional membrane disrupting peptides CALNN-HA2 (Fig. 4.8C) and/or the cell penetrating CALNN-Tat peptides (Fig. 4.8D) — the details of the monolayer compositions can be found in Tab. 4.1.

HeLa cells were then incubated separately with the nanoparticles (final concentration 500 nM) coated with or without the functional peptides CALNN-HA2 and CALNN-Tat or without nanoparticles (control) for three hours, fixed and imaged by photothermal microscopy.[e]

A representative sample of the images acquired is displayed in Fig. 4.9 for the five conditions. The contrast of the photothermal images (identical between conditions) was chosen to limit the displayed background and to allow the visualisation of the internalised nanoparticles in the four conditions where the cells were subjected to nanoparticle incubation (contrast range: [50,2000]). An immediate conclusion after image comparison is that more nanoparticles are taken up by the cells incubated with

[e] nanoparticle preparation and cell work: P. Free

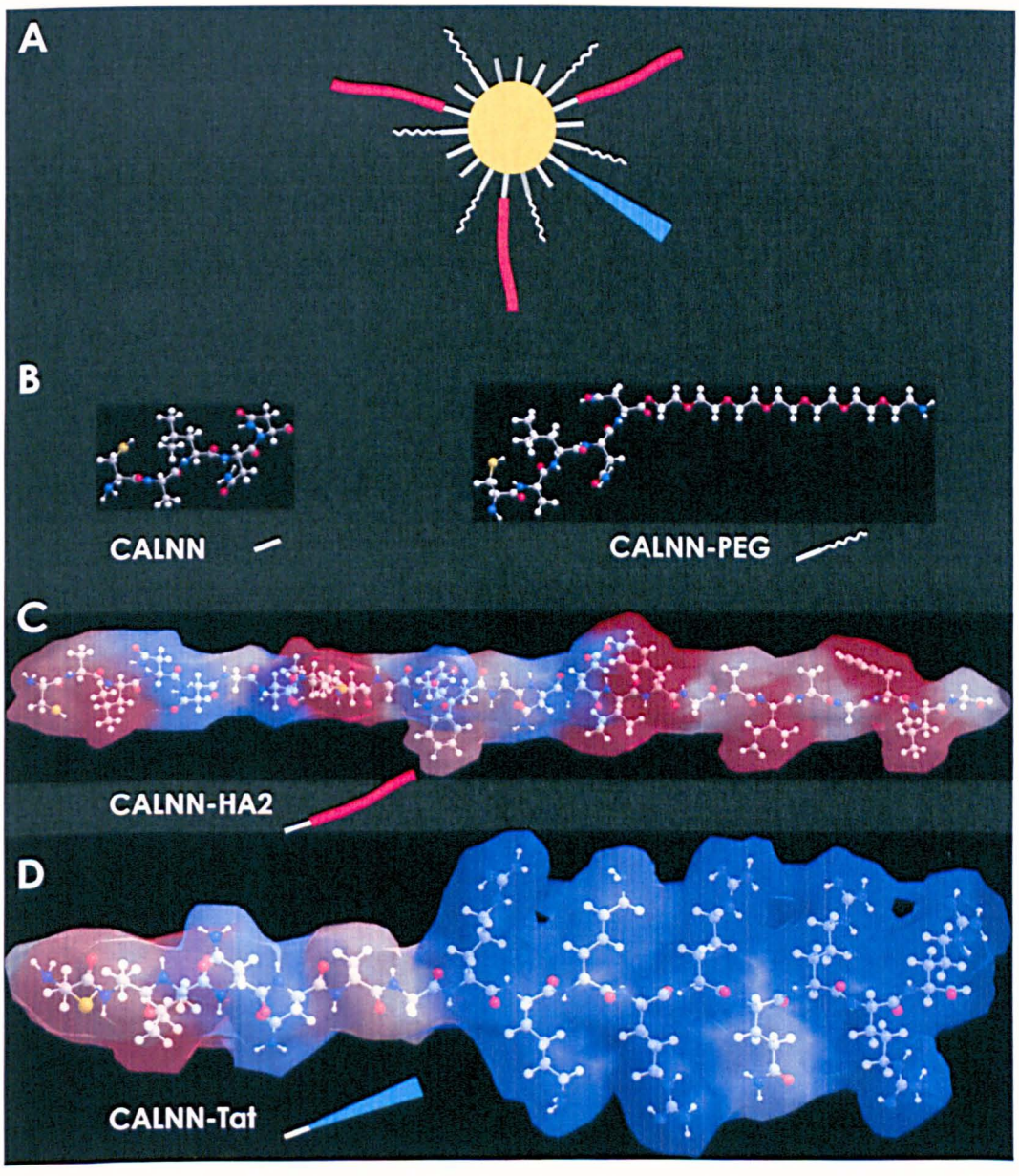

Fig. 4.8 – Nanoparticle functionalisation with HA2 and Tat peptides. (**A**) Gold nanoparticles were functionalised with the matrix peptides CALNN and CALNN-PEG and the addition of the functional peptides CALNN-HA2 or/and CALNN-Tat. (**B**) Structures of matrix peptides CALNN and CALNN-PEG (CALNN–$(EG)_6$–ol). (**C**–**D**) Peptide structures drawn with a coloured outer surface representing the hydrophilicity/hydrophobicity of the residues (red: hydrophobic; blue: hydrophilic). (**C**) Membrane destabilising CALNN-HA2 peptide (CALNNGDIMGEWGNEIFGAIAGFLG–amide). (**D**) Cell penetrating CALNN-Tat peptide (CALNNAGRKKRRQRRR).

Monolayer composition				Label
Functional peptides		Matrix peptides		(Fig. 4.9)
CALNN-HA2	CALNN-Tat	CALNN	CALNN-PEG	
–	–	80 %	20 %	B
10 %	–	72 %	18 %	C
–	1 %	79 %	20 %	D
10 %	1 %	71 %	18 %	E

Tab. 4.1 – Composition of the gold nanoparticle self-assembled monolayer prepared with/without the functional peptides CALNN-HA2 and CALNN-Tat.

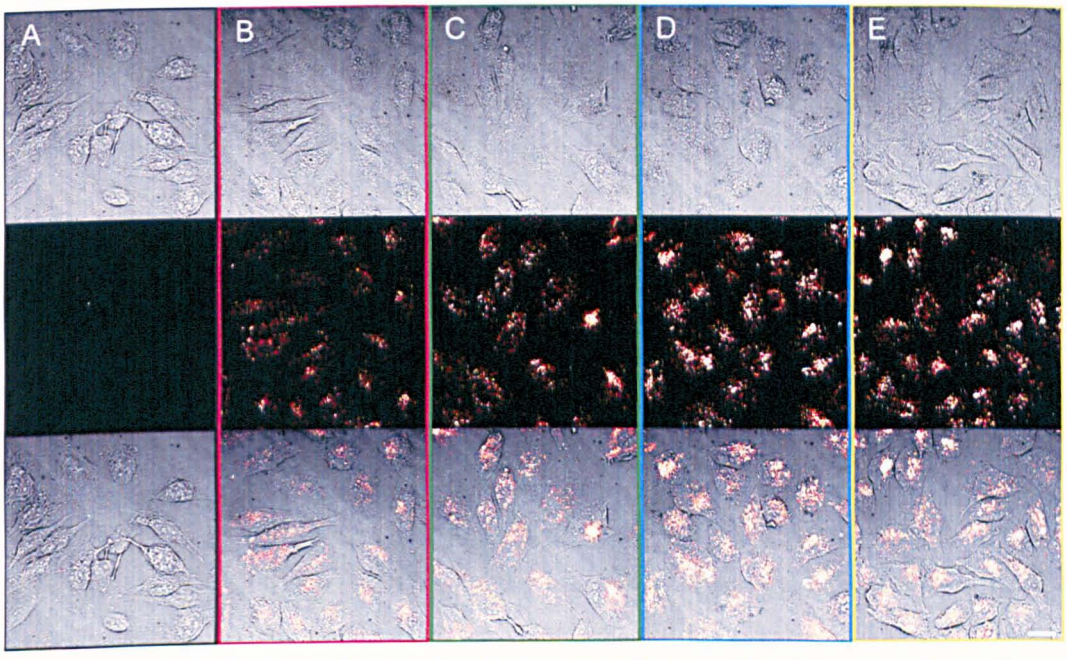

Fig. 4.9 – Intracellular delivery of gold nanoparticles assisted by monolayer functionalisation with HA2/Tat peptides. HeLa cells were incubated separately without nanoparticles or with 5 nm nanoparticles (final concentration 500 nM) functionalised with either no functional peptide (80 % CALNN — 20 % CALNN-PEG matrix peptides) or with a combination of HA2 and/or Tat peptides (10 % CALNN-HA2, 1 % CALNN-Tat, 10 % CALNN-HA2 — 1 % CALNN-Tat) for 3 h, fixed and imaged by photothermal microscopy. (**A**–**E**) Images of the nanoparticle uptake by HeLa cells for the five conditions. Top: bright field image; middle: photothermal image; bottom: overlay of the bright field and photothermal images. (**A**) Cells without nanoparticles incubation. (**B**) Cells incubated with nanoparticles coated with the matrix peptides (80 % CALNN — 20 % CALNN-PEG). (**C**) Cells incubated with nanoparticles functionalised with 10 % CALNN-HA2 peptides. (**D**) Cells incubated with nanoparticles functionalised with 1 % CALNN-Tat peptides. (**E**) Cells incubated with nanoparticles functionalised with 10 % CALNN-HA2 and 1 % CALNN-Tat peptides. Scale bar represents 20 μm.

the nanoparticles bearing the functional peptides CALNN-HA2 and/or CALNN-Tat than the ones incubated with the nanoparticles coated only with the matrix peptides CALNN and CALNN-PEG. An additional difference could also be estimated in first approximation within the samples containing the functional peptides CALNN-HA2 and CALNN-Tat in their nanoparticle monolayer, where the nanoparticles with CALNN-Tat and the ones with both CALNN-HA2 and CALNN-Tat appearing to experience more internalisation than the ones with only CALNN-HA2.

An analysis of the images was done by the "whole field" method on three (1 % CALNN-Tat) or four (other conditions) fields of view per condition (method description in Sect. B.2.9.3). The method used a threshold discarding the pixels below a value corresponding to 1.5 times the mean background intensity, to give a mean photothermal intensity value (per field of view) for each of the five conditions shown in Fig. 4.9. The results of the analysis are plotted as a bar chart in Fig. 4.10. The quantification demonstrates that the uptake of gold nanoparticles by the cells is on average increased by almost a factor two (1.72) by adding a proportion of 10 % of the functional peptide CALNN-HA2 in the monolayer and nearly by a factor three (2.71 and 2.76 respectively) when adding 1 % CALNN-Tat or 10 % CALNN-HA2 and 1 % CALNN-Tat in the monolayer.

An assessment of the statistical significance was done by a one-way ANOVA test followed by Holm-Bonferroni multiple comparison tests and showed a significant difference between the five different conditions. Unsurprisingly, it did not show a significant difference between the two samples containing the functional peptide Tat, as their mean values are very close and the error bars not negligible.

However, if for example one looks at the pair of samples formed by the cells incubated without nanoparticles and the cells incubated with nanoparticles coated only with the matrix peptides (80 % CALNN — 20 % CALNN-PEG), although a Holm-Bonferroni test show a significant difference between the samples means at the 0.05 level, which is often considered as acceptable, at the 0.01 level a Holm-Bonferroni test did not point towards a significant difference between those samples. It raises questions about the means and errors of the two aforementioned samples and therefore either on the images or more probably on the method used to analyse them, as the images clearly show a clear cut difference between the presence and absence of the CALNN coated nanoparticles during incubation. Maybe here a single cell analysis would reduce the contribution of a few cells with a higher intensity to the amplitude of the standard deviation and mechanically solve this discrepancy.

4.1.2.3 Intracellular localisation of HA2/Tat functionalised nanoparticles

The improvement of the nanoparticles uptake was noticeable with the addition of the different combination of CALNN-HA2 and CALNN-Tat peptides in the na-

Pairs of samples		Means difference significance (1/0)	
		0.05 level	0.01 level
10% HA2/1% Tat	Cells only	1	1
1% Tat	Cells only	1	1
10% HA2/1% Tat	Matrix peptides	1	1
1% Tat	Matrix peptides	1	1
10% HA2	Cells only	1	1
10% HA2/1% Tat	10% HA2	1	1
1% Tat	10% HA2	1	1
Matrix peptides	Cells only	1	0
10% HA2	Matrix peptides	1	0
10% HA2/1% Tat	1% Tat	0	0

Tab. 4.2 – Statistical significance of differences between mean photothermal intensities after uptake of nanoparticles bearing different combination of CALNN/CALNN-PEG/CALNN-HA2/CALNN-Tat peptides in HeLa cells. Holm-Bonferroni multiple comparison tests were carried on after ANOVA tests to assess the statistical significance of the differences between the mean photothermal intensities of cells incubated with (and without) nanoparticles coated with either matrix peptides (80 % CALNN — 20 %CALNN-PEG) only or with one or two of the functional peptides CALNN-HA2 and CALNN-Tat (10 % CALNN-HA2, 1 % CALNN-Tat, 10 % CALNN-HA2 — 1 % CALNN-Tat). The 0.05 and 0.01 significance levels are shown to allow an evaluation of the strength of the differences. 1 indicates that means difference is significant at the given level and 0 that it is not.

noparticle monolayer. However, the intracellular localisation of the nanoparticles was not examined throughout and still remains to be understood. In particular it would be interesting to know whether the HA2 has helped into a cytosolic entry of the nanoparticles or not. Figure 4.11 presents the photothermal images shown previously in Fig. 4.9B–E. The contrasts were set differently between the different images, as the comparison of the quantity of uptake between the conditions is not the purpose, with the goal to display the images with a contrast truly representative of the internal distribution of the nanoparticles for each image. The reason for this choice was partially driven by the fact the uptake differs between the images. A similar contrast for all the images would have either hidden some nanoparticles dense areas in the condition where less uptake is observed (Fig. 4.11A) while allowing a good representation of others (Fig. 4.11C–D), or it would have saturated the images with higher uptake to allow the correct display of the least uptake.

A closer view of the photothermal images of the cells incubated with nanoparticles with either the matrix peptides only as capping ligands (Fig. 4.11A) or with

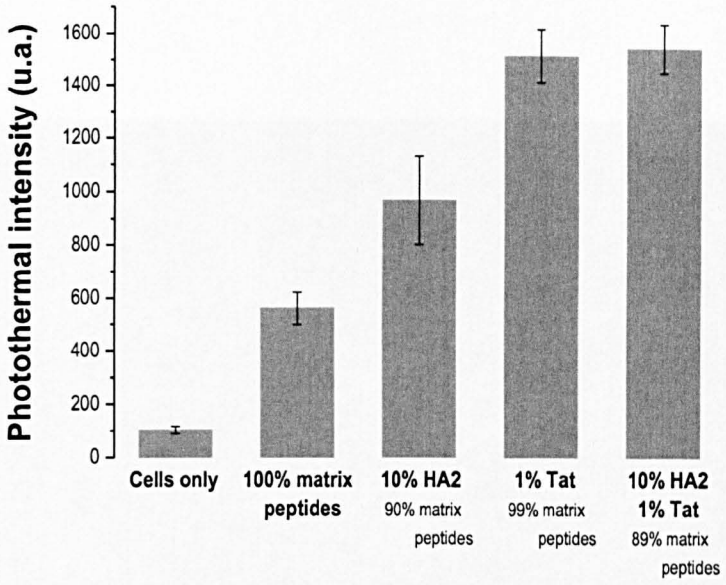

Fig. 4.10 – Quantification of CALNN-HA2/CALNN-Tat assisted cell delivery of gold nanoparticles. HeLa cells were incubated separately without nanoparticles or with 5 nm nanoparticles (final concentration 500 nM) functionalised with either no functional peptide (80 % CALNN/20 % CALNN-PEG, matrix peptides) or with a combination of CALNN-HA2 and/or CALNN-Tat peptides (10 % CALNN-HA2, 1 % CALNN-Tat, 10 % CALNN-HA2—1 % CALNN-Tat) for 3 h, fixed and imaged by photothermal microscopy. Three or four fields of view were analysed per condition to produce "whole field" mean photothermal intensities for the five conditions (average of 53 cells per condition) and a mean photothermal intensity was generated by taking the average of the fields mean values (weighted by the number of cells per field). Error bars represent the SE.

the addition of the functional peptides CALNN-HA2 (Fig. 4.11B) or CALNN-Tat (Fig. 4.11C) or with both (Fig. 4.11D) in the nanoparticles monolayer does not show a difference in nanoparticle distribution. The four conditions display numerous endosomal vesicles spread in the cells, a pattern attesting of an endocytosis mediated uptake. A few larger aggregates are appearing on the images representing the conditions where CALNN-Tat peptides were included in the monolayer (Fig. 4.11C–D), but the effect is not pronounced.

All in all the size of the nanoparticles dense areas in the four different conditions is quite similar. This can be put in perspective by comparing with the information present in the images displayed in an identical contrast for all conditions, which is visible in Fig. 4.12 (same contrast as in Fig. 4.9). This later figure shows that the increase in nanoparticles content inside the cells is essentially achieved by an increased amount of nanoparticles in the endosomes. To conclude on the localisation information given by the photothermal images, it is noteworthy to observe that none of the conditions have shown any tangible sign of cytosolic localisation, despite the effect that the HA2 peptides are supposed to have on the endosomal escape.

A comparison could though be made with a similar nanoparticle system, composed of 10 nm diameter nanoparticles coated with a monolayer comprising 10 %

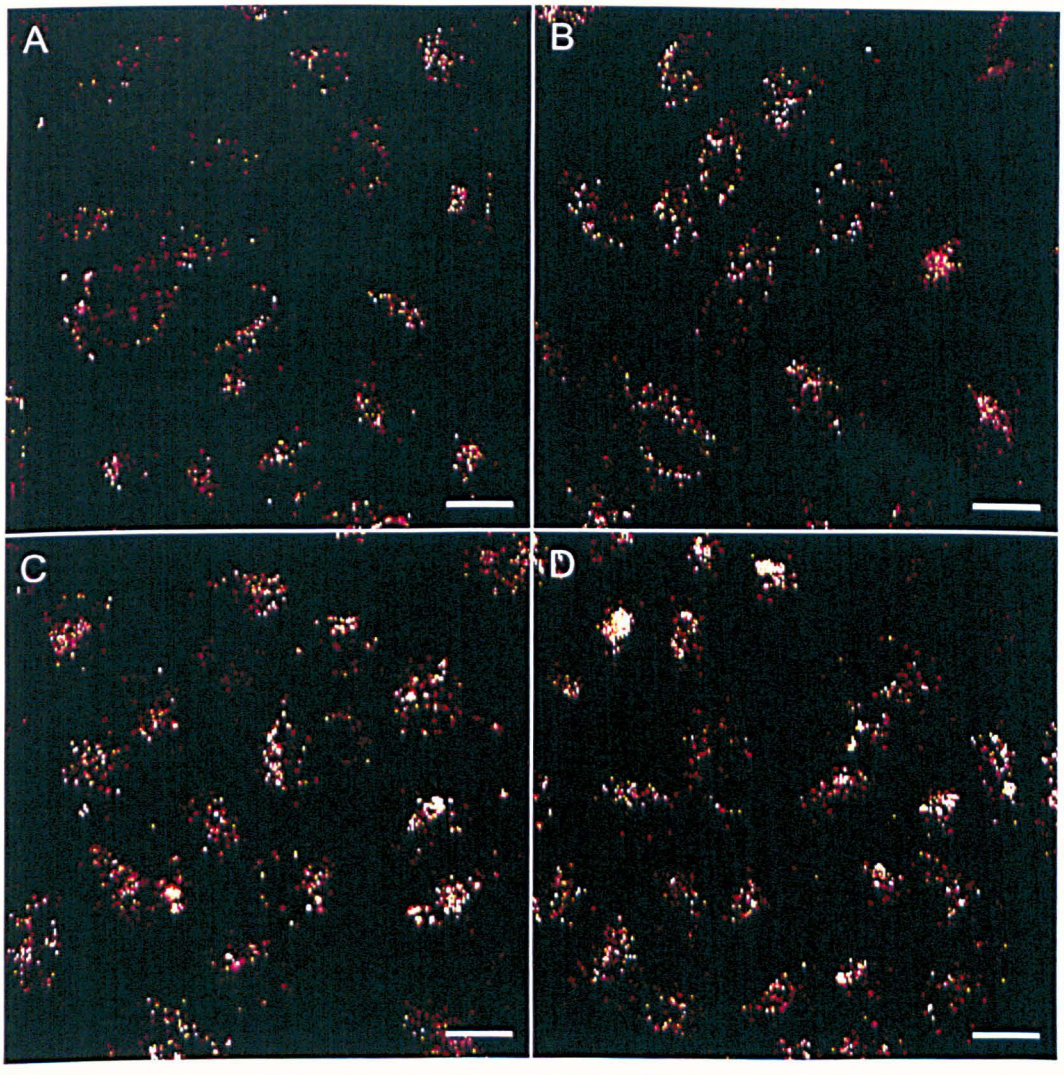

Fig. 4.11 – Intracellular localisation of CALNN-HA2/CALNN-Tat peptides coated nanoparticles in HeLa cells. The images of the uptake of gold nanoparticles functionalised with (and without) CALNN-HA2/CALNN-Tat peptides shown in Fig. 4.9B–E are displayed with different contrasts. The contrasts were chosen by the auto function of the ImageJ software in order to display the images with the best individual contrasts to better show the nanoparticles localisation regardless of the quantity of uptake. (**A**–**D**) Photothermal images of fixed HeLa cells previously incubated with nanoparticles coated with the matrix peptides CALNN/CALNN-PEG (4:1) (A) or with additional functional peptides CALNN-HA2 and/or CALNN-Tat (B–D). (**A**) Nanoparticle monolayer composed solely of the matrix peptides CALNN/CALNN-PEG (contrast [272,4586]). (**B**) 10 % of CALNN-HA2 peptides added in the monolayer (contrast [294,7966]). (**C**) 1 % of CALNN-Tat peptides added in the monolayer (contrast [287,14612]). (**D**) 10 % of CALNN-HA2 and 1 % of CALNN-Tat peptides added in the monolayer (contrast [275,16138]). Scale bars represent 20 μm.

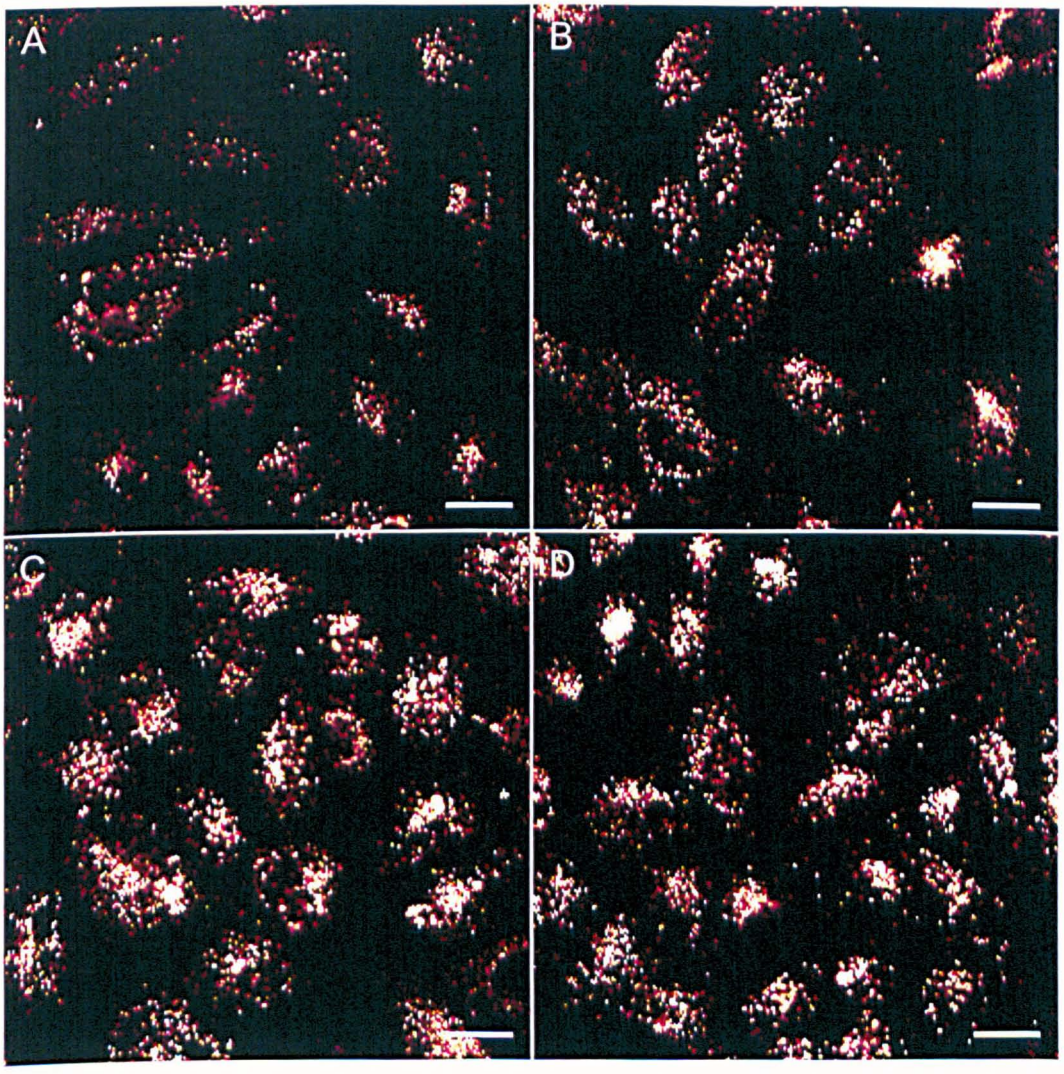

Fig. 4.12 – Intracellular localisation of CALNN-HA2/CALNN-Tat peptides coated nanoparticles in HeLa cells. The images of the uptake of gold nanoparticles functionalised with (and without) CALNN-HA2/CALNN-Tat peptides shown in Fig. 4.9B–E are displayed in a larger version for . (**A–D**) Photothermal images of fixed HeLa cells previously incubated with nanoparticles coated with the matrix peptides CALNN/CALNN-PEG (4:1) (A) or with additional functional peptides CALNN-HA2 and/or CALNN-Tat (B–D). (**A**) Nanoparticle monolayer composed solely of the matrix peptides CALNN/CALNN-PEG. (**B**) 10 % of CALNN-HA2 peptides added in the monolayer. (**C**) 1 % of CALNN-Tat peptides added in the monolayer. (**D**) 10 % of CALNN-HA2 and 1 % of CALNN-Tat peptides added in the monolayer. Scale bars represent 20 μm.

CALNN-HA2 functional peptides and 90 % of the matrix peptide CALNN, which has shown a limited endosomal escape. HeLa cells were incubated with nanoparticles (10 nm diameter, 6 nM concentration) functionalised with a peptide monolayer composed of 10 % CALNN-HA2 and 90 % CALNN for three hours before being prepared for transmission electron microscopy and imaged by TEM. The images show that some nanoparticles have managed to escape the endosomes (red arrows in Fig. 4.13), but they seem to be still interacting with the some pieces of membrane coming from the broken endosomes, and are staying in the close vicinity of the endosomes. The two situations cannot readily be compared, but this example shows that HA2 has indeed an effect on the endosomal membrane when it is present on the surface of nanoparticles.

A quantitative TEM study from U. Shaheen (unpublished data) was comparing 10 nm nanoparticles coated with 10 % CALNN-HA2 with either 90 % CALNN as a matrix or with 70 % CALNN and 20 % CALNN-PEG as matrix peptides. The later coating is similar to the one used above in Sect. 4.1.2.2, but a different size of nanoparticles was used. The results seem to show that more nanoparticles are found in the endosomes when CALNN-PEG is present in the monolayer, but at the same time that the nanoparticles are surprisingly more aggregated. Additionally, the nanoparticles bearing CALNN-PEG peptides are found to interact less with the membrane, which is expected. The nanoparticle aggregation and the probably subsequent absence of membrane interaction observed by TEM are consistent with what was observed by photothermal microscopy.

4.1.2.4 Summary

The addition of HA2 and Tat peptides in the nanoparticle monolayer has been displaying some interesting features on the uptake of the nanoparticles. The cell penetrating effect of Tat could be witnessed, but surprisingly HA2 did also improve the uptake of the nanoparticles to which it was functionalised. However, the prospect of a cytosolic localisation of the nanoparticles bearing the HA2 sequence in their self-assembled monolayer did not materialise. This fact was unexpected, but could be explained by the low degree of interaction that the nanoparticles must experience with the endosomes membrane, owing to property of reducing the non-specific interactions that poly-ethylene glycol possesses. It is not clear, with the present data, what the potential of these monolayer functionalisations is, but the addition of Tat to the monolayer has significantly increased the uptake of particles that possessed low non-specific interaction properties due to the presence of PEG terminated peptides in the monolayer. A TEM study could help getting some information on the behaviour of nanoparticles functionalised with Tat and HA2. Knowing how they interact together inside endosomes or with the membrane of the endosomes could help a better design of the monolayer composition and maybe improve the chances of HA2 to

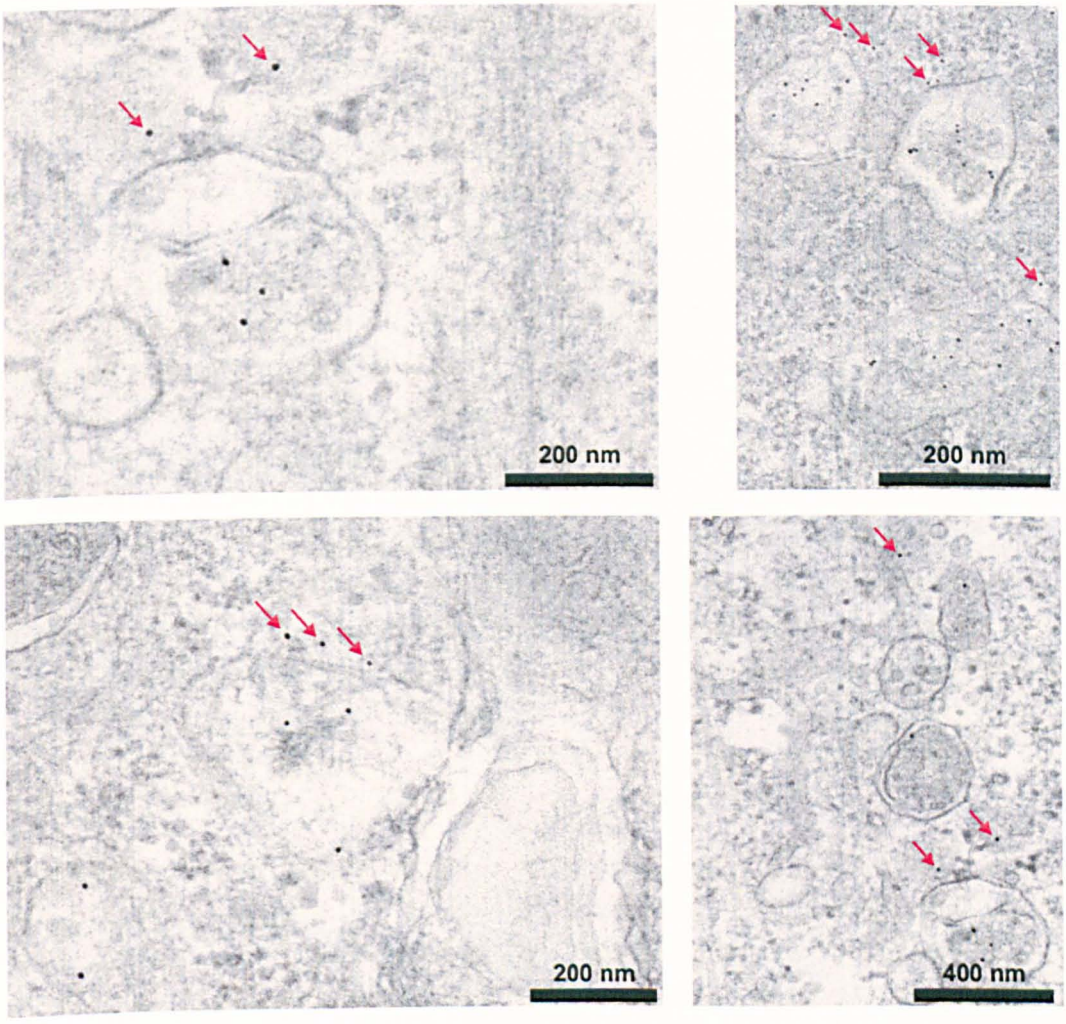

Fig. 4.13 – Gold nanoparticles functionalised with a peptide monolayer comprising 10 % CCALNN-HA2 can escape endosomes. HeLa cells were incubated for 3h with 10 nm gold nanoparticles coated with a 90 % CCALNN — 10 % CCALNN-HA2 mixed-peptide monolayer (6 nM final concentration), fixed, prepared for and imaged by TEM. The images show that some particles have escaped the endosomal compartments (red arrows).

perform its membrane disruption capabilities. Alternatively, chloroquine could be used in conjunction with nanoparticles functionalised with Tat and PEG terminated peptides to investigate whether nanoparticles with reduced non-specific interaction properties could be released away from broken endosomes instead of staying in their vicinity and display an evenly distributed localisation in the cytoplasm.

4.2 Toxin assisted internalisation

Streptolysin O is a bacterial toxin originating from the group A streptococci, which after insertion in cholesterol containing membrane forms some transient pores, which can be used as delivery channels. Spiller *et al.* used SLO in what they qualified as a

"biochemical microinjection" in anti-sense oligonucleotide delivery[27] improving by a 100-fold the delivery of oligodeoxynucleotides in KY01 myelogenous leukaemia cells in comparison to incubation in absence of SLO. The unspecific delivery of protein was also accomplished by streptolysin O treatment in rat basophile leukaemia cells, with proteins that were further demonstrated to be fully functional in the cytoplasm.[28] Similarly, isotopically labelled proteins were introduced in live 293-F embryonal human kidney cells using a SLO pore-formation mediated entry in order to observe the NMR signal of proteins that did not need any further modification of their sequence than the isotope labelling.[29] Recently, Brito *et al.* have used SLO to transfect siRNAs in human myeloma cells line and subsequently knockdown the expression of a targeted gene.[30]

The pores created by the toxin streptolysin O on cell membranes have been successfully utilised to introduce oligonucleotides[27], proteins[28] or siRNAs[30] in mammalian cells in the last fifteen years, but this strategy has not been applied yet to introduce nanoparticles inside cells. The uptake of gold nanoparticles was therefore investigated using this approach with a view to provide nanoparticles with a different entry route targeting the cell cytoplasm.

4.2.1 Streptolysin O pore-forming bacterial toxin

Streptolysin O is a bacterial protein toxin coming from the β-hemolytic group A streptococci, composed of 571 amino acids in its native form and 541 amino acids in its secreted form[31] arranged in a single polypeptide chain. Once activated by thiols or other reducing agents[32] it is forming pores in cholesterol containing cell membranes. The SLO monomers bind to cholesterol in the cell membrane through their hydrophobic C-terminal end, possibly subsequently associating into dimers[33]. Further monomers are assembling together resulting in the complexes forming arcs and later for some of them rings.The binding of the monomers is a temperature-independent process unlike the pore forming step which was proposed to require a conformational change of the oligomers during the ring formation with one of the SLO domain inserting in the membrane, increasing the ring width and subsequently creating the pore, although the precise mechanism has not been demonstrated.[34] Sekiya *et al.* have studied the pore formation on blood cells membranes by TEM and have identified the closed pores forming rings to have internal and external diameters of $\sim$24 and 34 nm, respectively.[35] Bhakdi *et al.* found a similar inner diameter for ring-shaped pores (26 nm). They also observed that most of the SLO complexes were forming semicircular unclosed arcs with 13–16 nm internal radii of curvature[36] and also rarely closed non-circularly shaped assemblies with a maximum one-direction dimension of $\sim$65 nm.

The size of the molecules able to enter the pores could be estimated by the entry FITC-labelled molecules of several size in cells. Fawcett *et al.* observed that 11,

38 and 148 kDa FITC-conjugated dextran and 67 kDa FITC-labelled bovin serum albumin complexes were present in the cytosol of SLO treated rat myocytes,[37] and Walev *et al.* found a cut-off of ~ 150 kDa after incubating THP-1 human leukemia blood cells with FITC-dextran (4,80, 150, 260, 500 kDa) in presence of SLO.[28]

The pore formation is a reversible process and the permeabilisation can be stopped and reversed by adding serum[38] or Ca^{2+}.[28] The resealing process in rat basophile leukemia cell was initiated by the presence of Ca^{2+} and could be considered as temperature-independent, since it occurred efficiently at 4 °C.[28] The membrane repair is only partially understood at the moment though and a global understanding of its mechanism is difficult to be made since contradictory reports exist on the different processes that may be involved. A study undergone by Idone *et al.* suggested that endocytosis is involved in the repair process of the plasma membrane of rat kidney cells and that the process can happen as quick as in a few minutes.[39] Walev *et al.* reported that the repair mechanism involve shedding SLO off the membrane, although this process cannot account alone for the resealing as over 50 % of SLO monomers were still membrane bound.[40]

Babiychuk *et al.* studied the Ca^{2+}-mediated repair of the membrane of human embryonic kidney HEK293 cells and showed that the intracellular Ca^{2+} concentration is linked to the ability of the cells to repair their membrane.[41] The intracellular localisation (membrane/cytoplasm) of a combination of transiently expressed annexin A1 and A6 (respectively labelled with YFP and CFP) provided a measure of the range of intracellular Ca^{2+} concentration $[Ca^{2+}]_i$, which allowed to find a critical value of 10 μM above which the cells could not efficiently proceed to the repair and led to cells death. Below this threshold the cell repair mechanism was accompanied by $[Ca^{2+}]_i$ oscillations and shedding of annexin A1 containing microparticles from the cells. Notably, no endocytosis or exocytosis involving the intracellular membrane could be observed, but this could be related to a inability of annexins to interact with phosphatidylserine poor membranes.

However, the exocytosis of ~ 10 % of the lysosomes present in SLO treated NHK cells was observed after addition of Ca^{2+} by Rodriguez *et al.*[42] and McNeil *et al.*[43] reported the co-localisation of fluorescently labelled lysosomes and cell membrane after addition of Ca^{2+}, which suggests that exocytosis might be involved in the repair process, although it is unknown to what extend.

Yet those contradictions could be the result of the heterogeneous shapes of arcs and rings of SLO oligomers observed at the surface of the membrane, with some functional pores and some non-functional oligomers aggregates (arcs with membrane still present). Those different objects could be dealt with differently by the cells and necessitate several distinct processes working jointly to produce an effective membrane repair process.

4.2.2 Nanoparticles/streptolysin O co-incubation *modus operandi*

Given the uncertainty on the exact size of nanoparticles that would be effectively internalised by the cells through the pores, the decision was made to keep it as low as possible. A diameter of 5 nm was thus chosen for the gold nanoparticles throughout the study of SLO mediated entry of nanoparticles in mammalian cells, as their observation would be possible using both TEM and photothermal microscopy.

The cells were first incubated for 10 minutes (37 °C) in suspension in serum-free MEM with gold nanoparticles (5 nm diameter) and SLO at the appropriate concentrations to promote a pore mediated uptake of the nanoparticles. The medium needed to be serum-free at that particular step of the incubation as serum inactivates the pore formation by streptolysin O. The nanoparticles incubation concentration was adapted depending on the type of peptide mixture used for the self-assembled monolayer to allow the uptake of a detectable amount of nanoparticles in the conditions where the nanoparticles were incubated in absence of SLO. A higher concentration was for instance necessary when nanoparticles coated with a monolayer comprising poly-ethylene glycol molecules were used, as PEG reduces the non-specific interactions and therefore the uptake of the nanoparticles (Sect. 3.3.2). The SLO concentration was chosen after a concentration optimisation procedure (see Sect. B.2.6.2 for details) that allowed the permeabilisation of a minimum of 50 % of the cells while keeping a low level of cytotoxicity. The optimisation is required to be repeated regularly as the activity of the toxin is decreasing over time and needs to be performed each time an experimental condition is modified, such as a change of type of medium, cell line, temperature or resealing duration.

In the second step of the protocol serum-containing medium was added to the cells to inactivate the toxin and stop the formation of pores in the cell membrane, and the cells were left to reseal for another 20 minutes at 37 °C. The nanoparticles were then discarded by removing the medium (centrifugation) to avoid any further endocytosis mediated uptake of the nanoparticles. At that time the cells were seeded on an Iwaki glass dish in serum-containing medium, where they were left to attach to the dish for 4 hours, before fixation and imaging by photothermal microscopy. The duration of the later incubation period (4 h) was driven by the necessity of the attachment of the cells to the glass dish following their incubation in suspension, to allow their subsequent fixation and imaging. This process was found to take a minimum of four hours.

4.2.3 Streptolysin O effect on the quantity of nanoparticle uptake

HeLa cells were incubated in suspension with 5 nm diameter gold nanoparticles (100 nM) coated with the matrix peptide CALNN in presence (or absence) of the membrane pore forming toxin streptolysin O in serum-free medium for 10 min at 37 °C. The cells were incubated another 20 min in serum-containing medium for cell

resealing, as serum deactivate the toxin, before the medium was changed for nanoparticles removal (see Sect. B.2.6.2 for incubation protocol details). The cells were then left to adhere on an Iwaki dish for 4 h in serum-containing medium, before fixation and photothermal imaging.[f]

A representative photothermal image of the uptake of the nanoparticles is shown in Fig. 4.14A and B, for the cells incubated respectively in absence or in presence of streptolysin O. A visual impression arises when observing those images that the uptake in the presence of streptolysin O is slightly more important than without. However, this impression was not proved to be true. A quantification of the internalisation was done by analysing single cells mean photothermal intensities, to obtain a mean value of the nanoparticles uptake per cell (see Sect. B.2.9.4 for method details). The outcome of the quantification is that the uptake was similar in the two samples (+/- SLO). The streptolysin O treated cells have photothermal intensities that seem individually more evenly distributed within the different fields of view, but the average of the mean cell intensities is below the one of non-streptolysin O-treated cells. The reason of this later statistical characteristic lies in the presence of a few cells with higher mean uptake in absence of streptolysin O. Indeed, in those cells the presence of aggregates that were taken up or that were stuck at the surface of those cells (Fig. 4.14A) is increasing a mean photothermal intensity that would otherwise be rather low. Nevertheless, even if the uptake in presence of streptolysin O appears to be slightly lower, the difference of the photothermal intensity means of the two conditions (+/- SLO) was not found to be significant (ANOVA one-way test). An average processed after removal of the outliers in both photothermal intensity populations (+/- SLO) of the analysed cells showed that the two means were even more markedly close. The higher/lower order was changing depending on the definition used for the outliers, but most importantly the difference between the two means was quite logically again not found to be significant.

The streptolysin O treatment in the case of nanoparticles functionalised with the matrix peptide CALNN alone can therefore be considered as void with respect to the nanoparticle uptake quantity, and the uptake probably dominated by endocytosis. This could be due to the natural high interaction of CALNN-coated nanoparticles with the cell membrane which would see the endocytosis prevail over a pore forming mediated uptake in term of quantity of uptake.

In order to test that hypothesis HeLa cells were incubated in the same conditions as previously, with nanoparticles coated with the addition of either 10 % or 20 % of CCALNN-PEG peptides in their monolayer, to reduce the non-specific interactions of the nanoparticles with the cell membrane and try to promote the pore mediated entry over endocytosis. The concentration had though to be changed as addition of CCALNN-PEG in the monolayer is reducing the uptake quite dramatically, es-

[f] nanoparticle preparation, SLO optimisation, cell work and SLO treatment: U. Shaheen

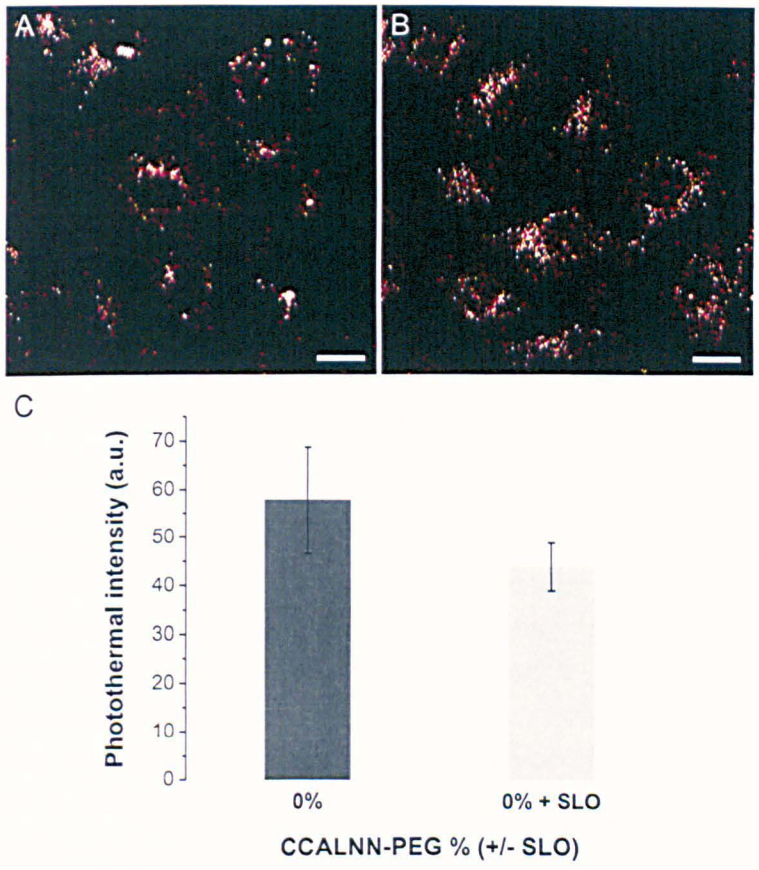

Fig. 4.14 – Influence of streptolysin O on the internalisation of CALNN peptides coated nanoparticles. HeLa cells were incubated in suspension with 5 nm gold nanoparticles (100 nM concentration) coated with the matrix peptide CALNN in presence (or absence) of the membrane pore forming toxin streptolysin O in serum-free medium for 10 min at 37 °C. The cells were incubated another 20 min in serum-containing medium (toxin inactivation) for resealing, before the medium was changed for nanoparticles removal (see Sect. B.2.6.2 for incubation protocol details). The cells were then left to adhere on an Iwaki dish for 4 h in serum-containing medium, before fixation and photothermal imaging. (**A**–**B**) Photothermal images of the cells in absence or presence of streptolysin O: (**A**) cells incubated in absence of SLO; (**B**) cells incubated in presence of SLO. (**C**) Quantification of 50 and 64 single cells mean photothermal intensities for the conditions shown in (A) and (B), respectively. The means were not found to be significantly different (one-way ANOVA test). Error bars represent the SE. Scale bars represent 20 μm.

pecially in the case of 20 % added CCALNN-PEG, as it was shown in Sect. 3.3.2. A nanoparticle concentration value of 600 nM, six times the one used for CALNN coated nanoparticles, was therefore chosen to allow a direct comparison between the two nanoparticle coatings and at the same time to enable the internalisation of an appropriate amount of 20 % CCALNN-PEG coated nanoparticles for them to be subsequently detected.

A representative photothermal image of each condition is shown in Fig. 4.15A–D. For both monolayer types, 10 % CCALNN-PEG — 90 % CALNN and 20 % CCALNN-PEG — 80 % CALNN, an increase of the nanoparticles uptake is visible in the cells incubated in presence of streptolysin O (as compared to incubation without toxin). The mean amount of nanoparticle uptake per cell of the four conditions was appraised by the analysis of ~ 50 single cells mean photothermal intensities in each condition (method details in Sect. B.2.9.4). The quantification (Fig. 4.15E) confirms a large increase of the cells uptake for the nanoparticles bearing 10 % of CCALNN-PEG in their monolayer in presence of streptolysin O during the incubation as compared to the absence of SLO. A more moderate increase is observed in the case of nanoparticles comprising 20 % of CCALNN-PEG in their monolayer. For both sets of nanoparticles containing CCALNN-PEG in their monolayer a significant difference ($p<0.01$) between the presence and absence of streptolysin O during the incubation was found by ANOVA tests and follow up Holm-Bonferroni tests processed on the photothermal intensities populations (+/- SLO) of each type of monolayer. It confirms statistically that streptolysin O increases the uptake of nanoparticles that have a limited interaction with the cell membrane (10 % or 20 % CCALNN-PEG), although the mechanism for this entry cannot be inferred from those first evidences.

4.2.4 Intracellular nanoparticle distribution after Streptolysin O mediated uptake

The images shown in Fig. 4.14A–B and Fig. 4.15A–D do provide a good estimation of the quantity of nanoparticles taken up by the cells in the different conditions (0 %, 10 %, 20 % CCALNN-PEG monolayer content ± SLO), but a better resolution is necessary to allow a deeper investigation on the intracellular distribution of the nanoparticles. A series of photothermal images with a pixel size twice smaller as before (310 nm here, 620 nm in the previous section) was therefore acquired on the same samples as the ones used for the nanoparticles uptake quantification (Sect. 4.2.3). Two images of each condition are shown in Fig. 4.16–4.18, for cells incubated in presence or absence of streptolysin O and co-incubated with nanoparticles composed of the matrix peptide CALNN and the addition of 0 % (Fig. 4.16), 10 % (Fig. 4.17) or 20 % (Fig. 4.18) of CCALNN-PEG peptides. The same image contrast was chosen for all the images in the three figures in order to allow a side by side comparison of

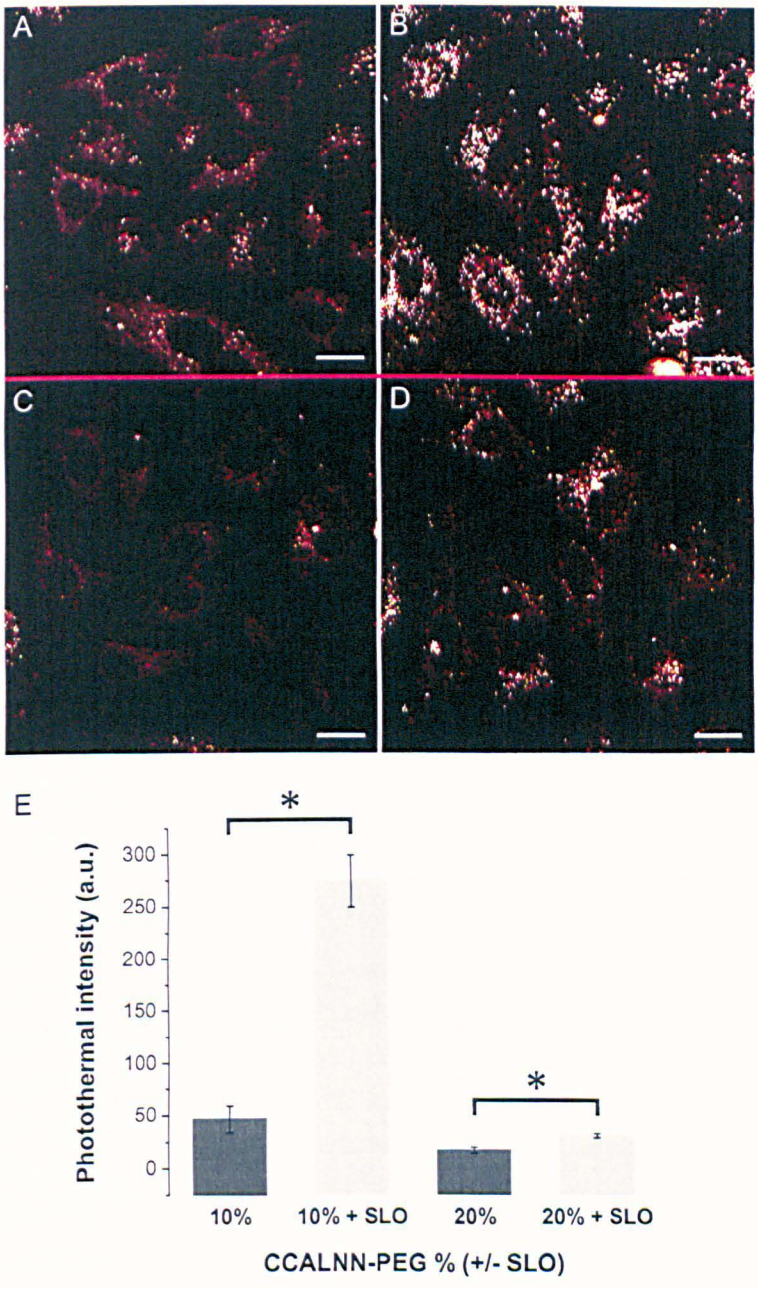

Fig. 4.15 – Streptolysin O induced increase of CCALNN-PEG functionalised gold nanoparticles uptake. HeLa cells were incubated in suspension with 5 nm gold nanoparticles (600 nM concentration) coated with the matrix peptide CALNN and 10 % or 20 % of CCALNN-PEG peptides in presence (or absence) of the membrane pore forming toxin streptolysin O (SLO) in serum-free medium for 10 min at 37 °C. The cells were incubated another 20 min in serum-containing medium (toxin inactivation) for resealing, before the medium was changed for nanoparticles removal. The cells were left to adhere on an Iwaki dish for 4 h in serum-containing medium, before fixation and imaging. (**A–B**) Photothermal images of cells incubated with nanoparticles containing 10 % CCALNN-PEG in their monolayer, in absence or presence of SLO. (**C–D**) Photothermal images of cells incubated with nanoparticles containing 20 % CCALNN-PEG in their monolayer, in absence or presence of SLO. (**A, C**) Cells incubated in absence of SLO. (**B, D**) Cells incubated in presence of SLO. (**E**) Quantification of ~50 single cells mean photothermal intensities for the conditions shown in (A–D). * indicate a statistically significant difference ($p<0.01$, one-way ANOVA and Holm-Bonferroni tests). Error bars represent the SE. Scale bars represent 20 μm.

the different conditions.

4.2.4.1 SLO influence on the nanoparticle uptake

The cells that were incubated with nanoparticles in presence of SLO display more numerous endosomes than the cells that were incubated without SLO. Additionally higher photothermal intensities are observed in the endosomes in presence of SLO, pointing towards a bigger number of nanoparticle per endosome in presence of SLO during the incubation. The endosomes are also more evenly spread across the cells in presence of SLO, when their location seems more sporadic without SLO.

Three types of nanoparticles were tested, each of them coated with CALNN peptides and the addition of varying CCALNN-PEG peptides proportions (0 %, 10 %, 20 %) to assess the influence of the degree of interaction with the cell membrane during the internalisation. The observations made are valid for the three nanoparticles type and show that SLO affects the quantity of nanoparticles uptake through the number of endosomes. However, no significant cytosolic presence of nanoparticles was observed in either samples in the conditions used for the experiments, leaving as an open question the mechanism by which SLO influences the nanoparticle uptake.

4.2.4.2 Monolayer CCALNN-PEG content influence on SLO mediated uptake

The quantity of nanoparticles taken up by the cells was shown to be increased by the co-incubation with streptolysin O for nanoparticles bearing either 10 % or 20 % of CCALNN-PEG in their monolayer. Introducing PEG molecules at the surface of the nanoparticles changed the interactions between the nanoparticle and cell membrane surfaces and allowed streptolysin O to influence the quantity of nanoparticle uptake, which did not happen without the addition of PEG to reduce the non-specific interactions.

A comparison of the photothermal images of cells incubated in presence of SLO and nanoparticles coated with a peptide monolayer bearing either 10 % (Fig. 4.17C–D) or 20 % (Fig. 4.18C–D) of CCALNN-PEG peptides with the same nanoparticles concentration (600 nM) shows that the endosomes have a higher nanoparticle density with a smaller proportion of PEG molecules at the surface of the nanoparticles. This demonstrate that the interaction of the nanoparticles and the cell membrane plays an important role during the internalisation, but again cannot give more insight on the role that SLO plays in it. Indeed, the increased internalisation observed with an increased nanoparticle-cell surfaces interaction (10 % CCALNN-PEG) could either be provoked by a more favoured endocytosis or a stronger interaction of the nanoparticles with the pore created by SLO. More endosomes also seem to be present in the cells incubated with 10 % CCALNN-PEG as compared to the ones incubated with 20 % CCALNN-PEG, although a definite statement on this matter is difficult

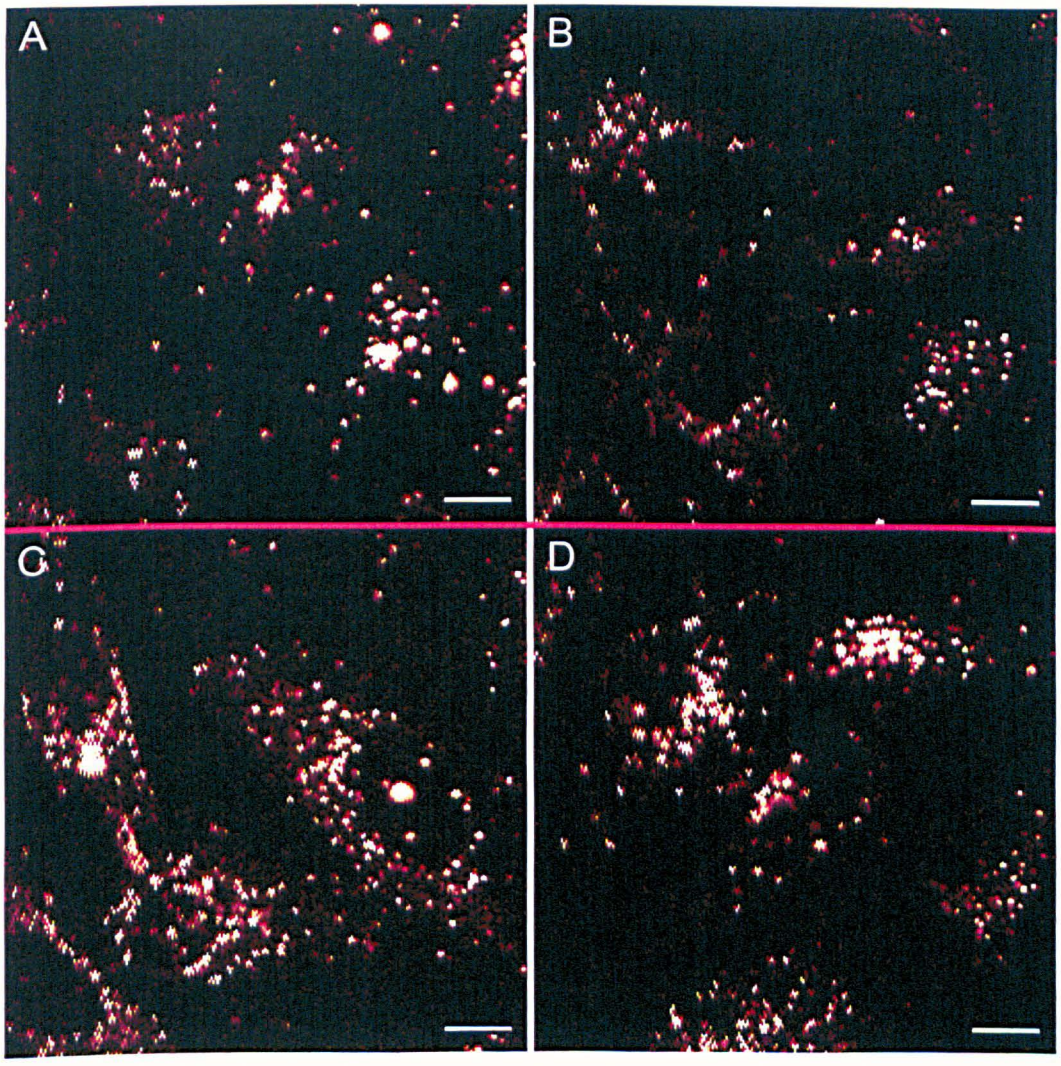

Fig. 4.16 – Intracellular distribution of CALNN coated gold nanoparticles after streptolysin O co-incubation. HeLa cells were incubated with gold nanoparticles (5 nm diameter, 100 nM concentration) coated with the matrix peptide CALNN in absence or in presence of the membrane pore forming toxin streptolysin O (SLO), as explained previously in Sect. 4.2.2, fixed and imaged by photothermal microscopy. Images of the same samples as in Fig. 4.14 were acquired with a twice finer resolution, to allow an enhanced visualisation of the intracellular nanoparticle distribution. (**A**–**D**) Photothermal images showing the nanoparticles distribution inside cells after co-incubation with or without SLO: (**A**–**B**) incubation in absence of SLO; (**C**–**D**) incubation in presence of SLO. Scale bars represent 10 μm.

to give as the presence of endosomes containing very few nanoparticles could have stayed undetected by the photothermal microscope in the conditions used for the experiments.

It would be useful to integrate some information on the distribution of the endosome sizes and their corresponding photothermal intensities within single cells to confirm the visual impressions, which could happen to be wrong. That kind of investigation would necessitate a throughout image analysis on every single cell consisting in performing a series of image transformations, typically erode and dilate

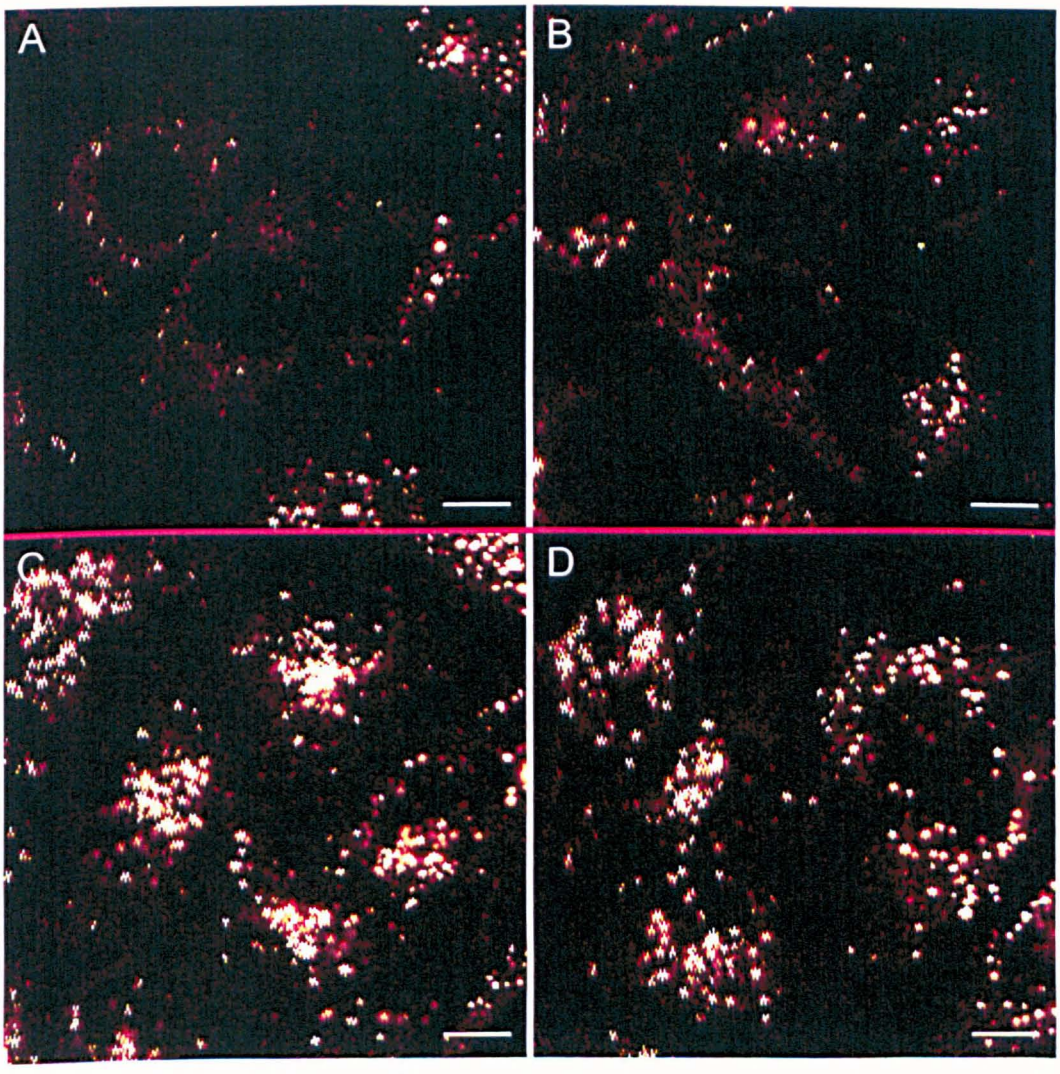

Fig. 4.17 – Intracellular distribution of gold nanoparticles coated with a 10 % CCALNN-PEG — 90 % CALNN monolayer after streptolysin O co-incubation. HeLa cells were incubated with gold nanoparticles (5 nm diameter, 100 nM concentration) coated with the matrix peptide CALNN and an additional 10 % of CCALNN-PEG peptides, in absence or in presence of the membrane pore forming toxin streptolysin O (SLO), as explained previously in Sect. 4.2.2, fixed and imaged by photothermal microscopy. Images of the same samples as in Fig. 4.14 were acquired with a twice finer resolution, to allow an enhanced visualisation of the intracellular nanoparticle distribution. (**A**–**D**) Photothermal images showing the nanoparticles distribution inside cells after co-incubation with or without SLO: (**A**–**B**) incubation in absence of SLO; (**C**–**D**) incubation in presence of SLO. Scale bars represent 10 μm.

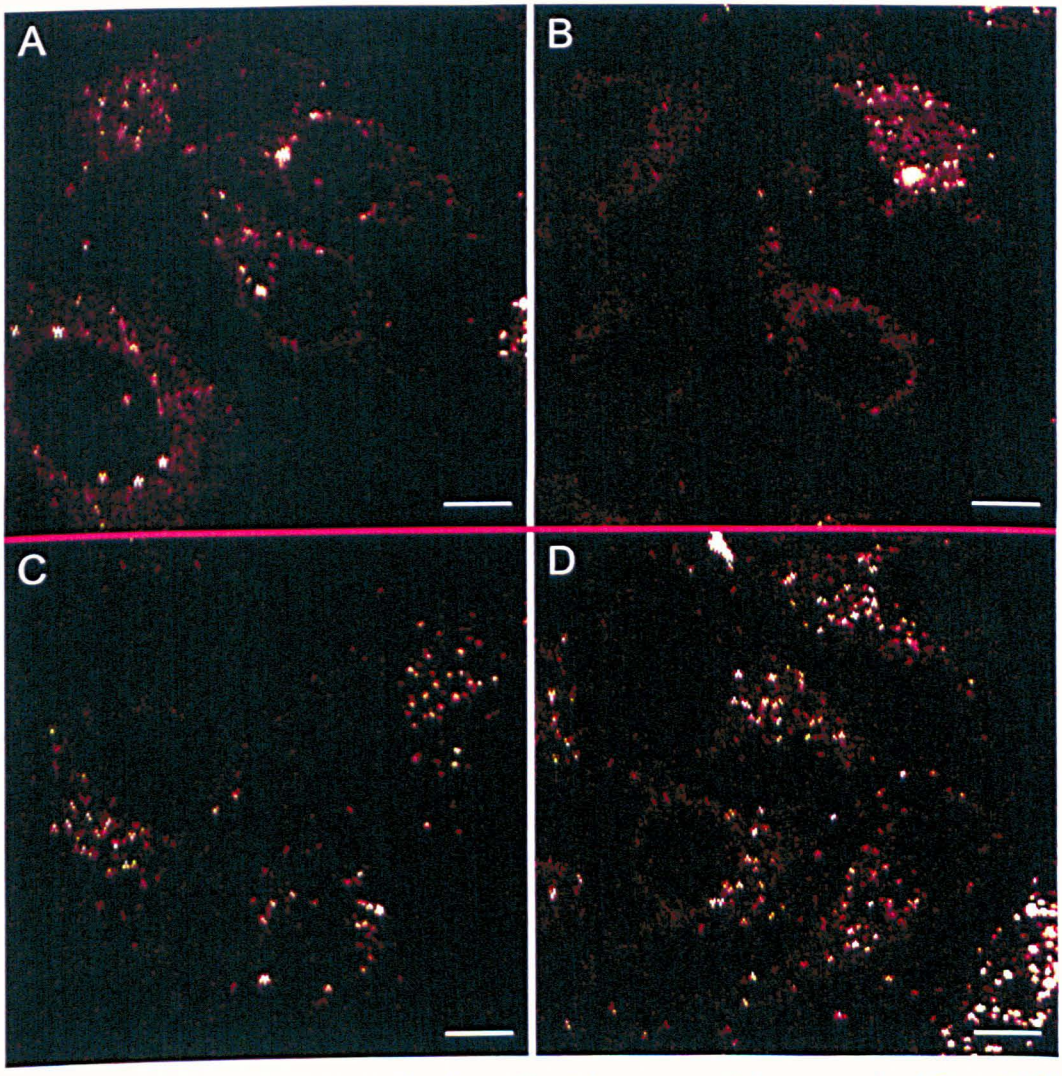

Fig. 4.18 – Intracellular distribution of gold nanoparticles coated with a 20 % CCALNN-PEG — 80 % CALNN monolayer after streptolysin O co-incubation. HeLa cells were incubated with gold nanoparticles (5 nm diameter, 100 nM concentration) coated with the matrix peptide CALNN and an additional 20 % of CCALNN-PEG peptides, in absence or in presence of the membrane pore forming toxin streptolysin O (SLO), as explained previously in Sect. 4.2.2, fixed and imaged by photothermal microscopy. Images of the same samples as in Fig. 4.14 were acquired with a twice finer resolution, to allow an enhanced visualisation of the intracellular nanoparticle distribution. (**A–D**) Photothermal images showing the nanoparticles distribution inside cells after co-incubation with or without SLO: (**A–B**) incubation in absence of SLO; (**C–D**) incubation in presence of SLO. Scale bars represent 10 μm.

processes, to allow a subsequent automatic recognition of the highlighted objects based on their aspect ratio (close to the one of a disk). Unfortunately, a series of new images would need to be acquired in order to perform such image analysis. Indeed, in the current images a misalignment between even and odd lines can be observed, especially on the left of the images. While going from the left to the right of the images, these defects progressively disappear along the image scan. This originated from a hardware related software based synchronisation problem during the image scan which was unsolved at the time when the images were acquired and has been fixed since then.

4.2.5 Cell mean nanoparticle quantity distribution

In a given condition, the nanoparticle uptake is varying from cell to cell, but a mean value can characterise the quantity of uptake of the cell population (Sect. 4.2.3). The populations of cells incubated with the three different monolayer composition (100 % CALNN, 10 % CCALNN-PEG — 90 % CALNN, 20 % CCALNN-PEG — 80 % CALNN) in presence or in absence or SLO will be examined through the distribution of the cells mean photothermal intensities, to appraise the effect that streptolysin O had on the nanoparticle uptake on the whole population.

Figure 4.19 show the distribution of mean photothermal intensities measured for the cells in the six different conditions. The distributions are similar in the populations that were incubated in absence of streptolysin O for the three types of nanoparticle monolayer, with a large number of cell exhibiting a low nanoparticle loading. The distributions of cell mean nanoparticle content change significantly when the cells were incubated with SLO, becoming broader and having some similarities to the characteristic bell-shaped normal distribution. This observation is valid for the three types of monolayer, but a particular emphasis should be made on the distribution of cells incubated with nanoparticles coated with a monolayer comprising 10 % of CCALNN-PEG peptides. This cell population was shown to display the largest increase of nanoparticle uptake while compared to cells incubated with the same nanoparticle type but without SLO, and shows here to have cell mean photothermal intensities well spread between the minimum and maximum intensities with a shape looking like a normal distribution.

In order to assess whether the populations of cells incubated in presence of SLO can statistically be considered as normally distributed or not, a series of statistical tests was conducted on the six cell populations (0 %, 10 %, 20 % CCALNN-PEG ± SLO). The Kolmogorov-Smirnov normality test showed that the three populations of cells incubated in presence of SLO are a normally distributed at the 0.05 level (Tab. 4.3), when the populations of cell incubated in absence of SLO are not normally distributed. However, the more powerful Lilliefors test only detected the cells co-incubated with 10 % CCALNN-PEG coated nanoparticles and SLO to have

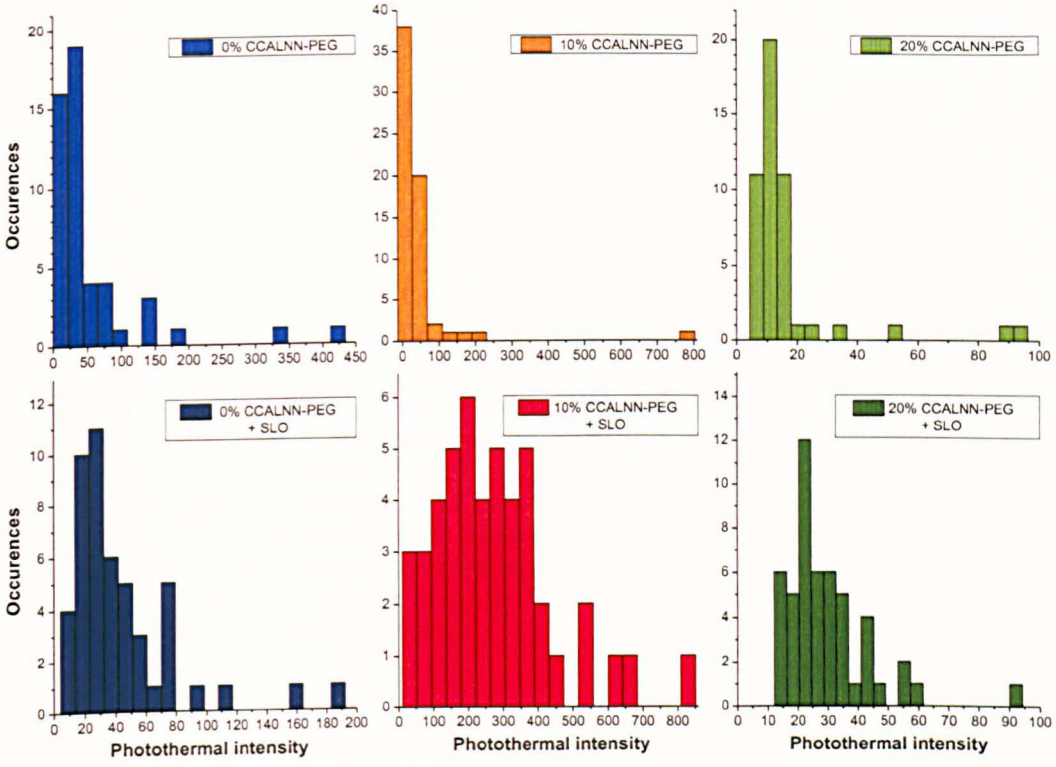

Fig. 4.19 – Distribution of the cells mean gold nanoparticles content after incubation with nanoparticles in presence or absence of streptolysin O. Nanoparticles coated with a peptide monolayer composed of either 100 % CALNN or 10 % CCALNN-PEG — 90 % CALNN or 20 % CCALNN-PEG — 80 % CALNN were used to study the influence of the membrane pore-forming toxin SLO on their uptake in HeLa cells. The photothermal intensities of individual cells used to produce a mean nanoparticle uptake per cell for each of the aforementioned monolayer type in presence and in absence of SLO during the incubation of the nanoparticles with cells (Fig. 4.14C and Fig. 4.15E) were used to build histograms representing the distribution of nanoparticle uptake of the different cell populations. From left to right: 100 % CALNN, 10 % CCALNN-PEG — 90 % CALNN. 20 % CCALNN-PEG — 80 % CALNN. Top: incubation without SLO; bottom: incubation in presence of SLO.

a normally distributed population and the Shapiro-Wilk test (increased power) did not qualify any of the distributions as normal (0.05 level).

To better estimate the meaning of the discrepancies exposed by the different statistical normality tests and provide a graphical tool to judge the degree of normality Q-Q plots can be utilised. For each cell population (incubation with nanoparticle coated with 0 %, 10 %, 20 % CCALNN-PEG; ± SLO), the quantiles of the cells mean photothermal intensities population are plotted against the quantiles of a normal distribution with the same mean and standard deviation as the cell population to allow for a comparison. A given cell mean nanoparticle content population would be well described by a normal distribution if the circles in Fig. 4.20 are aligned to the red line. The cells incubated without SLO display cell mean photothermal intensity distributions very distant from a normal distribution. In presence of SLO during

Monolayer type	Normality statistical test (± SLO)					
	← *statistical power*					
	Shapiro-Wilk		Lilliefors		K-S	
	− SLO	+ SLO	− SLO	+ SLO	− SLO	+ SLO
0 % CCALNN-PEG	×	×	×	×	×	✓
10 % CCALNN-PEG	×	×	×	✓	×	✓
20 % CCALNN-PEG	×	×	×	×	×	✓

Tab. 4.3 – Normality tests conducted on the cell mean nanoparticle content populations. Kolmogorov-Smirnov (K-S), Lilliefors and Shapiro-Wilk normality tests were undertaken to appraise the similarity of the cell nanoparticle mean content population distribution to a normal distribution and compare the cells populations in the case of a co-incubation of the nanoparticles with or without SLO (± SLO). ✓ indicates a cell population that was found to be drawn from a normally distributed population at the 0.05 level by the test considered (×: opposite conclusion).

the incubation, the cell population have indubitably a tendency to change towards normality. This is especially true for the cells incubated with nanoparticles coated with a 10 % proportion of CCALNN-PEG peptides in their monolayer in presence of SLO, for which the cell mean photothermal intensities are very close to a normal distribution on most of the intensity range.

4.2.6 Discussion

The influence of the non-specific interactions during the internalisation of gold nanoparticles via streptolysin O-induced pore formation was investigated. To change the surface properties of the gold nanoparticles, and the non-specific properties in particular, the composition of the protective self-assembled monolayer was varied. The introduction in the monolayer of different proportions of poly-ethylene glycol — known to reduce the non-specific interactions — through CCALNN-PEG peptides provided a proxy to assess the importance of the nanoparticle-membrane interactions during the streptolysin O facilitated entry of nanoparticle in HeLa cells.

Cells were incubated in presence or in absence of streptolysin O with nanoparticles coated with a monolayer composed of either 100 % CALNN peptides, which allow a natural interaction of the nanoparticles with the cell membrane as their quantitative endocytosis could witness, or 10 % CCALNN-PEG — 90 % CALNN, which provoke a diminished internalisation of the nanoparticles by endocytosis, or finally 20 % CCALNN-PEG — 80 % CALNN, whose ability to further reduce non-specific interactions between the nanoparticles and the membrane further hinders their endocytosis mediated uptake. Photothermal microscopy was employed to es-

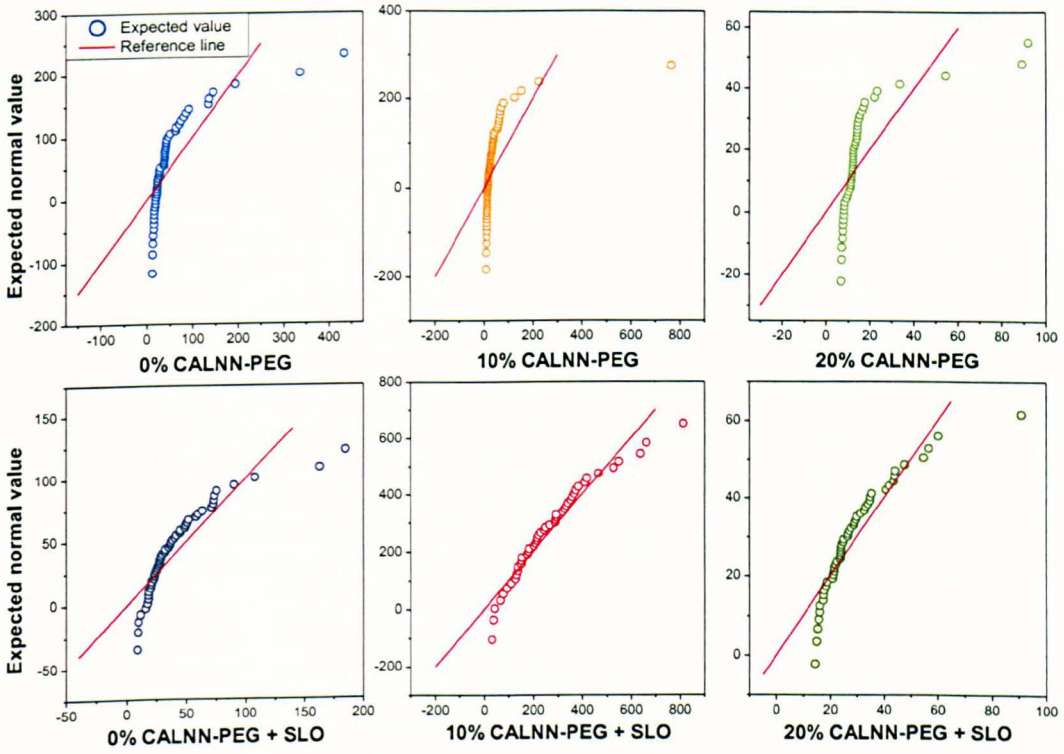

Fig. 4.20 – Q-Q plots comparing the cells mean gold nanoparticle content distribution to a normal distribution. The quantiles of the cells mean nanoparticle content distribution are plotted against the quantiles of a normal distribution with the same mean and standard deviation as the cell population to allow for a comparison. The cells mean nanoparticle content population would be well described by a normal distribution if the circles are aligned to the red line.

timate the nanoparticle uptake of the cells in the different conditions, and a summary of the location of the different representative images is available in Tab. 4.4, together with the monolayer compositions and nanoparticle incubation concentration.

The ratio of the mean uptake per cell after their incubation with 5 nm diameter gold nanoparticles in presence and in absence of streptolysin O provides a comparison of the influence of streptolysin O on the quantity of nanoparticle uptake. This can be evaluated through the ratio of the mean photothermal intensity per cells in the two incubation conditions (+ SLO/− SLO) for three the different nanoparticle monolayer compositions. The variances of the ratios were calculated using the Delta method which consists in using a Taylor series expansion to approximate the variance of the ratio of two variables (populations: − SLO and + SLO), further assuming the independence of the variables. The standard errors were further obtained from the calculated variances.

Figure 4.21 displays the nanoparticle uptake ratios and summarises effectively the impact that streptolysin O had on the uptake in the three different conditions, regardless of the nanoparticle concentration used. The quantity of nanoparticles uptake was shown not to be influenced by the presence of SLO for nanoparticles

Monolayer composition		Nanoparticle concentration (nM)	Corresponding figures (quantification/localisation)	
Matrix peptides				
CALNN	CCALNN-PEG		− SLO	+ SLO
100 %	–	100	4.14 A/4.16 A–B	4.14B/4.16 C–D
90 %	10 %	600	4.15 A/4.17 A–B	4.15B/4.17 C–D
80 %	20 %	600	4.15 C/4.18 A–B	4.15D/4.18 C–D

Tab. 4.4 – Monolayer compositions prepared for the assessment of streptolysin O influence on the uptake of gold nanoparticles. 5 nm diameter gold nanoparticles were prepared with a self-assembled monolayer composed of matrix peptides CALNN and different proportions (0 %, 10 %, 20 %) of CCALNN-PEG peptides. HeLa cells were incubated with those nanoparticles in the presence or absence of SLO (see Sect. B.2.6.2 for incubation details), fixed and imaged by photothermal microscopy. The monolayer compositions and the figures numbers where the corresponding photothermal images can be found are associated.

bearing solely CALNN peptides, which hints that endocytosis was dominating their internalisation. On the contrary, in the presence of non-specific interaction weakening peptides CCALNN-PEG in the nanoparticle monolayer, the uptake in presence of SLO was increased by a six fold with a 10 % proportion and by nearly two fold with 20 %, in comparison to the uptake of the same nanoparticle types without SLO.

If one considers that the nanoparticles are essentially delivered through the pores created by SLO for those types of nanoparticles, then the conclusion that too little interaction between the nanoparticles and the cell membrane is decreasing the efficiency of the uptake arises. Yet a delivery through the pores formed by SLO in the plasma membrane would normally imply a cytosolic delivery of the nanoparticles, but this was not observed by photothermal microscopy. However, the conditions in which the images were acquired did not allow the detection of single sparse nanoparticles that would be dispersed in the cytosol.

Despite that, if a significant number of nanoparticles was readily entering the cells through the pores formed by the toxin streptolysin O and stayed in the cytoplasm, the nanoparticles would be in a much closer proximity to one another, which would allow their detection and display an evenly distributed photothermal signal in the cytosol, which has not been monitored. None of the photothermal images of the cells incubated with SLO acquired in this study allow to demonstrate that a significant amount of nanoparticles has reached the cytosol.

Nevertheless, a comprehensive TEM study of the internalisation of CALNN/CCALNN-PEG coated nanoparticles in presence of streptolysin O proceeded by U. Shaheen (unpublished data) in conjunction with the present one showed a few na-

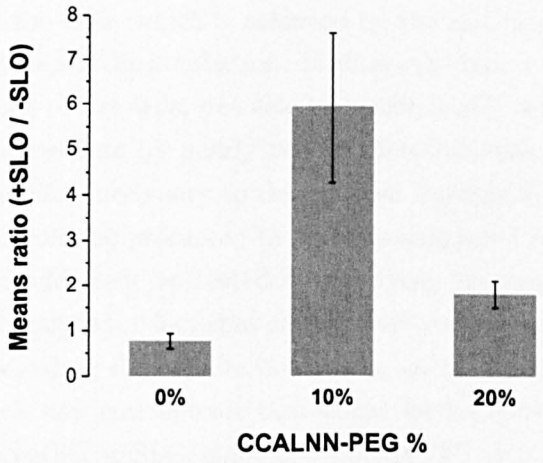

Fig. 4.21 – Influence of monolayer non-specific interactions on streptolysin O facilitated entry of gold nanoparticles. Nanoparticles coated with a peptide monolayer composed of either 100 % CALNN, 10 % CCALNN-PEG — 90 % CALNN or 20 % CCALNN-PEG — 80 % CALNN were used to study the influence of the membrane pore-forming toxin SLO on their uptake in HeLa cells. The mean photothermal intensity of the cells was used to estimate the mean quantity of nanoparticle internalised per cell with the three types of monolayer with decreasing non-specific interactions with the cell membrane (0 %, 10 %, 20 % CCALNN-PEG) in presence or in absence of streptolysin O. The ratio of the mean nanoparticle uptake per cell with and without co-incubation with SLO is plot for the three monolayer types studied. Error bars represent the SE.

noparticles located in the cytosol. It represented $\sim 1\,\%$ of the observations[g] in cells incubated with 10 % CCALNN-PEG coated nanoparticles, when it was possible to discriminate $\sim 13\,\%$ of them[h] in cells incubated with 20 % CCALNN-PEG coated nanoparticles. However, a comparison with nanoparticles incubated in absence of SLO would be needed to confirm that the cytosolic localisation is indeed due a toxin pore forming induced entry of the nanoparticles.

To explain the enhanced nanoparticle uptake provoked by their incubation with the pore forming toxin SLO and at the same time justify the presence of numerous endosomes and the absence of a significant proportion of nanoparticles in the cytosol some processes encouraging the nanoparticle entrapment in endosomes must be promoted by SLO. The following three not mutually exclusive hypotheses are proposed to explain the observed endosome captured nanoparticles:

1. NPs are trapped in endosomes during the SLO/NPs co-incubation:
   a) streptolysin O monomers or oligomers binding to the membrane is triggering an increased endocytosis
   b) an increased endocytosis is induced by the membrane repair mechanism
2. NPs are recycled from the cytosol into endosomes after a pore entry

[g] 9 cytosolic nanoparticles out of 809, statistics performed on 7 cells
[h] 13 cytosolic nanoparticles out of 103, statistics performed on 5 cells

The resealing of the cells, which is achieved by the addition of serum-containing medium, is a pivotal step of the incubation. It allows the inactivation of the toxin and the subsequent sealing of the cells, but also to mechanically reduce the nanoparticle concentration in the medium by nearly two third by the volume added. However, during the twenty minutes necessary to this process nanoparticles endocytosis is not prevented and could even be promoted by SLO as suggested by Idone *et al.*[39]

Hypotheses 1b could then be tested by changing the temperature during the resealing process. Owing to the fact that endocytosis is an energy dependent process, proceeding to the resealing step of the incubation at 4 °C (and 37 °C as a control) would allow to block any endocytosis that could be happening during that time period and verify whether a SLO enhanced uptake (10 and 20 % CCALNN-PEG conditions) is still fired or not and if the endosomes would be consequently less importantly represented.

However, the first two hypotheses fail to explain on their own the absence of effect of SLO on the quantity of nanoparticle uptake when PEG is not present in the monolayer. Indeed, nanoparticles coated solely with CALNN peptides are interacting more with the cell membrane than the ones bearing some additional CCALNN-PEG peptides, but their uptake is not promoted quantitatively by SLO.

Hypotheses 1a and 1b would therefore additionally require an interaction between SLO and PEG to take place or SLO to promote an interaction of the PEG coated nanoparticles with the cell membrane — which is very unlikely — to explain their increased uptake by endocytosis. At the same time this interaction would need to be hindered when the amount of CCALNN-PEG peptides in the monolayer is increased, as 10 % CCALNN-PEG coated nanoparticles displayed a stronger increase of their uptake in presence of SLO than the 20 % CCALNN-PEG coated ones. Taken together those evidences make hypothesis 2 a more suitable process candidate.

In order to determine if the nanoparticle endosomal loading is happening after the resealing process, the observation of the cells by photothermal microscopy should be proceeded to at an earlier time, ideally directly after the nanoparticle removal. This could be achieved by adapting the incubation protocol to allow an earlier fixation of the cells, just after the resealing step.

This is not a trivial modification of the protocol though, as it would require to proceed to the nanoparticle incubation on cells that would already be attached on the glass dish. The conformation of the cells is different when they are attached to a glass dish. They possess a wider surface area exposed to the incubation medium, as they stretch them-selves while stuck to the glass slide. This may induce more endosomal uptake, especially if endocytosis is the dominant process responsible for the SLO facilitated internalisation of the nanoparticles, and the reorganisation of the extracellular matrix components may also change the way the nanoparticles and cells surfaces interact with each others. The cell surface conformation changes may

therefore alter the processes by which SLO influence the internalisation of the nanoparticles, should it have a significant influence on grafted cells, and consequently disallow a comparison between the processes on adhering and non-adhering cells.

In conclusion, should SLO prove to be able to provide a route towards the cytosolic delivery of gold nanoparticles or not is still an open question, and the dynamics of nanoparticle entry which would be imaged by live photothermal microscopy could be giving new insights into the entry mechanisms.

4.3 Conclusion

Different strategies of facilitated entry of gold nanoparticles in mammalian cells owing to avoid endosomal entrapment or to disrupt them have been investigated in this chapter. First, the drug chloroquine has been utilised in combination with the cathepsin L protease inhibitor Z-FF-fmk to enhance the protection of the nanoparticles against proteolytic monolayer degradation. Chloroquine also helped breaking the endosomes by which the nanoparticles were internalised in the cells. However, the nanoparticles were observed to be staying in the vicinity of the broken endosomes, interacting with pieces of endosome membranes and globally not displaying the characteristics of dispersed cytosolic nanoparticles.

In a second phase, a combination of the cell-penetrating Tat terminated peptides and endosome disrupting HA2 terminated peptides were used to functionalise gold nanoparticles. The resulting compounds showed an increased uptake due the effect of Tat and surprisingly also HA2, but not a combined effect of both. Markedly, the nanoparticles were not observed to have significantly escaped the endosomes despite the capacity of HA2 to disrupt membranes, probably because of a lack of interaction with the endosome membrane preventing HA2 to act to break the membrane.

Finally, the membrane pore forming toxin streptolysin O was employed during the incubation of the nanoparticles to try to promote their cytosolic entry. This could not be witnessed, although the process did actually increase the quantity of uptake of particles when a proportion of poly-ethylene glycol terminated peptides was added to the monolayer. This was particularly significant when a proportion of 10 % of CCALNN-PEG peptides was introduced in the monolayer and slightly less important with further PEG containing peptides, but it was absent with nanoparticles possessing a stronger interaction with the cell membrane. The nanoparticles were shown by photothermal microscopy to be located in endosomes in all conditions. This could be originating from a nanoparticle recycling in endosomes after an initial cytosolic entry through the streptolysin O formed pores, although further in-depth investigations of the entry dynamics are required to provide a better view of the mechanism.

Materials and methods available in Appendix B.2

4.4 Bibliography

1. B. Poole and S. Ohkuma. Effect of weak bases on the intralysosomal ph in mouse peritoneal-macrophages. *Journal of Cell Biology*, 90(3), 665–669, 1981.

2. K. Ciftci and R. J. Levy. Enhanced plasmid DNA transfection with lysosomotropic agents in cultured fibroblasts. *International Journal of Pharmaceutics*, 218(1-2), 81–92, 2001.

3. N. J. Caron, S. P. Quenneville and J. P. Tremblay. Endosome disruption enhances the functional nuclear delivery of Tat-fusion proteins. *Biochemical and Biophysical Research Communications*, 319(1), 12–20, 2004.

4. T. Shiraishi and P. E. Nielsen. Photochemically enhanced cellular delivery of cell penetrating peptide-PNA conjugates. *Febs Letters*, 580(5), 1451–1456, 2006.

5. Y. Wolf, S. Pritz, S. Abes, M. Bienert, B. Lebleu and J. Oehlke. Structural requirements for cellular uptake and antisense activity of peptide nucleic acids conjugated with various peptides. *Biochemistry*, 45(50), 14944–14954, 2006.

6. J. J. Cheng, R. Zeidan, S. Mishra, A. Liu, S. H. Pun, R. P. Kulkarni, G. S. Jensen, N. C. Bellocq and M. E. Davis. Structure - Function correlation of chloroquine and analogues as transgene expression enhancers in nonviral gene delivery. *Journal of Medicinal Chemistry*, 49, 6522–6531, 2006.

7. S. Yang, D. J. Coles, A. Esposito, D. J. Mitchell, I. Toth and R. F. Minchin. Cellular uptake of self-assembled cationic peptide-DNA complexes: Multifunctional role of the enhancer chloroquine. *Journal of Controlled Release*, 135(2), 159–165, 2009.

8. K. K. Sandhu, C. M. McIntosh, J. M. Simard, S. W. Smith and V. M. Rotello. Gold nanoparticle-mediated Transfection of mammalian cells. *Bioconjugate Chemistry*, 13(1), 3–6, 2002.

9. D. Lasne, G. A. Blab, F. De Giorgi, F. Ichas, B. Lounis and L. Cognet. Label-free optical imaging of mitochondria in live cells. *Optics Express*, 15, 14184–14193, 2007.

10. B. Turk, I. Dolenc, V. Turk and J. G. Bieth. Kinetics of the pH-induced inactivation of human cathepsin L. *Biochemistry*, 32(1), 375–380, 1993.

11. B. Turk, I. Dolenc, B. Lenarcic, I. Krizaj, V. Turk, J. G. Bieth and I. Bjork. Acidic pH as a physiological regulator of human cathepsin L activity. *European Journal of Biochemistry*, 259(3), 926–932, 1999.

12. B. Gupta, T. S. Levchenko and V. P. Torchilin. Intracellular delivery of large molecules and small particles by cell-penetrating proteins and peptides. *Advanced Drug Delivery Reviews*, 57(4), 637–651, 2005.

13. A. D. Frankel and C. O. Pabo. Cellular uptake of the Tat protein from human immunodeficiency virus. *Cell*, 55(6), 1189–1193, 1988.

14. J. S. Wadia, R. V. Stan and S. F. Dowdy. Transducible TAT-HA fusogenic peptide enhances escape of TAT-fusion proteins after lipid raft macropinocytosis. *Nature Medicine*, 10(3), 310–315, 2004.

15. J. M. de la Fuente and C. C. Berry. Tat peptide as an efficient molecule to translocate gold nanoparticles into the cell nucleus. *Bioconjugate Chemistry*, 16(5), 1176–1180, 2005.

16. C. C. Berry, J. M. de la Fuente, M. Mullin, S. W. L. Chu and A. S. G. Curtis. Nuclear localization of HIV-1 tat functionalized gold nanoparticles. *IEEE Transactions on Nanobioscience*, 6(4), 262–269, 2007.

17. G. Ruan, A. Agrawal, A. I. Marcus and S. Nie. Imaging and tracking of Tat peptide-conjugated quantum dots in living cells: new insights into nanoparticle uptake, intracellular transport, and vesicle shedding. *Journal of the American Chemical Society*, 129, 14759–14766, 2007.

18. K. J. Cross, W. A. Langley, R. J. Russell, J. J. Skehel and D. A. Steinhauer. Composition and Functions of the Influenza Fusion Peptide. *Protein and Peptide Letters*, 16(7), 766–778, 2009.

19. S. Kumar, N. Harrison, R. Richards-Kortum and K. Sokolov. Plasmonic nanosensors for imaging intracellular biomarkers in live cells. *Nano Letters*, 7(5), 1338–1343, 2007.

20. J. Chen, J. J. Skehel and D. C. Wiley. N- and C-terminal residues combine in the fusion-pH influenza hemagglutinin HA2 subunit to form an N cap that terminates the triple-stranded coiled coil. *Proceedings of the National Academy of Sciences of the United States of America*, 96(16), 8967–8972, 1999.

21. J. J. Skehel, K. Cross, D. Steinhauer and D. C. Wiley. Influenza fusion peptides. *Biochemical Society Transactions*, 29, 623–626, 2001.

22. J. J. Skehel, P. M. Bayley, E. B. Brown, S. R. Martin, M. D. Waterfield, J. M. White, I. A. Wilson and D. C. Wiley. Changes in the conformation of influenza-virus hemagglutinin at the pH optimum of virus-mediated membrane-fusion. *Proceedings of the National Academy of Sciences of the United States of America-Biological Sciences*, 79(4), 968–972, 1982.

23. R. W. Doms, A. Helenius and J. White. Membrane-fusion activity of the influenza-virus hemagglutinin - the low pH-induced conformational change. *Journal of Biological Chemistry*, 260(5), 2973–2981, 1985.

24. X. Han, J. H. Bushweller, D. S. Cafiso and L. K. Tamm. Membrane structure and fusion-triggering conformational change of the fusion domain from influenza hemagglutinin. *Nature Structural Biology*, 8(8), 715–720, 2001.

25. P. Durrer, C. Galli, S. Hoenke, C. Corti, R. Gluck, T. Vorherr and J. Brunner. H+-induced membrane insertion of influenza virus hemagglutinin involves the HA2 amino-terminal fusion peptide but not the coiled coil region. *Journal of Biological Chemistry*, 271(23), 13417–13421, 1996.

26. R. F. Epand, J. C. Macosko, C. J. Russell, Y. K. Shin and R. M. Epand. The ectodomain of HA2 of influenza virus promotes rapid pH dependent membrane fusion. *Journal of Molecular Biology*, 286(2), 489–503, 1999.

27. D. G. Spiller and D. M. Tidd. Nuclear delivery of antisense oligodeoxynucleotides through reversible permeabilization of human leukemia cells with streptolysin O. *Antisense Research and Development*, 5(1), 13–21, 1995.

28. I. Walev, S. C. Bhakdi, F. Hofmann, N. Djonder, A. Valeva, K. Aktories and S. Bhakdi. Delivery of proteins into living cells by reversible membrane permeabilization with streptolysin-O. *Proceedings of the National Academy of Sciences of the United States of America*, 98(6), 3185–3190, 2001.

29. S. Ogino, S. Kubo, R. Umemoto, S. X. Huang, N. Nishida and I. Shimada. Observation of NMR Signals from Proteins Introduced into Living Mammalian Cells by Reversible Membrane Permeabilization Using a Pore-Forming Toxin, Streptolysin O. *Journal of the American Chemical Society*, 131(31), 10834–10835, 2009.

30. J. L. R. Brito, F. E. Davies, D. Gonzalez and G. J. Morgan. Streptolysin-O reversible permeabilisation is an effective method to transfect siRNAs into myeloma cells. *Journal of Immunological Methods*, 333(1-2), 147–155, 2008.

31. M. A. Kehoe, L. Miller, J. A. Walker and G. J. Boulnois. Nucleotide-sequence of the streptolysin O (SLO) gene - structural homologies between SLO and other membrane-damaging, thiol-activated toxins. *Infection and Immunity*, 55(12), 3228–3232, 1987.

32. J. E. Alouf. Streptococcal toxins (streptolysin O, streptolysin S, erythrogenic toxin). *Pharmacology & Therapeutics*, 11(3), 661–717, 1980.

33. S. Bhakdi, H. Bayley, A. Valeva, I. Walev, B. Walker, U. Weller, M. Kehoe and M. Palmer. Staphylococcal alpha-toxin, streptolysin-O, and Escherichia coli hemolysin: Prototypes of pore-forming bacterial cytolysins. *Archives of Microbiology*, 165(2), 73–79, 1996.

34. K. Sekiya, T. Akagi, K. Tatsuta, E. Sakakura, T. Hashikawa, A. Abe and H. Nagamune. Ultrastructural analysis of the membrane insertion of domain 3 of streptolysin O. *Microbes and Infection*, 9, 1341–1350, 2007.

35. K. Sekiya, R. Satoh, H. Danbara and Y. Futaesaku. A ring-shaped structure with a crown formed by streptolysin O on the erythrocyte membrane. *Journal of Bacteriology*, 175(18), 5953–5961, 1993.

36. S. Bhakdi, J. Tranumjensen and A. Sziegoleit. Mechanism of membrane damage by streptolysin-O. *Infection and Immunity*, 47(1), 52–60, 1985.

37. J. M. Fawcett, S. M. Harrison and C. H. Orchard. A method for reversible permeabilization of isolated rat ventricular myocytes. *Experimental Physiology*, 83(3), 293–303, 1998.

38. E. L. R. Barry, F. A. Gesek and P. A. Friedman. Introduction of antisense oligonucleotides into cells by permeabilization with streptolysin O. *Biotechniques*, 15(6), 1016–1018, 1993.

39. V. Idone, C. Tam, J. W. Goss, D. Toomre, M. Pypaert and N. W. Andrews. Repair of injured plasma membrane by rapid Ca2+-dependent endocytosis. *Journal of Cell Biology*, 180(5), 905–914, 2008.

40. I. Walev, M. Palmer, A. Valeva, U. Weller and S. Bhakdi. Binding, oligomerization, and pore formation by streptolysin O in erythrocytes and fibroblast membranes: detection of nonlytic polymers. *Infection and Immunity*, 63(4), 1188–1194, 1995.

41. E. B. Babiychuk, K. Monastyrskaya, S. Potez and A. Draeger. Intracellular Ca2+ operates a switch between repair and lysis of streptolysin O-perforated cells. *Cell Death and Differentiation*, 16(8), 1126–1134, 2009.

42. A. Rodriguez, P. Webster, J. Ortego and N. W. Andrews. Lysosomes behave as Ca2+-regulated exocytic vesicles in fibroblasts and epithelial cells. *Journal of Cell Biology*, 137(1), 93–104, 1997.

43. P. L. McNeil and R. A. Steinhardt. Plasma membrane disruption: Repair, prevention, adaptation. *Annual Review of Cell and Developmental Biology*, 19, 697–731, 2003.

Chapter 5

"Stripy" nanoparticles revisited

In 2004 Jackson *et al.* published the article entitled "*Spontaneous assembly of subnanometre-ordered domains in the ligand shell of monolayer-protected nanoparticles*"[1] in *Nature Materials*. This article became over the last seven years the foundation of a series of interlinked articles on "stripy" nanoparticles, published by the group of F. Stellacci in various high profile journals.

Those "stripy" nanoparticles are composed of a metal core — gold in general — of a few nanometres (2-8 nm) and coated with a self-assembled monolayer comprised of a mix of two types of thiolated ligands. This paper and the thirteen following ones[2–14] published by this group on "stripy" nanoparticles all claim that the ligands self-organise at the surface of the gold core to form ripples. Subsequently, a number of properties have been credited to those nanoparticles amongst them, the property to "*interact with the molecular environment in a novel way*" allowing them to "*avoid non-specific adsorption of proteins*"[1], a "*non-monotonic dependance on composition of solubility*"[7] or later, when "*water-soluble amphiphilic gold nanoparticles with structured ligand shells*" were reported[11], the ability to "*penetrate the plasma membrane without bilayer disruption*".[12]

The properties of those nanoparticles are attractive and important for the bionanomaterial and drug delivery community as they echo some of the current challenges in the field such as the controlled self-assembly of molecules on nanoparticles,[15] identifying the interactions of the nanomaterials with biomolecules and cells[16] or the intracellular delivery and fate[17] of these engineered nanomaterials. However, seven years after the publication of the first article of the series, the nanoscale organisation of mixed alkane thiol ligands on gold nanoparticles has not yet been reported by any other group. Additionally, claims presented in this series of articles are sometimes not consistent (for example: solubility, Fig. 5.6 in Sect. 5.1.5; interdigitation in Sect. 5.1.2), and results are often incorrectly or over-interpreted, commonly leading to unsupported conclusion by the authors (Sect. 5.1.6), but noticeably all start

hypothesising or lead to the conclusion of stripiness.

The evidences presented to support the existence of ripples on those particles will be revisited in this chapter, which will be divided in two parts. The first part is going to focus on the first article by Jackson *et al.*, reviewing the evidences, claims and interpretations provided to clearly demonstrate that the existence of ripples has not been proved herein. The second part will concentrate more on the interactions of nanoparticles with cells dealt with more recently by Verma *et al.*[12]

5.1 The underpinning of "stripy" nanoparticles

5.1.1 Sensible geometry: 2D images are projections of 3D objects

Geometrically predicted particles and experimentally imaged gold nanoparticles will be compared here. First, a 5.8 nm nanoparticle is taken as a theoretical example. The gold core is a 3.8 nm diameter sphere covered with a 1 nm thick layer, featuring stripes having a 1 nm regular spacing in 3D (Fig. 5.1A) and two "poles" (left and right side of the nanoparticle in Fig. 5.1B). This diameter of 5.8 nm (perimeter = $\pi \times d \simeq$ 18 nm) implies that there are 9 stripes on the sphere, owing to the pole symmetry, hence 9 per hemisphere.

If this nanoparticle was observed by Scanning Tunnelling Microscopy (STM), the apparent spacing of the stripes on the 2D image — the projection of their 3D structure on a 2D image plane — would certainly not be regular (Fig. 5.1B). Indeed while moving from the top of the observed hemisphere with a STM tip towards its edge, the apparent spacing between the stripes on the 2D image is decreasing quickly from stripe to stripe (1 nm, 0.9 nm, 0.6 nm, 0.3 nm). This is easily visible on the height profile of the theoretical nanoparticle (Fig. 5.1C), which has been taken at the position of the white line — in the middle of the nanoparticle— in the theoretical STM image in Fig. 5.1B.

But what has been reported by Jackson *et al.* is quite different. Figure 5.1D (adapted from Fig. 1b from Jackson *et al.*[1]) displays a STM image of a gold nanoparticle coated by a mix of 1-octanethiol (CH_3–$(CH_2)_7$–SH, OT) and mercaptopropionic acid (HOOC–$(CH_2)_2$–SH, MPA) ligands with a 2:1 molar ratio. The associated height profile (Fig. 5.1E, adapted from Fig. 1d in Jackson *et al.*) shows a constant stripe spacing of $\sim$1 nm, which is in contradiction with the geometrically predicted profile. This is not only the case for this particular nanoparticle as the ten nanoparticles of the same first STM image from Jackson *et al.* (Fig. 1a) display a similar propensity. Figure 5.2 shows the height profiles corresponding to those ten nanoparticles along with the predicted one. Looking at the height profile of those ten experimentally imaged nanoparticles, from the top of each individual sphere to its edge, the stripes spacing appears to be fairly constant. The values measured from these profiles, reported in Tab. 5.1, exhibit a rather small variation ($\sim$1.05–1.1 nm),

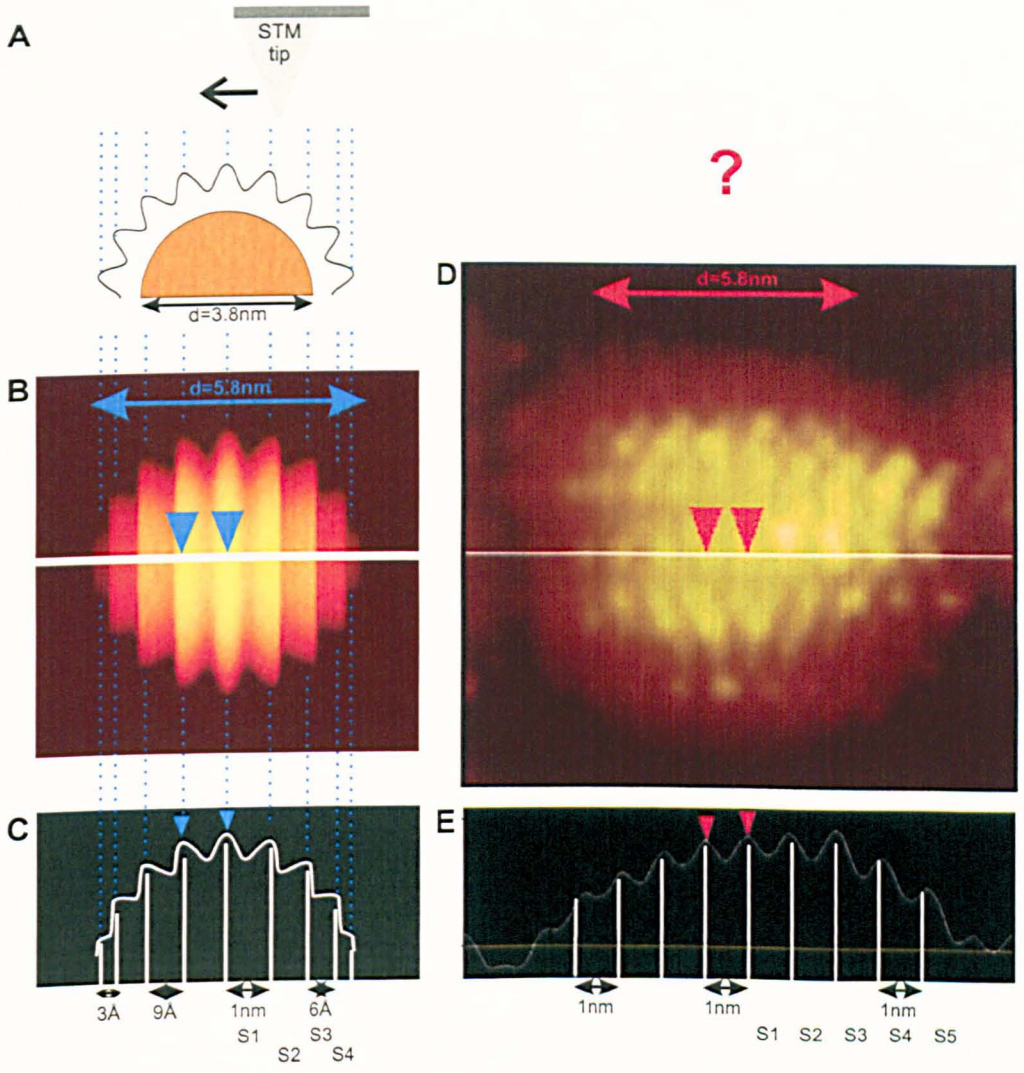

Fig. 5.1 – Theoretical and experimentally measured (STM) stripe widths of a 5.8 nm gold nanoparticle. (**A**) STM tip scanning over a stripy nanoparticle perpendicularly to the stripes orientation. (**B**) Theoretical STM image with colour-coded height of a 3.8 nm gold core with 1 nm stripes (in 3D). (**C**) Height profile at the position of the line in (B). (**D**) Experimental STM image (adapted from Fig. 1b of Jackson *et al.*[1]). (**E**) Height profile corresponding to the white line in (D) (adapted from Fig. 1d of Jackson *et al.*[1]). (D) and (E) are adapted by permission from Macmillan Publishers Ltd: Nature Materials,[1] copyright (2004).

but do not decrease with the same trend as it is expected from the predicted values.

5.1.2 Vertical alignment of neighbouring rippled nanoparticles: no plausible explanation has been proposed

The STM image provided by Jackson *et al.*[1] has another particular feature as the ten whole nanoparticles present all have their ripples aligned perpendicularly to the fast scanning axis. Nevertheless this alignment is not present solely on this image,

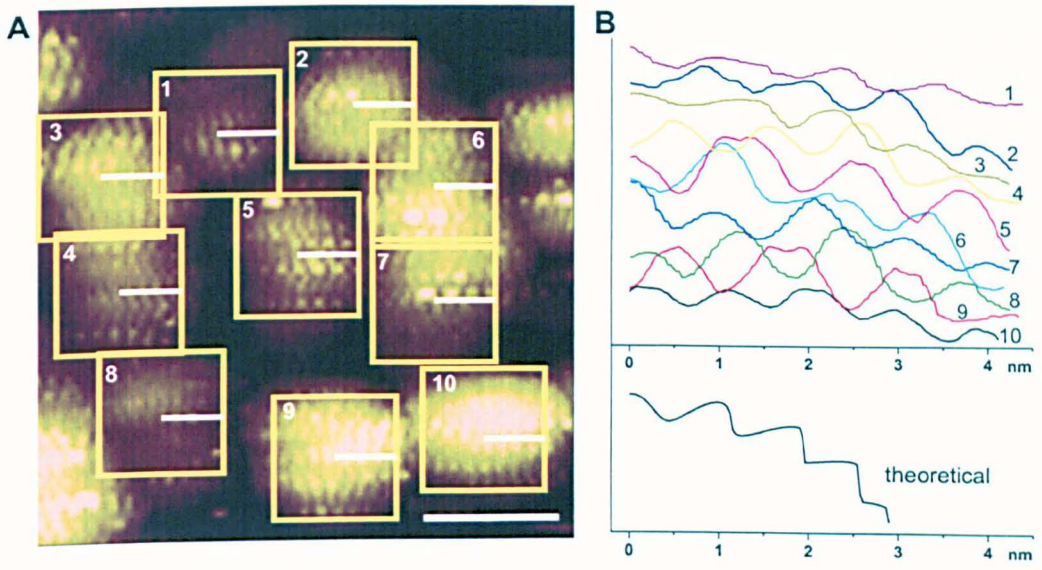

Fig. 5.2 – Height profiles of 10 nanoparticles observed by Jackson *et al.* (**A**) STM image taken from Fig. 1a of Jackson *et al.*[1] where 10 nanoparticles are numbered and selected in yellow squares. (**B**) Top: height profiles corresponding to the white lines for the nanoparticles 1–10 numbered in (A) (curves shifted vertically for a better visualisation); bottom: theoretical height profile for 1 nm stripes on a 5.8 nm nanoparticle (3.8 nm gold core). (A) is adapted by permission from Macmillan Publishers Ltd: Nature Materials,[1] copyright (2004).

Nanoparticle		1st stripe (nm)	2nd stripe (nm)	3rd stripe (nm)	4th stripe (nm)
Theoretical NP		0.98	0.86	0.64	0.34
NP 1		1.0	1.3	1.0	
NP 2		1.2	0.9	1.0	
NP 3		1.3	1.0	0.9	0.9
NP 4		1.0	1.0	1.1	
NP 5		1.2	1.4	1.1	
NP 6		1.1	1.2	1.0	
NP 7		1.0	1.0	1.0	1.0
NP 8		1.0	1.2	1.3	
NP 9		1.2	1.3	1.3	
NP 10		0.9	0.9	0.9	1.0
NP 1–10	Mean	1.09	1.12	1.06	
	SD	0.13	0.18	0.14	

Tab. 5.1 – Stripe widths of theoretical and experimental 5.8 nm diameter nanoparticles. The nanoparticles numbered (1–10) refer to the nanoparticles shown in Fig. 5.2. The mean and the standard deviation (SD) of the stripe widths for the nanoparticles 1 to 10 are given at the bottom.

but appears as a hallmark in almost all the papers of the series.

5.1.2.1 Interdigitation

The authors acknowledge this alignment in their article, but fail to explain its perpendicularity to the fast scanning axis. They propose interdigitation as an explanation for the alignment. They write (citation numbers modified to fit with the current text order):

> "*It is known that the nanoparticle ligands interdigitate*[18,19]*. We believe that this phenomenon leads to the observed macroscopic alignment of the ripples across many nanoparticles. Indeed, it can be observed that there is no clear separation between the ligand shells of the nanoparticles. On heating above the de-interdigitation temperature and subsequent gentle cooling, we improved ripple alignment across the sample. Samples self-assembled on a gold foil from a 1,2-dichlorobenezene solution kept at a temperature (150° C) above the de-interdigitation transition did not show consistent ripple alignment.*"

Although they suggest that they have been trying to improve this alignment and that it can also be non-systematical, they fail to provide the example images that would back these claims up. Interestingly, in a later article of the series, Centrone *et al.*[7] deny the incidence of interdigitation on OT/MPA nanoparticles, writing:

> "*in the nanoparticles chosen, because of the charges present in the NPs ligand shell, we can assume that the amount of interdigitation is negligible. We confirmed this using differential scanning calorimetry according to methods in the literature*".

This was not the last contradiction of the series, as slightly later during the same year, Hu *et al.*[9] write in the conclusion of their article:

> "*We have shown that ripples in the ligand shell enhance particle-particle interactions, leading to a stronger degree of interdigitation. This leads to a significantly less ordered assembly of particles into a nanoscale glassy state.*"

This paper from Hu *et al.* was received for reviewing on October 10 (2007), while the PNAS paper from Centrone *et al.* was received on August 30 (2007). However, as both papers were submitted — and maybe prepared — in a fairly close proximity, with the same corresponding authors, it is difficult to understand such a degree of inconsistency.

5.1.2.2 Alignment of the stripes to the slow scan axis

The authors[2] claim that stripes can only be seen when they are perpendicular to the fast scan axis:

> *"If one now examines an image of several nanoparticles (Figure 8), it is immediately evident that those particles with the most clear ripples (that is, ripples whose direction is easy to discern) almost always have domains which tend to run perpendicular, within ±30°, to the fast scan direction (or, equivalently, parallel to the slow scan direction). However, there are several other nanoparticles within the scan images that show nanostructuring, but whose ripples' direction is difficult to discern (Figure 8d). This disparity is likely due to how the tip scans across each ligand shell 'lattice' and the resulting merging of scan lines."*

It is often difficult to say if the nanoparticles in a STM image are supposed to show ripples or not without looking at the figure legend for any article of this series. Let us first admit that it is always possible to distinguish these stripes. Although their argument could explain why stripes would only appear on the STM images when they are perpendicular to the fast scanning direction, it fails to explain why a small deviation from the perpendicular would not allow any stripe to be visible. It also does not explain why the nanoparticles are aligned to one another, such as in Fig. 5.2A, or why the observation of ripples is not a rare event but a systematic observation.

5.1.3 Fast Fourier Transform: a useful tool to analyse noisy images

In a number of articles of the series, including the first one, some measures of the stripes spacing — or "*headgroup spacing*" for the homoligand — are reported by the authors. Although we have already seen earlier that those spacings should not be constant on nanoparticles 2D images if they are in 3D (see Tab. 5.1, Sect. 5.1.1), the authors always report a single value to represent them. In most of the articles, they do not mention clearly the method used to measure those distances, but hint that it is done directly on the STM images.

In JACS, Jackson *et al.*[2] describe how they measure the "STM-observed headgroup spacing" in the case of homoligand functionalised nanoparticles:

> *"The headgroup spacings on each nanoparticle were determined by measuring the peak to peak spacing between clearly visible headgroups located near the center of the particle, generally measuring four or more spacings per particle. We believe that spacings taken at particle edges are*

more subject to tip/sample distortions and, due to geometric considerations, may not be representative of the actual molecular configurations. In most cases we tried to measure spacing between neighboring headgroups horizontally aligned to minimize the possibility of line scan artifacts or sample drift."

The authors decision to measure the headgroup spacing near the centre of the nanoparticle, to discard the ones near the nanoparticles edges and their choice to output it as an average does not allows one to discover any regularity in the spacing measurement. Additionally, taking only horizontally aligned headgroups is also surprising as it inherently accounts for an hypothesis of vertically aligned stripes and could easily be subject to artifact as it is the direction perpendicular to the fast scan axis.

In 2009, Hu *et al.*[13] reported a detailed method used for the stripe spacing measurements. They describe the method as follows (reference numbers modified to fit with the present order):

"When oscillations are present in line scans, their periodicity is recorded (Fig. 5). Here we define oscillations as a periodic variation with at least three maxima and with the two periods not differing in spacing more than 10 %. (This latter condition is typically established by the operator, mostly visually).

"Note that for a 4.5 nm diameter particle with striation 0.9 nm thick (the theoretical minimum would be ~0.8 nm)[20,21] the maximum number of oscillations that could be imaged would be 5. When multiple oscillations are present the reader takes the distance between the two peaks that are furthest apart and then divides the distance by the number of peaks. Each nanoparticle in the image will be used to generate approximately three measurements at max. The reason for this limiting is to prevent excessively counting of particles whose properties lead to good images, and thus a biased population in further statistical analyses.

"In a given image (sometimes as large as 100 × 100 nm, with as many as 200 nanoparticles in each image), we try to record the spacing for 10 to 20 particles (never more than 50), each spacing an average of three separate measurements per particle, of which each measurement is the average of at least two periodicities. The measurements recorded in this way are averaged and lead to a single spacing measurement that we associate with a certain tip speed. It should be pointed out that oscillation periodicities are recorded with no operator bias, that is the reader will record periodicities independent of their position in the image. Many images are analyzed at varying tip speeds. In some cases we have analyzed as many as 10 images (which means in excess of 1000 oscillations and/or equivalently 1000 periodicities)."

Here again the method described by Hu *et al.* assumes that the stripe spacing does not vary.

To limit bias in the measurement of the ripples spacing, the Fast Fourier Transform (FFT) of the source images can be used. Figure 5.3 displays a grayscale version of the image of OT/MPA nanoparticles (2:1 molar ratio) published by Jackson *et al.* and its FFT (A and B, respectively). The FFT shows two oblong maxima that are aligned to the Y-axis. The values of the maxima on the FFT can be precisely identified in the integrated (X-axis) intensity profile (Fig. 5.3C), with a measured periodicity of 1.3 ± 0.5 nm (Jackson *et al.*[1] reported a value of 0.9 ± 0.1 nm). Along with those maxima, the FFT also displays two vertical lines going through the maxima. Those two lines are the result of a series of modes in the original image that have the same periodicity on the X-axis but different ones on the Y-axis. As a consequence, the wavelength λ is not defined for these X-values, and these vertical lines clearly cannot be features of a real material, and incidently the image cannot represent stripes.

A theoretical equivalent of the STM image was produced as a comparison, by gathering ten theoretical nanoparticles (same model as in Fig. 5.1) having small rotations (± 5 °) with one another (Fig. 5.3D). The corresponding FFT (Fig. 5.3E) show two weak semi-circular maxima with, this time, a defined wavelength λ=0.9 nm.

FFT can also be used to remove high and low frequency noises, through the use of a frequency filtering procedure. The ten nanoparticles present in Jackson *et al.*[1] (Fig. 5.2A) were cropped and a frequency filter was applied on those ten images (Fig. 5.4). The images on the right of Fig. 5.4 show the result of this process. This allows to see the phase reset of the oscillation that appears near the nanoparticles, shifting some of the scan lines with respect to one another.

5.1.4 Lack of structural evidences: X-ray diffraction and TEM

In order to better understand the coming discussion regarding the XRD and TEM data mentioned below, the X-ray diffraction plot and TEM image have been reproduced from Jackson *et al.*[1] (Fig. 5.5A and B, respectively), with their original figure legend quoted directly in the figure caption. In their 2004 article, Jackson *et al.* write:

> "*The presence of ripples on the nanoparticles has also been confirmed using X-ray diffraction (XRD). Indeed, all of the XRD plots of the rippled nanoparticles described in this paper showed peaks at 2θ ranging from 2.5° to 13°. Some of the peaks were temperature dependent, as is expected for peaks due to inter-particle packing arrangements*[19]*. However, one or two peaks were temperature independent, pointing to periodic arrangements, with 0.5–2.5 nm spacing, on single nanoparticles (see Sup-*

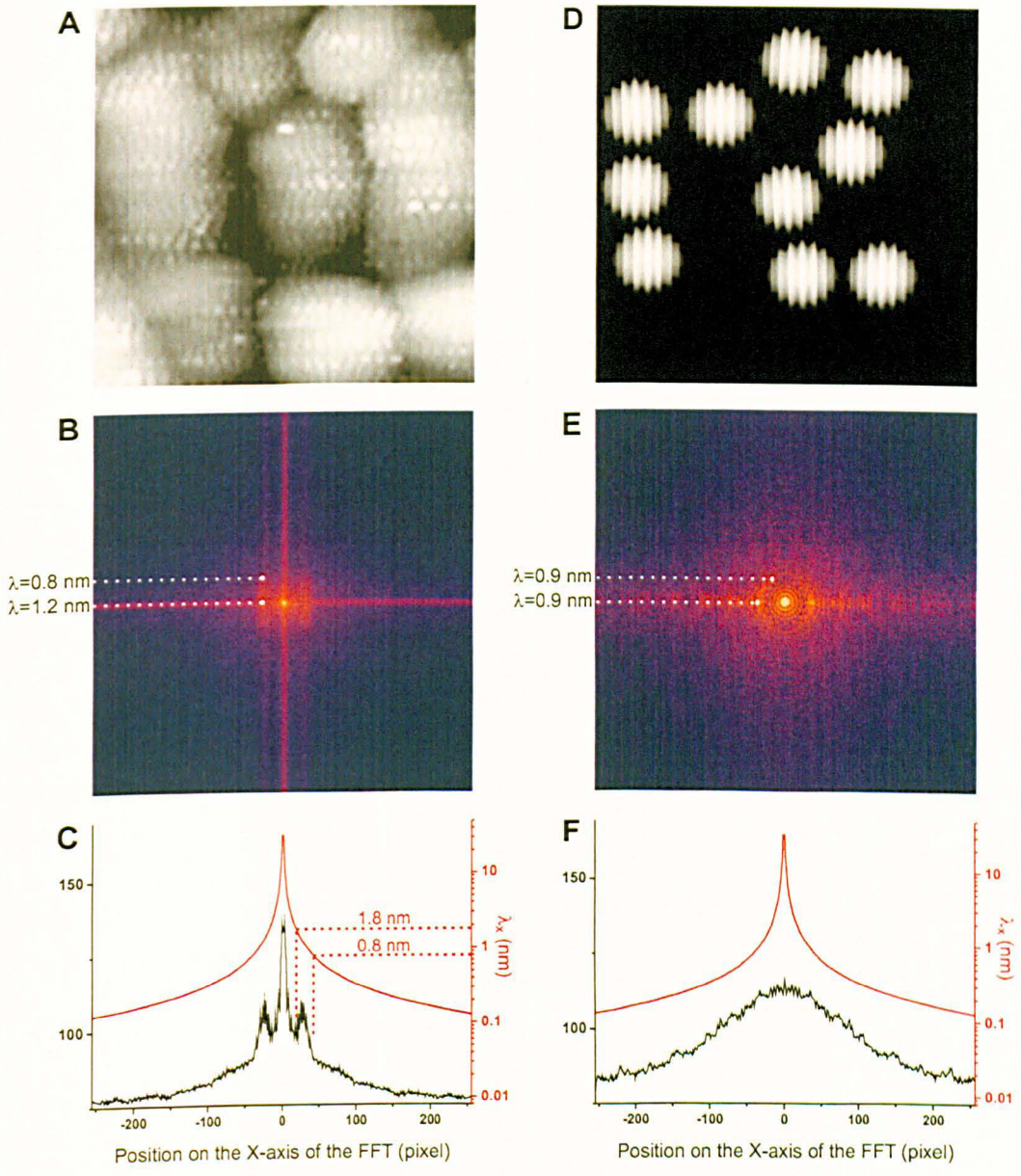

Fig. 5.3 – Fast Fourier Transform analysis of experimental and theoretical STM images of striped nanoparticles. (**A**) Experimental STM image (adapted from Fig. 1a of Jackson *et al.*[1]). (**B**) FFT of the image shown in (A). (**C**) Integrated profile of the FFT image shown in (B) along the x-axis (red curve: pixel to wavelength correspondence). (**D**) Exemplar theoretical image of 10 nanoparticles. (**E**) FFT of the image shown in (D). (**F**) Integrated profile of the FFT image shown in (E) along the x-axis (red curve: pixel to wavelength correspondence). (A) is adapted by permission from Macmillan Publishers Ltd: Nature Materials,[1] copyright (2004).

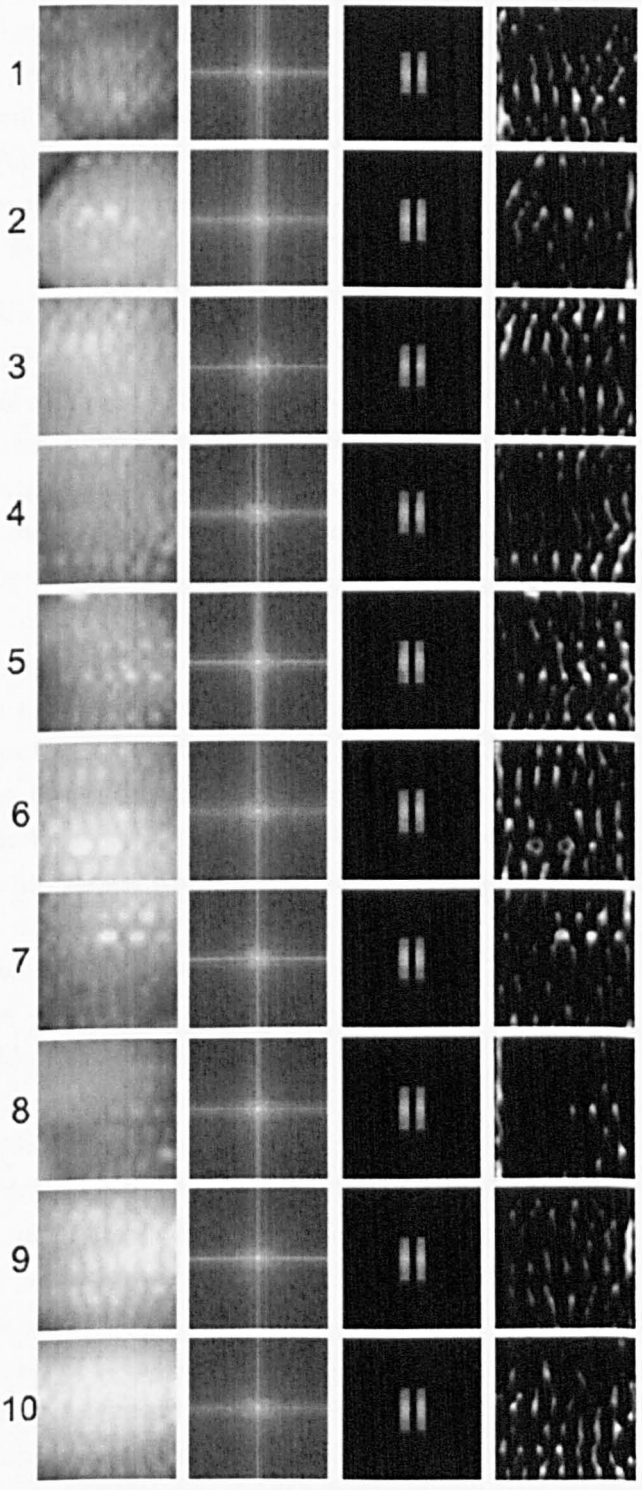

Fig. 5.4 – Frequency-filtered images of the "stripy" nanoparticles observed by Jackson *et al.* The ten images on the left correspond to the same ten nanoparticles highlighted in Fig. 5.2. For each of them and from left to right: image of individual nanoparticles cropped from the STM image in Jackson *et al.*; FFT of the image; frequency filter; frequency-filtered image. The images on the left are adapted by permission from Macmillan Publishers Ltd: Nature Materials,[1] copyright (2004).

> *plementary Information, Fig. S1). Such temperature-independent peaks were never observed in homo-ligand nanoparticles. Additional confirmation of the presence of ordered phase-separated domains was provided by transmission electron microscopy (TEM) images. In fact, in these images (see Supplementary Information, Fig. S2) we have found that there is an observable ring around the nanoparticles' metallic cores consisting of discrete dots spaced ~0.5–0.6 nm.*"

This is problematic, because in this article — and in the whole series by Stellacci *et al.* — only three XRD spectra are shown (in the supplementary information). Two of them are from the diffraction of OT/MPA (2:1 molar ratio) capped silver nanoparticles (3.8 nm diameter). Those two spectra differ by a thermal treatment between the two diffractions experiment, which allows one to find temperature-insensitive peaks. Those peaks, according to the authors, can be "*assigned to the ordered domains formed on the nanoparticles' ligand shell.*" Four temperature-insensitive peaks can be distinguished between the two curves, but only one of them "*indicated a domain spacing of ~0.7 nm, similar to the STM measured spacing (0.92 nm see table)*", according to the authors. No justification was provided as to why this peak was found to represent the stripes spacing or to what the other peaks were representing.

The third and last spectrum corresponds to the OT/MPA capped (molar ratio 2:1) gold nanoparticles of a 5.1 nm diameter (3.8nm for the STM images shown in the article). It is not stated which peaks are temperature-sensitive in this case, and it is not possible to know it as only one spectrum is provided, but nevertheless the authors associated one of them to the ripples spacing: "*the ripple spacing measured with XRD (2θ = ~12.5 °, equivalent to 0.7 nm) agrees even better with the one measured in STM (0.72 nm, see table).*" In this case, as for the silver nanoparticles, there is no specific reason why specific peaks should represent the ligand shell of the nanoparticles, rather than some structural features of the gold or silver core. The absence of a spectrum for the nanoparticles capped with homo-ligands (supposed to be ripples-free), which are said to show "*no temperature independent peak at small angles*" does not allow any comparison to be drawn and renders the use of the presented spectra void.

Regarding the TEM image provided by Jackson *et al.*, only one image of a single nanoparticle was shown. On this image (Fig. 5.5), Jackson *et al.* see "*quasi-ordered dots spaced 0.5 nm around the particle*" (figure legend), and add that the "*dots are attributed to ions captured but* [by] *the MPA head groups.*" Observing ions around a nanoparticle is a challenging task though. Recently Weinstock *et al.* were for example able to produce convincing evidences that they imaged self-assembled monolayers of inorganic anions on 14 nm gold nanoparticles.[22] However, to achieve that they used cryo-TEM and not classic TEM. In this way a rapid cryogenic cooling of the sample was allowing them to protect the samples and capture the gold na-

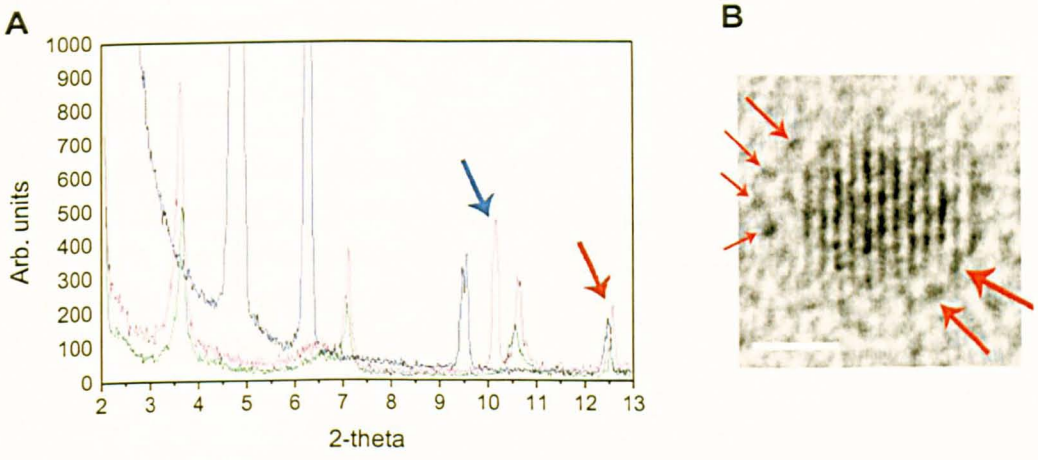

Fig. 5.5 – X-Ray diffraction and TEM evidences from Jackson *et al.* (**A**) Caption text is as it reads in Jackson *et al.*: "***XRD plot of homo- and mixed-ligand nanoparticles.*** *The pink and green curves were obtained from diffraction of OT:MPA 2:1 silver nanoparticles (3.8 nm in diameter). The particles were first analyzed at room temperature (green curve) and subsequently heated at 100° C for 1 hour and allowed to cool down at room temperature slowly. This type of heating cycle is known to help the formation of interdigitated super-lattices of nanoparticles, and consequently to generate new peaks in the XRD spectrum or to enhance the intensity of existing ones (see reference 27[19]). As evident from the comparison of the pink (spectrum taken on the same sample after thermal treatment) and the green curves, new peaks appear (one of them is indicated by the blue arrow) but a few peaks stay unmodified. These latter peaks were assigned to the ordered domains formed on the nanoparticles' ligand shell. In particular, the peak indicated by the red arrow ($2\theta = \sim 12.5°$) indicated a domain spacing of ~0.7 nm, similar to the STM measured spacing (0.92 nm see table). The blue curve is an XRD plot of OT:MPA 2:1 gold nanoparticles (5.1 nm in diameter). In this case the ripple spacing measured with XRD ($2\theta = \sim 12.5°$, equivalent to 0.7 nm) agrees even better with the one measured in STM (0.72 nm, see table). These curves are representative of all of the curves that we obtained. The homo-ligand nanoparticles showed no temperature independent peak at small angles, while the mixed ligands showed one or more temperature independent peak at 2θ ranging from 2.5° to 13°.*" (**B**) Caption text is as it reads in Jackson *et al.*: "***Transmission electron microscopy of OT: MPA (2:1) gold nanoparticles.*** *Bright field image of a nanoparticle showing quasi-ordered dots spaced 0.5 nm around the particle. These dots are attributed to ions captured but the MPA head groups.* [...] *Scale bar 1 nm .*" (A) and (B) are adapted by permission from Macmillan Publishers Ltd: Nature Materials,[1] copyright (2004).

noparticles in solution with the surrounding anions retaining their original local structure. It is quite a strong claim to assign those highlighted dots (red arrows) to any specific structure with a single image, especially when it is already difficult to state whether they can really be discriminated from the background or not, and all that with a sample that is not in the same conditions as in solution. But, again, the absence of TEM images of nanoparticles capped with homoligand, as controls images, renders the comparison impossible and the presented TEM image meaningless.

5.1.5 Solubility

The solubility of rippled nanoparticle was an early interest for the authors, as in 2004 Jackson *et al.*[1] report for the first time a non-monotonous behaviour of the solubility of OT/MPA nanoparticles in ethanol as a function of the monolayer composition. Four year later, Centrone *et al.*[7] studied the solubility of OT/MPA nanoparticles in twelve different solvents in a more systematic manner, and still mention a non-monotonic behaviour:

> *"solubility of nanoparticles as a function of composition show nonmonotonic behaviors indicative of physicochemical effects that go beyond those expected by a simple thermodynamic treatment[1]."*

However, if one compares their results on the solubility of OT/MPA nanoparticles in ethanol in 2004 and 2008, a clear contradiction arises (Fig. 5.6A).

To assess the dependance of the solubility on the monolayer composition the use of different solvent was replaced by a titration of tetrahydrofuran (THF) into water. THF is the most hydrophobic solvent miscible in water and thus provide the largest continuous hydrophobic to hydrophilic gradient to study the solubility of those nanoparticles. Homoligand-capped (OT, MPA) and OT/MPA mixed-ligand-capped nanoparticles with molar ratios of 1:3, 1:2, 1:1, 2:1 and 3:1 were prepared and mixed with the mixture of THF/H_2O solvent. After a centrifugation to remove insoluble aggregates, the absorbance of the supernatant was taken as a measure of the solubility of the nanoparticles.[a]

The results show that nanoparticles capped with 100 % OT (hydrophobic) resuspend well in THF but not in water and, at the opposite, the ones capped with 100 % MPA (hydrophilic) resuspend well in water but not in THF. For a given hydrophobicity/hydrophilicity (ratio of THF:H_2O) the solubility follows a smooth transition with respect to the monolayer composition, and there is here no indication of non-monotonic characteristics.

More interestingly, in their study Centrone *et al.* report saturation concentrations that are relatively low, with the maximum concentration for all the different mixes of nanoparticles in a given solvent in the range of 30–500 nM.[7] If one takes

[a] nanoparticle synthesis and solubility assay: C. P. Shaw

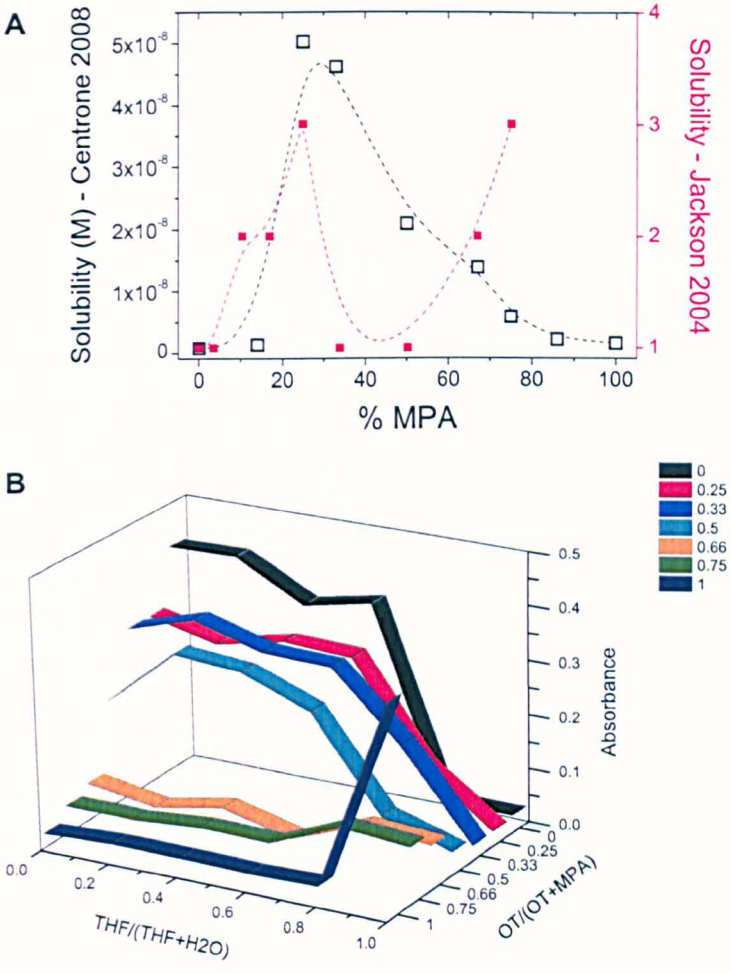

Fig. 5.6 – Solubility of nanoparticles capped with different OT:MPA ligand ratios. (**A**) Comparison of the solubility in ethanol reported by Centrone *et al.*[7] in 2008 (black squares, left Y axis) and by Jackson *et al.*[1] in 2004 (red squares, right Y axis). The solubility is expressed through the saturation concentration (molar) in the 2008 study, while the 2004 study defines the solubility scale as it writes: "*4 = highly soluble, that is, no precipitation visually observed, 3 = mostly soluble, that is, little precipitation observed over time with consequent slight decolouration of the solution; 2 = slightly soluble, that is, most of sample precipitated but a small coloration of the solution remains, 1 = totally insoluble*". (**B**) Solubility of the nanoparticles in different ratios of the solvent mixture THF:H_2O. The nanoparticles and the solvent mixture were mixed and then centrifuged (3000 RPM, 5s) to remove insoluble aggregates. The absorbance of the supernatant was taken as a measure of the solubility of the nanoparticles (C. P. Shaw). (A) is adapted from Centrone *et al.*[7] with permission from Proceedings of the National Academy of Sciences USA. © 2008 National Academy of Sciences, USA.

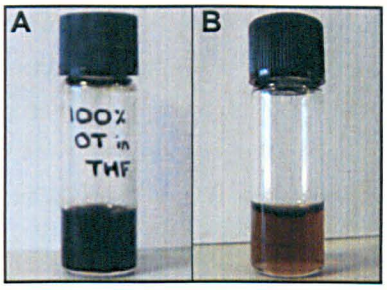

Fig. 5.7 – Saturation concentration of OT-capped gold nanoparticles in THF. (**A**) Photo of a 8 μM suspension of 3 nm diameter gold nanoparticles capped with OT three weeks after suspension in THF (C. P. Shaw). (**B**) A 450 nM suspension (reported as "*saturation concentration*" by Centrone *et al.*[3]) is shown for comparison.

the example of OT capped nanoparticles, the saturation concentration reported is in the 300–500 nM range for six different solvents (benzene, chloroform, hexane, carbon tetrachloride, THF and DCB). For example, in THF, the saturation concentration is reported to be 450 nM. An attempt to measure the saturation concentration was proceeded to, but after three weeks the nanoparticles were still in suspension for a concentration of 8 μM; no equilibrium between a solid and a liquid phase was observed (Fig. 5.7A) and the measurement could therefore not be taken. The saturation concentration must therefore be higher than that value of 8 μM, which is more than 18 times what Centrone *et al.* reported.

5.1.6 Non-specific interaction: a cartoon instead of data

Amongst other claims, Jackson *et al.* have ascribed to the rippled nanoparticles the property of preventing non-specific protein adsorption[1]. This is first written in the abstract and introduction of their 2004 article:

> "*(...) because the size of the domains is much smaller than the typical dimensions of a protein, these materials are extremely effective in avoiding non-specific adsorption of a variety of proteins.*"

> "*Because of the extremely small size of the domains (~ 5 Å) these particles interact with the molecular environment in a novel way; for example, they prevent non-specific adsorption of proteins.*"

Then, in a paragraph about the nanoparticles properties, they develop their argument by writing:

> "*More interestingly, we have observed that these nanoparticles avoid non-specific adsorption of proteins. We believe that this happens because of the unique subnanometre-ordered repetition of hydrophobic and hydrophilic regions on the particles' ligand shell. The 5-Å small domains on*

the outside of these particles are more than one order of magnitude smaller than the characteristic size of a protein globule; independently of the protein conformation, there will always be a series of attractive and repulsive forces between the protein's outer shell and the particle's domains (see Fig. 5). Consequently, there will be almost no net attraction, and the protein adsorption from solution will not be thermodynamically favourable."

They continue by describing how three chosen proteins (cytochrome C, lysozyme and fibrinogen) are not showing any adsorption on rippled nanoparticles:

"Following known procedures[23], (using STM, atomic force microscopy, and Fourier-transform infrared spectroscopy) we have confirmed that all of these proteins adsorb on MPA,OT and on mixed MPA/OT monolayers, and established that the same behaviour occurs on OT homo-ligand nanoparticle films, but the proteins do not adsorb on rippled or domained MPA/OTnanoparticle films, even after 24-h exposure to a concentrated solution. It should be pointed out that on rippled nanoparticle-coated surfaces we found no evidence for the presence of proteins with any of the characterization techniques used. We believe that this result is due to the unique size scale of the ordered hydrophobic and hydrophilic domains. These results are extremely promising, in fact, using three different characterization techniques we find that surfaces coated with nanostructured nanoparticles outperform surfaces that are known[23-25] to have good protein-resistance properties with all of the three very different protein systems used."

But a serious concern arises from this as only a cartoon displaying a nanoparticle and a model protein (Fig. 5 in Jackson *et al.*[1]) has been shown to support those claims. No data, neither in this article, nor in its supplementary information, nor in further articles by the group has been published at all on non-specific interaction of homoligand or mixed-ligand coated nanoparticles. The alleged nanoparticle property is further mentioned in nine articles of the series without any further investigation on its postulated property, but always a reference to the initial article:

"This unprecedented small size of the phases leads to unexpected properties of the nanoparticles such as a nonmonotonic dependence on composition of solubility and good resistance to protein nonspecific adsorption.[1]"

Jackson *et al.*[2] (p11136-11137)

"Understanding and controlling the properties of molecular coatings on surfaces is an important challenge for many applications, and is a key

factor in the fabrication of, e.g., protein repellent[1] *[...] surfaces.*"
Singh *et al.*[5] (p226106-1)

"*Rippled NPs also are highly resistant to protein nonspecific adsorption.*[1]"
Carney *et al.*[6] (p798)

"*we showed that it prevents efficiently protein nonspecific adsorption*[1]"
Centrone *et al.*[7] (p9886)

"*They were also effective at repelling protein nonspecific adsorption.*[1]"
Hu *et al.*[9] (p6279)

"*The presence of such a unique molecular arrangement on the surface of the nanoparticles determines a number of properties, ranging from the nonmonotonic dependence of solubility on composition to resistance to protein nonspecific adsorption and cell membrane penetration.*[1,11,12]"
Nakata *et al.*[10] (p4294)

"*In fact, the size of these domains is small enough (∼ 0.5 nm) to be comparable to the size of a small molecule; as a consequence the nanoparticles show a non-monotonic dependence of solubility in ethanol on ligand shell composition as well as some resistance to protein non-specific adsorption.*[1,2]"
Uzun *et al.*[11] (p196)

"*The similarity in the nanoparticle uptake in serum-containing and serum-free conditions suggests 'striped' particles are resistant to non-specific protein adsorption (as previously observed in similar systems)*[1]"
Verma *et al.*[12] (p591)

"*The presence of these molecularly defined domains confers the particles with unique properties, such as two diametrically opposed polar defect, a non-monotonic dependence of the solubility on the ligand shell composition, resistance to protein nonspecific adsorption, and cell membrane permeation.*[1,3,4,7,8,10,12]"
Hu *et al.*[13] (p24)

5.2 How do "stripy" nanoparticles interact with cells?

In 2008, Uzun *et al.* reported the synthesis of "*highly water-soluble mixed monolayer protected 'rippled' gold nanoparticles*" functionalised with sodium 11-mercaptoundecanesulfonate (MUS, hydrophilic) and octane thiolate (OT, hydrophobic) as capping ligands[11].

Later in the year the same group presented a study of the interaction of different compositions of the same mixed ligands monolayer protected nanoparticles with cells.

The nanoparticles described as bearing "ribbon-like domains" structured monolayers (previously referred to as striped or rippled) were able to "*penetrate the plasma membrane* [of cells] *without bilayer disruption*" to go directly to the cytosol[12], as opposed to the ones not showing stripes (homoligands and unstructured mixed-ligands) that were internalised by the conventional endosomal pathway.

In both articles the stripiness of those particles is a key point in the line of argument — water-solubility or cytosolic delivery — but only a single image of these "water-soluble/stripy" nanoparticles (2:1 MUS:OT) was published (Fig. 2 by Uzun *et al.*, Fig. 1 by Verma *et al.*).

5.2.1 Water-soluble "stripy" nanoparticles

The single water-soluble "stripy" nanoparticle (2:1 MUS:OT molar ratio) mentioned above is shown in Fig. 5.8A. Its FFT shows the same features than the previously published images of "stripy" nanoparticles (see Fig. 5.3B, Fig. 5.4), with the two characteristic oblong maxima crossed by a vertical line (Fig. 5.8B). After applying a frequency filter to the image (Fig. 5.8C), thus removing the high and low frequency noise in the image, the phase shifts between successive scan lines are markedly more distinct as highlighted by the red arrows in Fig. 5.8D. Figure 5.8E shows that the stipe widths do not vary from the middle of the nanoparticle to its edge, as expected from predicted values of theoretical nanoparticles (Fig. 5.3, Tab. 5.1). Subsequently this STM image cannot be the representation of a nanoparticle with regularly spaced stripes (in 3D), and neither can what appear as stripes on the image be a real feature of the sample since a series of modes in the STM image have the same periodicity on the X-axis (see discussion about the undefined wavelength of the FFT maxima in Sect. 5.1.3 for a detailed justification).

5.2.2 Uptake of "stripy" nanoparticles: what interaction with the cell membrane?

In their 2008 *Nature Materials* article, Verma *et al.* proposed that structured rippled nanoparticles enter cells without bilayer disruption due to the structure of the capping monolayer.[12] It read:

> "*With the ordered amphiphilic structure of some CPPs in mind, we explored the interaction of these nanoparticles with living cells. Here, we show that ~6 nm nanoparticles, coated with a shell of hydrophobic and anionic ligands regularly arranged in ribbon-like domains of alternating composition (Fig. 1a), penetrate cell membranes at 37° C and 4° C without evidence of membrane disruption. Particles with identical hydrophobic content but lacking structural order in the ligand shell for the most part do not penetrate cell membranes; hence, we conclude that the*

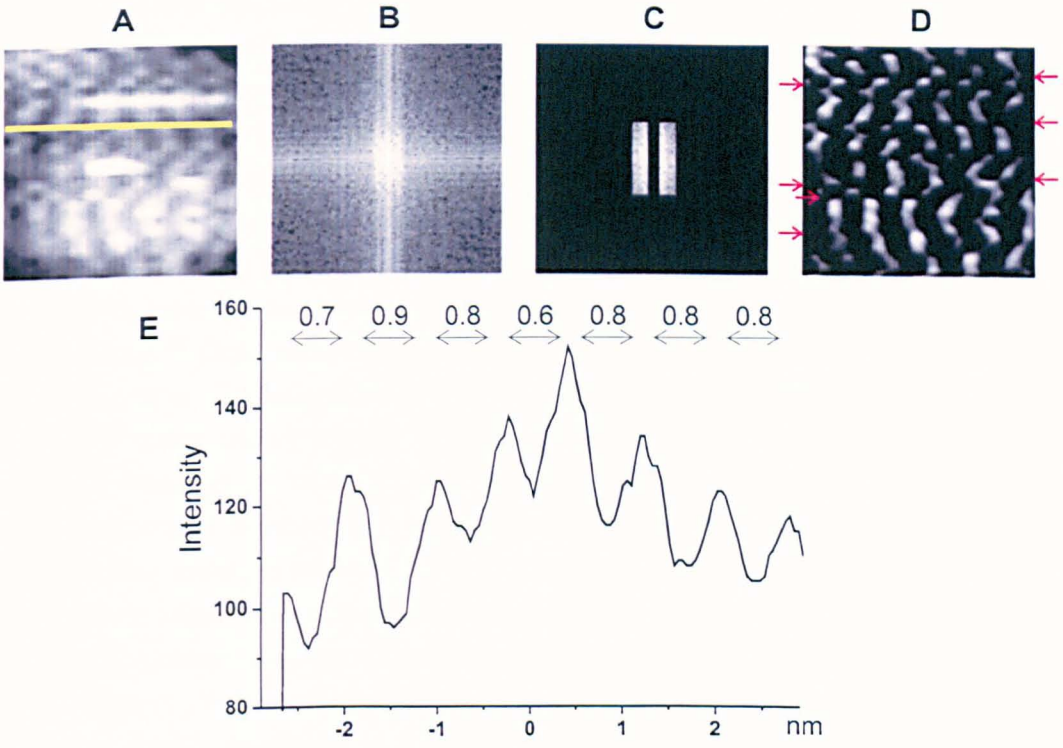

Fig. 5.8 – Water-soluble MUS/OT-coated "stripy" nanoparticles (2:1 molar ratio of MUS:OT). (**A**) STM image of a water-soluble nanoparticle adapted from Fig. 2 of Uzun *et al.*[11] (**B**) FFT of the image shown in (A). (**C**) Frequency filter. (**D**) Reverse FFT of the image in (C), i.e. frequency-filtered image. Red arrows point to phase shifts between consecutive scanning lines. (**E**) Intensity profile corresponding to the yellow line in (A). (A) is adapted from Uzun *et al.* [11] — Reproduced by permission of The Royal Society of Chemistry.

> *structural organization of surface chemical groups plays a key role in regulating cell-membrane penetration.*"

In order to study the nanoparticles entry and their intracellular distribution, the authors essentially used confocal fluorescence microscopy and TEM. However, the use of a fluorophore (thiolated BODIPY) to assess the entry of rippled nanoparticles can be considered as equivocal for several reasons. Firstly, the introduction of a new component in the monolayer is likely to modify the monolayer surface organisation by changing the ligands interactions and therefore its supposedly rippled structure. Secondly, the gold core has strong fluorescence quenching abilities and would prevent a significant part — if not all — of the fluorescence from being emitted by the fluorophore. And finally, the colocalisation of the thiolate fluorescent dye and the gold core would need to be proven as it has been shown previously that ligand exchange can occurs with free thiolated ligand present in the cytoplasm, such as glutathione.[26]

The authors described the fluorescence labelling, although they do not answer the above-mentioned concerns expressed. More importantly they do not display the STM images of fluorescently labelled nanoparticles to establish that the nanoparticles display ripples on their surfaces, when the presence of the ripples on the surface of the nanoparticles is the key argument in their explanation of the "cell-membrane penetration" of "structured" mixed ligand shell versus "unstructured" ones.

The experiment from Verma *et al.* were repeated on a different cell line (HeLa), in order to have results that are not inherent to a cell line having peculiar transport mechanisms.[27] Gold nanoparticles were synthesised according to the protocol used by Verma *et al.* Homoligand (100% MUS, 100% OT) and mixed-ligand (1:2 and 2:1 MUS:OT molar ratios) capped gold nanoparticles were prepared according to the protocol described by Verma *et al.* The TEM size characterisation and the resulting size distributions for these four types of nanoparticles are shown in Fig. 5.9, with a nanoparticle mean diameter of 3.2–3.8 nm and polydispersities within 18–29 %.[b]

Further assessment of their colloidal stability was made through a salt-induced aggregation assay. An aggregation parameter is evaluated through the ratio of the absorbance of the colloidal solution at two different wavelengths (λ = 650, 500 nm). The aggregation parameter is increasing monotonously with the degree of aggregation. For clarity in the representation, it has been normalised to the initial value where no salt is present (different nanoparticle sizes create arbitrary vertical shifts between the different curves as λ_{max} is size dependent). At physiological conditions (PBS $\sim$ 0.15 M) the 1:2 MUS:OT molar ratio nanoparticles already show some degree of aggregation (Fig. 5.10, red triangles). Overall the three different capping monolayers all show a poor colloidal stability, and the more OT ligands the monolayer bears (OT is hydrophobic), the smaller the concentration of salt needed to aggregate them is.

Internalisation of three types of nanoparticles (100 % MUS, 2:1 MUS:OT, 1:2 MUS:OT) in HeLa cells was studied by photothermal microscopy (see Chapter 2 for details about the technique), together with a control without nanoparticles. With this technique there is no requirement to include some fluorophores in the monolayer, which would most probably be significantly, if not totally, quenched by the nanoparticles, provided that they would still be bound to them. The signal acquired is therefore unambiguously ascribable to the nanoparticles themselves and proportional to their amount (to the volume of gold present in the focal volume), avoiding the difficult task of justifying the hypothesis of fluorophores-nanoparticles colocalisation.

The MUS/OT capped nanoparticles (100 % MUS, 2:1 MUS:OT, 1:2 MUS:OT) were mixed with medium and incubated with HeLa cells for three hours (400 nM final concentration). They were further washed and fixed before photothermal microscopy imaging.[c]

[b] nanoparticle synthesis, TEM imaging and colloidal stability assay: C. P. Shaw
[c] nanoparticle synthesis: C. P. Shaw; cell work: P. Free

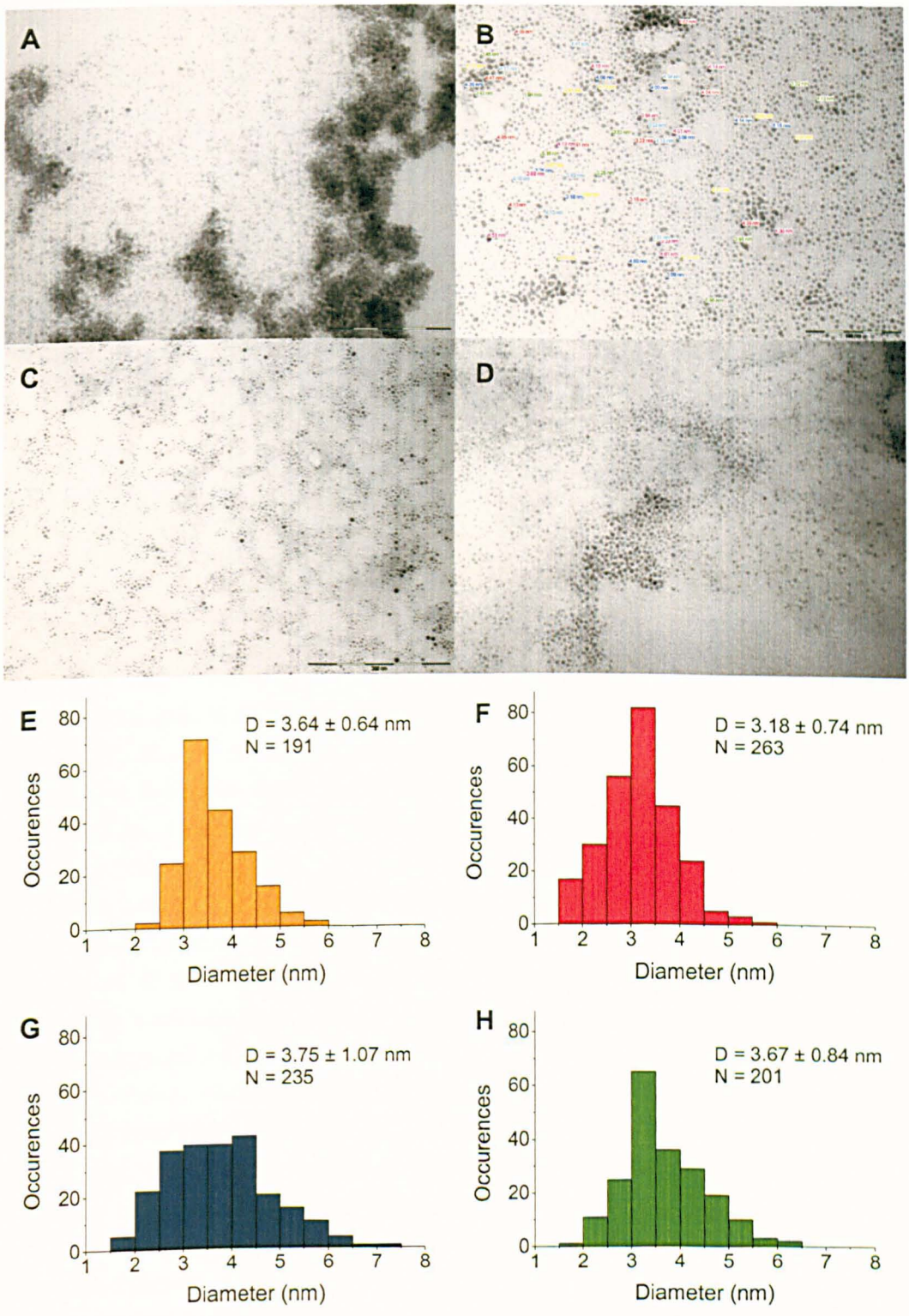

Fig. 5.9 – TEM and size distribution of MUS/OT coated gold nanoparticles. (**A**–**D**) TEM micrographs of gold nanoparticles coated with a SAM comprised of different molar ratios of MUS/OT (C. P. Shaw). (**A**) 100% OT, (**B**) 1:2 MUS:OT, (**C**) 2:1 MUS:OT, (**D**) 100% MUS. (**E**–**H**) Size distributions of gold nanoparticles coated with SAMs comprised of different molar ratios of MUS/OT. (**E**) 100% OT, (**F**) 1:2 MUS:OT, (**G**) 2:1 MUS:OT, (**H**) 100% MUS.

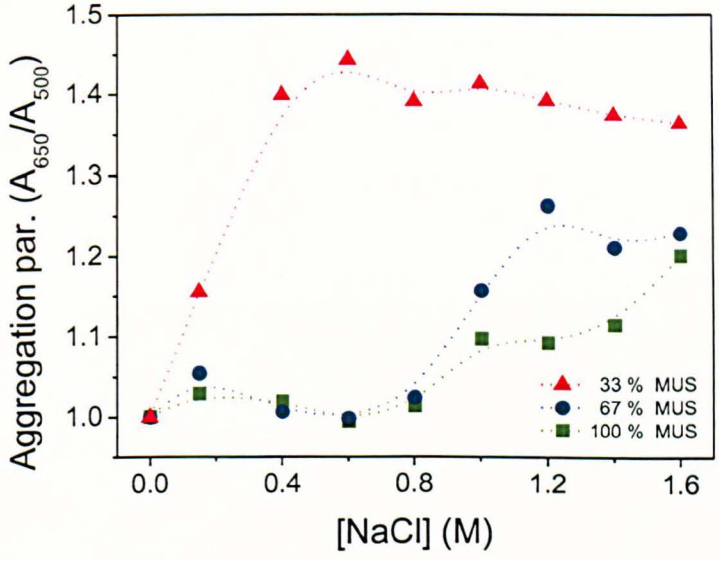

Fig. 5.10 – Colloidal stability of MUS/OT nanoparticles. The stability of a given nanoparticle solution is evaluated through an aggregation parameter (ratio of the absorbance at $\lambda = 650\,\text{nm}$ and at $\lambda = 500\,\text{nm}$) as a function of the concentration of salt (NaCl); Red triangles — 2:1 OT:MUS; Blue circles — 1:2 OT:MUS; Green squares — MUS.

Figure 5.11 is showing the uptake of the three different MUS/OT monolayer compositions (100 % MUS, 2:1 MUS:OT, 1:2 MUS:OT) with three different fields of view ($79.25 \times 79.25\,\mu\text{m}$) for each sample, to show the representativeness of the images. For each field of view an overlay of a bright field image and the corresponding photothermal image is shown, to better see the localisation of the nanoparticles within the cells.

The uptake of the nanoparticles is clearly visible for the three different conditions and well above the negligible cells background (Fig. 5.12). The intracellular localisation of the nanoparticles also show no difference between cells incubated with either homoligand (100 % MUS) or mixed ligand (2:1 MUS:OT, 1:2 MUS:OT) capped nanoparticles.

The contrast was chosen here to be displayed identically between samples for a straightforward visual comparison to be possible. However, the photothermal images have a large dynamical range (16-bit images, 65536 grey values) and are therefore not easily represented by a single snapshot.

Figure 5.13, Fig. 5.14 and Fig. 5.15 show the uptake of the nanoparticles for the three different monolayer compositions in more details. For each field of view, two images and an intensity profile are displayed. The first image is an overlay of a bright field image and the corresponding photothermal image (as in Fig. 5.11), and the second is the photothermal image alone (256×256 pixels, 1 pixel=$0.31\,\mu\text{m}$). The values of the contrast (34–2000) were thus chosen to highlight well the features present in the three different conditions. The intensity profile, corresponding

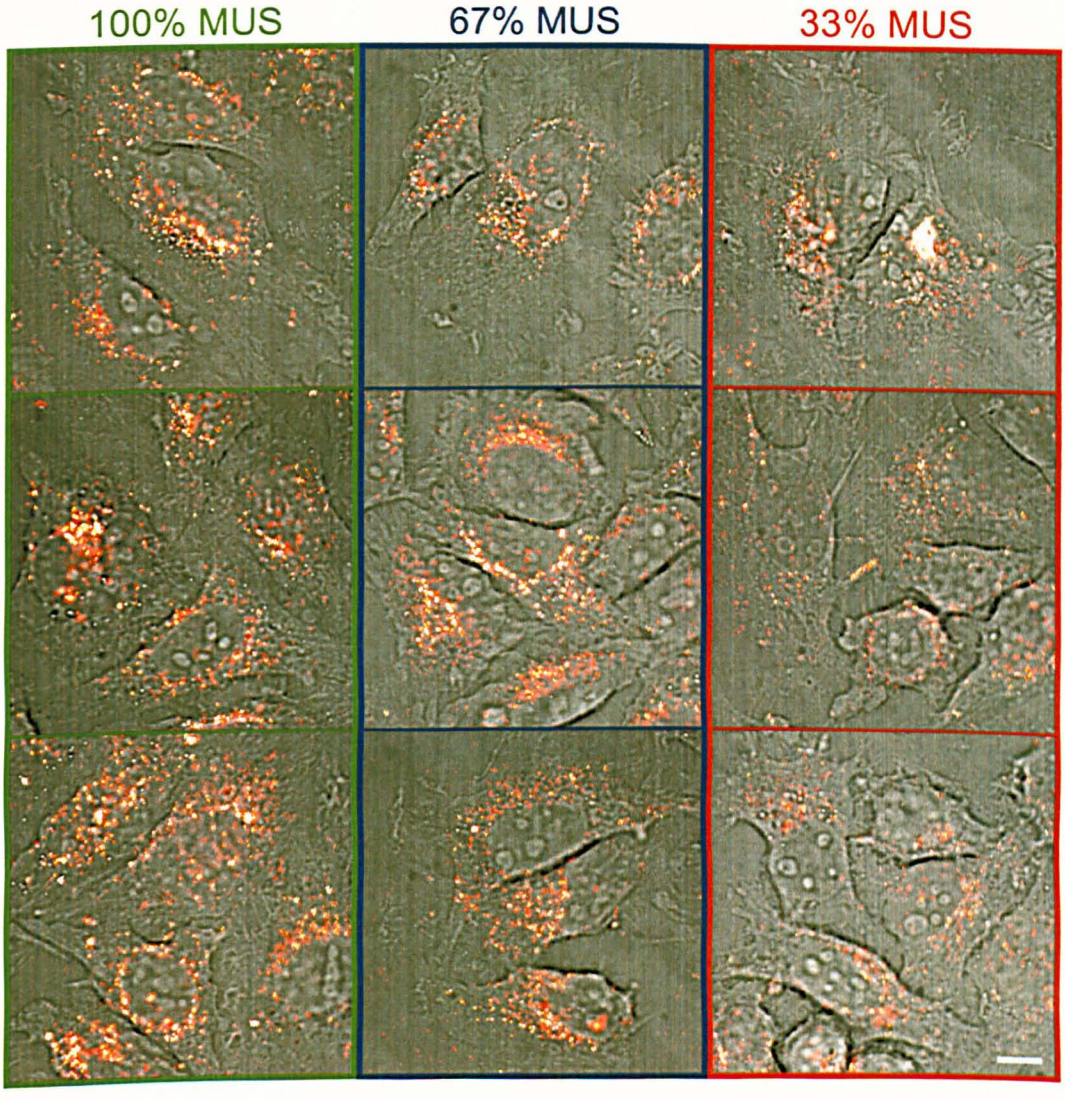

Fig. 5.11 – Internalisation of MUS/OT capped gold nanoparticles in HeLa cells. Overlays of photothermal and bright field images showing the uptake of homoligand (100 % MUS, left) and mixed ligand (2:1 MUS:OT, middle; 1:2 MUS:OT, right) capped gold nanoparticles. The scale bar represents 10 μm.

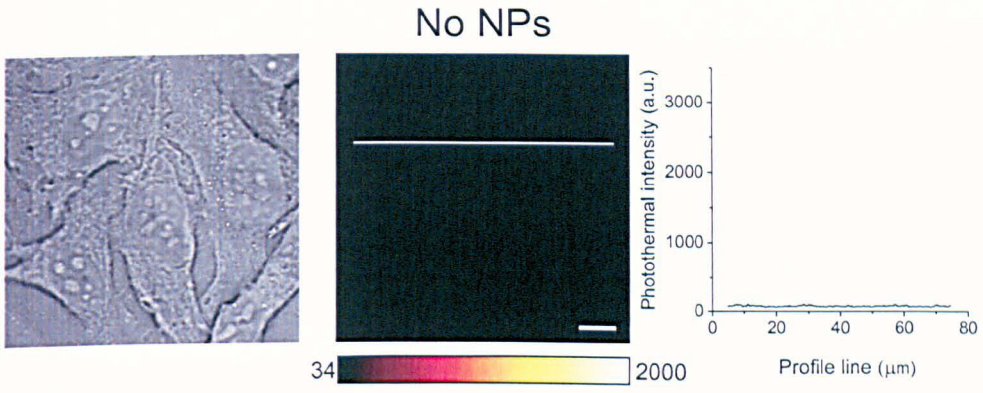

Fig. 5.12 – "Stripy" nanoparticles control: HeLa cells in absence of nanoparticles. Left: overlay of bright field and photothermal images of HeLa cells in absence of nanoparticles; middle: photothermal image of HeLa cells; right: 1D intensity profile section (white line in the photothermal image). The scale bar represents 10 μm.

to the white line drawn in the photothermal image, allows a visualisation of the full range of values in a relevant part of the field of view. It is thus easier to see distinguish between high (endosomes) and low (cytoplasm, nuclei, background) intensities regions within cells. This confirms the characteristic pattern of endocytosis visible in the images, and demonstrate that there is no significant presence of free nanoparticles within the cytoplasm in any of the conditions investigated.

5.3 Conclusion

The evidences for the presence of stripes on gold nanoparticles coated with mixed alkane thiolated ligands published by the group of F. Stellacci in a series of fourteen peer reviewed research article were revisited.

A geometrical argument allowed to show that the regularly spaced patterns present in the STM images, described as stripes, cannot represent regularly spaced ripples at the surface of the gold core. The unequivocal reason to explain that is that ligands regularly spaced in 3D cannot appear as regularly spaced on a 2D projection (STM image). Fast Fourier Transform analysis of the published STM images resulted in exposing what the real nature of the stripes was, a scanning artefact.

Then, homoligand-capped and mixed-ligand-capped gold nanoparticles (MUS/OT) were synthesised as reported by the authors. Their saturation concentration was further evaluated, and OT-capped gold nanoparticles were shown to have a saturation concentration at least eighteen times higher than what had been reported.

Finally, the localisation of MUS and mixed MUS/OT-capped nanoparticles (supposedly "stripy" or not) was observed by photothermal microscopy after their internalisation in HeLa cells. No difference appeared in localisation of the nanoparticles between the different types of monolayer, as all of them displayed a clear endocytosis

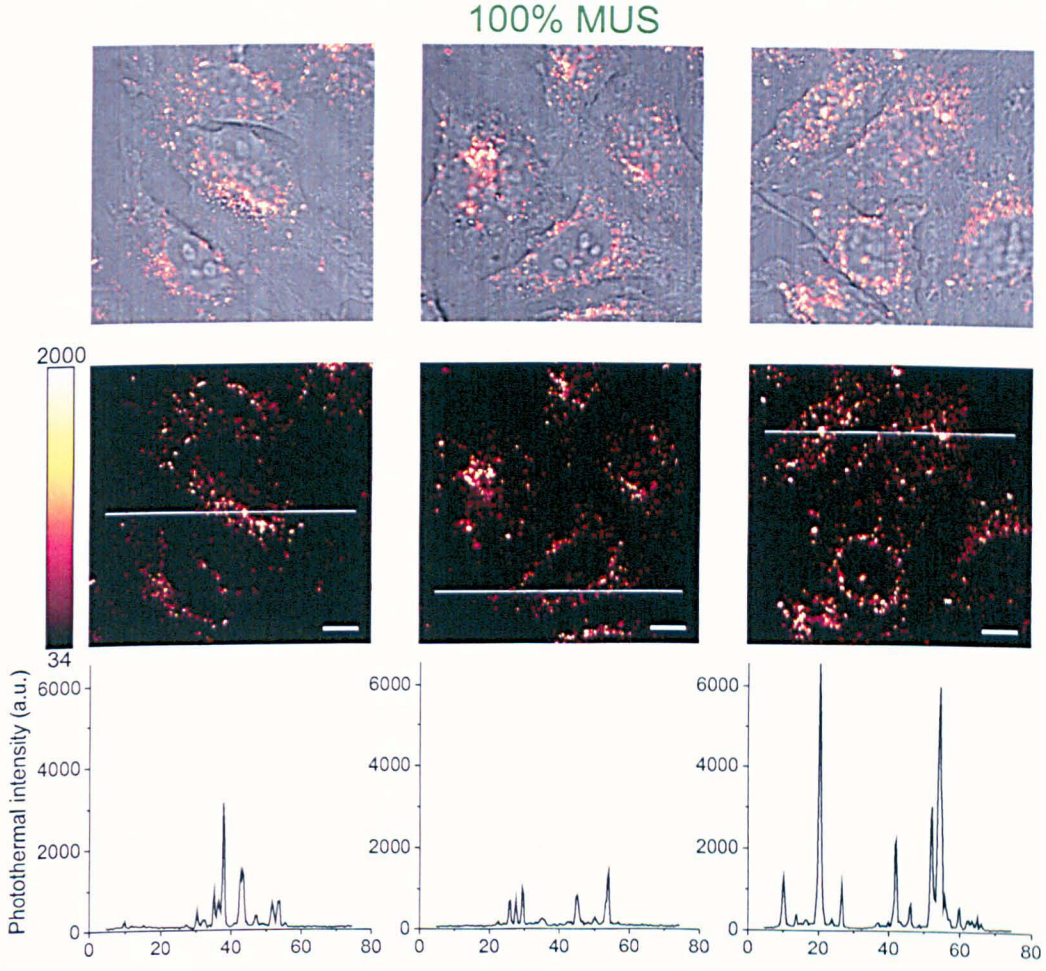

Fig. 5.13 – Internalisation of 100% MUS-functionalised nanoparticles in HeLa cells. From left to right: three different fields of view. Top: overlays of bright field and photothermal images; middle: corresponding photothermal images; bottom: 1D intensity profile sections (white lines in the photothermal images). The scale bars represent 10 μm.

pattern of internalisation, and the presence of cytosolic nanoparticles was ruled out by the measurement accomplished by photothermal microscopy.

Materials and methods available in Appendix B.3

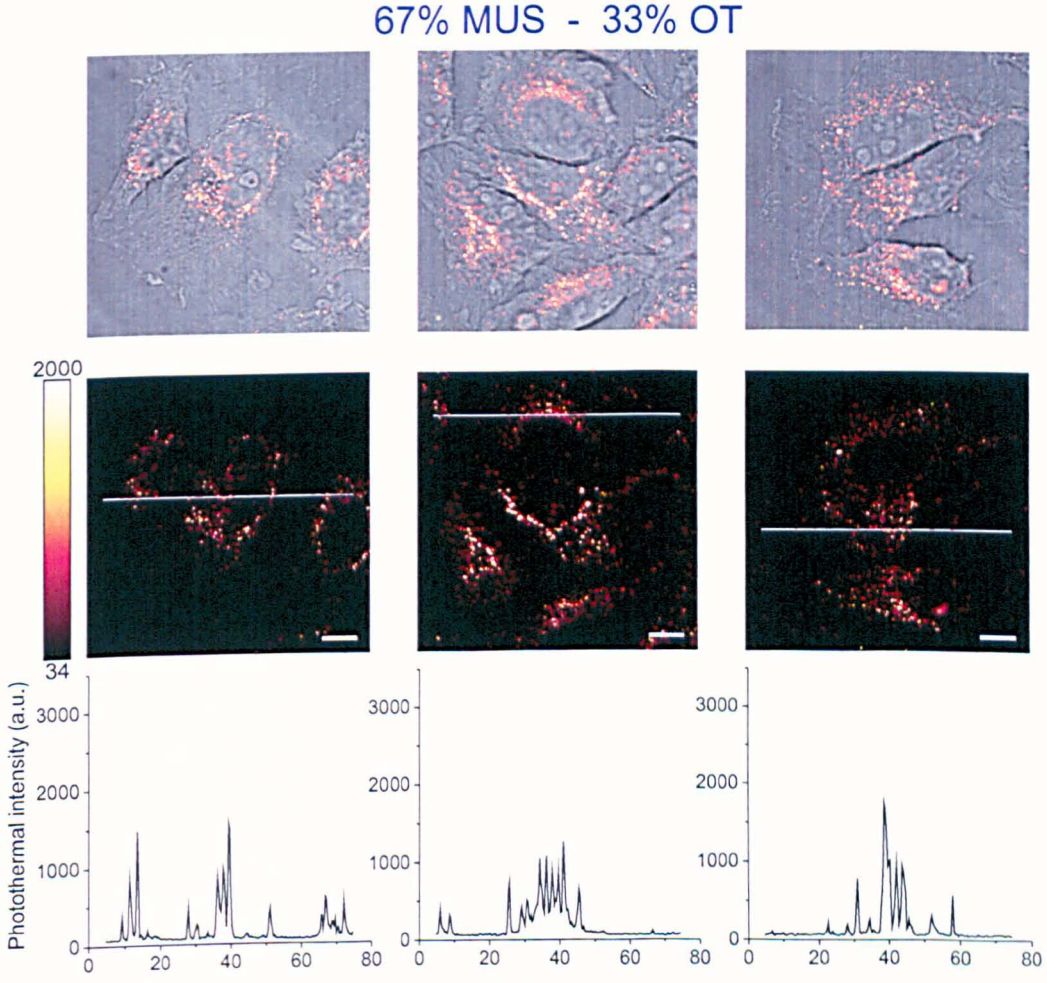

Fig. 5.14 – Internalisation of MUS/OT-functionalised (2:1 molar ratio) nanoparticles in HeLa cells. From left to right: three different fields of view. Top: overlays of bright field and photothermal images; middle: corresponding photothermal images; bottom: 1D intensity profile sections (white lines in the photothermal images). The scale bars represent 10 μm.

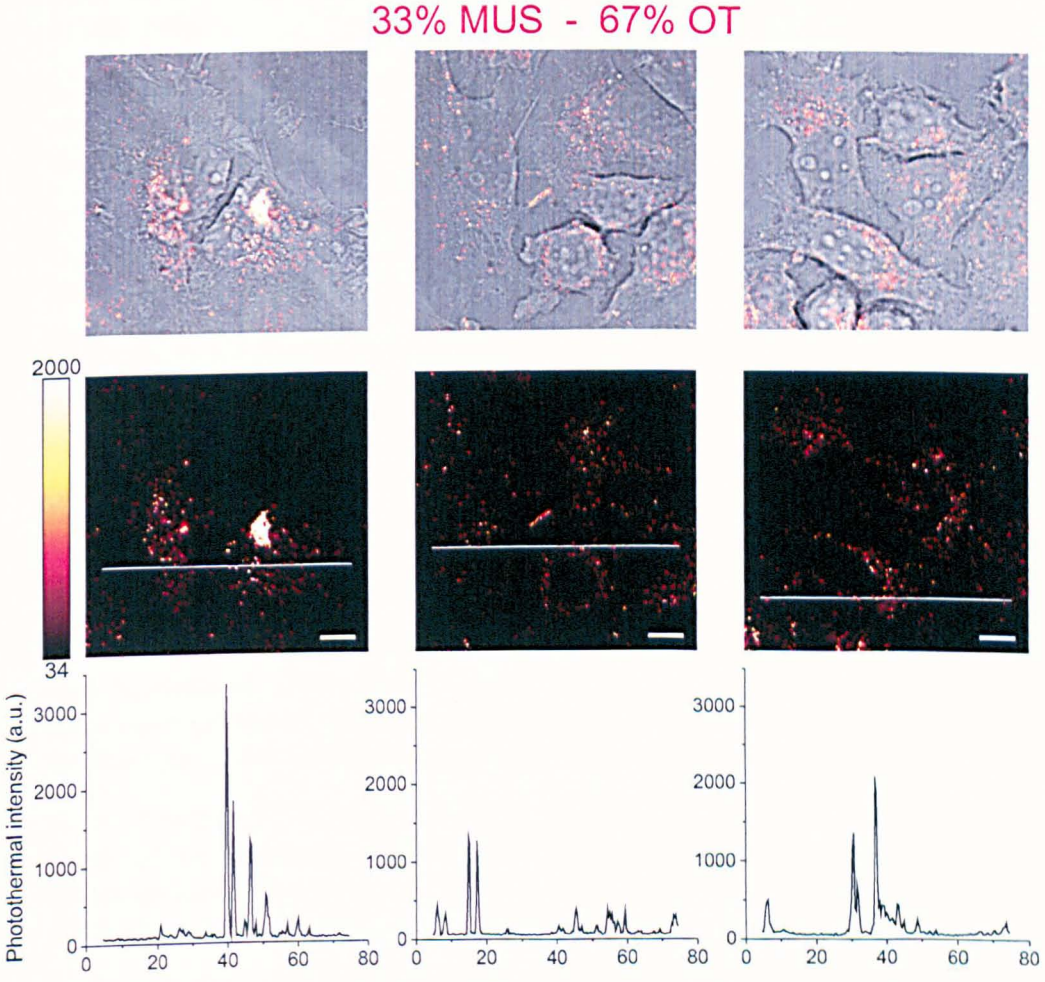

Fig. 5.15 – Internalisation of MUS/OT-functionalised (1:2 molar ratio) nanoparticles in HeLa cells. From left to right: three different fields of view. Top: overlays of bright field and photothermal images; middle: corresponding photothermal images; bottom: 1D intensity profile sections (white lines in the photothermal images). The scale bars represent 10 μm.

5.4 Bibliography

1. A. M. Jackson, J. W. Myerson and F. Stellacci. Spontaneous assembly of subnanometre-ordered domains in the ligand shell of monolayer-protected nanoparticles. *Nature Materials*, 3(5), 330–336, 2004.

2. A. M. Jackson, Y. Hu, P. J. Silva and F. Stellacci. From homoligand- to mixed-ligand-monolayer-protected metal nanoparticles: A scanning tunneling microscopy investigation. *Journal of the American Chemical Society*, 128(34), 11135–11149, 2006.

3. A. Centrone, Y. Hu, A. M. Jackson, G. Zerbi and F. Stellacci. Phase separation on mixed-monolayer-protected metal nanoparticles: A study by infrared spectroscopy and scanning tunneling microscopy. *Small*, 3(5), 814–817, 2007.

4. G. A. DeVries, M. Brunnbauer, Y. Hu, A. M. Jackson, B. Long, B. T. Neltner, O. Uzun, B. H. Wunsch and F. Stellacci. Divalent metal nanoparticles. *Science*, 315, 358–361, 2007.

5. C. Singh, P. K. Ghorai, M. A. Horsch, A. M. Jackson, R. G. Larson, F. Stellacci and S. C. Glotzer. Entropy-mediated patterning of surfactant-coated nanoparticles and surfaces. *Physical Review Letters*, 99(22), 226106, 2007.

6. R. P. Carney, G. A. DeVries, C. Dubois, H. Kim, J. Y. Kim, C. Singh, P. K. Ghorai, J. B. Tracy, R. L. Stiles, R. W. Murray, S. C. Glotzer and F. Stellacci. Size limitations for the formation of ordered striped nanoparticles. *Journal of the American Chemical Society*, 130(3), 798–799, 2008.

7. A. Centrone, E. Penzo, M. Sharma, J. W. Myerson, A. M. Jackson, N. Marzari and F. Stellacci. The role of nanostructure in the wetting behavior of mixed-monolayer-protected metal nanoparticles. *Proceedings of the National Academy of Sciences of the United States of America*, 105(29), 9886–9891, 2008.

8. G. A. DeVries, F. R. Talley, R. P. Carney and F. Stellacci. Thermodynamic Study of the Reactivity of the Two Topological Point Defects Present in Mixed Self-Assembled Monolayers on Gold Nanoparticles. *Advanced Materials*, 20(22), 4243–4247, 2008.

9. Y. Hu, O. Uzun, C. Dubois and F. Stellacci. Effect of ligand shell structure on the interaction between monolayer-protected gold nanoparticles. *Journal of Physical Chemistry C*, 112(16), 6279–6284, 2008.

10. K. Nakata, Y. Hu, O. Uzun, O. Bakr and F. Stellacci. Chains of Superparamagnetic Nanoplarticles. *Advanced Materials*, 20(22), 4294–4299, 2008.

11. O. Uzun, Y. Hu, A. Verma, S. Chen, A. Centrone and F. Stellacci. Water-soluble amphiphilic gold nanoparticles with structured ligand shells. *Chemical Communications*, (2), 196–198, 2008.

12. A. Verma, O. Uzun, Y. H. Hu, Y. Hu, H. S. Han, N. Watson, S. L. Chen, D. J. Irvine and F. Stellacci. Surface-structure-regulated cell-membrane penetration by monolayer-protected nanoparticles. *Nature Materials*, 7(7), 588–595, 2008.

13. Y. Hu, B. Wunsch, S. Sahni and F. Stellacci. Statistical Analysis of Scanning Tunneling Microscopy Images of 'Striped' Mixed Monolayer Protected Gold Nanoparticles. *Journal of Scanning Probe Microscopy*, 4(1), 24–35, 2009.

14. J. J. Kuna, K. Voitchovsky, C. Singh, H. Jiang, S. Mwenifumbo, P. K. Ghorai, M. M. Stevens, S. C. Glotzer and F. Stellacci. The effect of nanometre-scale structure on interfacial energy. *Nature Materials*, 8(10), 837–842, 2009.

15. F. Manea, F. B. Houillon, L. Pasquato and P. Scrimin. Nanozymes: gold nanoparticle-based transphosphorylation catalysts. *Angewandte Chemie International Edition*, 43(45), 6165–6169, 2004.

16. A. E. Nel, L. Madler, D. Velegol, T. Xia, E. M. V. Hoek, P. Somasundaran, F. Klaessig, V. Castranova and M. Thompson. Understanding biophysicochemical interactions at the nano-bio interface. *Nature Materials*, 8(7), 543–557, 2009.

17. V. Sée, P. Free, Y. Cesbron, P. Nativo, U. Shaheen, D. J. Rigden, D. G. Spiller, D. G. Fernig, M. R. H. White, I. A. Prior, M. Brust, B. Lounis and R. Lévy. Cathepsin L Digestion of Nanobioconjugates upon Endocytosis. *ACS Nano*, 3(9), 2461–2468, 2009.

18. A. Badia, S. Singh, L. Demers, L. Cuccia, G. R. Brown and R. B. Lennox. Self-assembled monolayers on gold nanoparticles. *Chemistry - A European Journal*, 2(3), 359–363, 1996.

19. N. Sandhyarani, T. Pradeep, J. Chakrabarti, M. Yousuf and H. K. Sahu. Distinct liquid phase in metal-cluster superlattice solids. *Physical Review B*, 62(2), R739–R742, 2000.

20. H. Hakkinen, R. N. Barnett and U. Landman. Electronic structure of passivated Au-38(SCH3)(24) nanocrystal. *Physical Review Letters*, 82(16), 3264–3267, 1999.

21. P. K. Ghorai and S. C. Glotzer. Molecular dynamics simulation study of self-assembled monolayers of alkanethiol surfactants on spherical gold nanoparticles. *Journal of Physical Chemistry C*, 111, 15857–15862, 2007.

22. Y. F. Wang, A. Neyman, E. Arkhangelsky, V. Gitis, L. Meshi and I. A. Weinstock. Self-Assembly and Structure of Directly Imaged Inorganic-Anion Monolayers on a Gold Nanoparticle. *Journal of the American Chemical Society*, 131(47), 17412–17422, 2009.

23. D. Hobara, S. Imabayashi and T. Kakiuchi. Preferential adsorption of horse heart cytochrome c on nanometer-scale domains of a phase-separated binary self-assembled monolayer of 3-mercaptopropionic acid and 1-hexadecanethiol on Au(111). *Nano Letters*, 2(9), 1021–1025, 2002.

24. J. Satulovsky, M. A. Carignano and I. Szleifer. Kinetic and thermodynamic control of protein adsorption. *Proceedings of the National Academy of Sciences of the United States of America*, 97(16), 9037–9041, 2000.

25. S. Kidoaki and T. Matsuda. Adhesion forces of the blood plasma proteins on self-assembled monolayer surfaces of alkanethiolates with different functional groups measured by an atomic force microscope. *Langmuir*, 15(22), 7639–7646, 1999.

26. G. Han, N. S. Chari, A. Verma, R. Hong, C. T. Martin and V. M. Rotello. Controlled recovery of the transcription of nanoparticle-bound DNA by intracellular concentrations of glutathione. *Bioconjugate Chemistry*, 16(6), 1356–1359, 2005.

27. J. Imai, H. Hasegawa, M. Maruya, S. Koyasu and I. Yahara. Exogenous antigens are processed through the endoplasmic reticulum-associated degradation (ERAD) in cross-presentation by dendritic cells. *International Immunology*, 17(1), 45–53, 2005.

Chapter 6

Active delivery of gold nanoparticles

Introducing nanomaterials in cells can be easily achieved in most cases by means of endocytosis. However, the nanometre sized objects introduced inside cells in this manner, and gold nanoparticles in particular, cannot readily access the cell cytosol. Indeed, indirect cytoplasm delivery strategies aiming either to escape from the endosomes using endosomes disrupting drugs or virus derived fusion peptides or to bypass endocytosis in a cell membrane pore formation mediated entry have not yet proven to allow for an evenly distributed, endosome-free, localisation of gold nanoparticles in the cytosol.

Under those circumstances more direct and pro-active nanoparticles internalisation processes requiring physical action such as a mechanical maneuver for microinjection, or an electromagnetic wave stimulus for electroporation, or even a photophysical operation for polyelectrolyte microcapsule cargo release mediated delivery could provide alternative solutions.

Microinjection allow the internalisation of small molecules or nanoparticles in cells via a micropipette, which upon introduction of its thin tip across the plasma membrane deliver the cargo in the cytoplasm or nuclei of targeted individual cells. Mei *et al.* developed DHLA[a]-PEG ligands shell allowing gold nanoparticles and quantum dots (QDs) to remain stable over an extended pH range[1]. They demonstrated the internalisation of DHLA–PEG–OCH_3–QDs by microinjection in monkey kidney COS-1 cells and showed that a significant proportion of the quantum dots retained a cytosolic localisation for up to 32 hours. Wang *et al.* have been microinjecting gold nanoparticles (40 nm) for SERS (Surface Enhanced Raman Spectroscopy) imaging[2] in zebrafish embryos by means of a micropipette and McDougall *et al.* have used an unusual optoinjection[b] to demonstrate the internalisation of

[a] dihydrolipoic acid

[b] injection by means of optical tweezers

single 100 nm gold nanoparticles in the nucleus of Chinese hamster ovary K1 cells.[3]

Electroporation consists in applying short electrical field pulses that create transient pores in the cell membrane (see Gehl[4] for a review). It was shown to successfully internalise fluorescently labelled antibodies or dextrans in mammalian cells,[5,6] which entered by diffusion. It has also been widely used to transfect DNA in mammalian cells, where internalisation of the highly charged molecule was shown to be favoured by the electrical field,[7] or for the uptake of oligonucleotides.[8] Chen *et al.* have applied this technique to internalise NLS peptides (SV40 nuclear localisation signal peptide) functionalised quantum dots in HeLa cells and observed both perinuclear and nuclear localisations of the NLS conjugated nanocrystals.[9]

Electroporation has not been extensively used for metal nanoparticle delivery, although an example can be found in the study of Lin *et al.* who used it to deliver bare 60 nm silver nanoparticles for SERS imaging.[10] However, although the nanoparticles were apparently localised in the cell cytosol (one TEM micrograph), they were aggregated in clusters of a several hundred nanometres.

Recently fluorescently labelled dextrans were shown to be released from polymer microcapsules by photophysical means inside live cells,[11] which opens a potential new route of cytosolic nanoparticle delivery. This chapter will therefore focus on the use of polyelectrolyte multilayer microcapsules as container for intracellular cargo delivery. After reviewing the potential of microcapsules composed of polyelectrolyte multilayers as delivery vehicles, the laser photophysical mediated damaging process of its polymer shell will be examined.

6.1 Polyelectrolyte microcapsule mediated delivery

Multilayer polyelectrolyte microcapsules were first introduced in 1998 by Donath *et al.*[12] and have emerged recently in the field of drug delivery as potential cargo vehicle. They are derived from the concept of layer-by-layer[13] (LbL) assembly of polyelectrolytes of opposite charges on a charged surface. Briefly, a charged surface of choice is incubated in an aqueous solution with a polyelectrolyte of an opposite charge and left to adsorb on the surface, then washed to remove the excess polymer and incubated in a solution containing an other type of polyelectrolyte with a charge opposite to the one of the first polymer, which in turn adsorbs on the polyelectrolytes of the first layer. The surface is again washed to remove the excess polymer and subsequent baths in oppositely charged polyelectrolytes can be continued until the desired number of layer is obtained. Consequently, it allows to choose the charge of the surface of the multilayer assembly through the one of the last deposited polyelectrolyte. This assembly process was first applied to flat surfaces, and is utilised to build polymer microcapsule. The process first consists in using the surface of a colloid as a template for a polyelectrolyte multilayers and proceed to the deposition of

the desired number of layers, to create a core-shell polymer microcapsule. Then, the colloid is removed by dissolution in acidic or aqueous solutions, depending on the core material, to yield to a hollow polymer microcapsule. The size of the microcapsule can be tuned over a full order of magnitude by adequately choosing the type of the colloidal template, from a few tenth of nanometres with silica nanoparticles[14] to a few micrometres with organic cores such as melamine formaldehyde[12] or inorganic crystals such as calcium carbonate.[15]

The composition of the microcapsule shell, integration of various elements in the walls or loading of the internal cavity can also be adapted to fulfil different requirements. Rivera-Gil *et al.* have for example used degradable dextran sulfate/poly-L-arginine microcapsule to demonstrate the intracellular fluorescence unquenching of DQ dyes previously linked to the protein ovalbumin upon proteolysis.[16] Gold nanoparticles[11], magnetic nanoparticles[17] or quantum dots[18] can be inserted in the walls of the polymer shell during the LbL assembly process. The introduction of gold nanoparticles within the polymer shell was shown to allow the intracellular release of fluorescently labelled dextrans upon illumination of the wall. Finally, the cavity can be loaded with various molecules, from fluorescent dyes,[11] to DNA[19], via a permeability that can be induced for example by a change of pH,[20] or temperature.[21] Kreft *et al.* used PSS[c]/PAH[d] microcapsule loaded with the pH-sensitive SNARF-1 fluorescent dye to show the local pH decrease upon acidification of the endosomal compartments in which the microcapsules where located.[22]

6.2 Laser irradiation microcapsule opening assay

In order to use the microcapsule as delivery agents, their content need to be released in the cytoplasm once they are inside the cells. To achieve this goal, the strategy chosen was to provoke a local temperature increase within the capsule wall upon illumination, to lead to its rupture.

Although the mechanism has not been studied throughout, it was shown to work. Javier *et al.* have used fluorescently labelled dextrans (Alexa Fluor 594 or Cascade Blue) encapsulated in microcapsules composed of multilayers of the two polyelectrolytes PDADMAC[e] and PSS with gold nanoparticles included in the walls to demonstrate the opening possibilities. A 830 nm wavelength laser illumination was used to open the microcapsule internalised in live MDA-MB-435s breast cancer cells by endocytosis. They showed that a power of 0.7 mW was not enough to release the dextran in the cytoplasm, but a power of 2.3 mW did actually provide a clear cytosolic distribution of the fluorophores.[11] The release process is thought to be

[c]PSS: poly(styrene sulfonate)
[d]PAH: poly(allylamine hydrochloride)
[e]PDADMAC: poly(diallyl dimethyl ammonium chloride)

the result of the capsule wall and endosome membrane damage subsequent to the heating of the nanoparticles present in the capsule wall upon laser illumination.

The capsules that were used in the present study were composed of different polyelectrolytes $(PSS/PAH)_5$, with nanoparticles pre-loaded inside the microcapsule cavity, and the laser illumination wavelengths available to open the capsules on the Liverpool photothermal microscope set up were different and limited to 633 nm and 523 nm. Therefore it was proceeded to an evaluation of the power necessary to open the capsules. In a first step a decision was made to examine the opening process using a HeNe laser (633 nm) as microcapsule wall damaging tool and for which the maximum power available was around 20 mW. However, this power is the output at the exit of the laser and due to the combination of optics on its path the maximum power at the entry of the microscope is going down to ~ 18.7 mW. At the output of the microscope objective used for this study (50×/0.9 NA) the maximum power is in turn again significantly lowered to a value of ~ 10.7 mW.

Although the plasmon band of individual nanoparticles included in the cavity of the microcapsules would have a peak wavelength better triggered by a laser of a 523 nm wavelength for nanoparticles heating by photothermal effect, the decision was made to use a wavelength of 633 nm. The first reason for this choice was coming from the perspective of intracellular microcapsule opening, for which a wavelength in the red would be less likely to be harmful for the cells. Furthermore, if some nanoparticles are aggregated on the wall, due to the core removal process, they should have an absorption peak that shifts towards the red and therefore a higher wavelength may be more suitable for their heating.

To assess the potential damages generated by laser illumination to polyelectrolyte microcapsules, positively charged (PAH outside layer) $(PSS/PAH)_5$ microcapsules composed of ten alternating layers of the two polyelectrolytes PSS and PAH and 20 nm diameter gold nanoparticles pre-loaded in the cavity,[f] were left to adsorb on the glass coverslip of an ultra-pure deionised water filled Iwaki dish for ~ 30 minutes. To open the capsules the approach chosen was to use a continuous wave (CW) HeNe laser irradiation immobile and focused on the wall of the capsules (Fig. 6.2A) as a tool to open them. After some initial tests, a power of 3.6 mW, as measured at the output of the objective, was first examined for capsule illumination, with an exposure time of 100 ms. The criterion used to judge whether the illumination had an effect on the microcapsule wall or not was to visually appraise if the appearance of the wall had changed in the area where the capsule was exposed. This was accomplished by comparing images extracted of movies acquired before, during and after the illumination by bright field microscopy. Fifteen capsules were exposed to a series of five illumination on the side of their wall, separated by a moment (typically 1-10 s) and a movie was acquired continuously at the same time. After a single

[f]microcapsule preparation: L. del Mercato

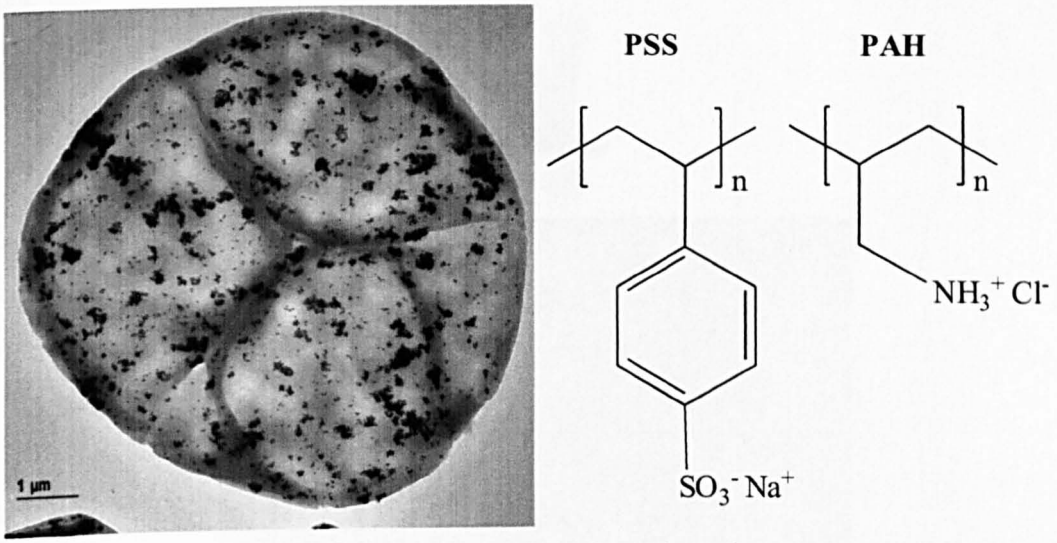

Fig. 6.1 – TEM image of a polyelectrolyte $(PSS/PAH)_5$ microcapsule containing gold nanoparticles in the cavity. Left: A droplet of an aqueous solution containing the poly(styrene sulfonate) /poly(allylamine hydrochloride) (PSS/PAH) polyelectrolyte multilayer microcapsules was deposited on a carbon coated grid and evaporated under vaccum before TEM imaging. Right: schemes of the PSS and PAH polyelectrolytes. Image courtesy of W. Parak.

illumination of 100 ms, only one microcapsule out of 15 did show a change in its shape. After five illuminations the situation did not change for the other fourteen microcapsules, with none of them displaying a visible shape change. The capsule that showed a change in its shape after the first illumination did exhibit a partial rupture of its wall at the place were it was exposed to the laser after the fourth illumination (Fig. 6.2B-G).

As 3.6 mW were not enough to obtain a wall damage on a significant number of microcapsules, a second assessment was made on fifteen other microcapsules with a laser power of 10.7 mW (maximum intensity available). The outcome was this time more conclusive as 80 % of the microcapsules did present a change in their shape after one illumination. The degree of the shape modification was different from one capsule to the other with moderate shape changes (Fig. 6.3A–B), stronger alterations for a few others (Fig. 6.3C) and what appeared microscopically as a damaged shell was observed for 20 % of all the microcapsules (Fig. 6.3D–E).

Further illumination of the microcapsules that were presenting a change in their shape without appearing microscopically as damaged did not provoke a rupture of their shell after at least three other illuminations on the same area[g]. Similarly, only one of the microcapsules that appeared not visibly changed after the first illumination showed a change after further illuminations (see Tab. 6.1 for a summary).

The method used to assess the conformational changes of the microcapsules relied

[g] not included in the statistics as one capsule was only exposed once after the first exposure

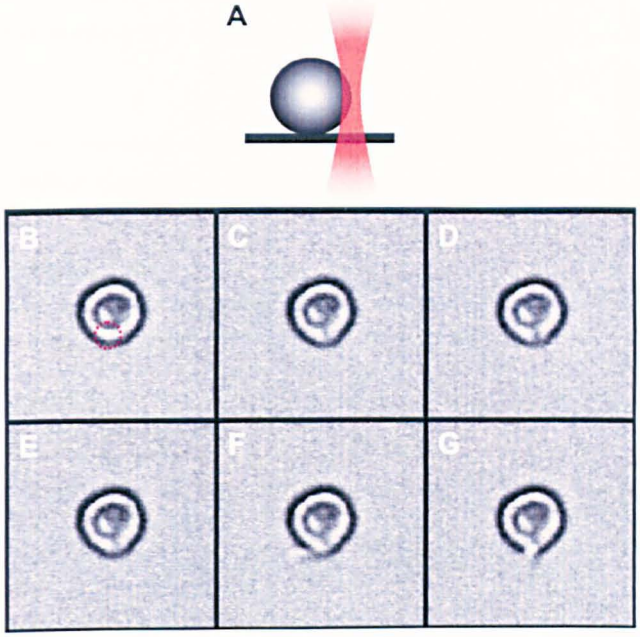

Fig. 6.2 – Polymer microcapsule damage induced by CW HeNe laser (3.6 mW) exposures. A polymer microcapsule adsorbed on the glass coverslip of an ultra-pure water filled Iwaki dish was exposed to successive 100 ms laser exposures (633 nm, CW) focused on the side of the capsule wall at the power of 3.6 mW until a damage of the shell could be observed. (**A**) Schematic of a microcapsule as seen from a plane perpendicular to the glass slide, showing a laser exposure on capsule wall. (**B**) Bright field image of the capsule before irradiation. (**C–G**) Bright field of the same capsule as in (A), respectively after the first, second, third, fourth and fifth 100 ms HeNe laser exposure (3.6 mW). The area exposed to the laser light source before the frames shown in (C–G) is highlighted by a red doted line circle in (B).

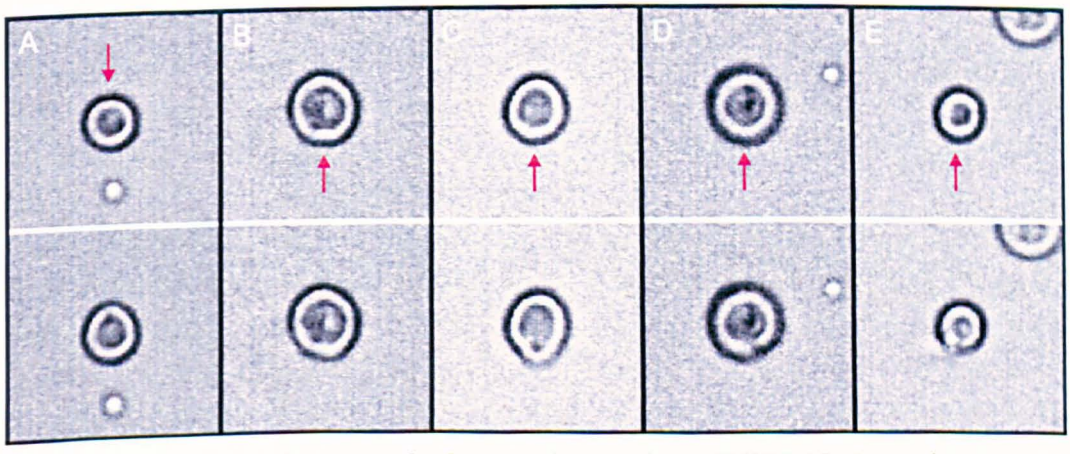

Fig. 6.3 – Polymer microcapsule damage induced by CW HeNe laser (10.7 mW) exposures. Five different polymer microcapsules adsorbed on the glass coverslip of an ultra-pure water filled Iwaki dish were each exposed to a single 100 ms laser exposure (633 nm, CW) focused on the side of the capsules wall at the power of 10.7 mW. (**A–E**) Bright field images of the microcapsule before (top) and after (bottom) the laser exposure (100 ms, 633 nm, 10.7 mW), showing different degree of damage: (**A–B**) moderate wall shape change; (**C**) stronger shape alteration; (**D–E**) microscopically visibly damaged shell. The area exposed to the laser light source between the top and bottom frames shown in (A–E) is pointed by a red arrow.

Laser exposure effect	Laser power (mW)	
	3.6	**10.7**
No visible change (after one exposure)	93 %	20 %
Modified shape		
after a single exposure	7 %	80 %
after four exposures	7 %	87 %
Damaged shell (counted in modified shape)	0 %	20 %

Tab. 6.1 – Laser exposure power dependence on polymer microcapsules shell impairment. The change in polymer microcapsules shape was observed by bright field microscopy before and after the illumination of the side of their shell with a focused CW HeNe laser beam at a power of either 3.6 mW or 10.7 mW. At the power of 3.6 mW most capsules did not exhibit any change, when most capsules did at 10.7 mW. The statistics were performed on populations of 15 microcapsules.

on microscopical observations and yet does not allow to determine unambiguously if a cargo present inside the microcapsule could be released. It is reasonable though to consider that it would happen for the capsules that presented a damaged shell, with visible polymer displaced from the shell. However, further evidences would be needed to determine if that could also happen for the microcapsules that did only show a change of their shape. This microscopically visible shape change could for example have led to a local porosity of the microcapsules, which could not be probed within these experiments, or even have induced a damage to the shell that was not visible with the microscopy technique used for this study. Alternatively, a transient porosity of the microcapsules could happen during the illumination, as suggested by Bedard *et al.*[23], and would not be detected here.

Further investigations of the opening process were initiated using similar PSS/PAH microcapsules containing gold nanoparticles in their walls and FITC-conjugated dextrans (500 kDa) in their cavities. However, the opening process had to be proceeded to with a different wavelength as the nanoparticles present in the walls were distributed in a dispersed manner, with an absence of aggregates (different production method). To achieve the damage on the capsules the frequency doubled Nd:YLF laser with an output wavelength of 523 nm (CW mode) was therefore used on the photothermal microscope. However, as the fluorescent dye (FITC) functionalised to the dextrans has a not negligible absorption at 523 nm, the illumination necessary to damage the capsules walls would also quench the dyes. This disallowed to distinguish between quenching and release of the dextrans upon microcapsule damage and the assessment of the release from the capsules could not be accomplished conclusively.

However, a selective photobleaching induced on the capsule wall or in the centre of the capsule achieved with the help of a confocal microscope showed no redistribution of fluorophores from the walls to the centre of the capsule. This allowed to determine that an immobile fraction of FITC-conjugated dextrans were either adhering to the inside part of the microcapsules wall or most probably were inserted within the walls where they stayed prisoners during the encapsulation of the dextrans. Indeed, to achieve the encapsulation the polyelectrolytes need to reach their glass transition temperature and allow the dextrans to enter the microcapsules cavities before being returned to their initial state when some of the dextrans could be kept captive within the polyelectrolyte multilayer assembly.

Recently, Dan Nieves and Raphaël Lévy were able to establish conclusively the opening of similar capsules with DyLight405-conjugated dextrans in their cavities with a power of 7.9 mW using the frequency doubled Nd:YLF laser (523 nm) of the photothermal set up. Nevertheless, this power is typically not bearable by the cells and a different wavelength would be needed for microcapsule opening within cells if such a power is necessary.

6.3 Microcapsule targeted opening: a realistic objective?

6.3.1 Nanoparticles distribution within a microcapsule

The illumination of polyelectrolyte microcapsules shell with a focused CW HeNe laser has shown the potential to provoke some damage on the shell with a power of 10.7 mW. However, the response of the capsules to the illumination was not boolean, as some capsules appeared damaged while others were only displaying a change of their shape and some others did not show any visible change (by bright field microscopy).

Increasing the power used to damage the microcapsule would quite certainly provide more efficiency in the damaging process, but this was not possible with the set up that was available in Liverpool. Additionally, limiting the illumination power in the view of providing a microcapsule cargo release within cells would be beneficial, as it could limit the potential harm to the cells.

A more efficient way of inducing the damage to the capsule shell could thus be explored using the same laser power as previously (10.7 mW). Indeed, if the damage process is directly linked to the heating provided locally by the illumination through nanoparticles adsorbed to the capsules walls, then targeting areas of the capsules retaining a higher density of nanoparticles could contribute to a more efficient damage of the shell.

To test that hypothesis a microcapsule adhering to the glass coverslip of a dish filled with deionised ultra-pure water was imaged by photothermal microscopy, to

establish a map of the local relative density of nanoparticles within the shell and identify the places where the density was the highest. In order not to damage the microcapsule during the acquisition of the photothermal images, the power of the probe beam was reduced to a value of 0.86 mW (output of the objective), which is less than a fourth of the smaller intensity examined during the microcapsule opening assay (3.6 mW), and that led to a single capsule damage out of attempts on fifteen of them.

Photothermal images of the microcapsule were acquired at different altitudes (z=0, 1, 2, 4 μm), where the origin of the altitude was defined at the capsule larger diameter in the direction perpendicular to the glass coverslip (Fig. 6.4A), as evaluated by focusing in bright field microscpoy.

The photothermal images presented in Fig. 6.4B were acquired with a 10 ms integration time per pixel, as for all images in this manuscript, but here the width of a pixel was only about 50 nm. It generated a significant misalignment between even and odd scanning lines,[h] which needed to be corrected to allow a meaningful display of the images. A software modification was therefore applied to the images to partially compensate the misalignment caused by a synchronisation issue during the process of image acquisition.

The images are displayed with four different contrasts ranges to better estimate the relative density of nanoparticles between different areas of the microcapsule. The photothermal intensity appear unevenly distributed along the perimeter of the microcapsule, showing a high nanoparticles density in some areas alongside weaker ones, which are still witnessing high content of nanoparticles as can attest the display of the smaller contrast range [0,5000].

The comparison of the images of the microcapsule at different altitudes also allows an estimation of the relative altitude between different areas of the microcapsule wall. For example, the photothermal intensity of the area *b* pointed by a white arrow in Fig. 6.4B is increasing between the altitude z=0 μm and z=1 μm and then decreasing between z=1 μm and z=2 μm, which tends to suggest that this cluster of aggregated nanoparticles is located at the top of the capsule. Similarly, the photothermal intensity of area *a* pointed by a grey arrow in Fig. 6.4B is decreasing with the altitude, which enables to state that the area *b* is positioned above the area *a*, and is probably located at the bottom of the capsule, towards the glass coverslip.

Additionally, the apparent diameter of the microcapsule does not decrease when the images are acquired at higher altitudes (z=1, 2 μm) than the origin, as it should happen if the volume of detection was possessing a very sharp vertical resolution. Instead the intensity of most areas decreases, to exception of the ones that are getting more in focus when the altitude is increased (as area b), to fade significantly

[h] this is due to a synchronisation issue during the image acquisition and has been solved since then

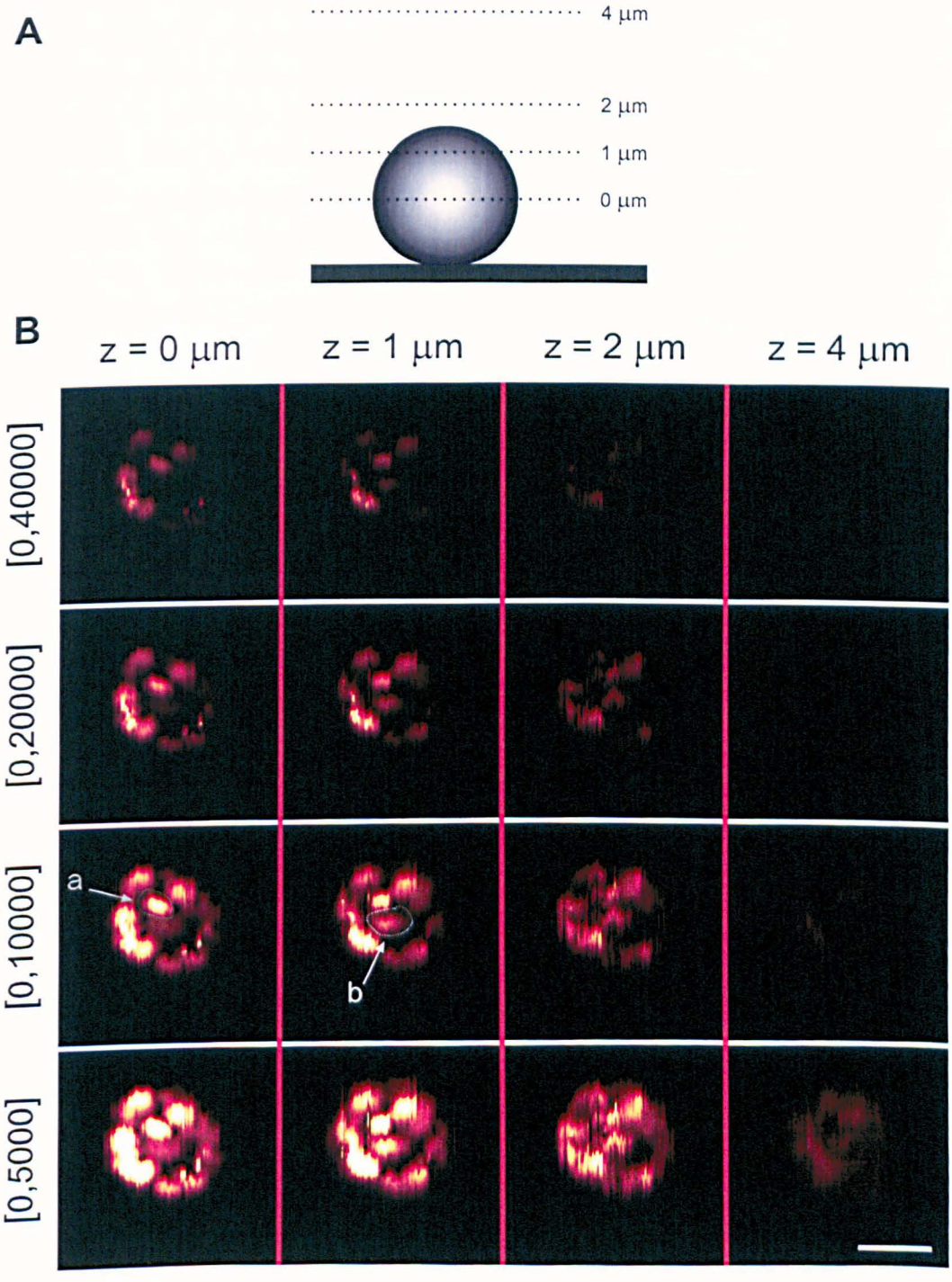

Fig. 6.4 – Photothermal images of a polymer microcapsule.
(**A**) Schematic of a polymer microcapsule as seen from a plane perpendicular to the glass slide. The origin of the altitude (z=0) of the frame of reference for photothermal microscopy imaging was chosen at the larger diameter of the capsule. Photothermal images were then acquired at the altitude of 0, 1, 2 and 4 μm. (**B**) A polymer microcapsule adsorbed on the glass coverslip of an ultra-pure water filled Iwaki dish was imaged by photothermal microscopy at the altitude of 0, 1, 2 and 4 μm (images from left to right). Different contrasts (from top to bottom) are presented for each altitude to appraise the different range of intensities that are appearing on the images. Area *a* and *b* are located respectively at the bottom and the top of the microcapsule. The scale bar represents 2 μm.

at the altitude of 4 μm, as predictable from a theoretical ellipsoid-shaped (prolate spheroid) detection volume[24].

Markedly, the photothermal signal measured at the altitude of 2 μm present a diminished intensity at the microcapsule perimeter, but is still significantly visible. Likewise, a photothermal signal is still present at the altitude of 4 μm, which is about 2.5 μm above the microcapsule with the approximation that the $\sim$3 μm microcapsule can be represented as a sphere lying intact on the glass coverslip. These two observations suggest that the volume of detection could be spread close to a value of 5 μm along the z-axis direction.

6.3.2 Targeted microcapsule shell damage

Based on the photothermal images of the microcapsule acquired and presented in the previous section (Fig. 6.4B), three areas of the capsule where identified for targeted illumination: area *2*, a nanoparticles dense domain, and area *1* and *3*, which were presenting weaker local quantities of nanoparticles. These areas are presented in Fig. 6.5A–B, respectively through the photothermal image of the microcapsule and its bright field image, both acquired at the altitude of z=0 μm.

The targeted illumination began with area *1*, expecting a not conclusive effect of the illumination on the microcapsule damage due to a local weaker density of nanoparticles. The result of two successive 100 ms illuminations with a CW HeNe laser at the power of 10.7 mW (separated by a few second) on area *1* did not show any modification of the shell, as can be seen on Fig. 6.5C (first row of bright field images). The illumination was therefore further moved to the nanoparticles dense area *2*, where four successive illuminations did not prove either to damage the shell or to modify visibly its shape (Fig. 6.5C, second row). Then, the laser was moved to the third area, a nanoparticles weak zone surrounded by two domains with higher nanoparticle density, where the microcapsule finally appeared as damaged after the fourth illumination.

A photothermal image was then acquired at the altitude z=1 μm. The images of the microcapsule acquired before the illumination needed to be modified to allow a easier understanding of their content, as a misalignment of odd and even scanning lines, consecutive to a synchronisation issue during the acquisition, was leaving them distorted. This was also appearing on the image acquired after the illumination (Fig. 6.6A). However, after applying the same correction as before (Fig. 6.4B), which consisted in sliding odd and even lines two pixels apart from one another, the image was still partially distorted (Fig. 6.6B). To improve the representation of the microcapsule, a frequency filter was applied to the photothermal image to remove the high frequency noises introduced by the scanning line misalignment. Briefly, the FFT

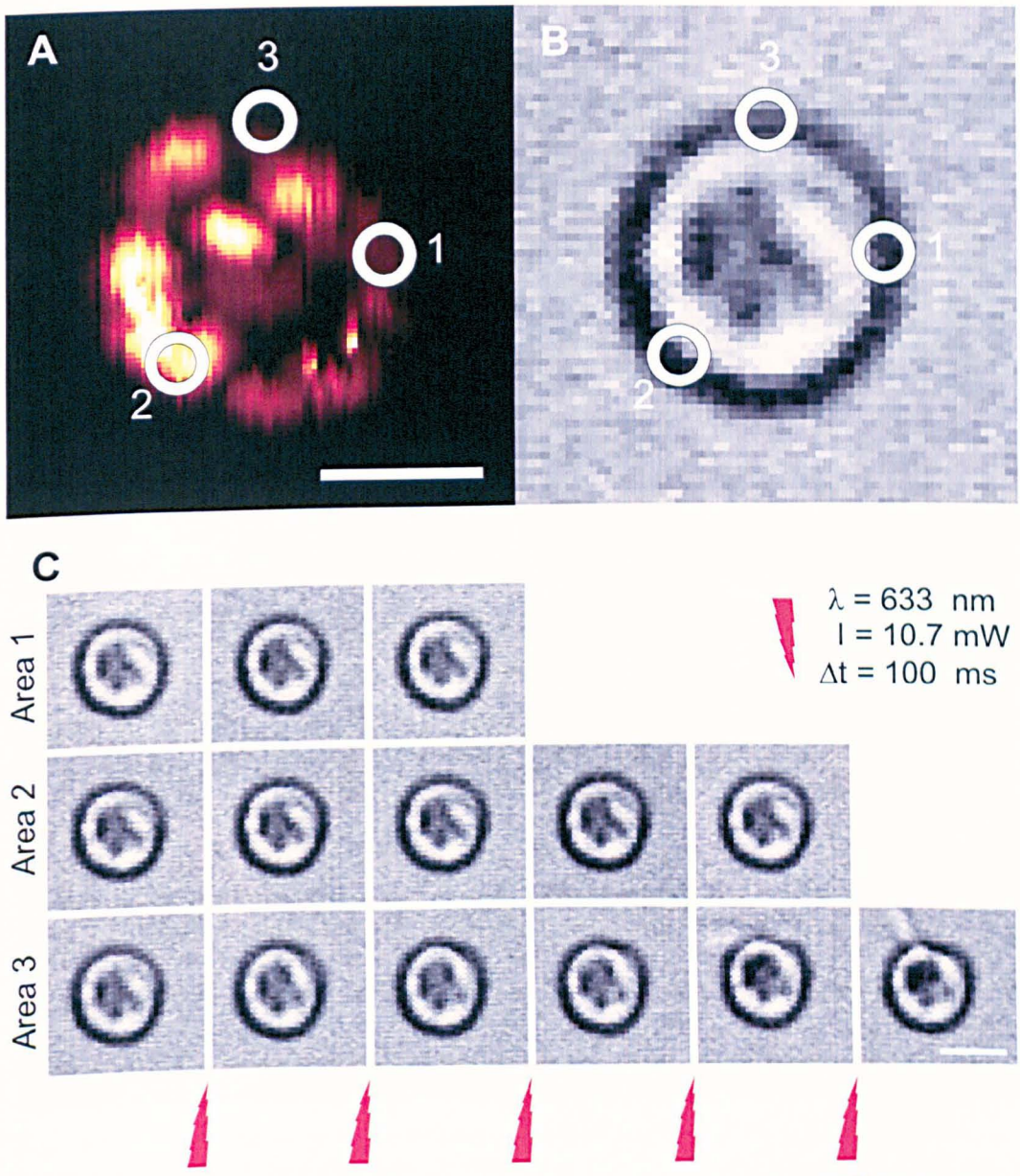

Fig. 6.5 – Microcapsule wall damaging process after successive CW HeNe laser illumination (10.7 mW). The capsule imaged by photothermal microscopy in Fig. 6.4B was exposed to a series of 100 ms laser illuminations (633 nm, 10.7 mW) in three different areas of the capsule wall at z=0 μm (as defined in Fig. 6.4A). Area 2 was nanoparticle dense, whereas 1 and 3 exhibited a less dense nanoparticle loading. (**A**–**B**) The areas of the capsule wall that were exposed to laser illuminations (z=0 μm) are highlighted by white rings on images acquired before illumination: (**A**) a photothermal image of the capsule, (**B**) a bright field image of the capsule. (**C**) Bright field images of the capsule before (left images) and after the successive laser illuminations (number of illumination increases towards the right) in the three areas indicated in (A) and (B). The capsule wall remained microscopically unimpaired until the fourth illumination in area 3. The scale bars represent 2 μm.

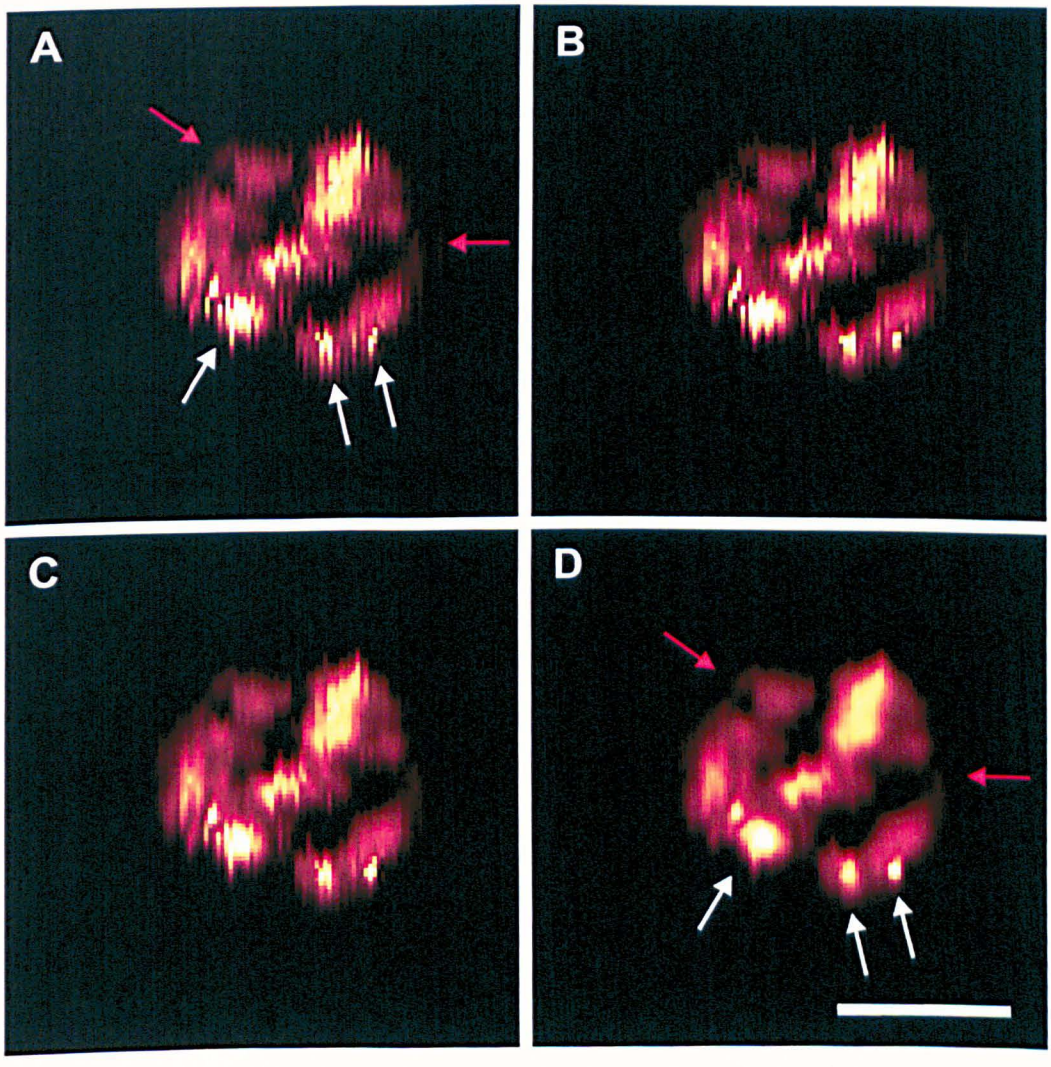

Fig. 6.6 – Filtering of a microcapsule distorted photothermal image. The microcapsule imaged by photothermal microscopy in Fig. 6.4B was damaged after a series of 100 ms illumination with a focused CW HeNe laser (Fig. 6.5). A photothermal image of the same microcapsule was acquired at the altitude of z=1 μm after the damage was provoked to its polymer shell. Modifications of the image were performed either by alignment of incorrectly interlaced scanning lines or with the help of a frequency filter (see Sect. B.4.5 for details) to remove the high frequency noise, and allow a visually easier understanding of the image. (**A**) Unmodified image. (**B**) Image after alignment of even and odd lines (2 px). (**C**) Frequency filtered image smoothing features smaller or equal to 1 pixels. (**D**) Frequency filtered image smoothing features smaller or equal to 2 pixels. The scale bar represents 2 μm.

bandpass filter[i] of the ImageJ software was used to discard the short wavelengths comprising the misalignment noise in the photothermal image (high frequencies), leaving the low frequency unaffected. A one pixel cut-off was first tried, as shown in Fig. 6.6C, and was giving similar results to the previous technique of line "re-interlacing". A cut-off of two pixels gave better results with a clear photothermal image (Fig. 6.6D). Additionally, if one compares the original image (Fig. 6.6A) to the frequency filtered one (Fig. 6.6D), which are both displayed with the same contrast range [0,10000], low intensity areas as the ones pointed by the red arrows in Fig. 6.6A and D and high density of nanoparticles domains (white arrows) are in good agreement in the two images.

The same frequency filtering process was therefore applied to images acquired before and after the series of illuminations on the microcapsule shell at the altitude z=1 μm. The resulting filtered images are presented in Fig. 6.7, where they are displayed in different contrast to allow a comparison in the whole range of intensities. The red marks representing the areas exposed to the laser illuminations have sizes of 0.5–0.7 μm, which means that they are assuredly larger than the real size of the laser beam that was irradiating these zones. The first area to be exposed (area *1*) exhibits a minor change of its local nanoparticle density after illumination. Area *2*, which was illuminated after area *1*, displays a more pronounced change in photothermal intensity and an area between the two aforementioned domains saw two high density of nanoparticles domains appearing after the illuminations (white arrows in Fig. 6.7). Similarly to the first area, area *3* does not uncover a major change of the local nanoparticle distribution. However, some domains near to this zone have had changed intensities, while as a result of the damage to the microcapsule, some domains have moved or disappeared, as for example the one pointed by the grey arrow in Fig. 6.7.

Although this example of a microcapsule damage cannot be considered as representing the general microcapsule damaging process, it clearly show that targeting a high density of nanoparticles for an illumination induced damage is not necessarily a factor for success. Provoking a damage to the shell in these conditions is therefore not ascertainably directly related to the quantity of heat produced locally, but could also be correlated to a local weakness of the polymer shell, possibly through areas presenting defects. This could be investigated further if such microcapsules were to be used as delivery containers.

Materials and methods available in Appendix B.4

[i]ImageJ FFT bandpass filter is a gaussian filtering process in the Fourier space removing the high (smoothing) and low (shading correction) spatial frequencies in the original image

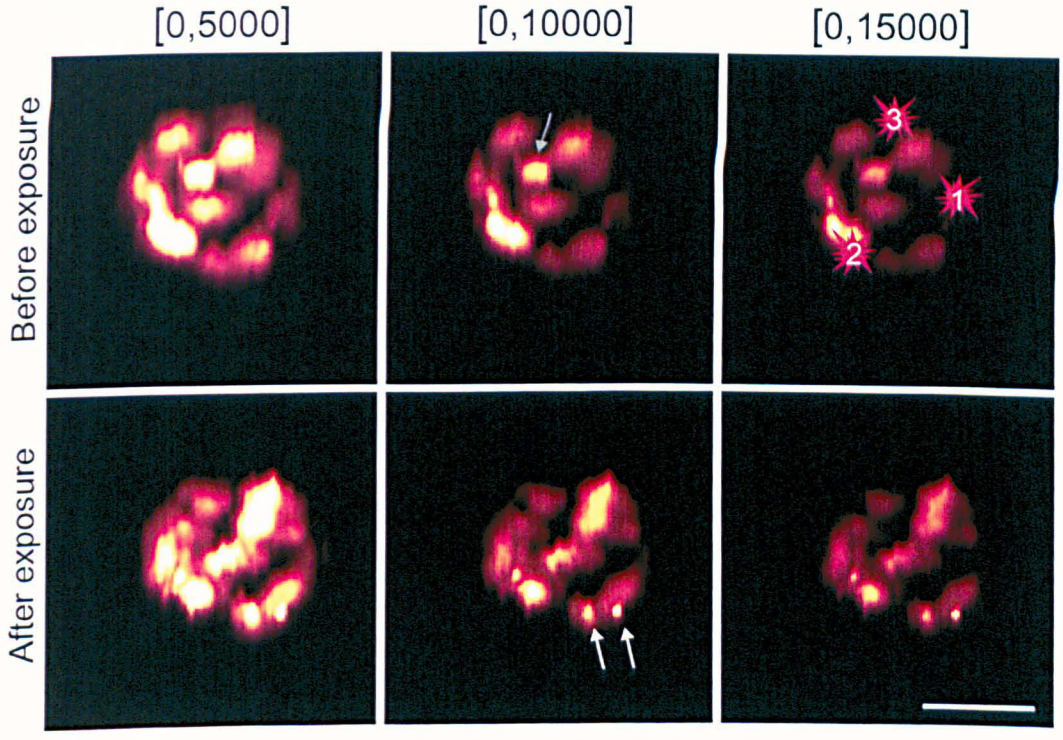

Fig. 6.7 – Changes of nanoparticle density distribution after microcapsule damage. The microcapsule displayed in Figs. 6.4 and 6.5 was imaged by photothermal microscopy before and after the wall damaging process had occurred. Photothermal images (z=1 μm) of the capsule before (top) and after (bottom) the 10.7 mW laser illuminations are displayed with different contrasts to allow a comparison of the distribution of nanoparticles density and appraise their changes. The white arrows show domains where the nanoparticles density increase upon laser illumination of the capsule, when the grey one points towards a nanoparticle dense area that has disappeared (or moved) after illumination. The scale bar represents 2 μm.

6.4 Bibliography

1. B. C. Mei, K. Susumu, I. L. Medintz, J. B. Delehanty, T. J. Mountziaris and H. Mattoussi. Modular poly(ethylene glycol) ligands for biocompatible semiconductor and gold nanocrystals with extended pH and ionic stability. *Journal of Materials Chemistry*, 18(41), 4949–4958, 2008.

2. Y. Wang, J. L. Seebald, D. P. Szeto and J. Irudayaraj. Biocompatibility and biodistribution of surface-enhanced raman scattering nanoprobes in zebrafish embryos: in vivo and multiplex imaging. *ACS Nano*, 4(7), 4039–53, 2010.

3. C. McDougall, D. J. Stevenson, C. T. A. Brown, F. Gunn-Moore and K. Dholakia. Targeted optical injection of gold nanoparticles into single mammalian cells. *Journal of Biophotonics*, 2(12), 736–743, 2009.

4. J. Gehl. Electroporation: theory and methods, perspectives for drug delivery, gene therapy and research. *Acta Physiologica Scandinavica*, 177(4), 437–447, 2003.

5. M. Glogauer and C. A. G. McCulloch. Introduction of large molecules into viable fibroblasts by electroporation: optimization of loading and identification of labeled cellular compartments. *Experimental Cell Research*, 200(2), 227–234, 1992.

6. E. J. Verspohl, I. KaiserlingBuddemeier and A. Wienecke. Introducing specific antibodies into electropermeabilized cells is a valuable tool for eliminating specific cell functions. *Cell Biochemistry and Function*, 15(2), 127–134, 1997.

7. L. M. Mir, M. F. Bureau, J. Gehl, R. Rangara, D. Rouy, J. M. Caillaud, P. Delaere, D. Branellec, B. Schwartz and D. Scherman. High-efficiency gene transfer into skeletal muscle mediated by electric pulses. *Proceedings of the National Academy of Sciences of the United States of America*, 96(8), 4262–4267, 1999.

8. D. G. Spiller, R. V. Giles, J. Grzybowski, D. M. Tidd and R. E. Clark. Improving the intracellular delivery and molecular efficacy of antisense oligonucleotides in chronic myeloid leukemia cells: A comparison of streptolysin-O permeabilization, electroporation, and lipophilic conjugation. *Blood*, 91(12), 4738–4746, 1998.

9. F. Q. Chen and D. Gerion. Fluorescent CdSe/ZnS nanocrystal-peptide conjugates for long-term, nontoxic imaging and nuclear targeting in living cells. *Nano Letters*, 4(10), 1827–1832, 2004.

10. J. Q. Lin, R. Chen, S. Y. Feng, Y. Z. Li, Z. F. Huang, S. S. Xie, Y. Yu, M. Cheng and H. S. Zeng. Rapid delivery of silver nanoparticles into living cells by electroporation for surface-enhanced Raman spectroscopy. *Biosensors & Bioelectronics*, 25(2), 388–394, 2009.

11. A. M. Javier, P. del Pino, M. F. Bedard, D. Ho, A. G. Skirtach, G. B. Sukhorukov, C. Plank and W. J. Parak. Photoactivated Release of Cargo from the Cavity of Polyelectrolyte Capsules to the Cytosol of Cells. *Langmuir*, 24(21), 12517–12520, 2008.

12. E. Donath, G. B. Sukhorukov, F. Caruso, S. A. Davis and H. Mohwald. Novel hollow polymer shells by colloid-templated assembly of polyelectrolytes. *Angewandte Chemie-International Edition*, 37(16), 2202–2205, 1998.

13. G. Decher. Fuzzy nanoassemblies: Toward layered polymeric multicomposites. *Science*, 277(5330), 1232–1237, 1997.

14. C. S. Peyratout and L. Dahne. Tailor-made polyelectrolyte microcapsules: From multilayers to smart containers. *Angewandte Chemie-International Edition*, 43(29), 3762–3783, 2004.

15. G. B. Sukhorukov, D. V. Volodkin, A. M. Gunther, A. I. Petrov, D. B. Shenoy and H. Mohwald. Porous calcium carbonate microparticles as templates for encapsulation of bioactive compounds. *Journal of Materials Chemistry*, 14(14), 2073–2081, 2004.

16. P. Rivera-Gil, S. De Koker, B. G. De Geest and W. J. Parak. Intracellular Processing of Proteins Mediated by Biodegradable Polyelectrolyte Capsules. *Nano Letters*, 9(12), 4398–4402, 2009.

17. F. Caruso, A. S. Susha, M. Giersig and H. Mohwald. Magnetic core-shell particles: Preparation of magnetite multilayers on polymer latex microspheres. *Advanced Materials*, 11(11), 950–953, 1999.

18. N. Gaponik, I. L. Radtchenko, M. R. Gerstenberger, Y. A. Fedutik, G. B. Sukhorukov and A. L. Rogach. Labeling of biocompatible polymer microcapsules with near-infrared emitting nanocrystals. *Nano Letters*, 3(3), 369–372, 2003.

19. O. Kreft, R. Georgieva, H. Baumler, M. Steup, B. Muller-Rober, G. B. Sukhorukov and H. Mohwald. Red blood cell templated polyelectrolyte capsules: A novel vehicle for the stable encapsulation of DNA and proteins. *Macromolecular Rapid Communications*, 27(6), 435–440, 2006.

20. Z. H. An, H. Mohwald and J. B. Li. pH controlled permeability of lipid/protein biomimetic microcapsules. *Biomacromolecules*, 7(2), 580–585, 2006.

21. K. Kohler and G. B. Sukhorukov. Heat treatment of polyelectrolyte multilayer capsules: A versatile method for encapsulation. *Advanced Functional Materials*, 17, 2053–2061, 2007.

22. O. Kreft, A. M. Javier, G. B. Sukhorukov and W. J. Parak. Polymer microcapsules as mobile local pH-sensors. *Journal of Materials Chemistry*, 17, 4471–4476, 2007.

23. M. F. Bedard, B. G. De Geest, A. G. Skirtach, H. Mohwald and G. B. Sukhorukov. Polymeric microcapsules with light responsive properties for encapsulation and release. *Advances in Colloid and Interface Science*, 158(1-2), 2–14, 2010.

24. V. Octeau, L. Cognet, L. Duchesne, D. Lasne, N. Schaeffer, D. G. Fernig and B. Lounis. Photothermal Absorption Correlation Spectroscopy. *ACS Nano*, 3(2), 345–350, 2009.

Chapter 7

Conclusions

The intracellular delivery of gold nanoparticles in mammalian cells has been studied in this manuscript. Firstly the non-specific internalisation of peptide-capped gold nanoparticles was examined in Chapter 3 using a combination of confocal fluorescence microscopy, transmission electron microscopy and photothermal microscopy. This fruitful gathering of techniques allowed to demonstrate that the amount of gold nanoparticles internalised by the cells was increasing over time to saturate after $\sim$2.5-3h. The uptake of the nanoparticles was shown to increase in a linear manner with the nanoparticle concentration after an endosomal mediated internalisation, which subsequently induced a degradation of the peptide self-assembled monolayer by the endosomal protease cathepsin L. The monolayer degradation could be prevented by inhibiting the enzyme to significantly reduce the degradation, but cathepsin L was demonstrated to have a broad cleavage potential and therefore to be likely to jeopardise numerous future nanoparticle functionalisation strategies if its effect was overlooked during bioconjugates design. Finally, the influence of the non-specific interactions was probed by changing the surface chemistry of the nanoparticles. The incorporation of increasing proportions of poly(ethylene glycol) end groups in the nanoparticles monolayer, known to limit the non-specific interaction, showed to reduce increasingly the amount of nanoparticle internalisation.

Chapter 4 proposed an overview of methods dedicated to facilitate the delivery of the nanoparticles in the cytosol by two different strategies aiming to avoid the endosomal entrapment. First an approach of endosome disruption was undertaken by using the endosome breaking drug chloroquine to help delivering the nanoparticles to the cytosol. Used in combination with a cathepsin L inhibition, chloroquine demonstrated to further protect the nanoparticle monolayer from proteolytic degradation, but the interaction of the nanoparticle with the endosome membrane debris hampered significantly their cytosolic dispersion. Then the nanoparticle functionalisation with addition of the cell-penetrating peptide Tat and the endosome disrupting

fusion peptide HA2 in the content of a PEG containing monolayer was examined in a similar goal of endosomal escape. Tat and HA2 both showed to increase the uptake of the gold nanoparticles, but no joint effect was observed. Surprisingly, the nanoparticles did not prove to have escaped the endosomes, maybe because of their lack of interaction with the endosome membrane preventing HA2 to disrupt the membrane. And eventually a pore mediated entry was examined with the use of the membrane pore forming toxin streptolysin O combined with a variation of the monolayer non-specific properties regulated by the introduction of a proportion of poly(ethylene glycol) in the monolayer. No cytosolic nanoparticles could be observed using this method, but an increase of the uptake was observed in presence of the toxin for nanoparticles bearing the PEG terminated molecules. Interestingly, the effect was more important when the non-specific interactions were not too much reduced, with a proportion of 10 % of PEG terminated ligands in the monolayer, suggesting that an interaction with the cell membrane was necessary to promote the internalisation.

In Chapter 5, a series of more than ten articles on "stripy nanoparticles" and their supposed extraordinary properties such as entering the cell to go in the cytosol without membrane disruption was critically reviewed. The evidences were revisited using Fast Fourier Transform analysis of the published STM images to demonstrate that the presence of the stripes observed on alkane thiol functionalised nanoparticles by the authors was the result of an imaging artifact. In a second part the interaction of different mixed MUS/OT functionalised gold nanoparticles with cells was examined and showed that these nanoparticles display a clear endocytosis mediated internalisation.

Finally, Chapter 6 was dedicated to a more active photophysically mediated approach of nanoparticle delivery. The opening of polymer microcapsules upon laser illumination was first studied, to try to find parameters allowing the damage of the capsule shell in order to later use them in a capsule mediated delivery of nanoparticles in the cell cytosol. The damage of some microcapsules upon 100 ms illuminations with a 633 nm laser at a power over 10 mW was observed, but an attempt to target specific nanoparticles dense areas of a capsule using a nanoparticle density map provided by photothermal images of the capsule did not give conclusive results. However, photothermal microscopy proved to give insights into the distribution of nanoparticles within the microcapsules and could be used to characterise the nanoparticle density in the cavity of the microcapsule while they remain in solution.

Appendices

Appendix A

Photothermal Microscope

A.1 Microscope components

Table and microscope

- Table: Linos
- Microscope: Axiovert 200, Zeiss (Germany)
- Motorised stage system
  - Stage: H117N1X4 ProScan stage, Prior Scientific Instruments Ltd (UK)
  - Controller: H30XYE ProScan controller, Prior Scientific Instruments Ltd (UK)
- Sample holder, home built

Illumination systems

- Lasers:
  - Heating beam: Nd:YLF Ventus 523, Laser Quantum (UK)
  - Probe beam: HeNe JDSU 1100, JDS Uniphase Corporation (USA)
- Modulation system:
  - Acousto-optic system:
    * Acousto-optics modulator: AOM-1060 model 532 C-L-V, Isomet Corporation (USA)
    * Power supply: EL301 power supply, TTi
  - Modulation (function generator): 33220A, 20MHz wave generator, Agilent (USA)

- Bright field and fluorescence illumination: X-Cite Series 120, EXFO (USA)
- Fluorescence filter sets, Zeiss (Germany):
  - 38HE:
    - Excitation: BP 470/40
    - Dichroic: FT 495
    - Emission: BP 525/50
  - 43HE:
    - Excitation: BP 550/25
    - Dichroic: FT 570
    - Emission: BP 605/70
- Shutter system:
  - Loan shutter system:
    - Stand alone shutter: HF202, Prior Scientific Instruments Ltd (UK)
    - Controller: H30XYZ2, Prior Scientific Instruments Ltd (UK)
  - Current shutter system:
    - Shutter: SH05 Beam Shutter, Thorlabs (USA)
    - Controller: TSC001 T-cube shutter controller, Thorlabs (USA)

Optics

- Objectives:
  - Achroplan 50x/0.9 NA, Zeiss (Germany)
  - Achroplan 40x/0.8 NA, Zeiss (Germany)
- Translation Z (top objective):
  - Motor: Z812, Thorlabs (USA)
  - Controller: apt dc servo controller TDC001, Thorlabs (USA)
- Cold mirror, Thorlabs (USA)

Detection

- Cameras:
  - ImageIM, Hamamatsu (Japan)
  - Thorlabs DC 310-C, Thorlabs (USA)
- Photodiode: 10 MHz adjustable photoreceiver model 2051, New Focus (USA)
- Lock-in amplifier: 7280 DSP, Signal recovery (USA)

Acquisition

Acquisition card: NI PCIe-6259, National Instrument (USA)

Scanning

- Piezoelectric device: P-563.3CD, Physik Instrumente (Germany)
- Piezoelectric device controller: E710.3CD, Physik Instrumente (Germany)
- PCIe-GPIB card (piezo controller — computer): NI PCIe-GPIB, National Instrument (USA)

Incubation system

- Incubator XL-3, Peacon (USA)
- Heating unit, Zeiss (Germany)
- Temperature control tempcontrol 37-2 digital, Zeiss (Germany)
- CO_2 control, Zeiss (Germany)

Appendix B

Material and methods

B.1 Non-specific delivery of gold nanoparticles

B.1.1 Materials

Tissue culture medium was from Gibco Life Technologies (Carlsbad, Ca); fetal calf serum (FCS) from Harlan Seralab (UK); pharmacological inhibitor Z-FF-fmk from Calbiochem (EMD Biosciences, Germany). Gold nanoparticles used in Sect. 3.1 and 3.2 were from BBInternational (Cardiff, UK). Gold nanoparticles used in Sect. 3.3 were synthesised as mentioned in Sect. B.1.3. Peptides used in Sect. 3.1 and 3.2 were from Anaspec (San Jose, CA) and PPR Ltd. (Fareham, UK). Purified human cathepsin L and purified bovine thrombin were from Sigma (St. Louis, MO). The peptides CALNN and CCALNN-PEG (CCALNN$-(EG)_6-$ol) used in Sect. 3.3 were purchased from Peptides Proteins Research Ltd (UK). The PEG-NHS-ester used in Sect. 3.3.1 was from Prochimia and daunorubicin was from Sigma Aldrich. The 16 % paraformaldehyde solution was from Agar Scientific (UK) and the 25 % glutaraldehyde solution from TAAB (UK). Centrifugation filters for nanoparticle purification and sterilisation were bought from VWR and PALL. 35mm glass cover slip dish were from Iwaki (Japan) and 35 x 10mm cell culture dish from Corning (USA). 96-well and 384-well plates were from Corning (USA), and 96-well and 384-well filter plates were from Millipore (USA). Ni-NTA beads were from Invitrogen (USA).

B.1.2 Peptide stock solutions

Stock solutions (2 mM) of CALNN and of CCALNN-PEG (CCALNN$-(EG)_6-$ol) were prepared by dissolving the peptides in concentrated phosphate buffer saline (10× PBS: 1.6 M NaCl, 30 mM KCl, 80 mM Na_2HPO_4, 10 mM KH_2PO_4). The stock solutions of the peptides CALNNGGGALVPRGSGTAK (5-carboxyfluorescein)-NH_2 (CALNN-th-fam), CCALNNGGGALVPRGSGTAK $(5-$carboxyfluorescein$)-NH_2$ (CCALNN-th-fam) were prepared by dissolving them in dimethyl sulfoxide. The resulting solutions were kept as aliquots at −80 °C.

B.1.3 Gold nanoparticle synthesis

The method was adapted from Slot *et al.*[1]
Briefly, 395 mL of deionised water and 5 mL of 1 % w/v $HAuCl_4$ is heated to 60 °C then a 100 mL solution of 20 mL 1 % w/v Na_3citrate, 6 mL 1 % w/v tannic acid, 6 mL 0.2 M KCO_3 and 68 mL of deionised water is added and left to stir at 60 °C to complete the reaction.

B.1.4 Formation of peptide self-assembled monolayers

A peptide solution was prepared by mixing the peptide stock solutions in the appropriate volume ratio. The peptide solution was mixed in a 1:1 ratio with 10× PBS (1.6 M NaCl, 30 mM KCl, 80 mM Na_2HPO_4, 10 mM KH_2PO_4). A suspension of 10 nm diameter gold nanoparticles (BBInternational, Cardiff, UK) for Sect. 3.1 and 3.2 or 5 nm gold nanoparticles (synthesis Sect. B.1.3) for Sect. 3.3 was added in a 9:1 volume ratio giving a 100 μM final concentration of peptide. The solution was briefly agitated before addition of Tween-20 to a final concentration of 0.05 % (v/v). The solutions were left overnight at room temperature, in the dark to avoid photobleaching of the fluorophores when necessary.

B.1.5 Nanoparticles purification procedure

B.1.5.1 10 nm nanoparticles

The nanoparticle solutions were centrifuged (16000 g, 60 min), and the pellet was resuspended in 1 mL of phosphate buffer saline (PBS: 160 mM NaCl, 3 mM KCl, 8 mM Na_2HPO_4, 1 mM KH_2PO_4) with 0.05 % Tween-20 before a second centrifugation step (16000 g, 60 min). This washing step was repeated three times with PBS only, before resuspension in PBS at a final nanoparticle concentration of 60 nM. Successful formation of the monolayer is immediately visible because of the increased colloidal stability and of a small red shift of the plasmon band.[2] The repeated centrifugation procedure ensures that the concentration of excess free peptide is in the picomolar range.

B.1.5.2 5 nm nanoparticles

The nanoparticles solutions were centrifuged at 21000 rpm for 2 h. The supernatant was then discarded, the nanoparticles pellet resuspended in a 1×PBS and eluted through a Sephadex G-25 column. The particles were sterilised by filtration using 0.22 μm centrifugation filters.

B.1.6 Cell culture and nanoparticles incubation

B.1.6.1 Nanoparticles internalisation and SAM degradation

HeLa cells were grown in Dulbecco's modified Eagle medium (DMEM) supplemented with 10 % FCS (v/v) and 1 % non-essential amino acids (v/v), at 37 °C, 5 % CO_2. Cells (between passages 8 to 20) were plated at 10^5 cells/mL in 35 mm Iwaki dishes. For all experiments, nanoparticles were incubated directly into the complete medium (containing 10 % FCS) for indicated times at the stated final concentration.

B.1.6.2 Effect of PEG in the monolayer

Cells (between passages 8 to 20) were detached from the cell culture dish with trypsin, pelleted and washed three times by centrifugation (3000 rpm, 3 min) in serum-free medium in 1.5 mL eppendorf tubes, removing carefully all the medium each time. 4.10^5 cells were resuspended in 400 μL of serum-free MEM. Gold nanoparticles at the appropriate concentrations were added to 200 μL of serum-free MEM. This mix was added to the cells and the eppendorf tube was left to incubate at 37 °C for 10 min. 1 mL of serum containing MEM (10 % FCS) was added and the tube returned to incubate at 37 °C for 20 min. The nanoparticles were removed by centrifugation (3 min, 3000 rpm) and the discarded medium was replaced by fresh medium. The cells were then seeded on an Iwaki dish and left for 4 h to attach to the dish before fixation (Sect. B.1.11.1). The cells were then imaged immediately or kept at 4 °C with 0.05 % azide until imaging.

B.1.7 Confocal microscopy

B.1.7.1 Time lapse

Cells were plated in 35 mm glass coverslip culture dishes (Iwaki). One day after plating, cells were then incubated on the microscope stage at 37 °C, 5 % CO_2, and observed by confocal microscopy using a Zeiss LSM510 with a Plan-apochromat 63×/1.3 NA oil immersion objective. Excitation of fluorescein was performed using an argon ion laser at 488 nm. Emitted light was detected through a 505–550 nm bandpass filter from a 545 nm dichroic mirror. Data capture was carried out with LSM510 version 3 software (Zeiss, Germany). For time-lapse experiments, mean fluorescence intensity was extracted and the fluorescence intensity relative to starting fluorescence was determined for each cell using LSM510 software. These experiments were performed at least three times, and each time, eight different fields which each contain ~5–10 cells were analysed.

B.1.7.2 Statistical analysis

For fluorescence intensity quantification, 10 images containing each $\sim$20 cells were taken for each condition. Number of fluorescent vesicles was then counted for each field as well as mean fluorescence intensity for each individual cell using kinetic tracking analysis software (2002 Kinetic Imaging, Ltd.). Statistical significance was determined by one-way ANOVA followed by a Bonferroni multiple comparison test. Difference was considered as significant at $p<0.01$. All of these experiments were performed at least three times.

B.1.8 *In vitro* fluorescence assay

For thrombin cleavage, each reaction (100 μL) was performed in PBS with 0.3 M NaCl (pH 7.4), with 6 nM of 98 % CALNN — 2 % CALNN-th-fam nanoparticles and 50 mU of purified thrombin. Fluorescence was measured using a BMG labtech POLARstar fluorimeter (Offenburg, Germany) and Corning (Corning Inc., NY) black NBS plates.

B.1.9 *In vitro* ligand exchange assay

Nanoparticles capped with five different mixed monolayer of CALNN:CCALNN (composition ratios 1:5, 1:2, 1:1, 2:1 and 5:1) and homogenous monolayers of CALNN and CCALNN were prepared in a 96-well plate. Peptides solutions were mixed together and added to the gold nanoparticles solution and incubated for 24 h for the monolayer to form. Excess unbound peptides were removed by repeated centrifugation and resuspension in water in a 96-well filter plate. The purified peptide-capped nanoparticles were transferred to a 384-well plate and incubated with free CALNN-Histag peptides at three concentrations (1.2, 2.4, 3.6 μM and a control at 0 nM) for 12 h. After incubation, the mix was transferred to a 384-well filter plate loaded with a gel of Ni-NTA beads, which was centrifuged above a normal 384-well plate. As the Ni-NTA has a strong affinity for Histag, the nanoparticles that have undergone ligand exchange with CALNN-Histag for one or more of their ligands will be immobilised on the Ni-NTA beads while the others will be eluted to the empty plate. The absorbance at 522 nm was taken for the eluted nanoparticles to compare the nanoparticles that undergone ligand exchange with those which did not.

B.1.10 TEM

Cells were plated at 2.10^5 cells/mL in a 35 mm Petri dish. One day after plating, cells were incubated for 3 h with nanoparticles at a 6 nM final concentration. After one PBS wash, cells were fixed with 4 % paraformaldehyde and 2 % glutaraldehyde in 0.1 M phosphate buffer solution, osmicated, and processed for epoxy resin embedding. Then, 70 nm sections were cut with a LKB ultramichrotome and stained

with 5 % aqueous uranyl acetate and 2 % lead citrate before viewing in a FEI Tecnai Spirit transmission electron microscope.

B.1.11 Photothermal microscopy

B.1.11.1 Cell fixation for photothermal microscopy

The fixative used was 4 % paraformaldehyde in phosphate buffer. The samples were washed twice with PBS (37 °C) and fixed with fixative (37 °C) for 20 minutes. The fixative was then removed and the sample washed again with PBS twice, each time for at least 5 minutes. The samples were then imaged immediately or kept at 4 °C with 0.05 % azide until imaging.

B.1.11.2 Photothermal imaging

The technique was described in details in Chapter 2, and particularly the imaging parameter were described in Sect. 2.2.3.

B.1.11.3 Image analysis: whole field method with threshold

The method consists in drawing a region of interest (ROI) around the cells in an image and measuring the photothermal intensity of that region above a threshold. The analysis was processed using the software AQM Advance 6.0.2.23 (Kinetic Imaging Ltd, UK). The bright field and photothermal images, both encoded in a 16-bit TIFF file format, were joined in a TIFF image file composed of two image planes (bright field, photothermal). A single region of interest (ROI) was drawn on the bright field image around all the cells that were appearing as whole in that field of view using the free hand polygon image tool of the AQM Advance software, leaving the areas which did not include cells outside of it as much as possible. A few regions were drawn on the image using the ellipse tool of AQM Advance in areas where no cells were present and the mean photothermal intensity of these regions was used to produce a mean photothermal background intensity. The mean photothermal intensity of the ROI including all the whole cells was measured by setting up a threshold corresponding to 1.5 times the mean background photothermal intensity of the field of view, to yield a mean photothermal intensity of the ROI. This procedure was repeated for each of the images acquired for a given condition and for each condition. For each condition, the mean photothermal intensities of the fields were averaged to produce a mean photothermal intensity and a standard error, representing respectively a measure of the mean nanoparticle uptake per cell for the given condition and its accuracy.

B.1.11.4 Image analysis: single cell method

The method consists in drawing a region of interest (ROI) around each of the cells present in an image and measuring the photothermal intensity of these regions once a mean background value is subtracted. The analysis was processed using the software AQM Advance 6.0.2.23 (Kinetic Imaging Ltd, UK). The bright field and photothermal images, both encoded in a 16-bit TIFF file format, were joined in a TIFF image file composed of two image planes (bright field, photothermal). A region of interest was drawn around each of the cells that were appearing as whole in that field of view using the bright field image and the free hand polygon image tool of the AQM Advance software. A few regions were drawn on the image using the ellipse tool of AQM Advance in areas where no cells were present and the mean photothermal intensity of these regions was used to produce a mean photothermal background intensity. The mean photothermal intensity of each of the ROIs including the cells was measured after subtraction of the average photothermal background intensity of the field of view, to yield a mean photothermal intensity for each whole cell. This procedure was repeated for each of the images acquired for a given condition and for each condition. For each condition, the mean single cell photothermal intensities were then averaged to produce a mean photothermal intensity and a standard error, representing respectively a measure of the mean nanoparticle uptake per cell for the given condition and its accuracy.

B.1.12 Bright field microscopy

The bright field images (16-bit resolution, 512×512 pixels maximum frame size) were acquired with an ImageEM ultra high sensitivity cooled EMCCD camera (Hamamatsu, Japan), fasten on the bottom port of an Axiovert 200 microscope (Zeiss, Germany) using the HCImage 1.1.1.0 image acquisition software (Hamamatsu, Japan). The images were acquired with a 122 ms time exposure, at the minimum camera gain (G=1) and minimum digital sensitivity gain (G=1).

The transmitted light illumination system was home built. It was composed of a X-Cite Series 120 (EXFO UK, UK) illuminator collimated through a EXFO microscope adaptor attached above the microscope as excitation source, an additional collimating lens (Thorlabs, USA), an Achroplan 40×/0.8 NA water dipping long working distance (2.5 mm) objective (Zeiss, Germany) to shed the light on the glass coverslip on which the sample was adhering and an Achroplan 50×/0.9 NA oil objective below the dish to collect the transmitted light.

B.1.13 Wide field fluorescence microscopy

The wide field fluorescence images were acquired on the same microscope as the bright field and photothermal images, using the same illumination system, camera

and acquisition software (details in Sect. B.2.10). The right excitation and emission wavelengths required for the fluorescence acquisition were provided by the addition of a band-pass BP 550/25 excitation filter (Zeiss, Germany), appropriate for the fam fluorophore, located between the collimation lens and the objective, and the combination of a FT 570 dichroic mirror (Zeiss, Germany) and a band-pass BP 605/ 70 emission filter (Zeiss, Germany) situated on the light path between the objective used for light collection and the camera. The images were acquired with a 622 ms time exposure, at the minimum camera gain (G=1) and a digital sensitivity gain at the value of 255, at a 3 μm altitude (missingcheck the altitude) above the glass coverslip.

B.2 Facilitated delivery of gold nanoparticles

B.2.1 Materials

Tissue culture medium was from Gibco Life Technologies (Carlsbad, Ca); fetal calf serum (FCS) from Harlan Seralab (UK); pharmacological inhibitor Z-FF-fmk from Calbiochem (EMD Biosciences, Germany), purified human cathepsin L and chloroquine were from Sigma (St. Louis, MO). Gold nanoparticles (10 nm) used in Sect. 4.1.1 were from BBInternational (Cardiff, UK). Gold nanoparticles (5 nm) used elsewhere in Chapter 4 were synthesised as mentioned in Sect. B.2.3. Peptides used in Sect. 4.1 were from Anaspec (San Jose, CA, USA) and PPR Ltd. (Fareham, UK) (CALNN-HA2: CALNNGDIMGEWGNEIFGAIAGFLG-amide; CALNN-Tat: CALNNAGRKKRRQRRR). The peptides CALNN and CCALNN-PEG (CCALNN-$(EG)_6$-ol) used in Sect. 4.2 were purchased from Peptides Proteins Research Ltd (UK). Streptolysin O, propidium iodide and fluorescein diacetate were from Sigma Aldrich. The 16 % paraformaldehyde solution was from Agar Scientific (UK) and the 25 % glutaraldehyde solution from TAAB (UK). Centrifugation filters for nanoparticle purification and sterilisation were bought from VWR and PALL. 35mm glass cover slip dish were from Iwaki (Japan) and 35 × 10 mm cell culture dish from Corning (USA).

B.2.2 Peptide stock solutions

Stock solutions (2 mM) of CALNN, of CCALNN–$(EG)_6$–ol and of CALNN–Tat were prepared by dissolving the peptides in concentrated phosphate buffer saline (10× PBS: 1.6 M NaCl, 30 mM KCl, 80 mM Na_2HPO_4, 10 mM KH_2PO_4). The solutions of the CALNNGGGALVPRGSGTAK (5-carboxyfluorescein)-NH_2 (CALNN-th-fam) and CALNN-HA2 peptides were prepared individually by dissolving them in dimethyl sulfoxide, at stock concentrations of 2 mM. The resulting solutions were kept as aliquots at −80 °C.

B.2.3 Gold nanoparticle synthesis

The method was adapted from Slot *et al.*[1]
Briefly, 395 mL of deionised water and 5 mL of 1 % w/v $HAuCl_4$ is heated to 60 °C then a 100 mL solution of 20 mL 1 % w/v Na_3citrate, 6 mL 1 % w/v tannic acid, 6 mL 0.2 M KCO_3 and 68 mL of deionised water is added and left to stir at 60 °C to complete the reaction.

B.2.4 Formation of peptide self-assembled monolayers

A peptide solution was prepared by mixing the peptide stock solutions in the appropriate volume ratio. The peptide solution was mixed in a 1:1 ratio with 10× PBS (1.6 M NaCl, 30 mM KCl, 80 mM Na_2HPO_4, 10 mM KH_2PO_4). A suspension of 10 nm diameter gold nanoparticles (BBInternational, Cardiff, UK) or 5 nm gold nanoparticles (synthesis Sect. B.2.3) was added in a 9:1 volume ratio giving a 100 μM final concentration of peptide. The solution was briefly agitated before addition of Tween-20 to a final concentration of 0.05 % (v/v). The solutions were left overnight at room temperature, in the dark to avoid photobleaching of the fluorophores when necessary.

B.2.5 Nanoparticles purification procedure

B.2.5.1 10 nm nanoparticles

The nanoparticle solutions were centrifuged (16000 g, 60 min), and the pellet was resuspended in 1 mL of phosphate buffer saline (PBS: 160 mM NaCl, 3 mM KCl, 8 mM Na_2HPO_4, 1 mM KH_2PO_4) with 0.05 % Tween-20 before a second centrifugation step (16000 g, 60 min). This washing step was repeated three times with PBS only, before resuspension in PBS at a final nanoparticle concentration of 60 nM. Successful formation of the monolayer is immediately visible because of the increased colloidal stability and of a small red shift of the plasmon band.[2] The repeated centrifugation procedure ensures that the concentration of excess free peptide is in the picomolar range.

B.2.5.2 5 nm nanoparticles

The nanoparticles solutions were centrifuged at 21000 rpm for 2 h. The supernatant was then discarded, the nanoparticles pellet resuspended in a 1×PBS and eluted through a Sephadex G-25 column. The particles were sterilised by filtration using 0.22 μm centrifugation filters.

B.2.6 Cell culture and nanoparticle incubation

B.2.6.1 Assisted endosomal escape

HeLa cells were grown in Dulbecco's modified Eagle medium (DMEM) supplemented with 10 % FCS (v/v) and 1 % non-essential amino acids (v/v), at 37 °C, 5 % CO_2. Cells (between passages 8 to 20) were plated at 10^5 cells/mL in 35 mm Iwaki dishes. For all experiments in Sect. 4.1, nanoparticles were incubated directly into the complete medium (containing 10 % FCS) for indicated times at the stated final concentration.

B.2.6.2 Streptolysin O assisted internalisation

Cell culture

HeLa cells were grown in MEM supplemented with 10 % FCS (v/v) and 1 % non-essential amino acids (v/v), at 37 °C, 5 % CO_2.

Streptolysin O concentration optimisation

A streptolysin O (SLO) concentration optimisation is required on a regular basis as the SLO activity decreases over time, but also if experimental parameters (temperature, medium, cell line, resealing time, ...) are to be modified. Dried streptolysin O was mixed in 0.1 % bovine serum albumin with 5 mM DTT (reagents prepared in deionised water and filter sterilised) and kept as aliquots at −80 °C. Cells (between passages 8 to 20) were detached from the cell culture dish with trypsin, pelleted and washed three times by centrifugation (3000 rpm, 3 min) in serum-free medium in 1.5 mL eppendorf tubes, removing carefully all the medium each time, as serum and trypsin could inhibit the streptolysin O. Cells (10^6 cells/mL) were finally suspended in 400 μL of MEM in several 2 mL eppendorf tubes (one tube per SLO concentration to be tested). Solutions of 200 μL serum-free MEM with propidium iodine (PI, 1 μg/mL) were added to the cells. PI is a non-membrane permeable DNA stain, usually used to mark the nuclei of dead cells, will assess the permeabilisation of the cells. Several streptolysin O concentration were made by mixing the streptolysin O solution in 200 μL of serum-free MEM and added to the well suspended cells (co-incubated with PI). The eppendorf tubes were then left for 10 min at 37 °C. After that 1 mL of serum-containing medium was added to the cells and the tubes were left at 37 °C for 20 min (toxin neutralisation and subsequent resealing of the cells). Fluorescein diacetate (FDA, 2 ng/mL) was added to the cells for resealing assessment and the tubes were left at 37 °C for 20 min. FDA is membrane permeable and is modified by esterases in live cells to yield a fluorescent green product. The medium was replaced by fresh serum-containing MEM and the cells were observed with a confocal fluorescent microscope (Zeiss LSM 510 or 710). Cells showing both green

and red fluorescence are live and were permeabilised and subsequently resealed. The SLO concentration was considered as optimal when at least 50 % of the cells were permeabilised while keeping a low level of cytotoxicity.

Nanoparticles incubation in presence of streptolysin O

Cells (between passages 8 to 20) were detached from the cell culture dish with trypsin, pelleted and washed three times by centrifugation (3000 rpm, 3 min) in serum-free medium in 1.5 mL eppendorf tubes, removing carefully all the medium each time, as serum and trypsin could inhibit the streptolysin O. 4.10^5 cells were resuspended in 400 μL of serum-free MEM. Streptolysin O and gold nanoparticles at the appropriate concentrations, depending on the SLO optimisation for SLO and experimental conditions for the nanoparticles, were added to 200 μL of serum-free MEM. This mix was added to the cells and the eppendorf tube was left to incubate at 37 °C for 10 min. After SLO incubation, 1 mL of serum containing MEM (10 % FCS) was added to the cells for their resealing and the tube were returned to incubate at 37 °C for 20 min. The medium was further removed (centrifugation 3 min, 3000 rpm) to withdraw the nanoparticles and replaced by fresh serum-containing medium. The cells were then seeded on an Iwaki dish and left for 4 h to attach to the dish before fixation (Sect. B.2.9.1). The cells were then imaged immediately or kept in the Iwaki dish at 4 °C in a PBS solution containing 0.05 % of azide until imaging.

Nanoparticles incubation in absence of streptolysin O

The exact same procedure as above was observed without addition of streptolysin O while mixing the nanoparticles with the cells.

B.2.7 Confocal microscopy

B.2.7.1 Confocal imaging

Cells were plated in 35 mm glass coverslip culture dishes (Iwaki). One day after plating the cells were incubated on the microscope stage (37 °C, 5 % CO_2), and observed by confocal microscopy using a Zeiss LSM510 with a Plan-apochromat 63×/1.3 NA oil immersion objective. Excitation of fluorescein was performed using an argon ion laser at 488 nm. Emitted light was detected through a 505–550 nm bandpass filter from a 545 nm dichroic mirror. Data capture was carried out with LSM510 version 3 software (Zeiss, Germany).

B.2.7.2 Statistical analysis

For fluorescence intensity quantification, ~ 9 images containing each ~ 20 cells were taken for each condition. The mean fluorescence intensity for each individual cell was done using kinetic tracking analysis software (2002 Kinetic Imaging Ltd.). Statistical

significance was determined by one-way ANOVA followed by a Holm-Bonferroni multiple comparison test. Differences were considered as significant at $p<0.01$. These experiments were performed at least three times.

B.2.8 Transmission electron microscopy

B.2.8.1 Assisted endosomal escape

Cells were plated at 2.10^5 cells/mL in a 35 mm Petri dish. One day after plating, cells were incubated for 3 h with nanoparticles at a 6 nM final concentration. After one PBS wash, cells were fixed with 4 % paraformaldehyde and 2 % glutaraldehyde in 0.1 M phosphate buffer solution, osmicated, and processed for epoxy resin embedding. Then, 70 nm sections were cut with a LKB ultramichrotome and stained with 5 % aqueous uranyl acetate and 2 % lead citrate before viewing in a FEI Tecnai Spirit transmission electron microscope.

B.2.8.2 SLO assisted delivery

The cells were thoroughly washed with PBS buffer. Cells were then scraped from the culture dish, centrifuged at 5000 g for 5 min, and the supernatant removed. The cell pellets were fixed in a 0.1 M PBS solution containing 2.5 % glutaraldehyde and 4 % paraformaldehyde for 1 h. They were then rinsed with 0.1 M PBS, embedded in a 2 % agarose gel, postfixed in a 4 % osmium tetroxide (caution! Extremely toxic) solution for 1 h, rinsed with distilled water, stained with 0.5 % uranyl acetate for 1 h, dehydrated in a graded series of ethanol (30, 60, 70, 90, and 100 %), and embedded in epoxy resin. The resin was polymerised at 60 °C for 48 h. Ultrathin sections (50-70 nm) obtained with a LKB ultramicrotome were stained with 5 % aqueous uranyl acetate and 2 % aqueous lead citrate and imaged under a 120 kV FEI Tecnai Spirit TEM.

B.2.9 Photothermal microscopy

B.2.9.1 Cell fixation for photothermal microscopy

The fixative used was 4 % paraformaldehyde in phosphate buffer. The samples were washed twice with PBS (37 °C) and fixed with fixative (37 °C) for 20 minutes. The fixative was then removed and the sample washed again with PBS twice, each time for at least 5 minutes. The samples were then imaged immediately or kept at 4 °C with 0.05 % azide until imaging.

B.2.9.2 Photothermal imaging

The technique was described in details in Chapter 2, and particularly the imaging parameter were described in Sect. 2.2.3

B.2.9.3 Image analysis: whole field method with threshold

The method consists in drawing a region of interest (ROI) around the cells in an image and measuring the photothermal intensity of that region above a threshold. The analysis was processed using the software AQM Advance 6.0.2.23 (Kinetic Imaging Ltd, UK). The bright field and photothermal images, both encoded in a 16-bit TIFF file format, were joined in a TIFF image file composed of two image planes (bright field, photothermal). A single region of interest (ROI) was drawn on the bright field image around all the cells that were appearing as whole in that field of view using the free hand polygon image tool of the AQM Advance software, leaving the areas which did not include cells outside of it as much as possible. A few regions were drawn on the image using the ellipse tool of AQM Advance in areas where no cells were present and the mean photothermal intensity of these regions was used to produce a mean photothermal background intensity. The mean photothermal intensity of the ROI including all the whole cells was measured by setting up a threshold corresponding to 1.5 times the mean background photothermal intensity of the field of view, to yield a mean photothermal intensity of the ROI. This procedure was repeated for each of the images acquired for a given condition and for each condition. For each condition, the mean photothermal intensities of the fields were weighted[a] by the number of cells in that field and averaged to produce a mean photothermal intensity and a standard error, representing respectively a measure of the mean nanoparticle uptake per cell for the given condition and its accuracy.

B.2.9.4 Image analysis: single cell method

The method consists in drawing a region of interest (ROI) around each of the cells present in an image and measuring the photothermal intensity of these regions once a mean background value is subtracted. The analysis was processed using the software AQM Advance 6.0.2.23 (Kinetic Imaging Ltd, UK). The bright field and photothermal images, both encoded in a 16-bit TIFF file format, were joined in a TIFF image file composed of two image planes (bright field, photothermal). A region of interest was drawn around each of the cells that were appearing as whole in that field of view using the bright field image and the free hand polygon image tool of the AQM Advance software. A few regions were drawn on the image using the ellipse tool of AQM Advance in areas where no cells were present and the mean photothermal intensity of these regions was used to produce a mean photothermal background intensity. The mean photothermal intensity of each of the ROIs including the cells was measured after subtraction of the average photothermal background intensity of the field of view, to yield a mean photothermal intensity for each whole cell. This procedure was repeated for each of the images acquired for a given condition and

[a]Number of cells in the field × Number of field for that condition / Total number of cells in the condition

for each condition. For each condition, the mean single cell photothermal intensities were then averaged to produce a mean photothermal intensity and a standard error, representing respectively a measure of the mean nanoparticle uptake per cell for the given condition and its accuracy.

B.2.10 Bright field microscopy

The bright field images (16-bit resolution, 512×512 pixels maximum frame size) were acquired with an ImageEM ultra high sensitivity cooled EMCCD camera (Hamamatsu, Japan), fasten on the bottom port of an Axiovert 200 microscope (Zeiss, Germany) using the HCImage 1.1.1.0 image acquisition software (Hamamatsu, Japan). The images were acquired with a 122 ms time exposure, at the minimum camera gain (G=1) and minimum digital sensitivity gain (G=1).

The transmitted light illumination system was home built. It was composed of a X-Cite Series 120 (EXFO UK, UK) illuminator collimated through a EXFO microscope adaptor attached above the microscope as excitation source, an additional collimating lens (Thorlabs, USA), an Achroplan 40×/0.8 NA water dipping long working distance (2.5 mm) objective (Zeiss, Germany) to shed the light on the glass coverslip on which the sample was adhering and an Achroplan 50×/0.9 NA oil objective below the dish to collect the transmitted light.

B.2.11 Wide field fluorescence microscopy

The wide field fluorescence images were acquired on the same microscope as the bright field and photothermal images, using the same illumination system, camera and acquisition software (details in Sect. B.2.10). The right excitation and emission wavelengths required for the fluorescence acquisition were provided by the addition of a band-pass BP 470/40 excitation filter (Zeiss, Germany), appropriate for the fam fluorophore, located between the collimation lens and the objective, and the combination of a FT 495 dichroic mirror (Zeiss, Germany) and a band-pass BP 525/ 50 emission filter (Zeiss, Germany) situated on the light path between the objective used for light collection and the camera. The images were acquired with a 620 ms time exposure, at the minimum camera gain (G=1) and a digital sensitivity gain at the value of 200, at a 3 μm altitude above the glass coverslip.

B.3 "Stripy" nanoparticles revisited

B.3.1 Image processing

The STM images were copied from the articles pdf. The red channel was used for the FFT analysis (shown as greyscale images in the Fig. 5.3A, Fig. 5.4 and Fig. 5.8). ImageJ was used for Fast Fourier Transform processing. The contrast and

brightness of the frequency-filtered images was automatically adjusted. There was no other processing or alteration of the images.

B.3.2 Nanoparticle synthesis

A saturated solution of $NaBH_4$ in HPLC grade ethanol was prepared, and left stirring at 4 °C for 30 minutes. Meanwhile 32 μmol of $HAuCl_4$ was dissolved in 18 mL of HPLC grade ethanol and left to stir for 10 minutes. 32 μmol of ligand or ligand mixture was added to the gold salt mixture and left stirring for another 10 minutes. To this gold and ligand mixture 7 mL of the $NaBH_4$ solution was slowly added drop wise. The solution turned from yellow, to orange, to brown and to a very dark brown. This mixture was left for a further two hours stirring to complete the reaction. The reaction was then transferred to the freezer to aid precipitation of the particles. The supernatant was removed, and the particles were resuspended in 10 mL of ethanol three times to wash away excess ligand. The absence of excess ligands was confirmed by NMR.

B.3.3 Solubility study

5 mg of 100 % OT-capped gold nanoparticles particles were suspended in 500 μL of THF and left undisturbed for 3 weeks. The concentration of nanoparticles was measured from the absorbance at 506 nm using an extinction coefficient $\varepsilon = 3.64 \times 10^6$ $M^{-1}.cm^{-1}$. The particles were first diluted in order to obtain a suitable absorbance ($A^{506} < 2$). The extinction coefficient was obtained (as Centrone *et al.*[3]) from Liu *et al.*[4]

B.3.4 Cell culture and nanoparticle delivery

HeLa cells were grown in Dulbecco's Modified Eagle Medium (DMEM) supplemented with 10 % FCS (v/v) and 1 % non essential amino acids (v/v), at 37 °C, 5 % CO_2. Cells (between passages 8 to 20) were plated at 1×10^5 cells/mL. For all experiments, nanoparticles (33 % MUS, 67 % MUS or 100 % MUS) were mixed with the complete medium (containing 10 % FCS) and added immediately to the cells. The cells were incubated for 3 hours (37 °C, 5 % CO2) with nanoparticles at a final concentration of 400 nM. The cells were then washed three times with PBS, fixed with 4 % paraformaldehyde/PBS (1 mL) for 15 minutes at room temperature, and then washed three times with PBS before adding purified water (2 mL). Fixed cells were stored at 4 °C until imaged by photothermal microscopy.

B.3.5 Photothermal microscopy

The cells were fixed and observed by photothermal heterodyne microscopy. The absorbing beam (523 nm, Nd:YLF frequency doubled laser) modulated at the frequency

ω ($\omega/2\pi = 692.5$ kHz) by an acousto-optic modulator and the probe beam (632.8 nm, HeNe laser) were focused on the sample using a Zeiss Achroplan 50× / 0.9 NA oil immersion objective. The beam intensities were respectively 0.44 mW and 10.65 mW. The forward interfering fields were collected with a Zeiss Achroplan 40× / 0.8 NA water dipping objective and sent onto a photodiode. The beat signal at the frequency ω was extracted via a lock-in amplifier and integrated over 10 ms. All images were completed by moving the sample with a piezo-electric device (Physik Instrumente) over the fixed laser beams and were taken at the altitude of 1 μm above the glass coverslip surface.

B.4 Active delivery of gold nanoparticles

B.4.1 Capsules

The polyelectrolyte microcapsule were used as received from the group of Prof. W. Parak, Philipps Universität Marburg (Germany), where they were produced. Briefly, the microcapsule was produced using a porous $CaCO_3$ core loaded with a mixture of PAH and 20 nm phosphine coated gold nanoparticles. They were composed of 10 alternating layers of PSS and PAH, giving a shell composition of $(PSS/PAH)_5$, with a final positively charged surface (PAH). After that the core was removed using EDTA, leaving gold nanoparticles encapsulated in a $(PSS/PAH)_5$ shell.

For all experiments, the microcapsules were left to adsorb on the glass coverslip of an Iwaki dish filled with deionised ultrapure water for ~ 30 min.

B.4.2 Laser irradiation

To induce a damage to the shell of a microcapsule, single 100 ms illuminations were administered using a CW HeNe laser focused through a 50×/0.9 NA Achroplan Zeiss (Germany) objective on the wall of the microcapsule at a power of either 3.6 mW or 10.7 mW, as measured by a powermeter (Thorlbas, USA) at the output of the objective. The focus in the direction perpendicular to the glass substrate was set, using bright field imaging (see Sect. B.4.3), to the larger diameter of the capsule. Bright field imaging was used to determine the location where the illumination should be delivered. The sample was moved at the desired position using a combination of the microscope motorised stage (Prior Scientific Instruments Ltd, UK) for coarse movements and the piezo-electric stage (Physik Instrumente, Germany) for fine movements. The precise timing of the illumination was provided via the opening a HF202 Prior beam shutter (Prior Scientific Instruments Ltd, UK) for 100 ms through a computer assisted communication provided to its H30XYZ2 controller (Prior Scientific Instruments Ltd, UK).

B.4.3 Bright field imaging

The transmitted light illumination system was home built. It was composed of a X-Cite Series 120 (EXFO UK, UK) illuminator collimated through a EXFO microscope adaptor attached above the microscope as excitation source, an additional collimating lens (Thorlabs, USA), an Achroplan 40×/0.8 NA water dipping long working distance (2.5 mm) objective (Zeiss, Germany) to shed the light on the glass coverslip on which the microcapsules were adhering and an Achroplan 50×/0.9 NA oil objective below the dish to collect the transmitted light and send it to the camera.

The bright field images (colour 24-bit resolution) were acquired with a DC 310-C Thorlabs CCD camera (Thorlabs, USA), fasten on the side port of an Axiovert 200 microscope (Zeiss, Germany) using the Thorsight image/movie acquisition software (Thorlabs, USA).

B.4.4 Photothermal imaging

The absorbing beam (523 nm, Nd:YLF frequency doubled laser) modulated at the frequency ω ($\omega/2\pi = 692.5$ kHz) by an acousto-optic modulator and the probe beam (632.8 nm, HeNe laser) were focused on the sample using a Zeiss Achroplan 50×/0.9 NA oil immersion objective. The beam intensities were respectively 0.44 mW and 0.86 mW. The forward interfering fields were collected with a Zeiss Achroplan 40×/0.8 NA water dipping objective and sent onto a photodiode. The beat signal at the frequency ω was extracted via a lock-in amplifier and integrated over 10 ms. All images were completed by moving the sample with a piezo-electric device (Physik Instrumente) over the fixed laser beams and were taken at the altitude indicated. The images were acquired with a size of 128 × 128 pixels, with a pixels size of $\sim$48.4 nm.

B.4.5 Image treatments

The bright field images were extracted from the avi file format movies using the software ImageJ 1.44i (NIH, USA) and saved in a TIFF file format.

Some of the photothermal images of a microcapsule (Sect. 6.3.2) were filtered using the FFT bandpass filter of ImageJ, setting up the upper limit to 256 pixels and the lower one to 1 or 2 pixels (as indicated in the text).

B.5 Bibliography

1. J. W. Slot and H. J. Geuze. A new method of preparing gold probes for multiple-labeling cyto-chemistry. *European Journal of Cell Biology*, 38(1), 87–93, 1985.

2. R. Levy, N. T. K. Thanh, R. C. Doty, I. Hussain, R. J. Nichols, D. J. Schiffrin, M. Brust and D. G. Fernig. Rational and combinatorial design of peptide capping Ligands for gold nanoparticles. *Journal of the American Chemical Society*, 126(32), 10076–10084, 2004.

3. A. Centrone, E. Penzo, M. Sharma, J. W. Myerson, A. M. Jackson, N. Marzari and F. Stellacci. The role of nanostructure in the wetting behavior of mixed-monolayer-protected metal nanoparticles. *Proceedings of the National Academy of Sciences of the United States of America*, 105(29), 9886–9891, 2008.

4. X. Liu, M. Atwater, J. Wang and Q. Huo. Extinction coefficient of gold nanoparticles with different sizes and different capping ligands. *Colloids and Surfaces B:Biointerfaces*, 58(1), 3–7, 2007.